The effect of microstructure and impurities on transport in actinide oxide films

Symington, Adam

Award date:
2020

Awarding institution:
University of Bath

Adam R. Symington

For the degree of DOCTOR OF PHILOSOPHY

The Effect of Microstructure and Impurities on Transport in Actinide Oxide Films

University of Bath

Department of Chemistry

30th March 2020

First printing, 13/12/2019

Declaration of Authorship

I, A R.Symington, declare that this thesis titled "The Effect of Microstructure and Impurities on Transport in Actinide Oxide Films" and the work presented in it are my own. I confirm that:

- where the thesis or any part of the thesis such as a published paper, has been produced jointly with others, that a substantial part is the original work of myself, and

- where the thesis incorporates material already submitted for another degree, the extent of that material and the degree, if any, obtained.

Signed:

_____

Date:

_____

Acknowledgements

I would like to thank my supervisor, Prof. Stephen C. Parker for his support, guidance and patience during my time at Bath. The freedom that was afforded to me allowed me to develop so many skills and I will be eternally grateful. I appreciate that I was not the easiest person to manage and I am sorry that I feel that Python is superior to fortran. Marco Molinari also deserves thanks for his continual support and guidance, we didn't always see eye to eye but our collaborations have yielded some really nice work and a good friendship. Thanks to James Grant for his help in the first year and for introducing me to scientific programming. The work in chapters 6 and 7 built on the work of Nick Williams and the work would not have been possible without his guidance and support.

Thanks to all the members of the Parker group, past and present, Joe / Joel, Wenkai, Layorla, Jakub, Marco, Josh, Tom, James / Andrew / Megan (From right to left). I enjoyed the political debates, conferences and work talk. Thanks to the members of CompChem for all of the trips to the pub, Phil, Georgie, Alex, Dan, Jacob and Victoria. A massive thank you needs to go to Andrew, my best friend, pub quiz partner and Python mentor, frankly my PhD would not have been completed without you. Thanks to all my friends who drank with me over the years, Olivia, Chris, Ali, Arthur, Doug, Martha, the Route 17 lads - Jack, Patrick, Peter, James, James, and the 3 Anglo lads, Ben (the sparkly eyed man), James (he likes to party), Joel (the sparkly eyed man), Charlie (DSS) and Jonnie.

Alice, thank you for putting up with me over the past three years, thank you for

letting me explain grain boundaries to you with coins and for being my favourite human/device/companion. Finally to my parents, grandparents, aunties and uncles for helping me fulfil this dream. Lynne, Gordon, Alison and Sinead thank you for helping along the way. My dad, while an appalling person to have a scientific conversation with has sacrificed so much to give me and my brother such a great start in life.

Abstract

Materials are never perfect. In a perfect world all materials would be single stoichiometric crystals but in reality they are not. In reality materials contain non stoichiometric defects, such as Frenkel and Schottky defects, chemical defects, such as foreign anions and cations substituted at lattice sites or free in the lattice and structural defects, such as surfaces, grain boundaries and dislocations. Furthermore, these different types of defects can combine, giving rise to further complexity. Predictions based upon stoichiometric materials are valid but without taking into account the atomistic effect of defects they neglect the reality of the state of a material. The main aim of this work is to utilise computational techniques to gain an understanding on how defects and combinations of defects influence and define the chemistry of UO_2 and CeO_2, and to ascertain methods for improving the function these materials. This thesis investigates the structure and dynamics of three structural defects (Surfaces, Grain boundaries and Surface-Grain boundary junctions) and how they are modified when the material is doped with foreign cations.

This thesis begins with an investigation of the surfaces of CeO_2 and M^{3+} doped CeO_2 surfaces in the presence of water and carbon dioxide adsorbants. The results demonstrate that M^{3+} dopants have a significant effect on the adsorption properties of water and carbon dioxide and alter the particle morphology of CeO_2 under certain conditions of temperature and pressure.

Analysis of UO_2 and CeO_2 grain boundaries has also been conducted and when doped with M^{3+} grain boundaries have significantly altered the structure, segrega-

tion and transport properties.

Finally, grain boundary-surface junctions have been investigated and M^{3+} dopant segregation explored. Dopants are predicted to segregate preferentially to the surface-grain boundary junctions followed by the surface and grain boundary.

A combination of DFT and potential based atomistic computational modelling has been used. Adsorption of water and carbon dioxide at the surface has been studied with density functional theory energy minimisation calculations, while potential based molecular dynamics simulations were used to evaluate transport properties in grain boundaries and defect segregation has been studied with potential based Monte Carlo simulations.

The results presented in this thesis provide insight into the effect of these different types of defects and allows experimental and further computational work to be carried out with a greater understanding of the effect of defects

At the end of the day, I have learned a lot

- Karl Pilkington

Contents

Publications

Publications related to this Thesis

1. A.R.Symington, M. Molinari, N.A.Brincat, N.R.Williams and S.C.Parker, Defect Segregation Facilitates Oxygen Transport at Fluorite UO_2 Grain Boundaries. *Philos. Trans. R. Soc. A*, 377(2152): 20190026, 2019. doi: 10.1098/rsta.2019.0026.

2. A.R. Symington, M. Molinari, J. Statham.;J. Wu, S. C. Parker, The role of dopant segregation on the oxygen vacancy distribution and oxygen diffusion in CeO_2 grain boundaries. *J Phys Energy*, 1(1): 042005, 2019. doi: 10.1088/2515-7655/ab28b5.

3. M. Molinari, A. R. Symington, D. C. Sayle, T. S. Sakthivel, S. Seal, S. C. Parker, Computer-Aided Design of Nanoceria Structures as Enzyme Mimetic Agents: The Role of Bodily Electrolytes on Maximizing Their Activity. *ACS Appl. Bio Mater.*, 2(3): 1098-1106, 2019. doi:10.1021/acsabm.8b00709.

4. A.R. Symington, J. T., M Molinari, A Marmier and S. C. Parker, surfinpy: A Surface Phase Diagram Generator. *J. Open Source Softw.*, 4(34), 1219, 2019. doi: 10.21105/joss.01210.

5. A.R.Symington, M. Molinari, S. Moxon, J. Flitcroft, D. Sayle, S. C. Parker, Strongly Bound Surface Water Affects the Shape Evolution of Cerium Oxide Nanoparticles. *J. Phys. Chem*, 124(6): 3577-3588, 2020. doi: 10.1021/acs.jpcc.9b09046

6. A.R.Symington, M. Molinari, S. C. Parker, Controlling Cerium Oxide Nanoparticle Morphology Using Carbonate Species. **Submitted JPCC** Available at 10.26434/chemrxiv.11522565.v2

Other Publications

1. J.M. Flitcroft, A. R. Symington, M. Molinari, N. A. Brincat, N. R. Williams, S. C. Parker, Impact of Hydrogen on the Intermediate Oxygen Clusters and Diffusion in Fluorite Structured UO_{2+x}. *Inorg*, 58(6): 3774-3779, 2019. doi 10.1021/acs.inorgchem.8b03317

2. A. R. McCluskey, J. Grant, A. R. Symington, T. Snow, J. Doutch, B. J. Morgan, S. C. Parker, K. J. Edler, An introduction to classical molecular dynamics simulation for experimental scattering users. *J. Appl. Crystallogr.* 52(3): 655-558, 2019 doi: 10.1107/S1600576719004333.

3. S. Moxon, A.R.Symington, J. Flitcroft, S. C. Parker, David J. Cooke, M. Molinari, The interaction of CO_2 with Surfaces of PuO_2: an ab initio investigation. **Accepted PCCP**

Presentations

Oral Presentations

1. Modelling the mineral-water interface of polycrystalline surfaces - Goldschmidt Barcelona 2019

2. Developing Software for Your PhD Research - surfin workshop Huddersfield - 2019 (Invited)

3. Predicting Cerium Oxide Nanoparticle Morphology: The Role of Surface Water - Bolland Bath 2019 - Presentation Prize

4. Dopants at Interfaces - Computational Chemistry Seminar Bath - 2019

5. Modelling Complex Interfaces In UO2 - Modelling Symposium AWE - 2019 (Invited)

6. Modelling the Interfaces of Fluorite Structured Oxides - SWCC Bath 2018

Poster Presentations

1. Predicting Cerium Oxide Nanoparticle Morphology: The Role of Surface Water - HPC Symposium 2019 - Poster Prize

2. Altering the Properties of Fluorite Oxide Interfaces with Trivalent Impurity Cations - Bolland Bath 2018 - Poster Prize

3. Trivalent Impurities Promote Oxygen Vacancy Segregation and Increase Oxygen Transport at Actinide Oxide Grain Boundaries - Plutonium Futures San Diego 2018 - Poster Prize

4. Against the Grain: The Effect of Grain Boundaries on the Diffusion Properties of Fluorite Oxides - SSCG 2017 - Poster Prize

Abbreviations

AGR: Advanced gas cooled reactor

BWR: Boiling water reactor

CCV: Charge Compensating Vacancy

CN: Coordination number

CSP: Concentrated solar power

DFT: Density Functional Theory

DNA: Deoxyribonucleic acid

EELS: Electron energy loss spectroscopy

GB: Grain Boundary

GDC: Gadolinium doped ceria

GDP: Gross Domestic Product

GGA: Generalised gradient approximation

HF: Hartree-Fock

LDA: Local density approximation

LSM: Lanthanum Strontium Manganate

MC: Monte Carlo

MD: Molecular dynamics

MOX: Mixed oxide

MSD: Mean squared displacement

NASA : National Aeronautics and Space Administration

NPT: constant number, pressure and temperature

NVT: constant number, volume and temperature

OH: Hydroxyl Group

OSC: Oxygen Storage Capacity

PAW: Projector Augmented Wave

PBC: Periodic boundary conditions

PBE: Perdew Burke Ernzerhof DFT functional

PEMFC: Proton-exchange membrane fuel cell

PHWR: Pressurised heavy water reactor

PROX: Preferential oxidation

PWR: Pressurised water reactor

RDF: Radial distribution function

ROS: Reactive oxygen species

SCL: Space Charge Layers

SEM: Scanning electron microscope

SOD: Superoxide Dismutase

STM: Scanning tunnelling microscope

TPD: Temperature Programmed Desorption

TWCs: Three way catalysts

VASP: Vienna Ab-Initio Simulation Package

VMD: Visual Molecular Dynamics

V_o: Oxygen Vacancy

VOCs: Volatile Organic Products

WGSR: Water gas shift reaction

WW2: World War 2

XC: Exchange-Correlation

XRD: X-Ray Diffraction

YSZ: Yttrium-stabilised zirconia

1 Introduction

1.1 Global Warming

Since the conclusion of WW2, there has been a worldwide drive for improvements in education, healthcare and quality of life. This has been a largely successful endeavour, with the number of children in full-time education rising by 9% and a large increase in global healthcare spending [1]. This has been arguably due to a sharp increase in global GDP per capita and there is an strong link between energy consumption/generation and the development of the economy. In the distant past, work was conducted entirely by humans, and thus there was a sharp correlation between production and the workforce, e.g. without modern farming equipment, the output of a farm was based on the physical output of the workers. In the modern era, the amount of energy being produced has grown and brought with it a huge increase in productivity and thus GDP. While economically beneficial, the vast majority of energy has been generated from fossil fuels (figure 1.1) which release carbon dioxide and other greenhouse gases into the atmosphere.

While it is easy to paint a damning picture on greenhouse gases, they are critical to the survival of life on earth. The earths atmosphere helps trap radiation from the sun which bounces off the earth and is reflected by greenhouse gases back to the earth. These gases include ozone, nitric oxide, water vapor, methane, nitrogen dioxide and carbon dioxide. Since the industrial revolution, mankind has increased the concentration of these gases in the atmosphere through the burning of fossil fuels. Carbon dioxide and methane concentrations in particular have risen sharply

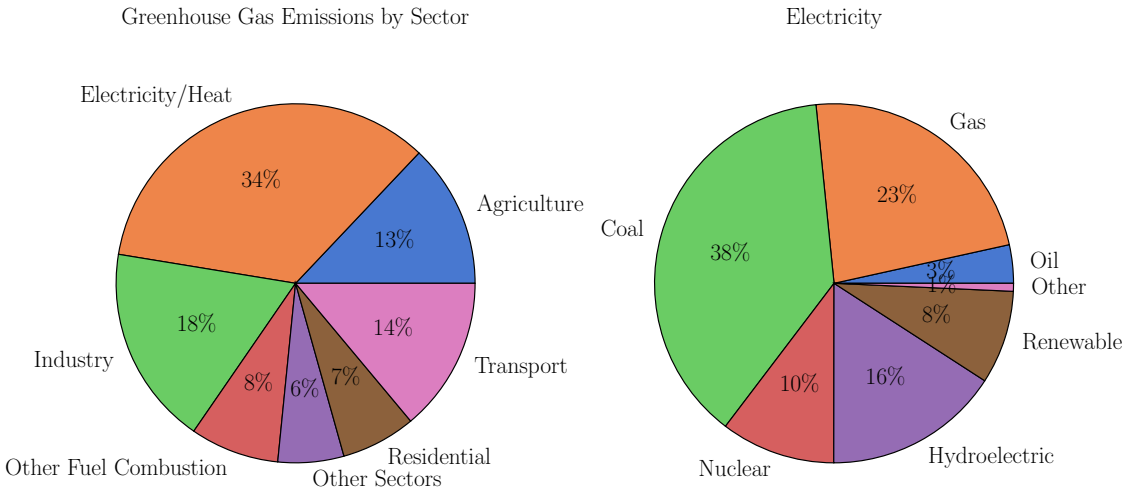

Figure 1.1: Global energy usage by sector and global energy production broken down into contributions from coal, oil, gas, nuclear, hydroelectric and renewables [2].

in recent times (figure 1.2).

Carbon dioxide concentration has fluctuated between 170 - 320 ppm for the last 800,000 years [4] and fluctuating concentrations of atmospheric CO_2 are normal. Since the start of the industrial revolution, atmospheric CO_2 has increased from 280 ppm to 405 ppm, an unprecedented change in geological terms (figure 1.3). Scientists believe that there is a 95% probability that the current warming is as a result of human activity industrial activity[5, 6, 7, 8].

Evidence shows that the average land temperature has increased by 0.8°C since the beginning of the 19th century and the average ocean temperature has risen by 0.06 degrees Celsius [10]. Furthermore, the Antarctic and Greenland ice sheets have lost 127 and 286 billion tonnes of ice per year since 1993 (figure 1.5), and global sea levels have risen by 8 inches in the 20th century. While fluctuations have occurred over the last 800,000 years, the rate of change can not be accounted for by natural factors [11].

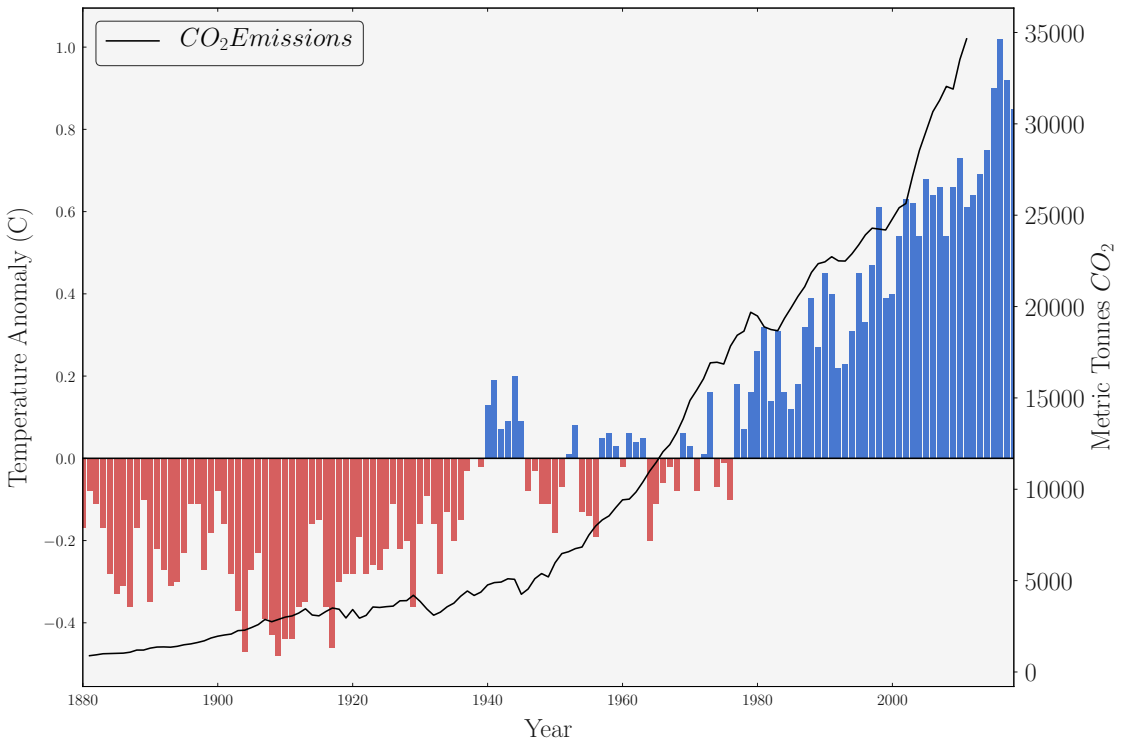

Figure 1.2: Carbon dioxide emissions and temperature change over the last 140 years. Data was taken and reproduced from Luthi et al.[3]

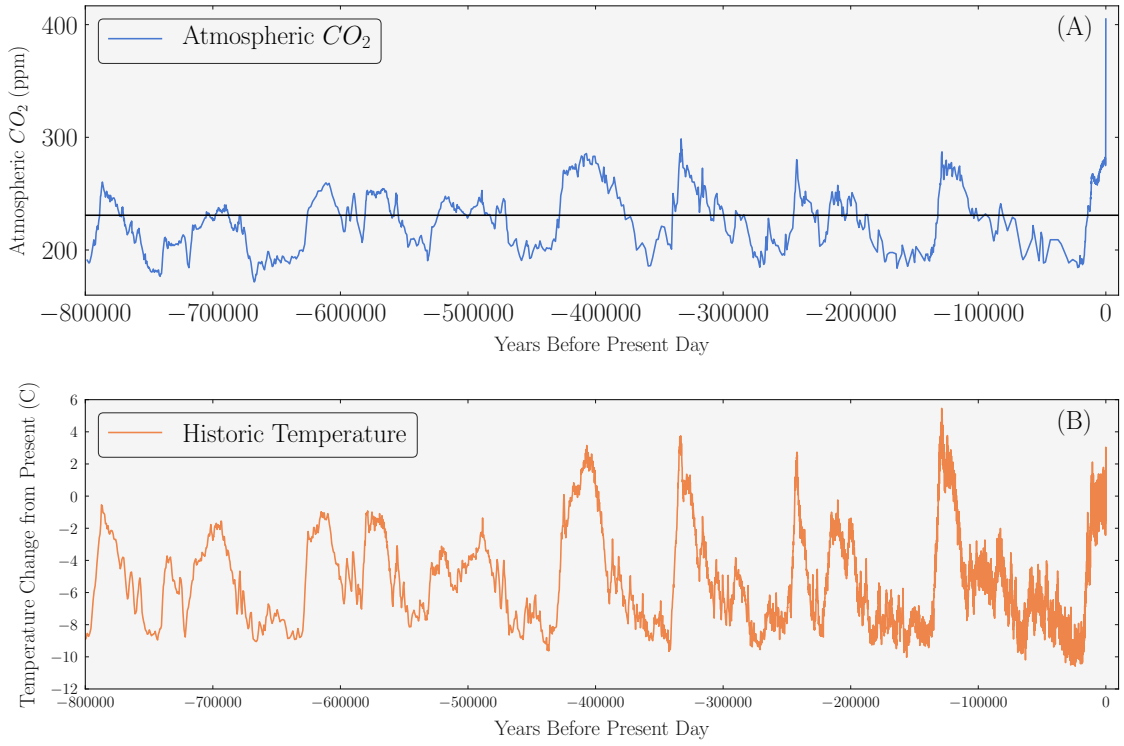

Figure 1.3: (A) Historic carbon dioxide emissions measured from the EPICA Dome C ice core in Antarctica. (B) Historic temperature change. Data was taken from the national oceanic and atmospheric administration (NOAA) [9]

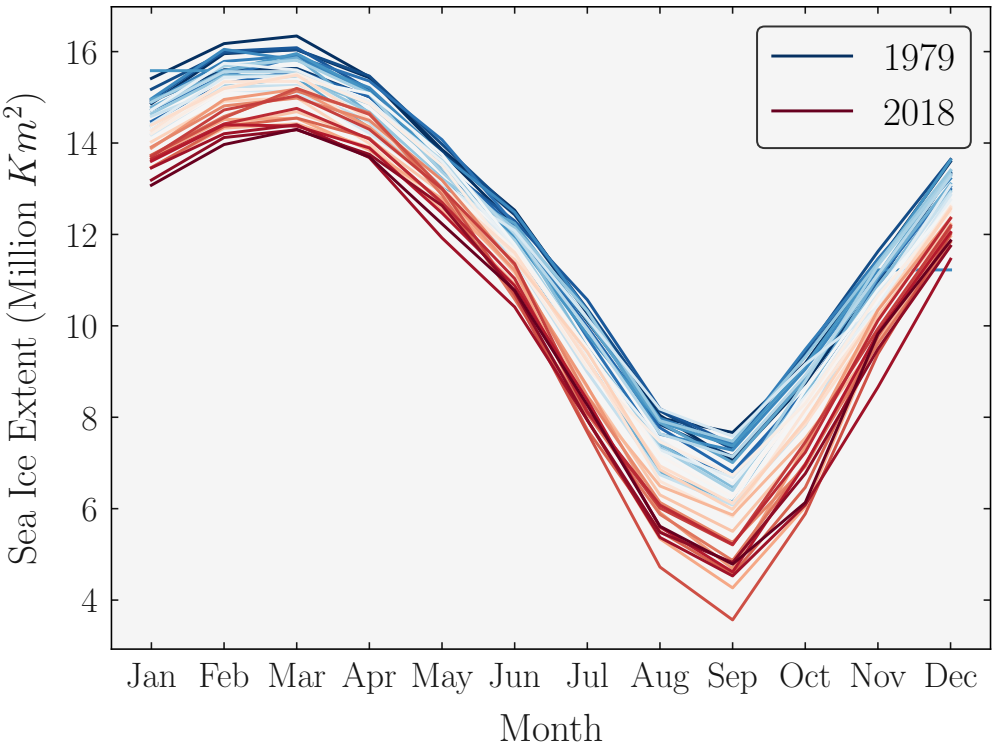

Figure 1.4: Monthly sea ice extent (In Million square kilometres) over the last 40 years [12].

1.2 Reduction of Greenhouse Gases

While the long-term goal is a 100% reduction in emissions, in the short term there are strategies to remove CO_2 from the atmosphere. There are various techniques being developed to actively remove carbon dioxide from the atmosphere.

1.2.1 Catalytic Removal of CO_2

A technique to remove carbon dioxide from the atmosphere is to use catalytic processes to convert greenhouse gases to a more benign species. Furthermore in industrial processes, greenhouse gases are often a by-product and their catalytic conversion into something useful can both offset the carbon cost of the reaction and increase the efficiency of the reaction.

Volatile organic products are a common by-product of industrial processes. They can be removed by thermal incineration or by eliminating solvents from the reaction. Both of these options have flaws, such as the high temperatures required and dangerous by-products produced by incineration. Volatile organic compound combustion can be achieved at lower temperatures and without the dangerous by-products (such as NO_x) with the use of a catalyst. It should be noted that the combustion of VOCs releases CO_2 into the atmosphere, but in terms of damage to the environment, VOCs are considerable worse.

It is possible to use catalysts to convert CO_2 into fuels such as methane and methanol with the use of a catalyst [13, 14]. Gases such as NO_x and N_2O can be converted into benign N_2 with vanadium oxide catalysts. Catalytic converters are now universally employed on car exhausts in order to reduce the severity of gas emissions [15]. These devices remove carbon monoxide (CO) and nitrogen oxide (NO_x) by converting them to CO_2 and N_2.

Catalytic removal of gases is a valuable method for greenhouse gas removal, there are several issues that limit their effectiveness. The obvious issue is that while these catalysts remove gases that are incredibly damaging to the environment, they

convert them into gases that are still damaging, e.g. a catalytic converter reduces the emissions of deadly CO, but releases CO_2.

1.2.2 Carbon Dioxide Sequestration

An obvious method for removing CO_2 from the atmosphere is to directly capture and store it. There are several different methods for carbon sequestration. Biological processes include forestation, where atmospheric carbon dioxide is converted into biomass [16], triggering algal blooms in the oceans by mixing ocean layers [17] and encouraging the growth of phytoplankton through iron fertilisation in the oceans [18]. Chemical carbon dioxide sequestration refers to the process of converting atmospheric CO_2 into solid carbonates. Physical carbon dioxide sequestration takes the biologically or chemically captured carbon. For example, biomass can be taken and buried underground, which mimics the process that originally created fossil fuels.

1.3 Renewable Energy

1.3.1 Hydroelectric

Hydroelectric power currently accounts for 6.8% of the worlds energy, 15.8% of the worlds electricity and countries like Brazil and Canada rely on it, generating 62.5% and 57.2% of their electricity by hydroelectric power plants [2]. The principles behind hydroelectricity are simple, the potential energy of water, stored in a reservoir, is used to drive turbines and generate electricity. The operational costs are low, and excluding the carbon cost associated with building the reservoir(which is considerable), operational reservoirs produce virtually no emissions. Furthermore, they have very flexible output levels which can be adjusted on demand to meet energy demands and overall, the energy for the consumer is very cheap. However, the construction of the reservoir is incredibly expensive and requires vast swathes of land be submerged. The Three Gorges dam in China is arguably one of the greatest engineering feats of the modern era and NASA has calculated that the sheer mass of water that has been displaced by the dam has increased the length of the earth's

day by 0.06 microseconds and altered the shape of the planet [19]. The reservoir cost $31.765 billion and displaced 1.24 million people living nearby and submerged 13 cities, 140 towns and 1350 villages [20]. Furthermore, if water levels drop below a certain threshold, such as through the effects of global warming, the reservoir becomes unsuitable for electricity generation, an issue currently plaguing the Hoover dam.

1.3.2 Solar

Solar energy is seen by many, as the future. Life on earth has depended on the sun since its emergence 4.5 billion years ago and given the abundance of solar energy throughout the universe, harnessing it for mankind's needs seems to be the logical future. There are two main ways to harness the power of the sun for energy production, concentrated solar power [21] and photovoltaics[22]. Concentrated solar power involves large arrays of mirrors which focus on a heat engine which drives a steam turbine. Photovoltaics are better known than CSP and involve solar panels. An advantage of using solar panels is that they can be applied to a wide range of applications, e.g. the roof of a house or a vast solar plant. The cost associated with solar panels has been steadily decreasing over the last two decades and is now at the point where it is affordable for personal energy production. Furthermore, once a solar farm has been constructed, there are virtually no emissions until the plant is decommissioned.

There are several disadvantages to solar energy however, there are areas on the planet that receive very little sunlight and nowhere receives any at night (when electricity demand increases). The amount of solar energy received is also heavily dependent on weather and so in certain areas, particularly outside of the tropics, cannot be relied upon. Furthermore, the production costs associated with building solar farms are incredibly high and some new materials are made of toxic elements (such as cadmium telluride) which creates future decommissioning issues.

1.3.3 Wind

Wind farms produce electricity from wind turbines that are driven by the wind. As with solar and hydroelectric power, once erected, wind farms do not produce any emissions and they have the added bonus of requiring very little maintenance. The obvious issue is that wind farms are totally dependent on the weather and thus are incredibly unreliable.

1.4 Fuel Cells

Fuel cells convert chemical energy directly into electricity and heat. There is no mechanical stage in the generation of electricity so there is minimal noise and they are highly efficient. Traditional combustion engines cannot directly use H_2 as a fuel, but fuel cells are capable of doing so. For example, proton exchange membrane fuel cells are capable of operating at low temperatures and utilise H_2. Solid oxide fuel cells (SOFCs) [23, 24, 25] are among the most effective fuel cells and display an efficiency of around 85% [24]. They are capable of taking fuel in the form of hydrogen or carbon based fuels and thus they are seen as a viable method of power generation in both the long and short term.

1.4.1 Operation

Typically, several cells are linked together, separated and supported by a connecting material. A SOFC is designed to have an impermeable solid electrolyte, separating the air and fuel sides. Oxygen containing air is injected in to the cathode side and the molecular oxygen adsorbs at the cathode surfaces and is reduced to O^{2-} ions. The cathode material is designed to have both ionic and electronic conductivity, the former allows electrons to distribute and facilitate oxygen reduction at the surface and the latter is to allow anions to move through the cathode to the electrolyte. The anions then adsorb into and diffuse through the electrolyte. Electrolyte materials need to be highly conductive for the anions and display minimal electrical conductivity (or the SOFC can short circuit). The electrolyte material also needs to be stable in different chemical environments as each side has different oxidation/re-

duction environment. Furthermore, the thermal expansion coefficient needs to be similar to that of the anode and cathode materials [26]. The anode material is usually porous to allow the fuel to penetrate within to aid its reduction by the anions. The anode needs to be a good ionic and electronic conductor, to transport anions from the electrolyte and to disperse the electrical current created by the oxidation of the fuel. For a SOFC using hydrogen as a fuel, the redox reactions are shown below

$$H_2 + O^{2-} \rightarrow H_2O + 2e^- \tag{1.1}$$

$$\frac{1}{2}O_2 + 2e^- \rightarrow O^{2-} \tag{1.2}$$

The oxidation of H_2 leaves behind two electrons which drives the electrical current, which flows through an external circuit and then reduces oxygen at the cathode. Electrons should only flow from anode to cathode and thus the electrolyte must be non conducting.

1.4.2 Materials

Traditionally the cathode material is lanthanum strontium manganite (LSM, $La_{1-x}Sr_xMnO_3$), the electrolyte is yttria stabilised zirconia (YSZ) and the anode material is a ceramic material such as Ni/YSZ.

$LaMnO_3$ is an intrinsic p-type conductor with a perovskite structure. It is doped with strontium atoms which sit on the La sites, this oxidises some of the Mn atoms from Mn(IV) to Mn(V) in order to maintain charge neutrality [27]. This makes it both an electronic and ionic conductor. It has a very high electrical conductivity (485 S cm^{-1}) and has displayed good electrochemical activity in the reduction of oxygen with activation energies in the region of 1.866 eV [28].

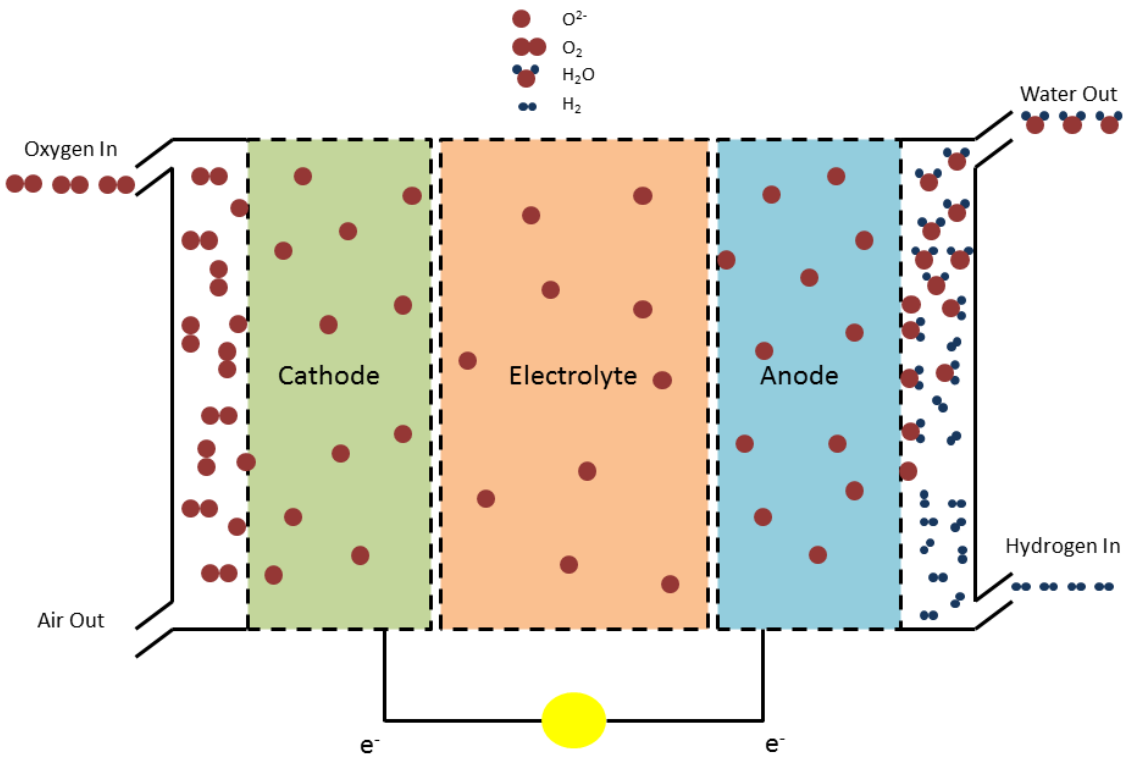

Figure 1.5: Schematic representation of a solid oxide fuel cell (SOFC). For clarity, the blue and red spheres are hydrogen and oxygen.

The electrolyte material is zirconia, doped with 8-10 mol% Y. Zirconia is doped with Y in order to stabilise the cubic phase, but the Y concentration is kept to a minimum because high levels of doping are associated with decreased conductivity due to dopant - dopant interactions and oxygen vacancy ordering [29]. However it does display the ideal properties for an electrolyte and has sufficiently high ionic conductivity at 1200 K [30, 31].

1.4.3 Research Challenges

There are considerable issues with current materials used in SOFC devices. Firstly, LSM and YSZ are chemically active and form layers of $La_2Zr_2O_7$ and $SrZrO_3$ which insulate the electrolyte - cathode boundary and reduce the ionic conductivity [32]. Furthermore, the electrical conductivity of LSM is dependent on the oxygen partial pressure and at low oxygen partial pressures the conductivity drops considerably [33]. The anode material also suffers from issues, it is not redox stable, is prone to Ni segregation over time and suffers from carbon deposition when carbon based fuels are used. Collectively this combination of materials also runs into problems

relating to the operating temperatures of the SOFC. These devices will only operate at temperatures exceeding 1200 K and there is now a drive to reduce the operating temperature in order to reduce the impact of thermal lattice expansions and thus increase the density that the cells can be constructed to, as well as allow cheaper connects to be used. The high temperatures also mean that long start-up and shut-down times are needed, so a reduction in operating temperature will improve safety, efficiency, overall durability and the stability of the components. The issue, and thus the drive for new materials, is that LSM cathodes suffer from polarization resistance and YSZ electrolytes display poor conductivity in the intermediate temperature range (500 - 1000 K). This has driven research into new materials.

1.5 Cerium Oxide

1.5.1 Ceria in Catalysis

Cerium oxide (CeO_2, ceria) is an important material in the field of catalysis. It can be employed either directly in the reduction of harmful pollutants or as a support material for other catalysts [34]. This is due to its high thermal stability[35] and high oxygen storage capacity (OSC) [36, 37], which allows ceria to release oxygen under reducing conditions and adsorb oxygen under oxidising conditions. The OSC is related to the ease of oxygen vacancy formation which results in the reduction of two cerium atoms from (IV) to (III) [38, 39]. This can be written as

$$O_O^x + 2Ce_{Ce}^x \rightarrow V_O^{\bullet\bullet} + 2Ce_{Ce}^{'} + \frac{1}{2}O_2(g), \tag{1.3}$$

where O_O^x is an O^{2-} ion and Ce_{Ce}^x is a Ce^{4+} ion at their lattice sites, the x indicates that these species are charge neutral with respect to their position in the cell. The left hand side of the equation therefore refers to the stoichiometric lattice. The $V_O^{\bullet\bullet}$ refers to an oxygen vacancy, $Ce_{Ce}^{'}$ is a Ce^{3+} ion and O_2 is oxygen gas. The vacancy is a missing 2- charge and thus it has a net charge of 2+, which is represented by $\bullet\bullet$. The formation of an oxygen vacancy leaves behind two electrons which reduce two

cerium atoms from 4+ to 3+. The Ce^{3+} ions have a net negative charge, and this is represented by $'$. The ease with which oxygen vacancies can form or be quenched allows both oxidation and reduction reactions to occur and this is the main reason for its success as a catalyst.

The most well known and successful application of ceria in catalysis are three-way catalysts (TWCs) [40, 41]. The catalyst is mounted after an internal combustion engine and its role is to oxidise carbon monoxide and any unburnt hydrocarbons and reduce NO_2/NO to N_2. A catalytic converter consists of a support material (usually doped Al_2O_3) with a honeycomb structure, with the inner channels coated by the active catalyst. The catalyst consists of an active phase, usually made of noble metals and a CeO_2 promoter. The oxidation reactions are promoted by Pt, while Rh is needed to catalyse the reduction. The conversion efficiency of the three pollutants is dependent on the air-to-fuel ratio and the removal of all pollutants is only obtained in a very narrow window, thus there must be a continual control of the oxygen pressure in the gas stream and also of the air and fuel flows within the engine. The role of CeO_2 in TWCs is to act as an oxygen buffer and extend the window of operation. Reduced ceria is able to store oxygen during oxygen-rich environments, promoting the reduction of NO_x. Whereas, CeO_2 is able to release oxygen in oxygen-poor environments, promoting the oxidation of CO/HC.

Along with NO_x, CO and HC, soot is one of the main pollutants emitted from a diesel engine. The health risks of diesel soot have been proven and there are now regulations governing the amount of emission [42]. Ceria is one of the best catalysts for soot oxidation due to its efficiency, but also because it can considerably lower the temperature of combustion, lowering the cost of process [43]. There are two mechanisms that are generally accepted for ceria catalysed soot oxidation.

Active Oxygen Mechanism

$$CeO_2 + C \rightarrow CeO_{2-x} + SOC, \tag{1.4}$$

$$CeO_{2-x} + \frac{1}{2}xO_2 \leftrightarrow CeO_2, \tag{1.5}$$

$$SOC \rightarrow CO/CO_2 + C_f, \tag{1.6}$$

$$O - Containing - gas + C_f \rightarrow SOC, \tag{1.7}$$

NO_2 Assisted Mechanism

$$CeO_2 + xNO \leftrightarrow CeO_{2-x} + xNO_2, \tag{1.8}$$

$$CeO_{2-x} + x2O_2 \leftrightarrow CeO_2, \tag{1.9}$$

$$NO_2 + C \leftrightarrow NO + SOC, \tag{1.10}$$

$$SOC \rightarrow CO/CO_2 + C_f, \tag{1.11}$$

$$O - Containinggas + C_f \rightarrow SOC, \tag{1.12}$$

In these schemes SOC refers to carbon-oxygen complexes at the surface and C_f refers to free carbon sites. The active oxygen mechanism involves a direct exchange of oxygen between the catalyst and the gas phase, while the NO_2 assisted mechanism

involves the high temperature induced oxidation of NO to NO_2.

TWCs and soot oxidation catalysts are the applications where ceria is a well established catalyst, and are of particular relevance to the work presented in this thesis. However, there are several emerging applications where ceria is receiving interest. Steam, dry and autothermal reforming of hydrocarbons [44], the water gas shift reaction / preferential oxidation of CO [45] and the oxidation of organic compounds [46], dehalogenation [47], partial hydrogenation[44], photocatalysis and thermochemical water splitting [48] are all applications that ceria is finding use in.

1.5.2 Ceria in Solid Oxide Fuel Cells

Ceria has been employed within solid oxide fuel cells in three ways

- Doped ceria is a promising electrolyte
- CeO_2 is used as a barrier layer to prevent a reaction between the cathode and electrolyte.
- CeO_2 is sometimes added to both the cathode and the anode as a catalyst.

The use of ceria as an electrolyte is the most promising of the three potential uses [34]. Ceria is doped with bi/trivalent cations in order to introduce charge compensating oxygen vacancies which act as charge carriers and improve the transport properties. The most well known example is gadolinium doped ceria (GDC) [49]. Pure ceria has poor ionic conductivity, and while this is improved with the addition of oxygen vacancies, this is accompanied by the reduction of cerium atoms and this has been linked to electronic conductivity, leading to short circuits. GDC does not have this problem because the presence of trivalent Gd means there is no reduction of Ce and thus no electronic conductivity.

A key consideration when doping ceria is the effect that the dopants have on the lattice of ceria. Dopants that are similar in size to cerium (such as Gd) are often

best because they cause minimum distortion to the lattice. Both experimental [50] and theoretical [51, 52] studies have shown that minimising the lattice distortion is key to achieving high ionic conductivities. Zha et al. have investigated the effect of dopant concentration on the conductivity of Sm doped CeO_2 and found that the ideal concentration was 15 mol% doping [53]. Considerable efforts have been made to understand the dynamics of oxygen vacancies, as these are the charge carriers in the electrolyte. Gopal et al. found that oxygen vacancy concentration increased with temperature and that vacancies tended to form clusters along the <111> and <110> directions [54]. Dhobabhai et al. found that at high dopant concentrations the conductivity is limited because dopant - vacancy clusters form and trap oxygen vacancies [55]. Molecular dynamics simulations have been employed to investigate the study oxygen diffusion in both ceria and doped ceria. It has been found that diffusion occurs via an oxygen vacancy mechanism, where oxygen hops into a nearby vacancy [56]. In stoichiometric ceria, oxygen vacancies form as the result of Frenkel pairs, whereas in doped ceria there are intrinsic oxygen vacancies (CCVs) which allow much faster diffusion. Oxygen vacancies tend to cluster along the <111> and <110> directions [57]. While it is generally accepted that Sm and Gd are the best dopants for increasing the conductivity of ceria SOFCs, there is still some debate. Recently, Dy doped ceria has been tested and found to have conductivities higher than Sm/Gd doped systems. These differences could be due to the synthesis conditions, analytical methods or the internal microstructure [58].

The overall message of these studies is that the conductivity of ceria increases with dopant (and thus oxygen vacancy) concentration until an upper limit is reached where oxygen vacancy mobility decreases due to clustering. Another crucial element that makes ceria a good candidate for electrolytes is that they have high mechanical strength and they are relatively unreactive towards other SOFC components.

1.6 Nuclear Energy

The Manhattan Project was a research and development undertaking during World War II that produced the first nuclear weapons through nuclear fission [59]. Nuclear

fission is the breakdown of a nuclear isotope (U^{235} U^{233} and Pu^{239}) into smaller nuclei (Sr^{90}, I^{129} Cs^{137}) by absorbing a neutron [60]. Nuclear fission was first harnessed in 1938 just prior to the Second World War, sparking a surge in research culminating in the Manhattan project [61] and the world's first nuclear explosion in the Japanese city of Hiroshima, changing the world forever. Between 1950 and 1989 the world's two superpowers, the USA and Soviet Union were locked in a nuclear arms struggle that threatened civilisation. A number of technologies were created from this arms race, one of which was harnessing the nuclear reaction for energy instead of destruction. In 1950 the first nuclear reactor was built in Idaho and 9 years later nuclear energy became commercially available.

1.6.1 Nuclear Fuel Cycle

The nuclear fuel cycle is the entire process from mining of the fuel to the production of electricity, including reprocessing and waste storage [62]. The front end of the cycle is the mining and production of the fuel material. Uranium ore is mined and milled into U_3O_8, known as yellowcake uranium [63]. There is a small amount of waste from this process in the form of waste ore. This waste ore has to be properly disposed of due to the high levels of radioactive material. U_3O_8 is then refined into UO_2 and is ready for use, although most is sent to an enrichment plant. UO_2 is enriched by first converting it into UF_6. The two isotopes are separated out in centrifuges and then converted back into UO_2. The final stage of this process is the fuel rod creation. UO_2 pellets are sintered at high temperatures (1400 - 1750C) in an argon atmosphere [64, 65] and encapsulated in a fuel rod composed of zircalloy.

The second stage of the cycle involves the fission process where the heat produced from nuclear fission is used to produce steam and drive turbines to generate electricity. Nuclear fission takes place in a reactor [66] and is accelerated by the addition of neutrons which split the nucleus. This process releases heat and another neutron causing a chain reaction. The overall reaction is moderated by control rods which prevent a runaway chain reaction by absorbing neutrons. These control rods are made of cadmium or graphite. If the process is not moderated then the reactor can go supercritical [67]. Control rods can be inserted or removed from the reactor in

order to regulate the reaction. The fissile isotopes are contained within fuel rods which are surrounded by water. The water is heated to steam and passes through turbines to generate electricity.

The final stage involves the reprocessing and removal of waste materials. The spent material typically contains 96% of the original uranium although U^{235} content is usually below 1% [68]. The other 4% is comprised of 1% plutonium and 3% high level radioactive waste. The spent material is typically reprocessed into enriched UO_2 or converted into a mixed oxide fuel, with plutonium taking up the role of U^{235}. Disposal of fuel with high levels of radioactive waste is as follows, the radioactive waste is incorporated into a borosilicate glass and placed in a steel container where it will go into long storage [69].

1.6.2 Nuclear Reactor

Nuclear reactors operate in a similar manner to traditional fossil-fuel power stations. Heat is used to generate steam which drives turbines. Each reactor consists of fuel, control rods, a coolant, a pressure vessel, a steam generator, a moderator and a containment mechanism [70].Nuclear fuel is traditionally based on uranium metal or uranium dioxide. Less common fuels include thorium dioxide [71], mixed uranium-plutonium oxide [72] and uranium-thorium mixed oxide fuels also exist [73]. Control rods are neutron absorbing materials e.g. cadmium and hafnium and they adsorb neutrons, reducing the number of neutrons that can induce fission and this reduces the reaction rate [74, 75]. The coolant and the reactor are contained within the pressure vessel which is built to moderate and contain the high pressure that is often reached (100-150 atm). A moderator reduces the speed of the neutrons and converts them from fast neutrons to thermal neutrons. Moderators are typically water or graphite [76].

The vast majority of reactors in use today are thermal reactors of which there are four main types. A thermal reactor has a moderator that slows neutrons released from the fission reactions in the reactor [77]. The four main thermal reactors are as follows;

- Pressurised water reactor (PWR) - The reactor core is completely surrounded by water, meaning that the core is only accessible when the reactor is completely offline.

- Pressurised heavy water reactor (PHWR) - Fuel elements are kept in individual pressure tubes. This allows them to be isolated and removed while the reactor is running.

- Boiling water reactor (BWR) - BWRs are similar to the PWR design but the coolant is used to directly drive the steam turbines.

- Advanced gas cooled reactor (AGR) - Rather than water, CO_2 is used as a coolant and the moderator is made from graphite. But it operates in the same manner as the PWR reactor.

A less common type of reactor is the fast reactor [77]. A fast reactor lacks a moderator and the main fuel used is mixed oxide (MOX) fuel composed of uranium and plutonium. A moderator slows down neutrons so in its absence there are fast neutrons. Fission of uranium by fast neutrons is inefficient but fission of plutonium is efficient. Fission of plutonium produces more neutrons than uranium per event and a large portion of the non-fissile U^{238} is converted to Pu^{239} and Pu^{241}, which can undergo fission. These Pu isotopes undergo fission in the same manner as uranium in fast reactors. There are three main types of fast reactor;

- Burner reactors - Consume more plutonium than produced

- Breeders - Produce more plutonium than is consumed

- Iso-breeders - Produce and consume and equal amount of plutonium.

Fast reactors have the advantage of being able to fission actinides and so they could "burn" spent nuclear waste. These reactors can use several different sources of fuel,

the most common of which being UO_2.

1.7 Uranium Oxide - Nuclear Fuel

The main nuclear fuel material currently in use is uranium dioxide (UO_2). UO_2 has good thermal stability, a high melting point, good irradiation and chemical stability [78]. It has two main limitations, firstly it can be readily oxidised, this results in the formation of higher oxides like U_3O_8 which corresponds to a 36% increase in volume and can cause the fuel cell to crack. Secondly it has very low thermal conductivity allowing it to build up a lot of heat and this was the cause of the Fukishima disaster. It requires little extraction or separation from other natural ores and it is compatible with cladding designs. This research focuses only on UO_2 so this section will be limited to investigations on UO_2; however there are other fuel types in use and in development.

Pellets of UO_2 are sintered together into an arrangement that allows control rods to penetrate them. The pellets are arranged into fuel rods and then covered in cladding of a zirconium oxide and steel alloy. This alloy has good thermal and mechanical stability and is transparent to neutrons, so they are structurally solid and do not affect the reaction.

There is and always will be a need to improve the fuel rod to minimise environmental risk and improve safety. With UO_2 the main issue that still needs to be addressed is its susceptibility to oxidation from species containing oxygen e.g. water. With increasing oxygen content ($UO_2 > UO_{2+x} > UO_3$) UO_2 changes from a fluorite structure (CaF_2) to U_2O_5, U_3O_8 and eventually UO_3. U_3O_8 is approximately 36% larger by cell volume than UO_2 which causes the fuel pellets and thus the rods to expand and crack - compromising the integrity and safety of the reactor. Furthermore another issue is the build-up of fission gases (Xe, He and Kr) within the lattice and these tend to segregate together, forming bubbles which can cause cracking of the fuel rod. Fission products (Gd, La, Fe, Ba, Sr, Cs) also form and are incredibly toxic if allowed to enter the environment. Their role in the behaviour of the fuel is

also poorly understood. When the fuel rod is eventually removed from the reactor, the UO_2 within the rod is far from pure and contains a vast array of impurities and defects that are not fully understood. Research into the effect of these impurities on the oxidation of UO_2 is important for designing new processes for increasing the fuel lifetime, reducing the amount of hazardous waste and increasing the efficiency of the waste storage. Thus to understand the material properties of UO_2 fuel rods, we need to be able to assess the influence of a range of defects from extended defects e.g. surfaces, grain boundaries and dislocations, to point defects such as vacancies, interstitials and dopants/impurities.

1.8 Thesis Outline

With increasing concerns over the environment, energy security and air pollution, replacement technologies for the now outdated fossil fuels industry are required. In this thesis two materials, similar in structure but remarkably different in chemistry and applications have been investigated. Uranium oxide and cerium oxide share the same fluorite structure but find use in two vastly different fields that both aim to reduce global emissions and clean up the environment.

Details of the computational methodology employed in this work are discussed in Chapter 2. This chapter provides an overview of both quantum mechanical and classical methods and the theories on which they are based.

In chapter 3, density functional theory calculations on cerium oxide and doped cerium oxide surfaces are discussed. In chapters 4 and 5 water and carbon dioxide adsorption on these surfaces is discussed. Surface phase diagrams as a function of temperature and pressure have been generated and used to predict the particle morphology of ceria under certain conditions. In chapter 6, phosphate anion adsorption on the surface of ceria is discussed within the context of biomedicine.

In chapter 7, grain boundaries of uranium oxide and cerium oxide have been generated and simulated with molecular dynamics. The structure, stability and transport

of these boundaries has been discussed within the context of fuel cells and nuclear reactors. In chapters 8 and 9 the structure, stability and transport of doped uranium and cerium oxide grain boundaries is discussed.

Finally in chapter 10 the distribution of dopants within uranium oxide surfaces, grain boundaries and surface - grain boundary junctions is investigated with Monte Carlo simulations.

2 Computational Methodology

There are two distinct methods for simulating systems at the atomic level: quantum mechanical and potential based methods. Quantum mechanical methods model the electrons explicitly and use the electron density or wave functions of the system to predict the system properties. In contrast, potential-based methods do not model the electrons explicitly and instead treat the atoms as point charges. Potential-based methods use a set of parameterised equations to calculate the attraction and repulsion between atoms.

In the context of this thesis, energy minimisation, molecular dynamics and Monte Carlo are the main algorithms used. Energy minimisation is an algorithm that iteratively reduces the energy of the system by updating the atom positions until a pre-defined convergence criteria is met. Molecular dynamics is a sampling technique that uses Newton's laws to simulate a system through time. Monte Carlo is another sampling technique where the system is randomly perturbed (e.g. atom moves) and the moves are accepted or rejected based on the system energy.

In this thesis, energy minimisation with density functional theory has been used to investigate the adsorption of atmospheric molecules (water, carbon dioxide and phosphate) on cerium oxide surfaces. When studying the adsorption of molecules, highly accurate energies are needed, but the problem for modelling molecules interacting with inorganic surfaces is that the parameters for the atom-level or experimental descripton are not always well defined, thus DFT was used. Potential based molecular dynamics has been used to study the transport properties of grain

boundaries in cerium and uranium oxides. Grain boundary configurations need to be large (10,000 atoms) and while DFT is highly accurate, it is very computationally expensive and thus not suited for this problem. Potential-based Monte Carlo has been used to study the cation distribution in doped uranium oxide. While potential based molecular dynamics is a good tool to study the segregation behaviour of certain materials, cation diffusion is notoriously slow and the timescales required for cation segregation to occur make these calculations very computationally expensive, Monte Carlo allows this to be evaluated in a more efficient manner.

In this chapter the theory relating to the simulations used in this work will be summarised, followed by the algorithms used within these methods. These methods simply generate data, thus the approaches used to extract properties will also be discussed.

2.1 Quantum Mechanical Methods

The quantum structure of a system can be calculated through the Schrödinger equation:

$$\hat{H}\Psi = E\Psi \tag{2.1}$$

where $\hat{H}$ is the Hamiltonian operator, Ψ is the electronic wavefunction and E is the total energy of the system. The Hamiltonian operator [79] can be broken down into the operators for the kinetic and potential energy of the electrons and nuclei:

$$\hat{H} = T_n + T_e + V_{nn} + V_{ee} + V_{ne} \tag{2.2}$$

where T_e and V_{ne} are the kinetic and potential electronic operators, T_n and V_{nn} are the kinetic and potential nuclear operators and V_{ne} is the nuclear-electron interaction. The exact solution to the Schrödinger wave equation cannot be found for

multi-electron systems because V_{ee} prevents the wave function from being decoupled into a set of independent equations. For many-body (electron) systems the Born Oppenheimer approximation is used [80]. This separates the nuclear and electronic degrees of freedom. This approximation states that although the forces acting on the electrons and nucleus are the same, the mass of the electron is considerably less and thus the nucleus is essentially stationary with respect to the electrons. Now that the wavefunction can be separated into a nuclear and electronic component, the electronic wavefunction is solved for a fixed set of nuclear positions and thus only electronic terms need to be considered for the Hamiltonian:

$$\hat{H}_e = T_e + V_{ee} + V_{ne} \tag{2.3}$$

which can be more formally written as:

$$\hat{H}_e = -\sum_i \frac{h^2}{2m_i} \bigtriangledown_i^2 + \sum_{i \neq j} \frac{e^2}{r_{ij}} - \sum_i \sum_I \frac{e^2 Z_I}{r_{iI}} \tag{2.4}$$

where I and i refer to nuclei and electrons respectively, m is the mass, e is the charge of an electron, Z is the charge, r is the distance and $\bigtriangledown^2$ is the Laplacian operator). From this point, only the electronic terms will be considered.

2.2 The Hartree-Fock method

The Hartree-Fock method [81, 82] makes two key assumptions. The first is that the n-electron wavefunction can be approximated as a set of one-electron wavefunctions, meaning that the Hamiltonian is the sum of one electron Hamiltonians:

$$\hat{H} = \sum_i \hat{h}_i \tag{2.5}$$

where, because the Hamiltonian is comprised of single electron wavefunctions, the electron-electron interaction term can be dropped:

$$\hat{H}_e = -\sum_i \frac{h^2}{2m_i} \bigtriangledown_i^2 - \sum_i \sum_I \frac{e^2 Z_I}{r_{iI}} \tag{2.6}$$

where i and I denote electrons and nuclei respectively, m is the mass, e is the electron charge, r is distance, Z is charge and $\bigtriangledown^2$ is the Laplacian operator. This is known as the independent electron approximation. The Schrödinger equation can the be calculated for each one-electron wavefunction ψ_i to get the eigenvalue ϵ_i and the wavefunction of the system can be calculated from their product:

$$\begin{aligned} h_i \psi_i &= \epsilon_i \psi_i \\ \Psi &= \psi_1 \psi_2 ... \psi_i \end{aligned} \tag{2.7}$$

The second assumption reintroduces some electrostatic interaction energy due to other electrons, whilst maintaining the simplicity of the one-electron method. The mean-field approximation is used to achieve this. It states that each electron experiences an average field of the other electrons is the system. The Hartree potential term v_i is added to the one-electron Hamiltonian [83]:

$$\begin{aligned} v_i &= \sum_j \int \frac{\rho_j}{r_{ij}} dr' \\ \hat{h}_i &= -\frac{h^2}{2m_i} \bigtriangledown_i^2 - \sum_I \frac{e^2 Z_I}{r_i I} + v_i \end{aligned} \tag{2.8}$$

where the electron density (ρ_j) is given by:

$$\rho_j = |\psi_j|^2 \tag{2.9}$$

The electron density needs to be known in order to construct the Hamiltonian and solve the eigenvalue for the one electron. In contradiction, the electron density itself is calculated using the one electron wavefunction. Practically, the solution is an iterative process, whereby a trial set of one-electron wavefunctions (ψ_i) are used to construct the corresponding set of $\hat{h}_i$, which are used to generate the new ψ_i through the Schrödinger equation. The electron density can be recalculated and the process repeats until a solution is reached where the density generated by the wavefunction is equal to the density they produce. This is called the self-consistent field method and relies on the variational principle that states that the true ground-state energy of a system is less than or equal to the value produced by any trial Hamiltonian [84].

Further constraints must be applied in order to form an acceptable set of wavefunctions and these come from the fundamental physics of fermions. Fermions are characterised as having half-integer spin and obeying the Pauli exclusion principle, which states that no two electrons, possessing the same spin, can occupy the same quantum state. So the total wavefunction of the system (Ψ) must be anti-symmetric with respect to electron exchange, i.e the sign of the wavefunction is reversed when the position of two electrons is switched. The Pauli exclusion principle is enforced by writing the total wavefunction as a matrix determinant, known as a Slater determinant [85]:

$$\Psi = \frac{1}{\sqrt{n!}} \begin{bmatrix} \psi_1(x_1) & \psi_2(x_1) & \cdots & \psi_n(x_1) \\ \psi_1(x_2) & \psi_2(x_2) & \cdots & \psi_n(x_2) \\ \vdots & \vdots & \ddots & \vdots \\ \psi_1(x_n) & \psi_2(x_n) & \cdots & \psi_n(x_n) \end{bmatrix} \tag{2.10}$$

The Slater determinant for an n-electron system must also satisfy the requirement of normalisation. As the square of the wavefunction represents the electron density, the probability of finding the n electrons anywhere in space must be exactly unity:

$$\int ... \int |\Psi(x_1, x_2, ...x_n)|^2 dx_1 dx_2 ... dx_n = 1 \tag{2.11}$$

The restriction of orthogonality must also be enforced, which means that there is no net overlap for any two wavefunctions in a system:

$$\int \psi_i \psi_j dr = 0 (if i \neq j) \tag{2.12}$$

Both normalisation and orthogonality can be described together as orthonormality.

By approximating the exact n-electron wavefunction from Slater determinant, the Slater determinant that yields the lowest energy is selected by individually varying one-electron wavefunctions.

The final parameter in the Hartree-Fock method is a potential term:

$$U_{ij}^X = -\sum_j \psi_j(r) \int \frac{\psi * (r')\psi(r')}{|r - r'|} dr' \tag{2.13}$$

This is the exchange potential and represents a quantum effect felt between electrons of like spin at positions r and r'. The self-interaction occurs due to electrons experiencing their own field (when $i = j$ in 2.12). A corresponding effect between electrons of different spins is not accounted for. This is the correlation energy and must be incorporated by taking a different approach to approximating solutions to the Schrödinger equation [79].

2.3 Density Functional Theory

Hartree-Fock neglects electron correlation and the way in which each electron contributes to the field that is felt by the other electrons is not actually independent.

Density Functional Theory (DFT) is an electronic structure method where the many electron wavefunction is replaced by the electron density. Unlike the Hartree-Fock method, density functional theory uses single electron wave functions to calculate the electron density.

This relies on the principle that the ground-state energy of a system can be expressed solely as a function of the ground-state charge density. This has the advantage of increasing the computational efficiency by decreasing the dimensionality of the problem. The 4N degrees of freedom of the spin orbitals is now reduced to just three spatial coordinates. Thomas and Fermi were the first to attempt this in 1927 [86, 87], however the exclusion of exchange and correlation effects made it inaccurate.

2.3.1 Hohenberg-Kohn Theorems

There are two theorems that DFT depends on and both come from the work of Hohenberg and Kohn in 1964 [88]. The first is that the external potential v_{ext} is a unique functional of the electron density (Ψ). The consequence of this of course is that because v_{ext} is part of the Hamiltonian, the many-body ground-state wave function is also a unique function of the electron density (ρ). Thus, all ground-state and excited-state properties can be determined by the electron density. The second is that the total energy can be calculated from the electron density:

$$E[\rho] = \int v_{ext}(r)\rho(r)dr + F[\rho] = E_{ne}[\rho] + F[\rho], \tag{2.14}$$

where,

$$F[\rho] = T[\rho] + E_{ee}[\rho], \tag{2.15}$$

where,

$$E_{ee}[\rho] = J[\rho] + E_{ncl}[\rho] \tag{2.16}$$

The functional in this equation produces the lowest energy for a system, provided it has the true ground-state electron density. The $F[\rho]$ term is the Hohenberg-Kohn functional and is composed of the kinetic energy term ($T[\rho]$) and a total energy term for the interelectronic interactions ($E_{ee}[\rho]$, which contains the term for the potential energy V_{ee}). The inter-electronic interaction energy is defined by a classical, Coulomb contribution ($J\rho$) and non classical, exchange and correlation contribution ($E_{nel}[\rho)$. The classical contribution is the only contribution to the functional that is explicitly known (if all contributions are known then the Schrödinger wave equation can be solved in full).

2.3.2 Kohn-Sham Equations

The Hohenberg-Kohn theorems do not offer a means to a solution. The work of Kohn and Sham in 1965 builds on the Hohenberg-Kohn theorems in order to provide a means of arriving at a solution [89]. Equations 2.15 and 2.16 can be combined:

$$E[\rho] = E_{ne}[\rho] + T[\rho] + J[\rho] + E_{ncl}[\rho] \tag{2.17}$$

$E_{ne}[\rho]$ and $J[\rho]$ were both defined by the Hohenberg-Kohn theorem but the other functionals were not defined. The kinetic energy ($T[\rho]$) is dependent on the electron velocities and is thus non local. This means that the kinetic energy has a complicated relationship with the electron density wherein only the spatial distribution of the electrons are considered. Previous methods failed to properly account for this as they tried to consider the kinetic energy entirely as a function of the electron density [86, 87]. The Kohn-Sham approach tries to overcome this by calculating as much of the kinetic energy as possible in an exact manner before using an approximation to deal with the rest.

The approximation uses a reference system of non-interacting electrons which is defined so as to have an identical electron density to the real system:

$$H_{ref} = \sum_{i=1}^{n}[-\frac{1}{2} \bigtriangledown_i^2 + V_{ref}(r_i)] \tag{2.18}$$

V_{ref} is the reference potential, which is designed to have an equal ground-state electron density to that of the true system. The ground-state energy of the non-interacting system and the real system is equal.

The solution for the reference system can be represented by a Slater determinant consisting of all of the single-electron functions known as Kohn-Sham orbitals. As the reference system contains non-interacting electrons, the single-particle solutions can be found independently of one another:

$$[-\frac{1}{2} + \bigtriangledown_i^2 + V_{ref}(r_i)] = \epsilon_i \psi_i \tag{2.19}$$

where ψ_i are the Kohn-Sham orbitals.

The kinetic energy of the non-interacting system can be determined exactly:

$$T_{ref} = -\frac{1}{2} \sum_{i=1}^{n} \int \psi_i^* \bigtriangledown^2 \psi_i d\tau \tag{2.20}$$

The reference system can now be added to the energy expression for the real system of interacting electrons:

$$E_{KS}[\rho] = E_{ne}[\rho] + T_{ref}[\rho] + J[\rho] + E_{xc}[\rho] \tag{2.21}$$

The exchange-correlation functional ($E_{xc}[\rho]$) contains the exchange and correlation energies as well as the remainder of the true kinetic energy (which arises from electron-electron interactions). All unknown parts of the system can be collectively grouped into the exchange-correlation functional:

$$E_{xc}[\rho] = (T[\rho] - T_{ref}[\rho]) + (E_{ee}[\rho] - J[\rho]) = T_{corr}[\rho] + E_{ncl}[\rho] \tag{2.22}$$

The final consideration is to find a reference potential (V_{ref}) that gives a non-interacting system with the same electron density as the real system. If $\bar{\rho}$ represents a trial density and E_0 is the ground-state energy of the real system, $E[\bar{\rho}] \geq E_0$ is true for both the interacting and non-interacting systems and thus $E[\bar{\rho}] = E_0$ is true only when $\bar{\rho}$ is the true electron density.:

$$V_{ref}(r) = V_{ext}(r) + \int \frac{\rho(r^{'})}{|r - r^{i}|} dr^{'} + V_{xc}(r) \tag{2.23}$$

where,

$$V_{xc}(r) = \frac{\delta E_{xc}}{\delta \rho(r)} \tag{2.24}$$

2.3.3 Exchange-Correlation Functionals

The uncertainty with the Kohn-Sham equations is grouped into the exchange correlation functional. Exact functionals are known only for free electron gas but there are a number of methods to approximate it.

Local Density Approximation

This is the simplest XC functional and is derived from the uniform electron gas model

[88]. The exchange-correlation energy is calculated locally, assuming a uniform electron gas. The exchange-correlation energy is assumed to depend solely on the local electron density where the functional is evaluated.

$$E_{xc}^{LDA}[\rho] = \int \rho(r)\epsilon_{xc}[\rho]dr \tag{2.25}$$

where $E_{xc}^{LDA}[\rho]$ is the energy per particle of the uniform electron gas of density ρ

The obvious assumption of LDA is that at a given position (r), the value of E_{xc} will be identical to that of the homogeneous electron gas. Hence, LDA has been shown to be effective for systems with uniform electron densities but less effective at describing systems where the electron density changes rapidly e.g. defects in solid-state materials [90]. Furthermore LDA overbinds electrons which causes an underestimation of bond lengths and an overestimation of atomisation and ionisation energies.

Generalised Gradient Approximation

GGA builds on the LDA functional by considering not just the local density but the gradient of the density at that point. In practice, GGA applies a correction to the LDA XC functional and this correction is dependent on the density gradient:

$$E_{xc}^{GGA}[\rho] = \int \rho(r)\epsilon_{xc}[\rho|\bigtriangledown\rho|]dr \tag{2.26}$$

This is achieved by a function with a single empirical parameter, that is fitted to experimental data for the rare gas atoms [90]. Alternatively, a correction can be calculated computationally [91], although this can cause the structure to underbind and this causes an overestimation of the lattice parameters. This is the method employed by the PBE functional, which is used in this work [92]. An alternative

version of the PBE functional was developed to correct the issues of PBE, PBEsol [93]. PBEsol was developed to improve the accuracy of calculated equilibrium properties of densely packed solids, by compressing the lattice.

Van der Waals corrected DFT

Most local functionals fail to correctly describe the van der Waals interactions that arise from dynamical correlations between shifting charge distributions. This is corrected in VASP by applying a dispersion energy to the Kohn-SHam DFT energy. This term is applied to the potential energy, stress tensor and interatomic forces.

2.3.4 The Hubbard Correction

A shortcoming of DFT is its failure to accurately describe strongly correlated systems of d and f-electrons. This is due to the fractional numbers of electrons that are assigned to atoms, which causes a self-interaction error that favours delocalised states [94]. The Hubbard coefficient is introduced to overcome this problem. This accounts for the strong on-site Coulomb interaction in a mean-field Hartree-Fock type manner [95]. There are two parameters, the effective on site Coulomb parameter (U) and the effective exchange parameter (J). In the Dudarev implementation, only the difference between these terms is important, with the individual parameters being insignificant [96].

2.4 The Application of DFT

2.4.1 Periodic Boundary Conditions

DFT is typically limited to simulations of 200 atoms which is clearly not on the scale of real chemical systems which have 10^{23} atoms. In order to gain meaningful results it is necessary to employ periodic boundary conditions where an infinite system is simulated by a finite number of species, this is illustrated in figure 2.1.

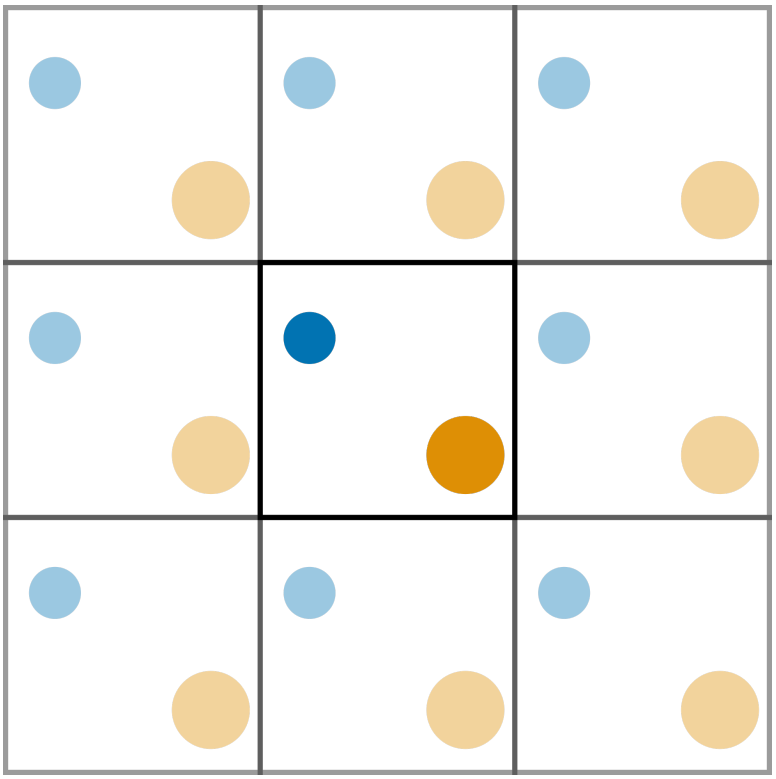

Figure 2.1: Schematic illustrating periodic boundary conditions

2.4.2 The Reciprocal Lattice

The reciprocal lattice is a representation of the crystal lattice defined in reciprocal space. This is routinely used by x-ray crystallographers, who define 3 reciprocal lattice vectors:

$$a* = \frac{b \times c}{a \cdot b \times c}; b* = \frac{a \times c}{b \cdot a \times c}; c* = \frac{a \times b}{c \cdot a \times b} \tag{2.27}$$

It is possible to construct an infinite reciprocal lattice from the primitive cell in the same manner as the real space lattice. The first primitive reciprocal lattice is known as the first Brillouin zone. The first Brillouin zone is important for DFT calculations because the wave function can be completely characterised within this space.

2.4.3 Plane Waves

Periodic boundary conditions allow the simulation of an infinite crystal from a finite number of species, however there are problems. Firstly, because the crystal is infinite, there are an infinite number of electrons and secondly, the wave functions of these electrons are spread across the entire crystal, resulting in the need for an infinite basis set [97].

Within Bloch's theorem, an electrons wave function in a periodic potential, can be expressed as a product of a wave-like term which has the same periodicity as the unit cell (known as a Bloch wave):

$$\psi_i(r) = e^{ik.r} f_i(r) \tag{2.28}$$

ψ_i is the wave function for an electron (i), k is the wave vector, which is in the first Brillouin zone and determines the frequency and direction of the wave-like term. The cell dependent part of the wave function consists of a discrete set of plane waves, where G corresponds to the wave vectors of all possible reciprocal lattice vectors:

$$f_i(r) = \sum_G C_i, G^{e^{iG.r}} \tag{2.29}$$

The wave function for each electron is the sum of all of the plane waves defined by the coefficients c_i and $k + G$:

$$\psi_n(r) = \sum_G c_{i,k+G} exp^{i(k+G)\bullet r} \tag{2.30}$$

Truncating the series allows the basis set to be limited to a finite size, because plane

waves with a higher kinetic energy contribute less to the wave function. In practical terms a plane-wave cutoff energy is chosen and only plane waves with a kinetic energy lower than this value are included. Convergence tests must be conducted in order to establish an appropriate cutoff value.

As the wave function is a continuous function of k, two points close together will have similar wave functions. Thus, ψ over a certain volume of k-space can be represented by a single k-point. Overall, the system can be described by a certain number of k-points, which removes the need for an infinite number of electrons. The k-points must also be tested in order to achieve an accurate representation of the system. The work in this thesis uses the Monkhorst-Pack scheme [98], which distributes k-points evenly in the system, centred on the origin of the reciprocal lattice ($\Gamma - Point$):

$$k = x_1 a* + x_2 b* + x_3 c* \tag{2.31}$$

where x_i dictates the density of the k-point grid in direction i and is determined by the folding parameter:

$$x_i = \frac{l}{n_i} with\, l = 1, ..., n_i. \tag{2.32}$$

The density of k-points is dictated by the material being simulated. For example, conducting materials require dense k-points and consequently have large folding parameters, whereas insulating materials can be represented with a coarser k-point mesh and a smaller folding parameter is used.

2.4.4 Pseudopotentials

Plane waves are not usually appropriate for expanding electronic wave functions because a large number of plane waves are needed to expand the tightly bound orbitals of core electrons and accurately represent the rapid oscillations of their wave

functions. The pseudopotential approximation assumes that the physical properties of a system are determined by the valence electrons [99] to a far greater extent than the core electrons. The approximation operates by replacing the core electrons and strong ionic potential with a weaker pseudopotential that acts on pseudo wave functions instead of the true valence electrons. The pseudo wavefunction is the same as the true wavefunction outside of a certain cutoff and so is only representative outside of this cutoff.

Pseudopotentials are categorised by softness, which measures both the magnitude of the cutoff radius and the smoothness of the function. Smooth pseudopotentials have a greater cutoff radiusand so need fewer basis functions but give a poor description of the atoms. Ultrasoft pseudopotentials has a large cutoff, high levels of smoothness and use an auxiliary function close to each ion to represent the rapidly varying charge density.

This work uses the projector augmented wave (PAW) method [100], which is similar to ultrasoft pseudopotentials as it uses localised auxiliary functions, but it treats the full all-electron wavefunction by using mathematical operations to convert the smooth pseudopotential back to the real wave function.

2.5 Potential-based Methods

Potential-based methods use a potential model to calculate the forces acting on atoms. In the same way that the Born-Oppenheimer approximation is used in quantum methods, it is applied in the reverse sense in potential-based methods. On the timescales that nuclei move, electrons have moved so much that their effect can be considered uniformly and thus atoms can be modelled as point charges. The potential model used in this study is based on the Born model of solids [101]. Under the Born model, it is assumed that the sum of all interactions gives the total lattice energy (E_{Tot}):

$$E_{Tot} = E_{Bond} + E_{Angle} + E_{Dihedral} + E_{Coulomb}, \tag{2.33}$$

where, E_{Bond}, E_{Angle} and $E_{Dihedral}$ are the energies associated with all of the bonded interactions, and $E_{Coulomb}$ is the energy associated with the electrostatic interaction between two charged particles, modelled using Coulombs law [102, 103]:

$$E_{Coulomb}(r_{ij}) = \frac{1}{4\pi\epsilon_0}\frac{q_i q_j e^2}{r_{ij}}, \tag{2.34}$$

where, q_i and q_j are the charges on particles i and j, e is the charge of the electron, ϵ is the dielectric permittivity of vacuum, and r_{ij} is the distance between the two particles. When q_i and q_j are oppositely charged, the particles are attracted [104].

2.6 Short-Range Interactions

When describing the short-range interactions a number of functional forms can be used which consider both attraction and repulsion. At very short distances electron clouds repel one another and there is repulsion between atoms, this represents the Pauli exclusion principle. At longer distances van der Waals interactions become more significant and attraction occurs. A number of short-range interactions used in this work are considered and are listed below.

2.6.1 Lennard-Jones Model

One commonly applied model is the Lennard-Jones (12-6) model, which considers the attractive London dispersion effects:

$$E_{attractive}(r_{ij}) = \frac{-B_{ij}}{r_{ij}^6}, \tag{2.35}$$

where B is some constant for the interaction, and r_{ij} is the distance between the

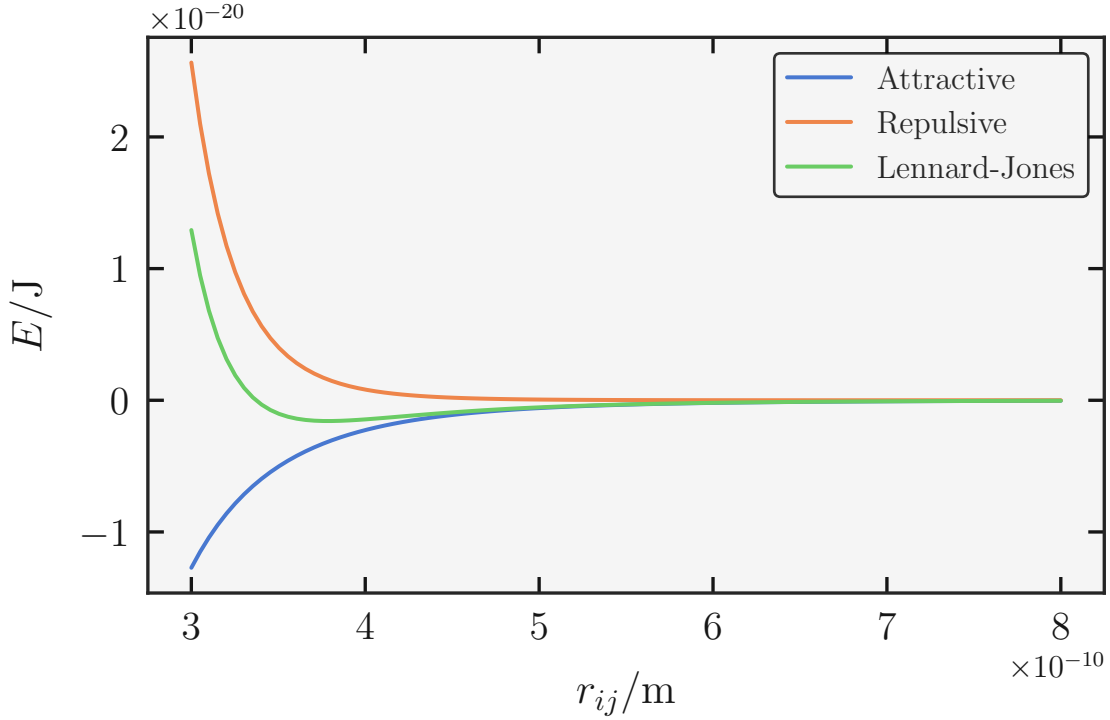

Figure 2.2: The potential form of each component of the Lennard-Jones potential for argon, using the parameters in Rahman et al. [105]

two atoms. The Pauli exclusion principle is repulsive and only presented over very short distances:

$$E_{repulsive}(r_{ij}) = \frac{A_{ij}}{r_{ij}^{12}} \tag{2.36}$$

again, A is some constant for the interaction. The total Lennard-Jones interaction is then the linear combination of these two terms:

$$E_{LJ}(r_{ij}) = E_{repulsive}(r_{ij}) - E_{attractive}(r_{ij}) = \frac{A_{ij}}{r_{ij}^{12}} - \frac{B_{ij}}{r_{ij}^{6}}. \tag{2.37}$$

2.6.2 Morse Potential Model

The Morse potential is well suited for modelling a typical potential energy curve for a chemical bond:

$$E_{Morse}(r_{ij}) = De_{ij}(1 - e^{[-B_{ij}(r_{ij}-r0_{ij})]})^2 - D_{ij}, \tag{2.38}$$

where r_m refers to the ion separation at the energy minimum of the well, De_{ij} is the depth of the well and B_{ij} is the curvature of the slope of the well.

2.6.3 Morl Potential

In this study we have used a rigid-ion potential model based upon that of Pedone et al. [106]. The model consists of a Morse potential with the repulsive terms of the Lennard-Jones potential to ensure that at short distances the repulsion is strong enough:

$$E_{Morse}(r_{ij}) = De_{ij}(1 - e^{[-B_{ij}(r_{ij}-r0_{ij})]})^2 - D_{ij} + \frac{A_{ij}}{r_{ij}^{12}}, \tag{2.39}$$

2.7 Computational Methodologies

2.7.1 Energy Minimisation

Energy minimisation iteratively computes the forces between atoms and adjusts their positions until a predefined convergence criterion is met. Energy minimisation follows the same basic procedure. An initial configuration is chosen, for example a experimental crystal structure. The forces are computed and the atomic positions are updated and the forces are computed. If the predefined convergence criterion is met the algorithm is terminated and if not, the process is repeated. There are two different approaches in energy minimisation: constant-pressure minimisation, where both the cell dimensions and the ions are allowed to relax, and constant-volume minimisation, where only the ions are allowed to relax. When the forces are equal to zero the system is at a minimum:

$$\frac{\delta E}{\delta r_i} = 0 \tag{2.40}$$

where the δE is the change in energy and δr_i is the change in ion position. The strain on the lattice is given by Hooke's law:

$$\epsilon = C^{-1}\sigma \tag{2.41}$$

where C^{-1} is the second-order derivative of the lattice energy with respect to σ is the stress, which is the sum of the applied and static pressure:

$$P_{static} = (\frac{1}{V})(\frac{\delta E}{\delta \epsilon}) \tag{2.42}$$

There are several common energy minimisation techniques, two common iterative techniques for energy minimisation, conjugate gradient and Newton-Raphson, will be discussed in more detail:

Conjugate Gradient

The conjugate gradient minimisation uses information from the previous step [107]. This method uses an initial steepest descent minimisation step:

$$r_{i+1} = r_i + \alpha_i S_i \tag{2.43}$$

where S_i is the gradient vector, α_i is the step length and r_i is the starting configuration:

$$S_i = -g_i \tag{2.44}$$

where

$$g_i = \frac{\sigma E}{\sigma r_i} \tag{2.45}$$

where g_i is the gradient. The steepest descent method is limited by the fact that the new displacement vector is orthogonal to the previous step, but not steps previous to that. Thus it can be incredibly slow to converge. Conjugate gradient performs an initial steepest descent step and then all subsequent steps calculate the displacement vector using information from the previous gradients:

$$s_i = -g_i + \gamma_i S_{n-1} \tag{2.46}$$

where,

$$\gamma_i = \frac{g_i^T g_n}{g_{i-1} g_{i-1}} \tag{2.47}$$

The transpose of the vector is represented by T:

Newton-Raphson

In Newton-Raphson, α is calculated as the inverse of the second-order derivative matric with respect to displacement [108]:

$$W_n = \frac{\delta^2 E}{\delta r^2} \tag{2.48}$$

$$\alpha = W_n^{-1} \tag{2.49}$$

This has the advantage of being able to find the minimum in a small number of steps, in fact in a harmonic energy well it will find it in a single step. The drawback however is that the calculation of the inverse Hessian matrix is computationally expensive.

2.7.2 Ensemble Properties

Energy minimisation gives a low-energy configuration that sits in the base of an energy well. In order to calculate an ensemble or "average" property the contributions from all possible structures need to be considered [109]. For example, take the energy E, the average energy of the system will contain contributions from all configurations. The probability of being in a given configuration needs to be considered, because unlikely configurations will contribute less to this average property while likely configurations will contribute more. The probability of being in a configuration is directly proportional to the "Boltzmann factor":

$$P_i \propto e^{\frac{-Ei}{k_B T}}, \tag{2.50}$$

where E_i is the energy at configuration i, k_B is the Boltzmann constant and T is the temperature. This relates to the partition function of the system:

$$q = \sum_{n=1}^{\infty} e^{-\frac{E_r}{k_B T}} \tag{2.51}$$

and the probability of being in a given state is given by

$$P_i = \frac{e^{-\frac{E_i}{k_B T}}}{q} \tag{2.52}$$

Here, the probability is normalised relative to the partition function. To calculate the average energy of the system:

$$E = \sum_{n=1}^{\infty} P_i E_i, \tag{2.53}$$

$$E = \sum_{n=1}^{\infty} (\frac{e^{\frac{-E_i}{k_B T}}}{q}) E_i, \tag{2.54}$$

In principle, if we know the partition function, then we know everything that we can about the system. However in reality it is practically impossible to compute. Higher-energy structures do not contribute meaningfully to the properties of the system and in reality systems will exist somewhere in the region surrounding the energy minimum. The challenge then is to accurately sample this region and calculate the properties of the system. Two common sampling techniques used for this are molecular dynamics and Monte Carlo and these will be discussed in the following sections.

2.7.3 Molecular Dynamics

Molecular dynamics is defined as solving Newton's equations of motion over a finite time period. The aim, is to probe the positions, acceleration and velocities on each atom. The acceleration is defined by Newton's second law of motion:

$$f = ma \tag{2.55}$$

where m is the mass of the particle, a is the acceleration and f is the force, which is the negative of the first derivative of the energy with respect to the atomic configuration:

$$f(r) = \frac{-\delta_{total}(r)}{\delta r} \tag{2.56}$$

where r is the atomic configuration. The force in equation 2.56 is a vector quantity, whereas in 2.55 it is not. It is necessary to obtain the force vector in three dimensions by multiplication of the unit vector in that dimension:

$$\mathbf{f}_x = f\hat{\mathbf{r}}_x, \quad \text{where } \hat{\mathbf{r}}_x = \frac{r_x}{|\mathbf{r}|}, \tag{2.57}$$

This must be carried out to determine the force acting on each particle in each dimension. Once the acceleration and positions are known, the new velocities and positions can be calculated. This is achieved by applying Newtonian equations, e.g. in the Velocity-Verlet algorithm[110]:

$$x(t + \Delta t) = x(t) + v(t)\Delta t + \frac{1}{2}a(t)\Delta t^2, \tag{2.58}$$

$$v(t + \Delta t) = v(t) + \frac{[a(t) + a(t + \Delta t)]\Delta t}{2}, \tag{2.59}$$

where x is the position of the particle, v is its velocity, a its acceleration, t is the current simulation time and Δt is the timestep of the simulation.The procedure works as follows, first the forces and accelerations on each particle are calculated, the new positions after the timestep are determined, the new velocities, based on the old and new positions and accelerations are calculated and the acceleration is

updated.

After an initial equilibration period, these steps can be repeated as many times as needed to generate sufficient statistics to make reliable predictions of some property. It is important to consider the size of the timestep. Too small and the calculations can be very expensive, too large and atoms can move unphysical distances.

There are two missing elements to the method so far, both relate to the initial starting configuration, the original positions and the starting velocities. The particle positions can be taken from an experimental crystal structure or based on prior knowledge of the system e.g. structure and lattice parameter. The initial velocities require more nuance, the total kinetic energy (E_K) of the system is dependent on the temperature of the simulation (T)

$$E_k = \sum_{i=1}^{N} \frac{m_i |\mathbf{v}_i|^2}{2} = \frac{3}{2} N k_B T, \tag{2.60}$$

where m_i and v_i are the masses and velocities of the particles, N is the number of particles in the configuration and k_B is the Boltzmann constant.

An ensemble is the name given to the conditions of a molecular dynamics simulation. Two ensembles were used frequently within the context of this thesis. The canonical NVT ensemble keeps the number of particles, volume and temperature constant throughout the simulation. The simulation uses a thermostat to control the temperature. The isobaric-isothermal NPT ensemble is similar to the NVT ensemble but allows the volume to vary while the overall system pressure is held constant using a barostat.

There are several thermostats that can be used, Nose-Hoover, Anderson and Berendsen [111, 112, 113, 114], however the simplest thermostat is velocity rescaling [115], where the velocities for a random subset of particles is altered:

$$v_i \leftarrow v_i \sqrt{\frac{T_{target}}{T}} \tag{2.61}$$

where t_{target} is the desired temperature and T is the average simulation temperature.

Barostats are used to control the simulation pressure and they involve carrying the simulation cell parameters and the atom distances. This is similar to the thermostating methods, where the simulation dimensions are altered by some value in a bid to control the pressure [116].

2.7.4 Property Calculations

In this work, two properties where calculated from the molecular dynamics trajectories. Tracer-diffusion data can be obtained from mean squared displacements (MSD):

$$\langle r_i^2(t) \rangle = 6 D_0 t, \tag{2.62}$$

where $\langle r_i^2(t) \rangle$ is the MSD, D_0 is the diffusion coefficient for oxygen, and t is time.

Residence time τ can be used to evaluate the average length of time that atom A spends within the coordination sphere of atom B. The τ was calculated from the residence time correlation function:

$$\langle R(t) \rangle = \langle \frac{1}{N_0} \sum_{i=1}^{N_t} \Theta_i(0) \Theta_i(t) \rangle, \tag{2.63}$$

where N is the number of atom A within a 3Å radius of atom B and $\Theta_i(t)$ is the heavyside function, which is 1 if the ith atom A is in the 3Å radius at t and 0 otherwise. Atom A was only considered to have left the 3Å radius if it did so for

at least 2 ps, which allowed molecules that temporarily left then re-entered to be included in τ. Equation 2.2 is integrated to calculate τ:

$$\tau = \int_0^\infty R(t)dt. \tag{2.64}$$

The electrostatic potential in one dimension across grain boundaries was calculated:

$$\Delta_\varphi(x) = -\int_{x0}^{x} E(x)dx, \tag{2.65}$$

where $E(x)$ is the electric field and given by:

$$E(x) = \frac{1}{-\epsilon_0}\int_{x0}^{x} \rho_q(x)dx, \tag{2.66}$$

where ρ_q is the total charge density perpendicular to the interface and ϵ_0 is the permittivity of free space.

2.7.5 Monte Carlo

Monte Carlo uses random numbers in order to propose moves to sample states. In practice, a random change is made to the system and based upon the energy of this change compared to the previous configuration, the move is accepted or rejected. Unlike molecular dynamics, the system does not evolve over time however it is useful at overcoming energy barriers by making unphysical moves. For example, cation diffusion in solid oxides is slow and and hence it would require long timescales for the cations to reach their equilibrium positions using molecular dynamics. In Monte Carlo, unphysical swap moves can be employed and atoms can jump to a new position in the configuration.

High-energy structures do not contribute in a meaningful way to the ensemble prop-

erty of interest and so Monte Carlo is biased towards lower-energy structures. The Metropolis algorithm is used to determine the probability of accepting a move. The probability of being in a given state for a thermodynamic system at equilibrium is

$$P_i^{eq} = \frac{e^{\frac{-E_i}{k_B T}}}{q} \tag{2.67}$$

In general the probability of finding a state can be given by

$$P_i(t + \Delta t) = P_i(t) + \sum_M (W_{j>i} P_j(t) - W_{i>j} P_i)(t)) \tag{2.68}$$

where $P_i(t)$ is the probability of being in configuration i at time (t) (note, this is computer time and not real time), $P_j(t)$ is the probability of being in configuration j at time t, $W_{i>j}$ is the transition probability from i to j, and $W_{j>i}$ is the transition probability from j to i.

This is restricted because $P_i(t + \Delta t)$ is dependent only on $P_i(t)$. At equilibrium the transition probabilities must be such that $P_i(t + \Delta t) = P_i(t) = P_i^{eq}$ so that,

$$\sum_{i \neg j} (W_{i>j} P_j(t) - W_{j>i} P_i(t)) = 0, \tag{2.69}$$

so the probability of being in a given configuration must be constant throughout the simulation. Thus, at any given point, the probability of transition from configuration i to j must be the same.

$$\frac{W_{i>j}}{W_{j>i}} = \frac{P(j)}{P(i)} = \frac{\frac{e^{\frac{-E_j}{k_B T}}}{N}}{\frac{e^{\frac{-E_i}{k_B T}}}{N}} = e^{\frac{-E_j}{k_B T}} \tag{2.70}$$

where E_i and E_j are the enegies for configurations i and j and $E_j i = E_j - E_i$. N cancels, and thus the ratio of transition states depends only on the energy difference between configuration i and j

In practice Monte Carlo has the following steps. Atom coordinates are initially assigned e.g. from an experimental crystal structure. The system is randomly perturbed e.g. $x_{i+1} = x_i + \Delta x_{ran}$. The energy of the new configuration is computed and if the energy has decreased, the move is accepted. If only the moves that lower the energy of the system are accepted then the system will never leave an energy well. The Metropolis method overcomes this and accepts proposed moves with probability,

$$P = min(1, \frac{-E_{ij}}{k_B T}) \tag{2.71}$$

where E_{ij} is the energy the energy of the new configuration. The method works by computing the probability and comparing it to a random number between 0 and 1. If P is less than the random number then the move will be accepted. This gives the potential for the system to move uphill.

2.8 Model Generation

The simplest method to get a starting configuration for any of the simulation techniques outlined is to take an experimental crystal structure. However these structures are not representative of the real material because they are not defective. In this work, extended defects (surfaces, Grain boundaries and T-Interfaces) in fluorite materials are being studied and first must be generated. In this section, the methods for generating extended defects will be discussed

2.8.1 Surface Structures

Surface slabs were generated using the METADISE code [117] by cutting bulk CeO_2 along Miller planes. By cutting the crystal along different planes, different surfaces,

with varying stability can be produced. Tasker defined three possible types of surface that can be generated depending on the cleavage location [118].

- Type I surfaces - Consist of neutral planes, with cations and anions existing in the same plane. These surfaces can be terminated at any plane in the unit cell. The {110} of CeO_2 is a type I surface.

- Type II surfaces - Consist of symmetrically arranged layers of cations and anions. The {111} of CeO_2 is a type II surface.

- Type III surfaces - Consists of charged layers of cations and anions and thus there is a dipole perpendicular to the surface. The dipole is removed by shifting half of one charged layer to the opposite surface.

The surfaces were generated using the two region approach [118]. In this method, the system is treated as two blocks, with two distinct regions in each, region 1 and region 2. Atoms in region 1 are allowed to relax and atoms in region 2 represent atoms in the bulk material and are held fixed. To simulate the bulk, the two boxes are modelled with the two regions 1 adjacent to one another, and to simulate the surface a single block is used with the surface being present at the top of region 1. This method is illustrated in figure 2.3. The energy of the bulk and the surface can be calculated from the energies of the individual blocks.

$$U_B = (E^B_{I-I} + E^B_{I-II}) + (E^B_{II-I} + E^B_{II-II}) \tag{2.72}$$

$$U_S = (E^S_{I-I} + E^S_{I-II}) + (E^S_{II-I} + E^S_{II-II}) \tag{2.73}$$

where the superscripts S and B refer to the surface and bulk components. $E_{I\text{-}I}$ refers to the energy of the atoms in region 1 of block 1 interacting with the atoms in region

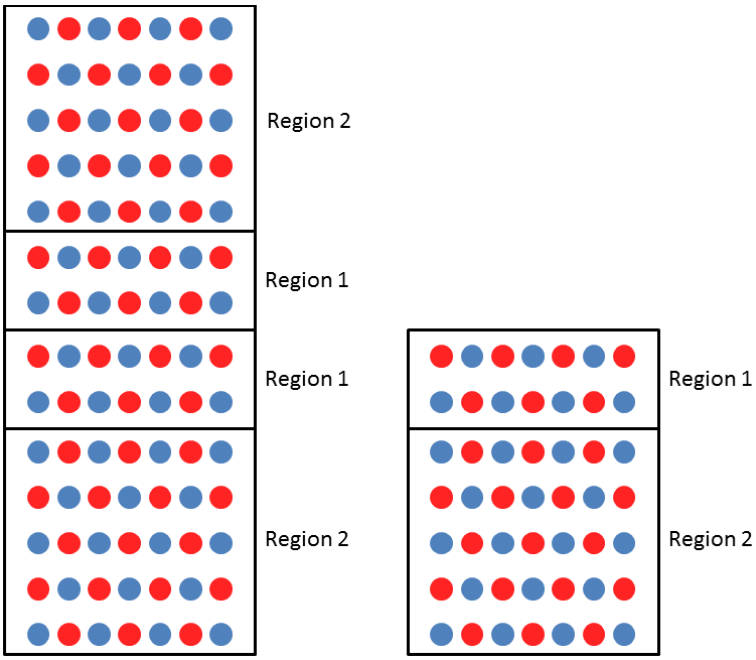

Figure 2.3: Schematic representation of the two region approach

1 of block 2. $E_{I\text{-}II}$ refers to the energy of the atoms in region 1 of block 1 interacting with the atoms in region 2 of block 2.

The surface energy can be calculated with these energies according to

$$\gamma = \frac{U_S - U_B}{S} \tag{2.74}$$

2.8.2 Grain Boundaries

Grain boundaries were generated using the two region approach. Block 1 was mirrored with respect to block 2 and an offset by a displacement vector was applied so as to create a shear plane. The grain boundary region consists of the two region 1's of the two blocks and these are allowed to relax while region 2 is held fixed. A scan of displacement vectors is performed in order to find the most stable displacement vector. A theoretical grid is constructed parallel to the surface with each grid point corresponding to a particular displacement. A scan is performed and the energy of all grid points is calculated in search of a low-energy structure. This is illustrated in figure 2.4

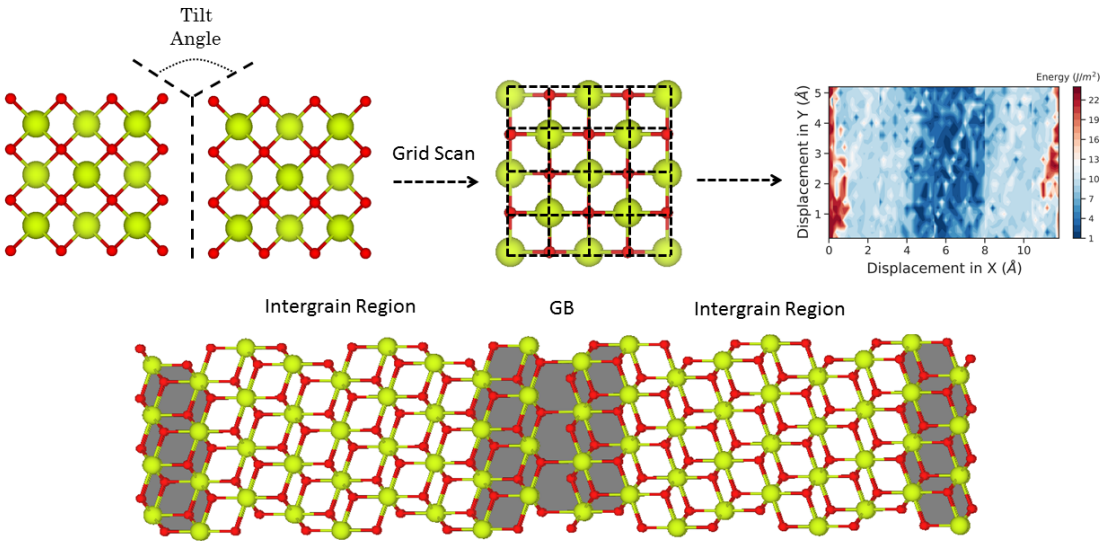

Figure 2.4: Schematic representation of grain boundary generation

Grain boundary stability is expressed in terms of formation and cleavage energy, defined as

$$E_f = \frac{E_{gb} - E_{bulk}}{A} \tag{2.75}$$

$$E_c = \frac{E_{gb} - 2E_{surf}}{A} \tag{2.76}$$

where E_{gb} is the energy of the grain boundary, E_{bulk} is the bulk energy, E_{surf} is the energy of the surface and A is the surface area. The cleavage energy is the energy to separate the two surfaces and the formation energy is the energy needed to form the grain boundary from the bulk.

2.9 Phase Diagrams

A surface phase diagram is a graphical representation of the different physical states of a surface under different conditions. The *surfinpy* code [119] was developed to

Figure 2.5: surfinpy logo

produce surface phase diagrams from *ab initio* data. At its core, *surfinpy* is a code that calculates the surface energy of different slabs at varying temperature and pressure and uses these surface energies to construct a phase diagram. The physical quantity defining stable surface compositions is the surface energy γ (Jm^{-2}). Using the slab method, which uses a simulation cell with two symmetric surfaces, the surface energy of a stoichiometric slab (γ_{Stoich}) can be calculated from the energy of the systems containing the slab ($E_{Stoich,Bare}$), the energy of ceria stoichiometric bulk (E_{Bulk,CeO_2}) and the surface area (S),

$$\gamma_{Stoich} = \frac{E_{Stoich,Bare} - E_{Bulk,CeO_2}}{2S} \tag{2.77}$$

In this work, doped surfaces have been studied and the surface energy of the doped surfaces (γ_{Doped}) was calculated according to

$$\gamma_{Doped} = \frac{E_{Slab,M_2O_3} - (E_{Bulk,CeO_2} + E_{Bulk,M_2O_3})}{2S} \tag{2.78}$$

where E_{Slab,M_2O_3} is the energy of the doped slab and E_{Bulk,M_2O_3} is the energy of the bulk dopant.

This provides the surface energy neglecting temperature and hence are not representative of real conditions. For surfaces with adsorbed molecules, the effect of temperature can be introduced as follows,

$$\gamma_{adsorbed,T,P} = \gamma_{bare} + (C(E_{ads,T} - RTln(\frac{p}{p^o}))) \tag{2.79}$$

where $\gamma_{adsorbed,T,p}$ is the surface energy of the surface with adsorbed species at temperature (T) and pressure (P), γ_{bare} is the surface energy of the bare surface, C is the coverage of adsorbed species and,

$$E_{ads,T} = E_{slab+adsorbant} - (E_{slab,bare} + n_{adsorbants}E_{adsorbant,(T)})/n_{adsorbant} \tag{2.80}$$

where $E_{slab,adsorbant}$ is the energy of the surface and the adsorbed species, $n_{adsorbant}$ is the number of adsorbed species and ,

$$E_{adsorbant,(T)} = E_{adsorbant,(0K,g)} - TS_{(T)} \tag{2.81}$$

where $S_{(T)}$ is the experimental entropy of the gaseous adsorbant in the standard state.

Crystal morphology

Surface energies can be used to predict the equilibrium morphology of a crystal. This is based on the work of Gibbs which states that for a given volume, the equilibrium shape with be that which minimises the total surface energy:

$$\gamma A = \sum \gamma_i A_i \tag{2.82}$$

where γ_i and A are the surface energy and surface area.

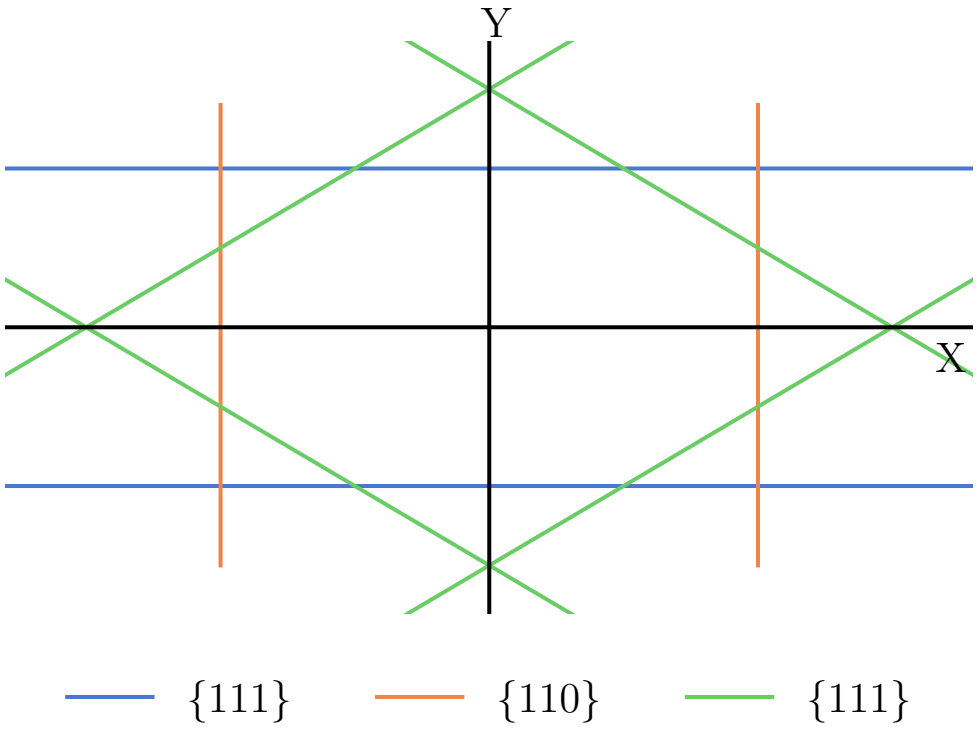

Figure 2.6: Schematic representation of a Wulff construction

This was built upon by Wulff who proposed that the crystal morphology formed would be a result of h_i, which is a vector, normal to the face from the centre of the crystal, being proportional to the surface energy [120]:

$$h_i = \lambda \gamma_i \tag{2.83}$$

where λ is a constant that depends on the absolute size of the crystal. This method is only valid for crystals where all surfaces are in equilibrium, neglecting kinetic effects, e.g. growth rate. A 2D schematic illustration of a Wulff construction is shown in figure 2.6.

3 CeO_2 Surfaces

Some of the contents of this chapter have been previously published by the author as part of this PhD project and can be found at the following reference A.R.Symington, M. Molinari, S. Moxon, J. Flitcroft, D. Sayle, S. C. Parker, Strongly Bound Surface Water Affects the Shape Evolution of Cerium Oxide Nanoparticles. *J. Phys. Chem*, 124(6): 3577-3588, 2020. doi: 10.1021/acs.jpcc.9b09046

As stated by Barteau in 1996 in relation to organic reactions on metal oxide surfaces [121], there are three key concepts in understanding the surface chemistry of metal oxides.

1. The coordination environment of the surface atoms

2. The redox properties of the materials

3. The surface oxidation state

There are three common surfaces expressed in cerium oxide (CeO_2, ceria) nanoparticles and each has a unique set of properties within the context of these concepts. Each surface subjects the surface cerium atoms to different coordination environments. It has been shown that oxygen vacancy formation at the surface is lower in energy than formation in the bulk [39, 122, 123], but also that this energy changes depending on the surface. Furthermore, this means that the reduction of ceria is more favourable at the surface than in the bulk and that different surfaces have

different redox properties.

Cerium oxide, CeO_2 (Ceria), and doped derivatives, are important technological materials. Thanks to the easily accessible redox conversion between Ce^{3+} and Ce^{4+} and the oxygen vacancy (V_o) tolerance of the fluorite structure, ceria enjoys a wide spectrum of applications like electrochemical sensors [124, 125], solid oxide fuel cells (SOFCs) [126, 127, 128, 129], catalytic exhaust treatment [130], hydrogen fuel generation [131] and biomedicine [132, 133]. Among its many applications, the redox capability is essential to the performance of the materials. As the redox reactions involved take place at the materials surfaces, the understanding of surface morphology and chemistry is key to the design and engineering of ceria based materials.

In subsequent chapters, the adsorption of carbon dioxide and water on ceria and doped ceria will be discussed, however the adsorption properties cannot be explored without an understanding of the bare surfaces. In this chapter the stoichiometric, reduced and doped surfaces of CeO_2 will be discussed.

3.1 Background

There are three low index surfaces of CeO_2 that are expressed in nanoparticles, the {111}, {110} and {100} surfaces (figure 3.1). The {111} surface has been shown computationally to be the most stable in terms of surface energy and is seen experimentally in nanoparticles. The {110} and {100} surfaces are less stable, with the order of stability following {111} > {110} > {100}.

The {111} surface is a Tasker type 2 surface [118]with alternating layers of cations and anions, thus each layer is charged but the 3-layer repeat units that make up the structure are neutral. At the {111} surface, cerium atoms are 7-fold coordinated. The {110} is a Tasker [118] type 1 surface, consisting of CeO_2 layers with a net zero charge due to the charge of anions and cations in each layer. Cerium atoms, are 6-fold coordinated at this surface. The {100} surface is a type 3 surface, with alternating charged planes but only two repeat units. This gives rise to a dipole

moment perpendicular to the surface. Cerium atoms are 6-fold coordinated at this surface.

Computational calculations have shown that the amount of surface relaxation that occurs is greatest on the {100} followed by the {110} and {111} surfaces [122, 134]. In order to overcome the dipole issue at the {100} surface, theorists have experimented with removing half of the oxygen on the top layer of the {100} surface and adding them to the bottom of the slab in order to remove the dipole moment[122, 135, 136, 137]. This displacement can be thought of as micro-faceting and occurs in nature. Different arrangements have been tested with the arrangement in 3.1 being the lowest in energy, although there are minimal differences in energy between different arrangements, this indicates that this layer can be easily altered. Experimental analysis of the {100} has not been conclusive, Norenberg et al concluded from STM images that the surface structure was that presented in Figure 3.1 [138], however high resolution electron microscopy experiments have also shown that the surface can be Ce, O and CeO terminated. The conclusion being that the small energy differences between surface models mean that the surface structure is in constant flux [139].

Due to the prevalence of CeO_2 in many catalytic reactions, there is significant theoretical and experimental impetus to improve the operation of these processes. There are two methods that are typically used to alter the properties of the material, and both involve controlling the reducibility of the material.

The first method, aims to control the nanoparticle shape and thus the expression of certain surfaces. Due to the different reduction energies, different shapes have different reduction properties and thus the shape can control the reducibility of the material. The ratio of surface area between the {111}, {110} and {100} surfaces determines the nanoparticle shape. The effect of shape has been studied in relation to several catalytic processes. Nanocubes (Displaying the {100} surface) or nanorods (displaying the {110} surface) are more reactive compared to nanocrystals (displaying the {111} surface) [139, 140, 141, 142, 143, 144, 145, 146]. For example, CO

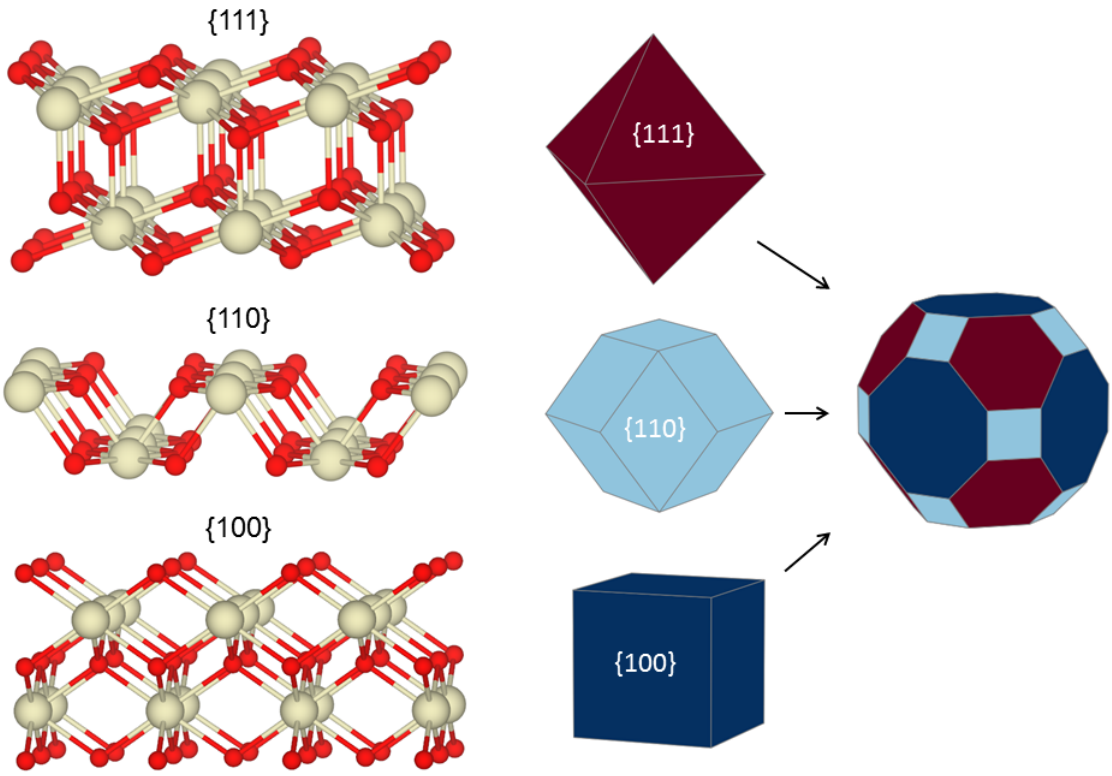

Figure 3.1: Surface structures for the {111}, {110} and {100} surfaces. The idealised morphologies for a {111}, {110} and {100} dominated nanoparticle are shown along with a nanoparticle displaying equal surface areas of each surface, to highlight the relationship between the three morphologies.

oxidation catalysts displaying the {100} and {110} surfaces are much more effective than those expressing the {111}. Morphology is also becoming a key concern in emerging applications. Nanocubes and nanorods being more active in dry reforming of methane. Furthermore, water - gas shift reaction (WGSR) catalysts, have a morphology dependent activity that follows Nanorods > Nanocubes > Octahedra, which is in parallel with the reducibility and thus the concentration of oxygen vacancies.

The second method involves, controlling the oxygen vacancy concentration through oxygen partial pressure (reducing ceria) or through doping the material with foreign cations such as Gd^{3+}, Sm^{3+} or Y^{3+}. A classic example is gadolinium doped ceria (GDC) for solid oxide fuel cells. The introduction of Gd^{3+} to the lattice promotes the formation of charge compensating oxygen vacancies which increases the ionic conductivity. Dopants are of particular note in catalysis because they can promote the formation of oxygen vacancies, but also alter the surface area of the catalyst. Gd^{3+}, Y^{3+}, and La^{3+} have been tested in conjunction with steam-reforming catalysts but found to decrease the activity.

Oxygen vacancies in ceria are the most studied surface defect as it is linked to the oxygen storage capacity. The extra electrons associated with the oxygen vacancy localise on to two cerium atoms, reducing them to the 3 oxidation state. It has been shown computationally that the reduction of the surfaces does not follow the order of stability, and is easiest on the {110}, followed by the {100} and {111} surfaces[39, 136, 147]. Experimental and theoretical studies have investigated the structure of reduced ceria and universally report, local relaxation/reconstruction around the vacancy with the oxygen atoms that surround the vacancy being displaced [39, 134, 136, 137, 147, 148, 149, 150, 151, 152]. At high vacancy concentrations it has also been shown that the vacancies cluster [138].

In this chapter, the low-index surfaces of ceria have been generated and analysed within the context of stability, reducibility and doping.

3.2 Calculation Details

The models used in this chapter and chapters 5 and 6 were generated using the METADISE code[153]. The slab method was used, where a finite number of crystal layers is used to generate two identical surfaces via the introduction of a vacuum gap perpendicular to the surface. A vacuum gap of 15 Å was used to ensure no interaction between the two surfaces between periodic boundary images. The {110}/{100} slabs are a p(2x2) expansion of the surface unit cell and consist of 13 and 7 atomic layers, which equates to 24 and 28 CeO_2 units respectively. The {111} slab is a p(2x3) expansion of the surface unit cell and consists of 12 atomic layers (24 CeO_2 units).

The slabs were modelled using density functional theory (DFT) with the Vienna Ab-Initio Simulation Package (VASP) within which projector augmented-wave pseudopotentials and a 500 eV cutoff were used. The sampling of the Brillouin zone was conducted using a 2x2x1 Monkhorst-Pack grid, with the third vector perpendicular to the surface. The generalized gradient approximation (GGA) exchange-correlation function of Perdew (PBE) was used along with a +U correction to account for on-site Coulombic interactions. A value of 5 eV for the cerium f states was chosen as it has been used successfully in other studies.

The surface energy, evaluated using DFT can be calculated according to,

$$\gamma_{doped} = \frac{E_{Slab} - E_{CeO_2,Bulk}}{S} \tag{3.1}$$

where E_{Slab} is the energy of the slab, $E_{CeO_2,Bulk}$ is the energy of the bulk and S is the surface area. The heat of surface reduction was calculated for the three low index surfaces of ceria by creating an oxygen vacancy through the removal of a surface oxygen atom. Two electrons are left behind and localise on the cerium ions neighbouring the vacancy. The heat of reduction is calculated according to

$$E_{Red} = \frac{E(CeO_{2-x}) + E(O_2) - E(CeO_2)}{2} \tag{3.2}$$

where E_{Red} is the reduction energy, $E(CeO_{2-x})$ is the DFT energy of the surface containing an oxygen vacancy, $E(O_2)$ is the DFT energy of oxygen and $E(CeO_2)$ is the DFT energy of the stoichiometric slab.

Gd^{3+}, Sm^{3+} and Y^{3+} cations dopants were investigated. Due to the difference between the 3+ charge of dopants and the 4+ charge of the cerium cations, two dopants cations were introduced and an oxygen atom was removed in order to maintain charge neutrality. All possible configurations of the anion and cation sublattices were generated and ranked according to the Ewald summation. The configuration with the lowest energy was used in this and subsequent chapters.

The surface segregation energies (E_{Seg}) of dopants have been calculated according to

$$E_{Seg} = E_{Def}^{Bulk} - E_{Def}^{Slab} \tag{3.3}$$

where E_{Def}^{Bulk} is the energy of dopants in the bulk and E_{Def}^{Slab} is the energy of dopants at the surface.

The surface energy of the M_2O_3 doped surfaces γ_{doped} was calculated according to

$$\gamma_{doped} = \frac{E_{Slab} - E_{CeO_2,Bulk} + E_{M_2O_3,Bulk}}{S} \tag{3.4}$$

where $E_{M_2O_3,Bulk}$ is the energy of bulk M_2O_3.

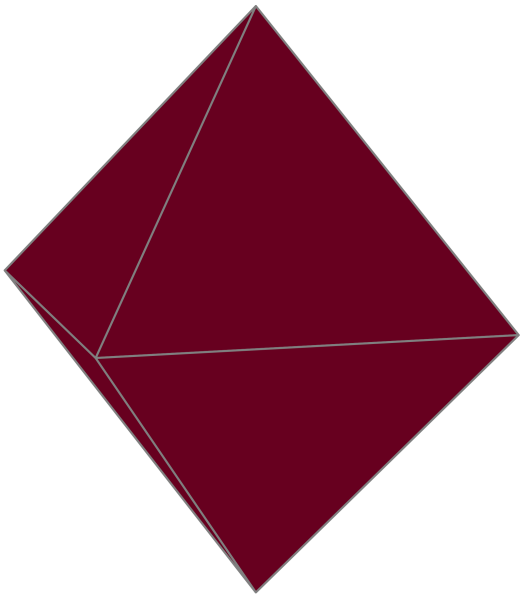

Figure 3.2: Equilibrium particle morphology generated from a Wulff construction. The shape is an octahedron displaying {111} surfaces.

3.3 Surface Energy

The structure of the three low index surfaces of ceria are shown in Figure 3.1. Surface energies follow the order {111} 0.71 > {110} 1.06 > {100} 1.44 Jm^2. The stability of the {111} can be rationalised by looking at the surface cerium coordination. Cerium at the {111} surface is 7 fold coordinated whereas 6 fold coordinated at the {100} and {110} surfaces.

Using a Wulff construction, the morphology of CeO_2 was calculated from the surface energies. The calculated morphology is a octahedral nanoparticle displaying the {111} surface (figure 3.2). This is in line with other theoretical and experimental work.

The heat of reduction of the three surfaces, which corresponds to the ease to remove surface oxygen ions, follows the order {111}, {100} and {110} with values of 1.98 eV, 1.55 and 1.07 eV respectively which agree with those already reported in the literature [136, 147, 154]. Literature studies have suggested oxygen vacancies are stable in the surface layer [136, 147, 154], but there is debate with others suggesting that vacancies prefer to exist in the sub surface [155, 156, 157]. In reality, different

distributions of 3+ cations and V_o are accessible, [158, 159]. For example Aparicio-Angles et al. have shown that “Gd can be placed fairly randomly in the surface" of CeO2 {111} as there is little difference in the energetics between the different configurations; however the $_o$ is more stable if situated in the second oxygen layer [159]. It has been shown previously, that at the operating conditions of SOFCs, oxygen vacancies will be mobile and hence occupy both surface and sub-surface sites. [160] Furthermore, large scale molecular dynamics simulations have shown that vacancies occupy both the surface and sub surface layers.[129]

3.4 Phase Diagrams

A surface phase diagram displays the most stable surface configuration as a function of temperature and pressure. Using the method outlined in the methodology, surface phase diagrams where the surface energy of CeO_2 is plotted as a function of oxygen partial pressure and temperature were generated. This method has been successfully implemented in other work [161, 162], as well as on CeO_2 [163] (later verified experimentally [164]) and more recently on fluorite-structured UO_2 [165].

Only stoichiometric CeO_2 surface and reduced $CeO_{1.9}$ ($CeO_{1.9}$ corresponds to one oxygen vacancy per surface in this model) surfaces were considered. According to these diagrams, at lower temperatures the surfaces of CeO_2 are stoichiometric, whereas at high temperatures the surfaces are reduced, i.e. high temperatures facilitate the formation of oxygen vacancies.

The desorption temperature (or reduction temperature in this case) under a certain pressure is the temperature at which the surface free energy of the stoichiometric and reduced surfaces are equal, i.e the temperature that oxygen will adsorb or desorb from the surface. This is summarized in Figure 3.3 where the reduction temperature (the temperature required to remove a surface oxygen atom, creating an oxygen vacancy and reducing two cerium atoms) is plotted as a function of oxygen partial pressure. The reduction temperatures are highest for the {111} and lowest for the {110}. This follows the same trend as the heat of reduction.

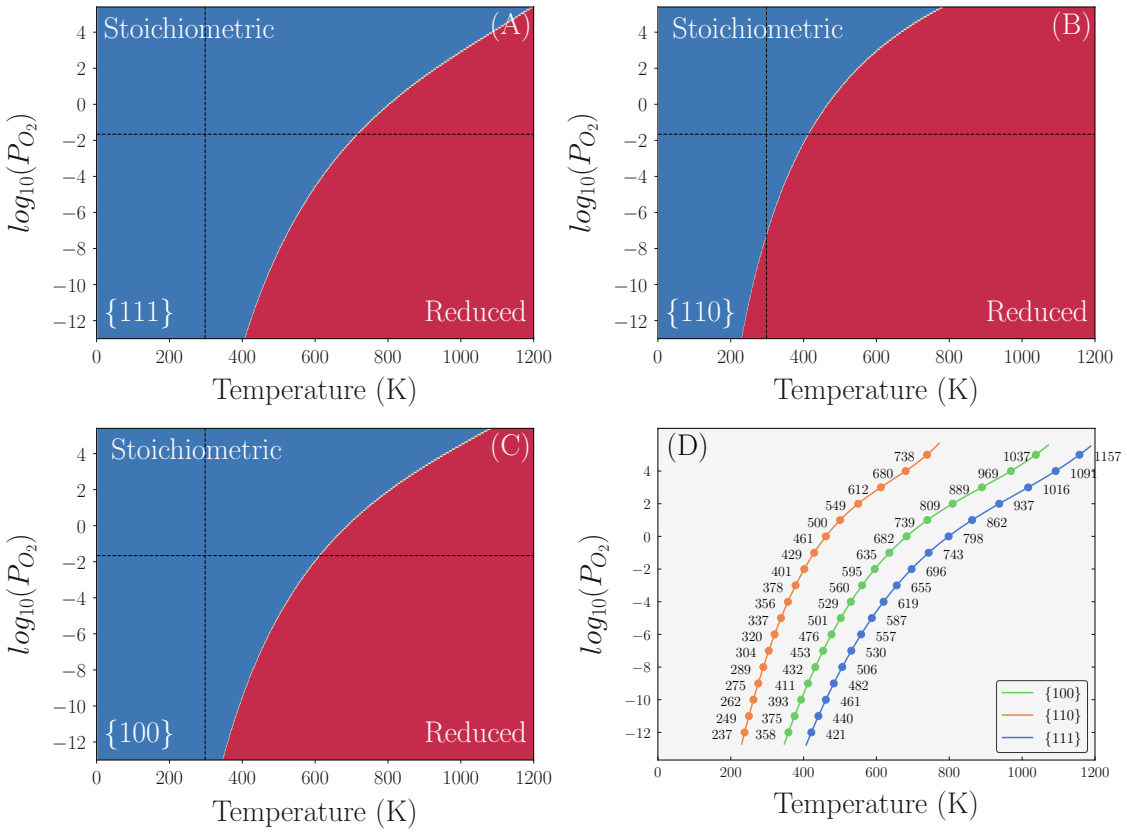

Figure 3.3: Oxygen partial pressure vs temperature phase diagrams for the stoichiometric {100} (A), {110} (B), {100} (C) surfaces. (D) Desorption temperature for oxygen (reduction temperature) on the bare {111}, {110}, {100} (blue, green and purple lines). Desorption temperatures in Kelvin have been marked between -12 and 5 $log_{10}P$ in increments of 1. The atmospheric oxygen pressure at 298 K has been marked with dashed black lines.

3.5 Dopants

The segregation energies (figure 3.4) are all negative and thus it is favourable for dopants to segregate to the surfaces of CeO_2 [1]. At all surfaces, with the exception of Y^{3+} on the {100}, the segregation energy for a dopant is more favourable than for Ce^{3+}. There segregation energies for the {111} and {100} surfaces are similar (-0.2 eV per cation) and much more favourable for the {110} surface (-0.6 eV per dopant).

The is a decrease in surface energy on reduction of the {110}/{100} surfaces and an increase on the {111} (figure 3.5). All surfaces see an increase in surface energy on addition of M_2O_3 (M = Gd^{3+}, Sm^{3+} and Y^{3+}) dopants when compared to the reduced system. While there is an order of stability that follows Ce(III) < Gd^{3+} < Sm^{3+} < Y^{3+}, there is only a difference of 0.02 J/m^2 between the lowest (Gd^{3+}) and highest (Y^{3+}) on each surface.

There is no change the morphology of the nanoparticles as these surface energies give rise to octahedral nanoparticles.

[1] This is based purely on the energies evaluated with DFT. Defect segregation in relation to surfaces is discussed in greater detail in Chapter 10

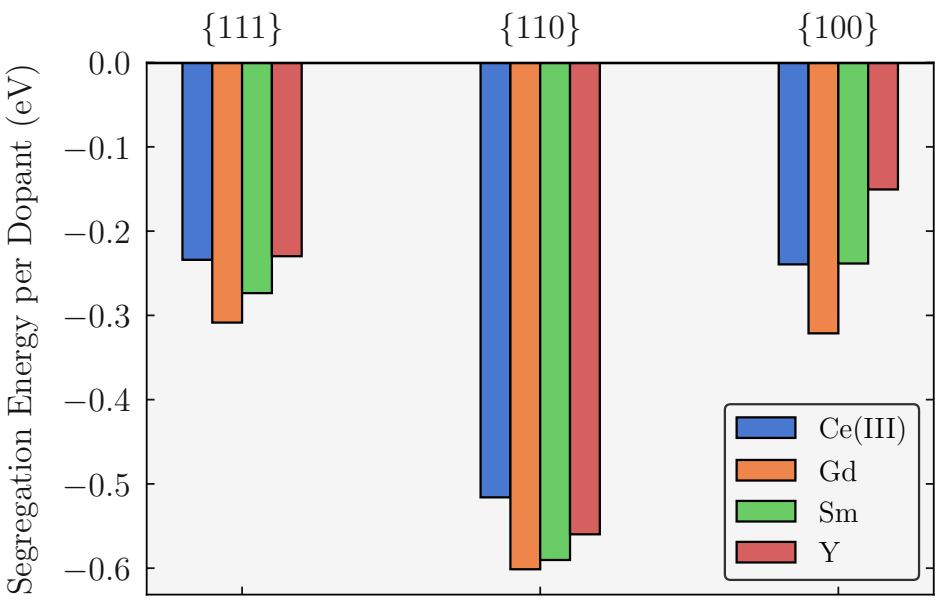

Figure 3.4: Segregation energies for the reduced (blue), Gd^{3+} doped (orange), Sm^{3+} doped (green) and Y^{3+} doped (red){111}, {110} and {100} surfaces.

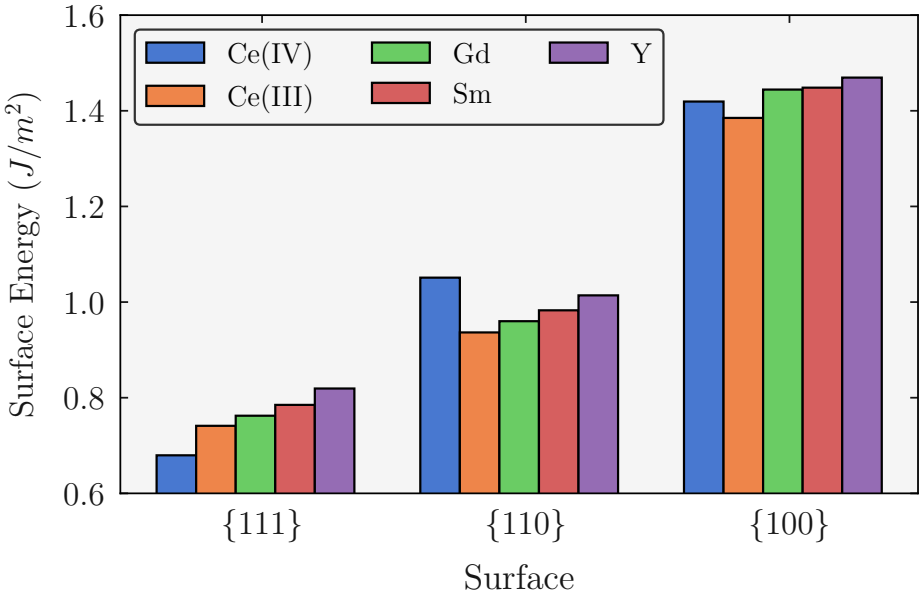

Figure 3.5: Surface energies for the Gd^{3+} doped, Sm^{3+} doped and Y^{3+} doped {111}, {110} and {100} surfaces (green, red and purple) in comparison to the stoichiometric (Ce(IV))and reduced (Ce(III)) surfaces (blue and orange).

3.6 Conclusions

The aim of this chapter has been to generate realistic surface models that accurately capture the surface properties of cerium oxide. The surfaces generated show strong structural agreement with those predicted computationally and also experimentally. Furthermore, the surface energies and reduction energies show good agreement with those already reported in the literature. The results in this chapter provide information on the conditions under which surface reduction occurs.

4 The Influence of Water on the Catalytic Activity of Doped CeO_2 Surfaces

The contents of this chapter have been previously published by the author as part of this PhD project and can be found at the following reference,A.R.Symington, M. Molinari, S. Moxon, J. Flitcroft, D. Sayle, S. C. Parker, Strongly Bound Surface Water Affects the Shape Evolution of Cerium Oxide Nanoparticles. *J. Phys. Chem*, 124(6): 3577-3588, 2020. doi: 10.1021/acs.jpcc.9b09046. This chapter includes the work conducted by the author and does not include any work carried out by collaborators. Notably, molecular dynamics simulations which aid in the conclusions of this work, carried out by Dr Dean Sayle, have been omitted but can be found in the referenced article.

4.1 Background

A key challenge in materials science and catalysis is understanding how to control the expression of different surfaces as well as how the environment effects this expression. In this chapter the adsorption of water at the surface of CeO_2 and doped CeO_2 is evaluated and, using phase diagrams, the particle morphology is predicted as a function of water partial pressure and temperature.

Despite its ubiquity in many chemical reactions as a solvent, spectator or reagent,

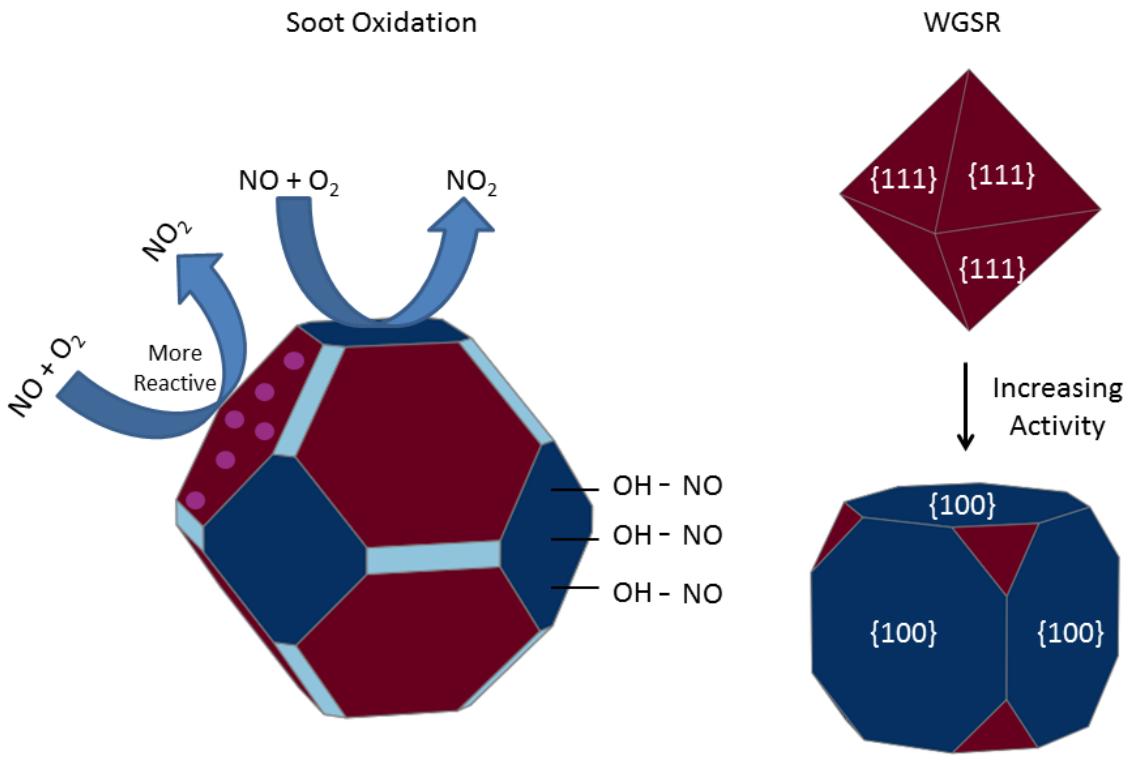

Figure 4.1: Schematic illustrating the influence of dopants and water in soot oxidation catalysts and the effect of morphology on WGSR catalysts.

water and its effect on the morphology of ceria nanoparticles is often overlooked. For example, literature studies usually only focus on the oxygen reduction and incorporation at the electrolyte-cathode-gas triple phase boundary in SOFCs. However, instead of pure oxygen, it is steam-containing, ambient air being fed at the cathode of the SOFC. Experiments have shown that steam does have a significant impact on the oxygen transport properties of both pure and doped ceria [166], but the details behind these changes are largely unclear [167]. Furthermore, it has been proposed that surface hydroxyl groups (OH) hinder the performance of soot oxidation catalysts. While surface water is undesirable in soot oxidation and SOFCs, other catalytic processes depend on water dissociation at the surface, e.g. the water gas shift reaction. It is unclear how the morphology of the material (generally in the form of nanoparticles) affects and is affected by the interaction with water especially if the material is in use over a long period of time, i.e. over repeated catalytic cycles.

Significant theoretical effort has been made to predict how water adsorbs at and alters the surface of both stoichiometric and reduced ceria [163, 168, 169, 170].

However the interplay between water and doped ceria surfaces has not yet been fully explored. Ceria is often aliovalently substituted with metals in the 3+ oxidation state, such as Y^{3+}, Sm^{3+} and Gd^{3+}. These dopants promote the formation of oxygen vacancies, enhance oxygen diffusion rate, materials stability under reducing conditions and improve catalytic activity[34]. Compared to stoichiometric ceria, reduced or oxygen deficient ceria interacts with humidity (water) differently[163]. Clearly, given the technological importance and the wide range of uses of doped ceria, the effect of water adsorption warrants further study.

In this chapter, the interaction of water with the most important low-index surfaces of CeO_2 ({111}, {110} and {100}) will be discussed. To date, the study of water on the doped surfaces has not received attention from a modelling point of view, and adsorption on the stoichiometric, reduced and doped surfaces has not received attention within the context of its stability as a function of temperature and pressure. Furthermore, the influence of water on the the adsorption of water on stoichiometric and reduced surfaces will be discussed followed by the adsorption of water on surfaces doped with three common dopants, Sm^{3+}, Y^{3+} and Gd^{3+}.

4.2 Calculation Details

Water adsorption on the stoichiometric surface of ceria, referred to as Ce(IV) surfaces, reduced surfaces, where an oxygen vacancy has been introduced to the surface, referred to as Ce(III) and doped surfaces, referred to as M^{3+}, where M is Sm, Gd and Y has been considered in this chapter. The distribution of M^{3+} cations is the same as that discussed in chapter 3.

As the number of configurations for adsorbed water on surfaces of ceria is extremely large, the number of structures studied has been limited to structures that have previously been suggested and that maximize the coordination between the adsorbate and the surface [163, 165]. Several configurations for each water coverage were then computed, but only the most stable one is reported. In order to investigate the effect of concentration, four concentrations of H_2O were investigated for the {110}

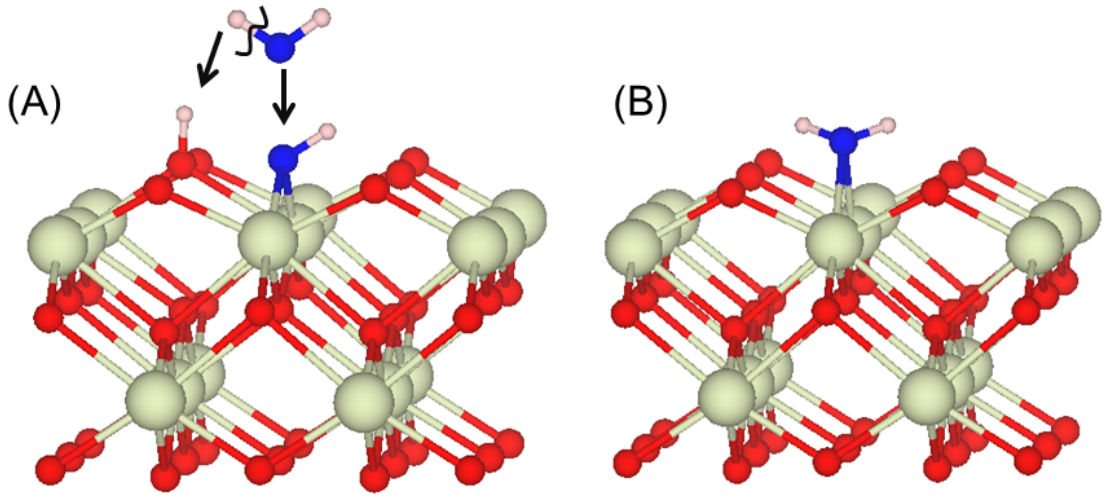

Figure 4.2: Schematic illustrating dissociative water adsorption (A) and associative adsorption (B)

and {100}: 0.12, 0.23, 0.35 and 0.47 H_2O/nm^2 on the {110} and 0.17, 0.33, 0.50 and 0.67 H_2O/nm^2 on the {100}. Six concentrations were studied on the {111}; 0.12, 0.23, 0.35, 0.47, 0.59 and 0.67 H_2O/nm^2. These concentrations correspond to one water molecule per CeO_2 unit (Smallest) up to a full coverage of water per CeO_2 unit (Largest). Full coverage refers to one molecule of water per surface CeO_2 unit. The slab method is employed in this chapter, so water molecules are added symmetrically to both the top and bottom surface.

The DFT calculations, surface models and the analysis methods are the same as those outlined in chapter 3.

Nanoparticle morphologies at varying temperature and pressure values are calculated and displayed as heatmaps in this chapter. The surface energy for the three surfaces at varying values of temperature and pressure were calculated according to equation 2.79. This generates a grid of surface energies as a function of temperature and pressure. A Wulff construction was performed at each point of this grid in order to predict the particle morphology as a function of temperature and pressure.

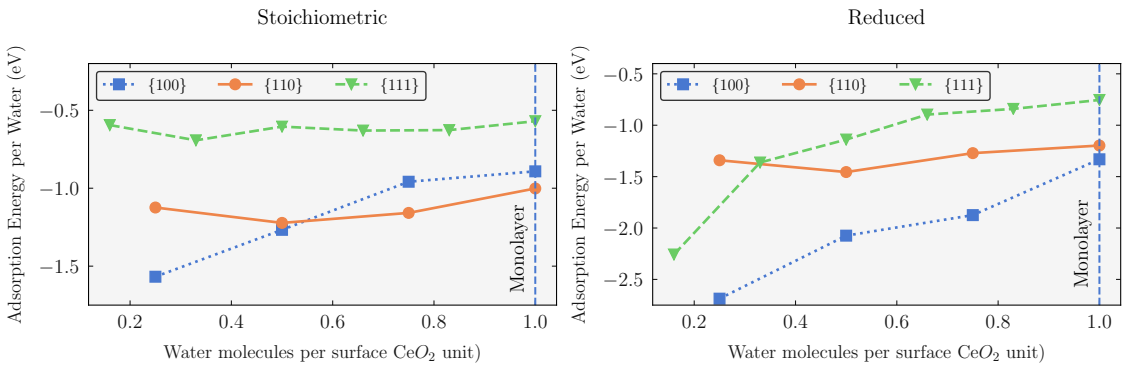

Figure 4.3: Adsorption energy for water as a function of coverage on the stoichiometric (A) and reduced (B) {111} (Red), {110} (Green) and {100} (Blue) surfaces.

4.3 Water Adsorption At CeO_2 Surfaces

4.3.1 Adsorption Energy

Both associative (water adsorbing as H_2O) and dissociative (water adsorbing as hydrogen and an OH) water adsorption was investigated. Dissociative water adsorption is favoured on both stoichiometric and reduced surfaces. On the {110} and {100} surfaces the water in the associative configurations dissociated during minimisation, indicating that the dissociation is barrierless in terms of energy. Dissociative adsorption is favoured on the {111} surface, but water can still be adsorbed as a molecular species, in line with previous experimental [164] and computational [163, 170, 171] literature.

Adsorption is stronger on the reduced surfaces compared to the stoichiometric surfaces (figure 4.3). This is because hydroxyl groups can fill the vacant oxygen lattice site and "heal" the surface enabling the surface cerium to recover coordination. Associatively adsorbed water cannot adequately enable this healing and thus surface oxygen vacancies promote dissociation of water molecules. We find spontaneous dissociation of water molecules in the presence of surface oxygen vacancy, implying a barrierless process.

As expected, the water adsorption energies on stoichiometric surfaces follow the surface energy, i.e. the least stable has a larger adsorption energy at the lowest

coverage.

The three surfaces show remarkably different behaviour when the water coverage increases. The strength of adsorption at the lowest coverage is stronger on the {100} followed by the {111} and finally the {110}, however at higher coverage it follows the order {100} > {110} > {111}. The strength of adsorption on the {111} and {100} surfaces is less energetically favourable with increasing water coverage up to the monolayer adsorption (i.e. a water molecule per surface Ce). On the {110} surface there is an initial stabilization at 25% and 50% coverage followed by a destabilization of the adsorption when monolayer coverage is reached. This is likely due to the surface area available per surface Ce atom on the {110}, 0.21 nm^2 against the 0.19 and 0.15 nm^2 on the {111} and {100}, which can accommodate a greater coverage of water before steric effects start destabilizing further adsorption of water. It is clear that the hydrogen bonding network on the {111} and {100} surfaces can easily form as the coverage of water increases; this is not the case for the {110}, where the water molecules are adsorbed and isolated by direct interaction with surface Ce. Cerium at the {111} is 7-fold coordinated, whereas 6-fold coordinated on the {100} {110}. The stronger adsorption energies for the {110} and{100} surfaces is due to the surface cerium regaining coordination from 6 to 7/8 depending on the concentration of water. The Ce atoms at the {111} surface are already 7-fold coordinated and thus there is less energetic gain in regaining coordination.

Adsorption energies are in good agreement with Molinari et al. who studied a range of water coverages on the stoichiometric surface and the lowest coverage on the reduced surfaces [163].

4.3.2 Phase Diagrams

To define ceria surface stability in the presence of adsorbed water molecules as a function of water partial pressure and temperature, surface phase diagrams for the stoichiometric and reduced {100}, {110} and {111} surfaces have been generated. Figure 4.4 shows the water partial pressure vs temperature diagrams for each surface, where the different regions of the phase diagrams represent the most stable surface

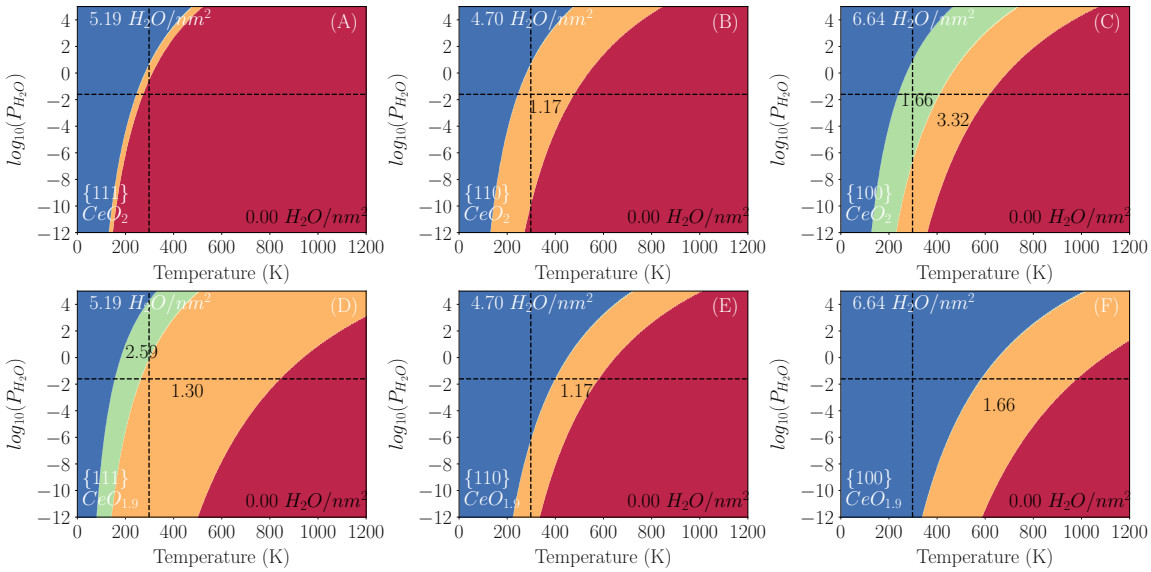

Figure 4.4: Pressure vs temperature phase diagrams for the stoichiometric {111} (A), {110} (B), {100} (C) and the reduced {111} (D), {110} (E) and {100} (F) surfaces. The water coverage (H_2O/nm^2) of each phase is added to the phase diagram. The atmospheric water pressure at 298 K has been marked with dashed black lines. The colours represent different water concentrations at the surface.

composition.

On the stoichiometric surfaces, water will desorb from the {111} first, followed by the {110} and then the {100} at any given pressure (Figure 4.4 A,B,C). The reduced surface has a much greater temperature range where water is stable. This is due to the surface healing effect, where an OH group from dissociatively adsorbed water adsorbs at an oxygen vacancy site. This allows the surface cerium atoms to regain their partial coordination. At low temperature (Blue regions) the surfaces are partially covered with water molecules, whereas at high temperature (red region), water molecules are not stable at the surface and thus the surface is bare.

The atmospheric water partial pressure at 100% humidity at 298 K is marked on each phase diagram in Figure 4.4 as a reference. Under these conditions water will not be present at the stoichiometric {111} surface, but will be present on the stoichiometric {110} and {100} surfaces and the three reduced surfaces. The amount of adsorbed water on each surface at these conditions varies between the surfaces, indicating that nanoparticles displaying different surface area ratios will have varying amounts of water on each facet.

4.3.3 Desorption Temperature

Based upon the pressure vs temperature phase diagrams, the desorption temperatures for water molecules at the three low-index surfaces of ceria have been calculated. The desorption temperatures represent the transition between a bare surface and a surface with adsorbed H_2O. These temperatures can be directly compared with experimental values determined by temperature-programmed desorption (TPD) experiments. The calculated desorption temperatures are in good agreement with those calculated by Molinari et al. for the stoichiometric surfaces and show reasonable agreement with the reduced surfaces, although it should be noted that we examined the full coverage range whereas only a single coverage was considered previously [163]. Our work is also in agreement with the TPD experiments of Maolin et al. who measured the desorption temperature of water from the {111} surface. Furthermore, other theoretical work has calculated the desorption temperature on the {111} to be between 170-185 K, which agrees with the temperature calculated in this work (163 K) [164, 170].

4.3.4 Effect on Reduction

The reduction temperature of each surface was presented in the previous chapter. In this section, the reduction temperature in the presence of water is presented (figure 4.6). This shows whether the presence of water at the surface affects the redox properties. For all surfaces, water at the surface lowers the temperature at which oxygen can desorb from the surface. This is likely due to the ability of water to heal the coordination of the surface cerium atoms. The extra oxygen from the water adsorbs at surface cerium sites, and this lowers the impact to the surface cerium coordination of losing an oxygen, thus oxygen can desorb easier.

4.3.5 Particle Morphology

Using the surface energies calculated and displayed in phase diagrams, a Wulff construction was used to calculate the surface area of a nanoparticle under specific conditions of water partial pressure and temperature. This data is then displayed in Figure 4.7 as a ratio of surface areas. Figure 4.7 shows the relative stability of

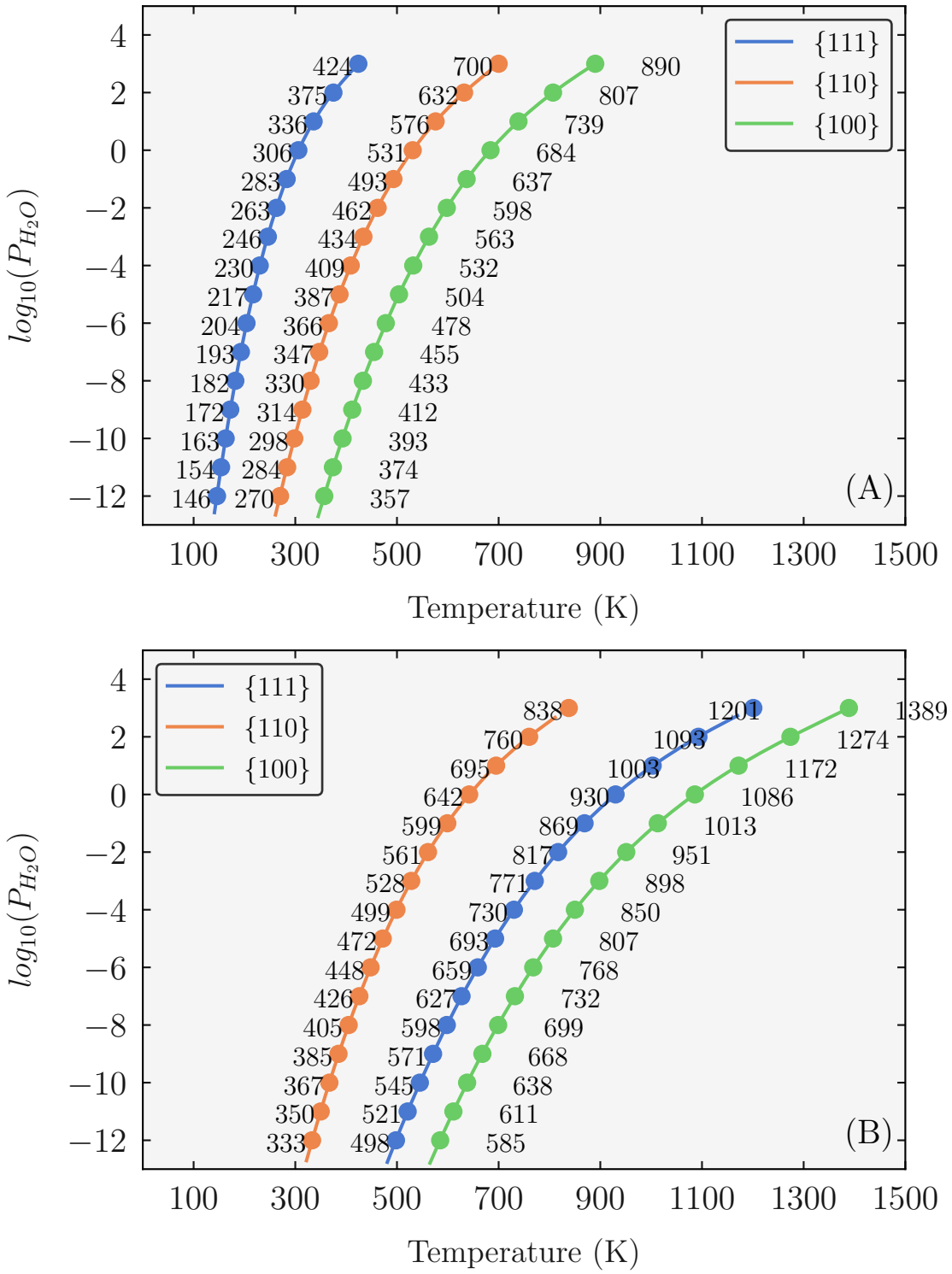

Figure 4.5: Temperature of desorption of water for the stoichiometric (A) and reduced (B) surfaces. The {111}, {110} and the {100} surfaces are shown in blue, red and purple. The temperature of desorption at pressures ranging from -12 $\log_{10}$ (P_{H_2O}) (bar) to 5 $\log_{10}$ (P_{H_2O}) (bar) in increments of 1 are marked at the corresponding locations on the plots.

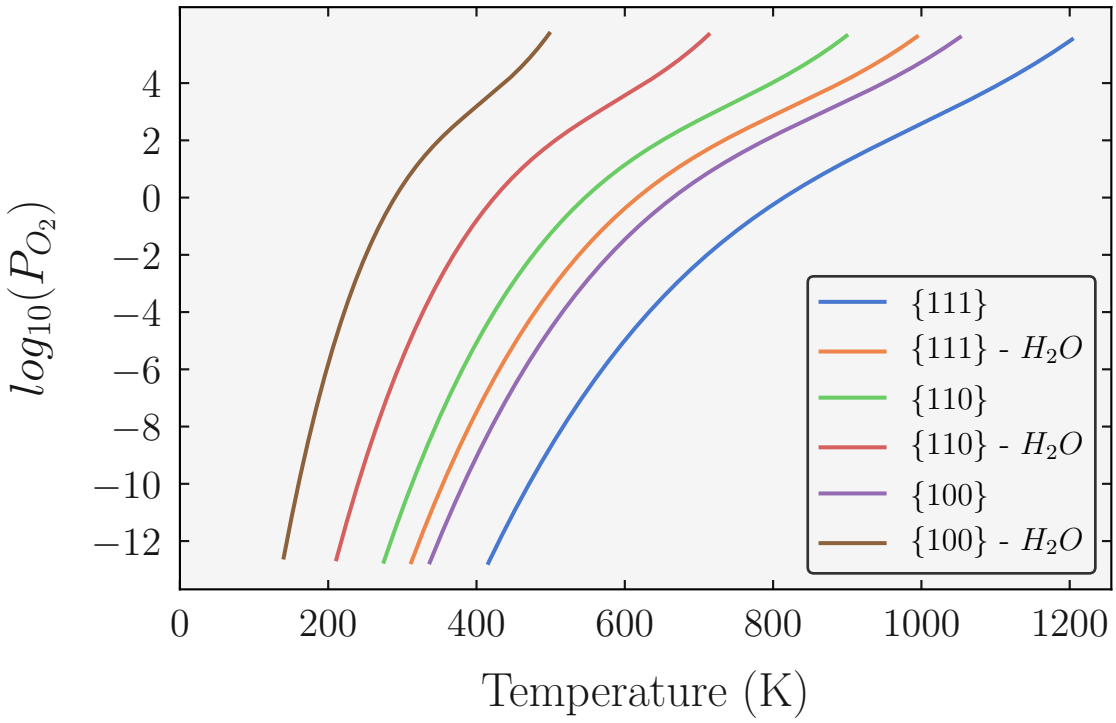

Figure 4.6: Desorption temperature for oxygen (Reduction temperature) on the bare {111}, {110}, {100} (Blue, green and purple lines) and the hydrated {111}, {110}, {100} (Orange, red and brown lines)

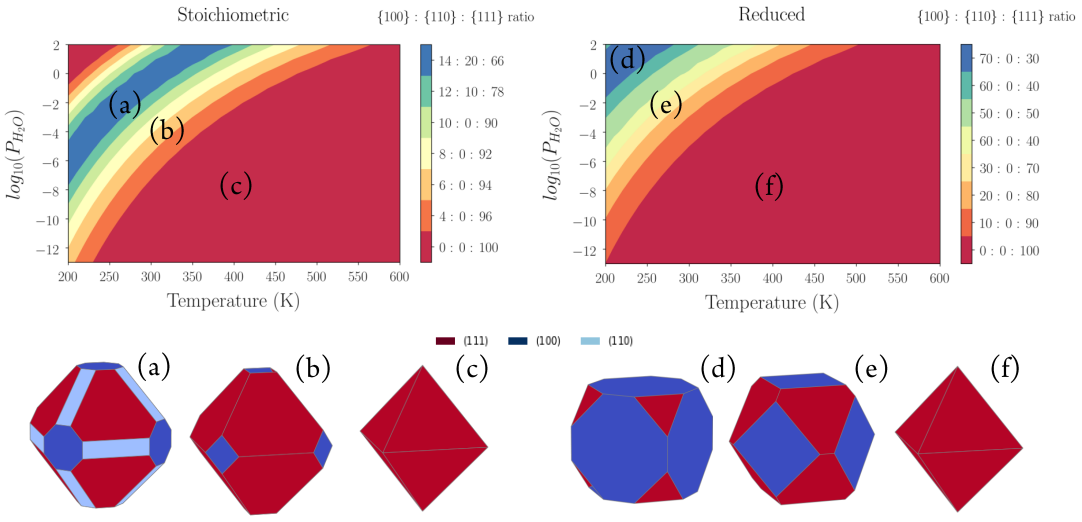

Figure 4.7: Particle morphology phase diagram for the stoichiometric and reduced surfaces. Wulff constructions are shown for the stoichiometric and reduced surfaces. These correspond to a {100}:{110}:{111} ratio of 14:20:66 (a), 10:0:90 (b) and 0:0:100 (c) for the stoichiometric surface and 70:0:30 (d), 40:0:60 (e) and 0:0:100 (f) for the reduced surface. For clarify the {111}, {110} and {100} facets are shown in red, light blue and dark blue respectively.

the surfaces relative to one another in the presence of water.

The particle morphology in the absence of water at 0 K is shown in the previous chapter and highlights the stability of the {111} surface relative to the {110} and {100} surfaces. When a water molecules adsorbs at the surface, it lowers the surface energy of that surface. Given that the three surfaces have very different desorption temperatures, there are temperature and pressure ranges where water is stabilising one surface but not another. This is particularly relevant for the {111} and {100} surfaces. The {110} surface does not appear in the reduced system.

Using a pressure of -12 log_{10}, water desorbs from the {111} surface at 146 K, whereas it desorbs from the {100} at 357 K. In this 211 K region, the surface energy of the {100} is being lowered and the {111} is not. This results in the {100} surface being expressed in the morphology when the partial pressure of water is high and the temperature is low.

The reason for the expression of the {100} surface on the introduction of water can be explained by looking at the desorption temperatures. When there is water at the surface, the surface energy is being lowered by the water, otherwise the water would desorb. Above the desorption temperature, there is no water and no lowering if the surface energy. The {111} and {100} surfaces have different desorption temperatures and thus there is a range of conditions where the surface energy of the {100} is being lowered while the {111} is not, this is illustrated in figure 4.8.

The reason for the increased expression of the {100} surface on the doped surfaces can be explained by looking at the desorption temperatures. The desorption temperature of the {111} is lowered by dopants whereas it is increased on the {100}. Thus the temperature and pressure range where the surface energy of the {100} is being lowered while the {111} is not in increased compared to the reduced surface.

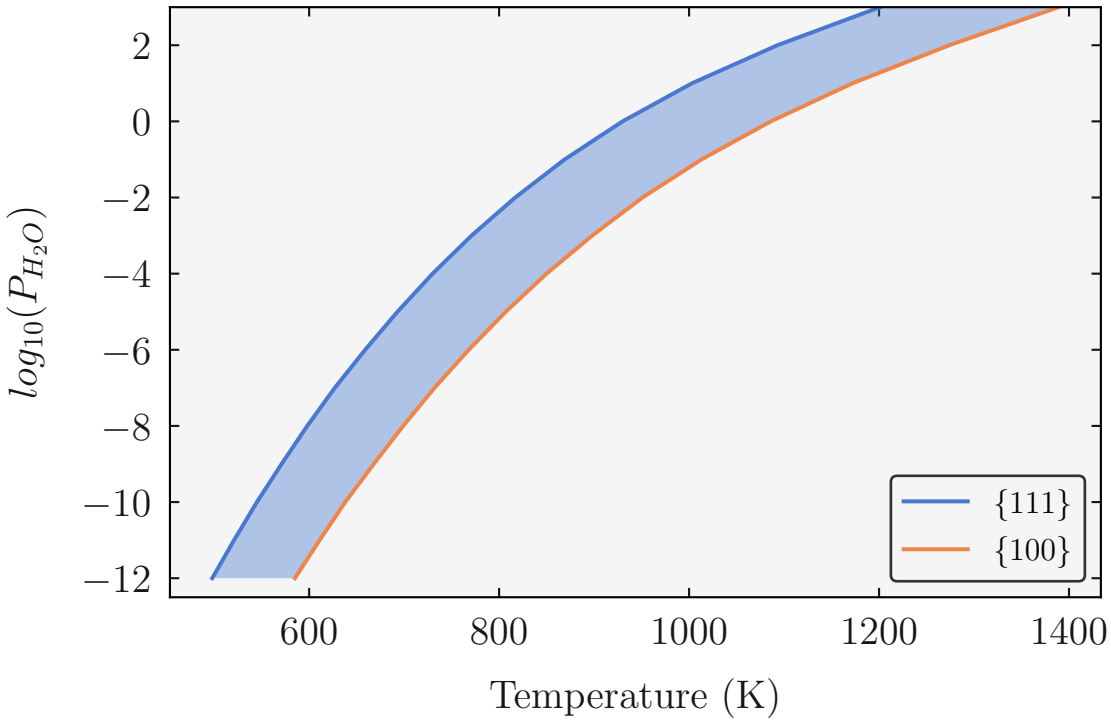

Figure 4.8: Desorption temperature of the {111} (Blue) and the {100} (Orange) on the reduced surface. The shaded region is the range where the {100} surface is being stabilised by water (surface energy lowered) while the {111} is not.

4.4 Water Adsorption on Doped Surfaces

In the previous section, the adsorption of water on cerium oxide surfaces was discussed. As ceria is often doped with foreign cations in order to improve its properties, in this chapter the interaction between water and the doped surfaces of ceria are discussed. As with the stoichiometric and reduced surfaces discussed in the previous section, the adsorption energies, phase diagrams, desorption temperatures and particle morphologies have been generated and will be discussed within the context of catalysis with cerium oxide.

4.4.1 Adsorption at the Lowest Coverage

The water adsorption energy is shown in Figure 4.9. The adsorption energy at low water coverage is found by evaluating the energy of an isolated single water molecule at the surfaces.

All M^{3+} doped and reduced (CeIII) surfaces have a stronger affinity for water than the corresponding stoichiometric surfaces [163]. This is due to the presence of a vacancy, which binds 3+ cations at the surface, as shown in previous experimental and theoretical studies [172]. Experimental observation of dissociation of water is found for Gd^{3+} doped CeO_2 surfaces by Perez-Coll et al. [173], and Kossoy et al. [174].

Dopants and the reduced surfaces are comparable in the sense that they have equal concentrations of oxygen. Comparison between M^{3+} and Ce(III), shows that dopants decrease the affinity of the {111} and {110} surfaces for water but enhance the affinity for water on the {100} surface(Figure 4.9). On all surfaces there is a clear order of stability between the dopants and this follows the order $Sm^{3+} > Gd^{3+} > Y^{3+}$. The difference in adsorption energy is likely to arise from surface strain due to the impurity. The order of ionic radii follows $Ce(III) > Sm^{3+} > Gd^{3+} > Y^{3+}$ with Sm^{3+} being the closest in size to Ce^{3+}. The average Sm^{3+} - O bond length (2.36 Å) is the longest and closest to the Ce – O bond distance (2.34 Å), whereas the average Y^{3+} - O is slightly shorter (2.30 Å).

4.4.2 Water Coverage Dependence

The adsorption energies for the doped surfaces follow the same trend as the reduced surfaces. All surfaces stabilize dissociative adsorption at low coverage but a mixture of associatively and dissociatively adsorbed water adsorption occurs at the monolayer, to maximize hydrogen bonding at the surface. Sm^{3+} shows the greatest strength of adsorption compared to Y^{3+} and Gd^{3+} at the lowest coverage (Figure 4.9), although at the monolayer coverage this relationship is lost. This suggests that the M^{3+} - water interaction dominates, but at higher water coverage this is lost as the hydrogen bonding network becomes the discriminating factor defining surface stabilization. The hydrogen bonding network describes the hydrogen bonds that form between the surface oxygen and the water molecules, as well as the hydrogen bonds that form between water molecules.

The data indicates that dopants have very little impact on the water adsorption on

the {111} surface at all coverages. The largest difference in water adsorption energies is at the lowest coverage of 1.30 H_2O/nm^2 (0.4 eV); at higher coverages there is only a minimal difference between the impurity covered and reduced surfaces. On the {100} surface, there is a modest difference (up to 0.1 eV) in adsorption energy at all coverages. The greatest impact is found for the {110} surface, with the exception of 3.5 H_2O/nm^2 which marks the change in water behaviour (from dissociative to a mixture of dissociative/associative) where there is virtually no difference between the strength of adsorption of water depending on the nature of the dopant, all other coverage see a marked influence: Ce(III) is always the cation that stabilized the adsorption the most and Y^{3+} the least.

Our data support the findings of Mullins et al. who performed XRD analysis on stoichiometric {111} and {100} surfaces and concluded that both associatively and dissociatively adsorbed water is present at the surface [164]. They also conclude that dissociatively adsorbed water is considerably more stable on the {100} than the {111}. There are no data available on the {110}, however our data suggest that this would also be the case for the {110} (Figure 4.9).

4.4.3 Phase Diagrams

Figure 4.10 shows the phase boundaries as a function of water partial pressure and temperature for the stoichiometric, reduced and doped surfaces. Generally the dopants moderate the interaction with water depending on the surface. In the case of the {111} and {110} surfaces dopants reduce the surface stability of water at the surface and thus the surface will lose water at lower temperatures. In contrast, on the {100} surface, the dopants stabilize adsorbed water.

The introduction of oxygen vacancies alongside the dopants Ce(III), Sm^{3+}, Gd^{3+}, Y^{3+}) greatly increases the temperature range that water is stable adsorbed on the surface. This is due to a "healing" effect that occurs whereby water, in the form of hydroxyl groups, persists at the surface, at the vacant oxygen sites. This is illustrated in figure 4.4, where at low temperatures (blue region) the surfaces are fully covered by a monolayer of water, whereas at higher temperatures (white region)

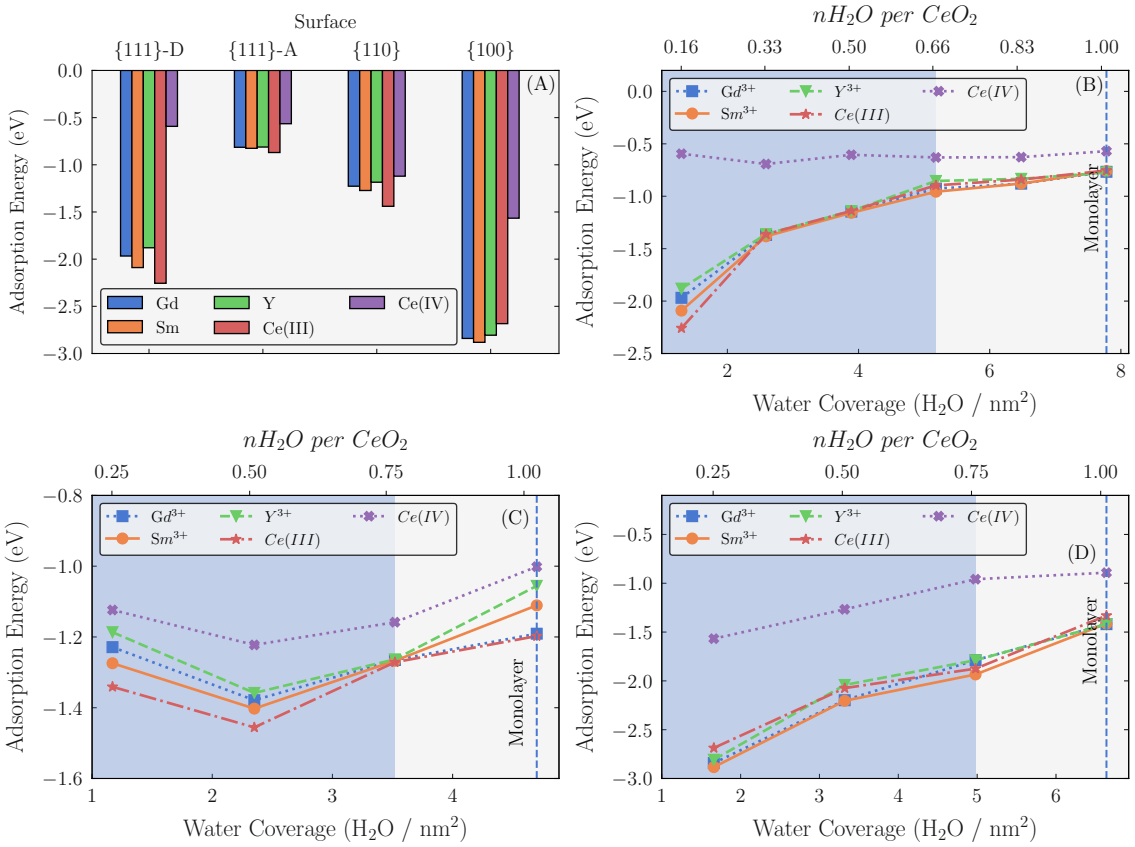

Figure 4.9: (A) Adsorption energies for water on the low index surfaces of ceria for a coverage of 1.66, 1.17 and 1.30 H_2O/nm^2 for dissociative water on the {111}, associative water on the {111} and dissociative water on the {110} and {100}. Ce(IV), Ce(III), Sm^{3+}, Gd^{3+}, Y^{3+} are denoted by blue, orange, green, red and purple bars, respectively. As both dissociatively and associatively adsorbed water can be stabilized on the {111} both have been shown and are denoted by their first letters. (B, C, D) Adsorption energy (eV) per water as a function of coverage for (B) {111}; (C) {110}; (D) {100}; for Gd^{3+} doped (blue squares), Sm^{3+} doped (orange circles), Y^{3+} doped (green triangles), Ce(III) (red stars) and Ce(IV) (purple crosses) ceria. The shaded area corresponds to the coverage range where dissociative adsorption is favoured and the unshaded region corresponds to a coverage range where a mixture of molecular and dissociative water occurs.

the bare stoichiometric surface is more stable. When M_2O_3 doping occurs, at intermediate temperatures, the healed region (green) is the pressures and temperatures where the dissociative water "heals" and stabilizes the surface. This observation is supported by Chen et al., who proposed that the first layer of water on the {111} reduced surface adsorbs dissociatively and fills the oxygen vacancies [175], and Kossoy who proposed that oxygen vacancy sites are the first to be occupied on Gd doped ceria {111} surfaces [174].

4.4.4 Desorption Temperature

The temperature of desorption can be evaluated from the phase diagrams. Desorption temperatures have not been previously calculated for M_2O_3 doped ceria surfaces. The difference between the desorption temperature of the M^{3+} doped and stoichiometric surfaces is shown in Figure 4.11 and the difference between the desorption temperature on the reduced surfaces and doped surfaces is shown in Figure 4.11. These were calculated as $T_{M^{3+}\text{ - surface}}$ - $T_{\text{stoichsurface}}$ and $T_{\text{doped surface}}$- $T_{\text{reduced surface}}$ respectively.

Introducing dopants and reduction of the surface (controlling oxygen partial pressure) are two ways of modifying the oxygen stoichiometry of the surface. In these models, the reduced and doped surface have an equal concentration of oxygen vacancies, thus the variable at the surface is the cation, e.g. Gd^{3+} vs Ce^{3+}. Reduction of the {111} / {110} surfaces increases the temperature where water is stable, compared with doping the surface (Figure 4.11). In contrast, doping the {100} surface increases the temperature range where water is stable, compared with reducing the surface. When comparing the doped surfaces with the reduced surfaces dopants on the {111} and {110} surfaces reduce the temperature of desorption for water compared with reduced Ce(III) containing ceria surfaces (Figure 4.11).

This indicates that catalysts designed for applications where water is unfavourable could employ such a combination of dopants and morphology to prevent water adsorption at the surface. For example at a pressure of 1 bar $p_{(H_2O)}$, Y^{3+} doping reduces the desorption temperature of water by 134 K on the {111} and 35 K on

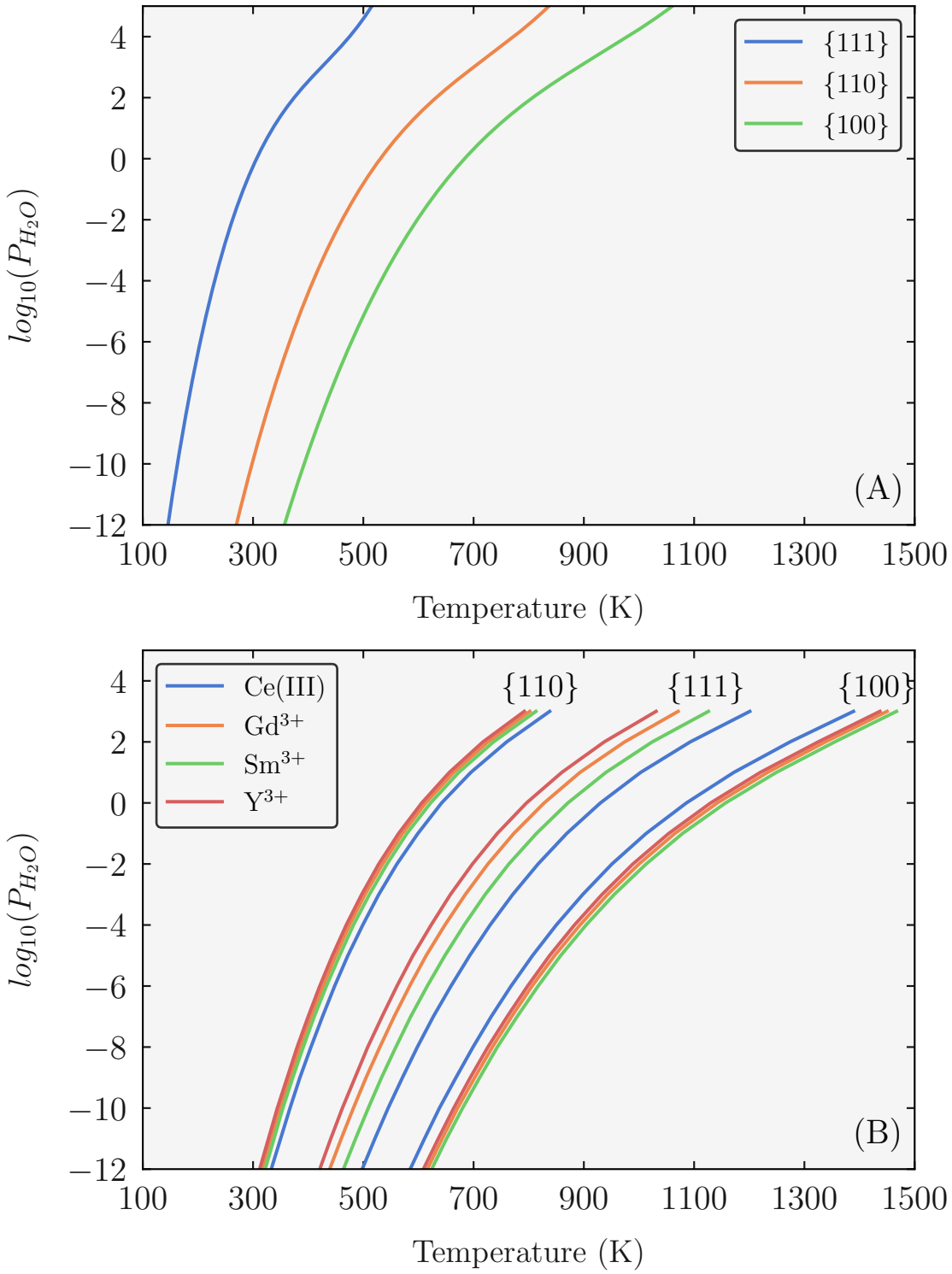

Figure 4.10: The phase boundary between dry and wet surfaces as a function of water partial pressure and temperature. (A) Water desorption temperatures at different partial pressures of water on stoichiometric {111} (Blue), {110} (Orange) and {100} (Green) surfaces (CeIV), (B) Desorption temperatures for water on the reduced (Ce(III)), Sm^{3+}, Gd^{3+} and Y^{3+} surfaces (Blue, orange, green and red lines) surfaces. The desorption regions are labelled for each surface.

the {110}. This effect increases with increasing pressure for the {111} surface but remains relatively constant for the {110}(Figure 4.11). In contrast, dopants on the {100} surface increase the temperature of desorption compared with reduced surface, indicating that catalysts designed for applications where water is required could employ doped nanocube morphologies. For example, at a pressure of 1 bar, Sm^{3+} dopants increase the desorption temperature by 72 K on the {100}. This effect increases with increasing pressure (Figure 4.11).

4.4.5 Predicted Particle Morphology

Using the surface energies displayed in the surface phase diagrams, the relative surface area of each surface at equilibrium as a function of temperature and pressure via a Wulff construction can be calculated. Thus the effect of water exposure on the particle morphology can be evaluated. These results predict the equilibrium particle shape as a function of temperature and pressure, and hence suggest that there could be a thermodynamic driving force for the reconstruction of nanoparticles under conditions different from the synthesis conditions, such as those in a catalytic cycle.

Figure 4.12 shows the ratio between the {100} and {111} surface areas as a function of temperature and pressure. It should be noted that on reduced and doped surfaces within this temperature and pressure range, the {110} surface is not expressed. There are two key features from the results. First, due to the increased stability of water on the doped {100} surfaces, {100} surfaces will begin to form (forming truncated octahedral) under more extreme conditions than for undoped reduced surface-containing Ce^{3+}. For example, our results suggest that doped octahedral nanoparticles, used at ultra-high vacuum (-10 log_{10}) at 200 K, will truncate to express {100} surfaces, whereas undoped reduced (Ce^{3+} containing) surfaces will not. Whereas in contrast, nanocubes used at high temperatures, will be driven towards {111} bearing octahedral nanoparticles.

The reason for the increased stability of the {100} surface on the doped surfaces compared to the reduced surfaces can be explained with the desorption tempera-

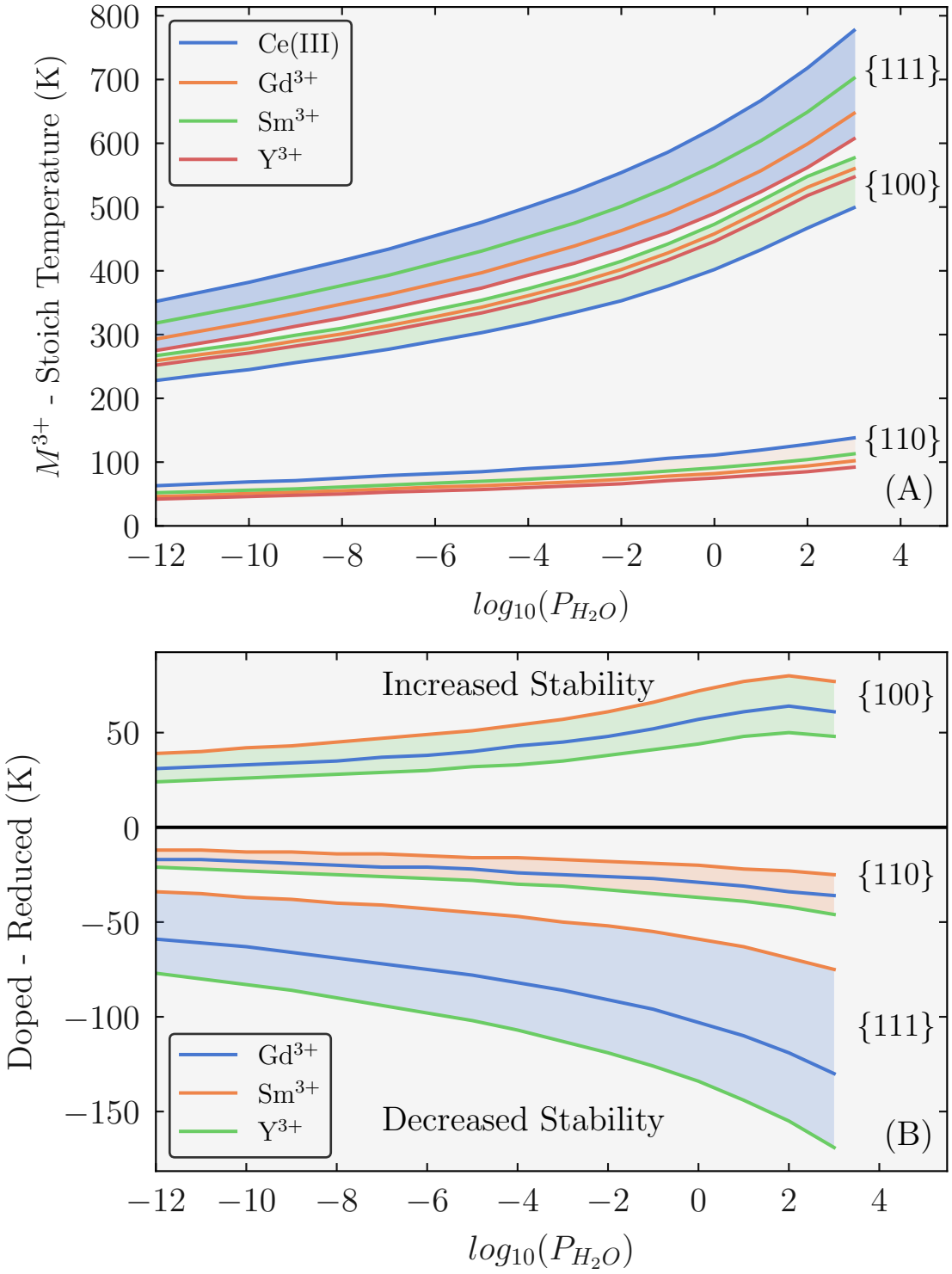

Figure 4.11: (A) The difference in desorption temperatures for doped surfaces compared to stoichiometric surfaces, calculated as $T_{M^{3+}\text{ - surface}}$- $T_{stoichsurface}$. The reduced (Ce(III)), Gd^{3+} doped, Sm^{3+} doped and Y^{3+} doped surfaces are shown in blue, orange, green and red, respectively. (B) The difference in desorption temperature between doped surfaces and reduced surfaces, calculated as $T_{\text{doped surface}}$- $T_{\text{reduced surface}}$. Gd^{3+} Sm^{3+} and Y^{3+} are denoted by the blue, orange and green lines. The blue, orange and green shaded areas correspond to the {111}, {110} and {100} datasets.

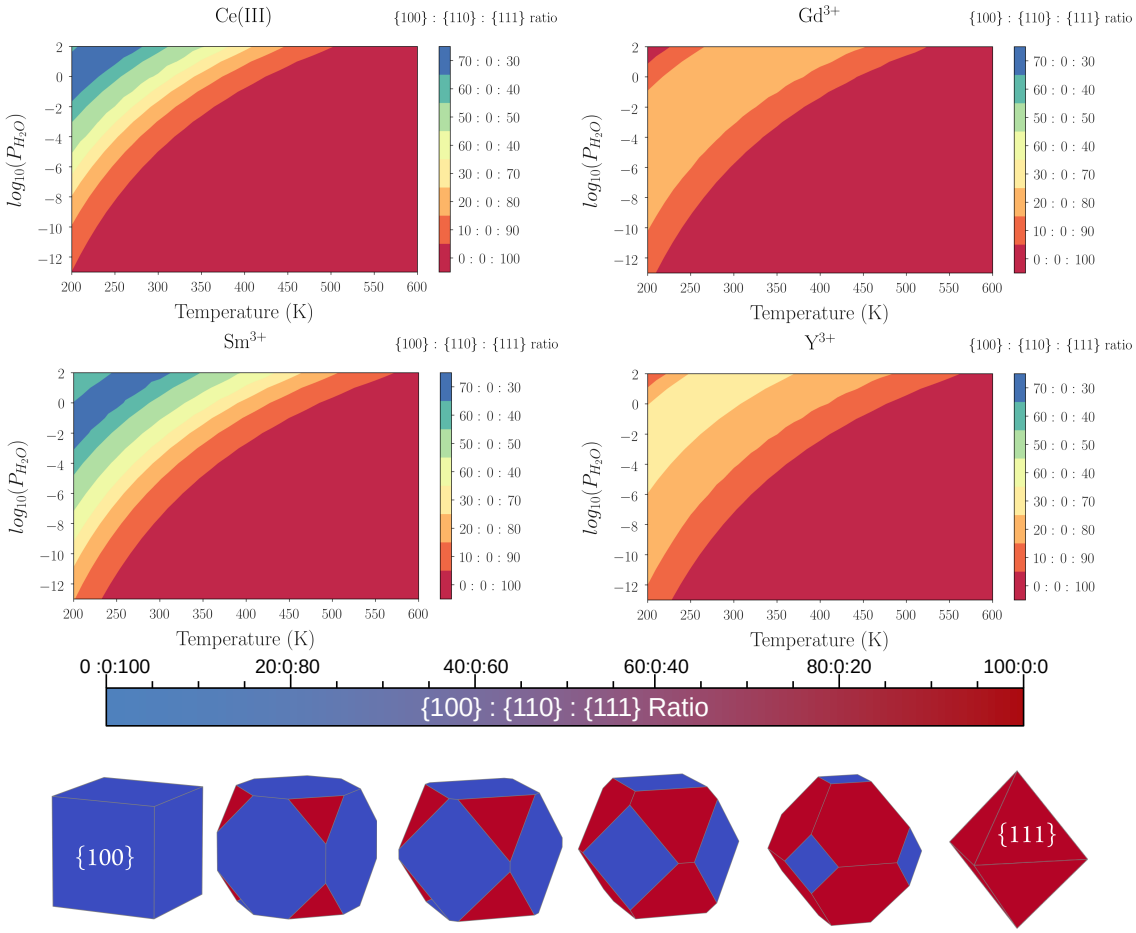

Figure 4.12: Ratio between the {100}, {110} and {111} surface areas as a function of temperature and pressure for the stoichiometric system. For visual clarity, nanoparticles corresponding to these ratios are shown. The ratio between the {100}, {110} and {111} reduced, Gd^{3+}, Sm^{3+} and Y^{3+} doped systems as a function of temperature and pressure are shown. Predicted particle morphologies across a range of surface area rations are shown for visualization of these ratios.

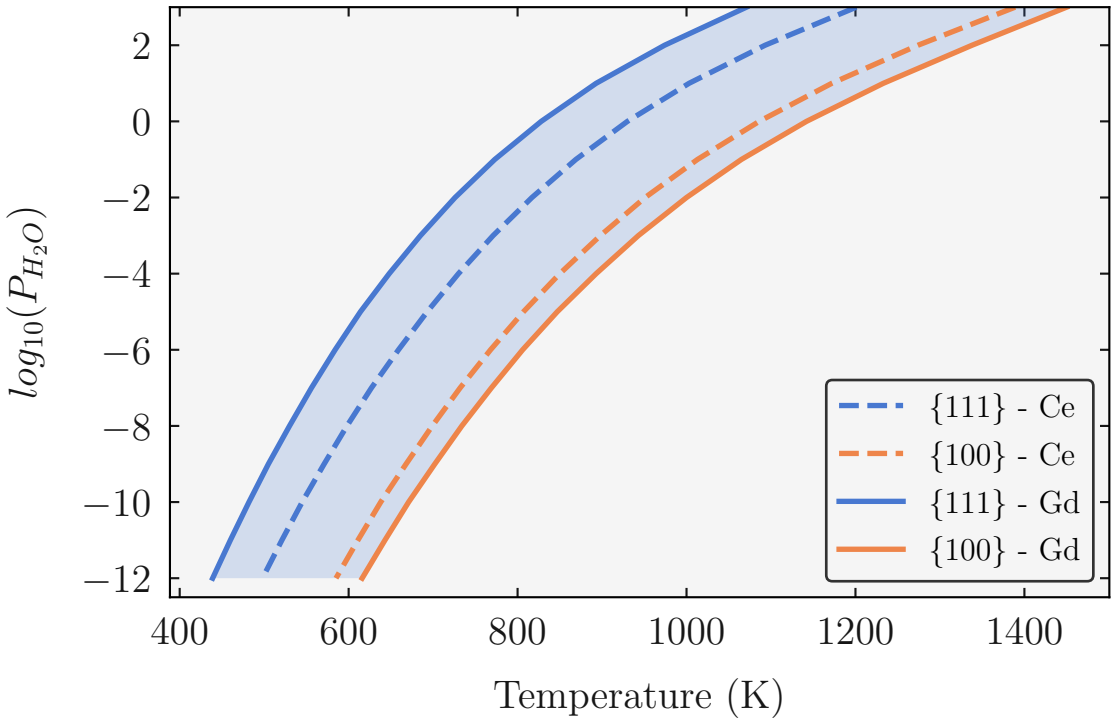

Figure 4.13: Desorption temperature of the {111} (dashed blue line) and the {100} (dashed orange line) on the reduced surface and the {111} (solid blue line) and {100} (solid orange line) on the Gd doped surface. The shaded region is the range where the surface energy of the {100} is being lowered and the {111} is not on the Gd doped surface.

tures. The dopants destabilise water on the {111} and stabilise water on the {100} surface. Thus, the region where the {100} surface is being stabilised while the {111} surface is not is increased or widened (figure 4.13).

4.5 Discussion

The performance of nanoceria catalysts in the form of nanoparticles is strongly affected by the type and nature of exposed surfaces. Recent advances in the preparation of ceria nanoparticles have enabled the study of the effect of different facets on different catalytic process [139, 141, 142, 143, 144, 145, 146]. The particle morphology strongly affects the interaction with water and can potentially in turn impact upon catalytic reactions.

Ceria is used in diesel engines for the oxidation of soot, which is a major air-pollutant.

The presence of water vapor within the exhaust mixture has been shown to negatively affect the catalyst behaviour [176]. Dissociatively adsorbed water at the surface interferes with the NO_2 assisted soot combustion mechanism (which exploits the high temperature induced oxidation of NO to NO_2). Surface OH groups act as adsorption sites for NO and thus hinder the catalytic oxidation of NO to NO_2. Sm and Y doped ceria has been shown to have enhanced activity than its undoped counterpart for soot oxidation [177]. At the operating temperatures (500 – 900 K [43]) there is likely a dominance of {111} surfaces and our results indicate that the OH groups desorb at lower temperatures relative to their undoped counterparts. Sm^{3+} doping could provide and effective strategy to reduce the impact of moisture within the exhaust.

On reduced surfaces, water dissociates in order to recover surface cerium coordination. This represents the healing process that the surface undergoes in order to regain surface stability. The dissociation of water is also a crucial process in the water gas shift reaction (WGSR), which is used for the oxidation of CO to CO_2 and reduction of H_2O to H_2 [178, 179]. Ceria is used in conjunction with a supported metal, usually Au or Pt. Two mechanisms have been proposed for CeO_2 catalysts in the WGSR. The first is the formate route, where water dissociates at the surface, yielding OH groups which react with CO to form formates. H_2 and CO_2 form from the decomposition of the intermediate species. The role of the metal is to allow the adsorption of CO and to promote the cleavage of the C-H bond [180, 181]. The second is the redox route, where reactive oxygen atoms are transferred to the metal particles, leading to oxygen vacancies on the ceria surface. The active oxygens react with CO producing CO_2, while H_2O adsorbs at the ceria surface to heal the oxygen vacancy [182, 183]. It is clear that water adsorption is essential in both routes and that water must dissociate. Surface selectivity has also been investigated as, it has been shown that nanocubes expressing the {100} surface have the highest activity compared with octahedral ({111} and nanorods ({110}) [143, 184].

These results show that on reduced surfaces, the dissociation of water is energetically favourable and sometimes barrierless, with this being the most favourable on the

{100}. This provides an explanation for nanocubes having the highest activity for the WGSR, given that water dissociation is strongest on the {100} surface. Furthermore, Sm doping would further improve the activity of nanocubes for the WGSR for two reasons, firstly, the interaction between water and the Sm doped {100} surfaces is stronger, and secondly, water is stable at the surface at much higher temperatures. This is not limited to the WGSR however and any process that requires surface water dissociation would benefit from these observations. For example, water dissociation is a key step in water splitting catalysts and in steam reforming of hydrocarbons.

Ab initio modelling can be linked to experimental observables, via surface phase diagram evaluation, which allow the prediction of nanoparticle morphology and nanoparticle evolution. Furthermore, by calculating reliable adsorption energies for water on different surfaces of stoichiometric and doped CeO_2, a thermodynamic strategy to evaluate the nanoparticle morphology of the materials as a function of temperature and water partial pressure can be developed.

There is a driving force towards cuboidal and octahedral morphologies at low and high temperatures respectively, due to dopants reducing the affinity of water on {111} and {110} surfaces, while increasing it on {100} surfaces. Enhancing our fundamental understanding of these interactions, as well as our predictive power and analysis, provides a valuable framework for the future optimization of energy and catalysis applications and can be generally applicable to a range of materials.

4.6 Conclusions

Initially the work in this chapter was limited to water adsorption at stoichiometric surfaces of CeO_2 and explored how the adsorption of water affected the relative stability of the three surfaces. It was found that each surface has a different interaction with water and adsorbed water molecules have a modest impact on the morphology of ceria. Adsorbed water at low temperatures and high water partial pressures promotes a change of surface stability and the more reactive, less stable {100} and

{110} surfaces are stabilised relative to the {111} and are consequently expressed in the particle morphology. Reducing the surface or doping the surface with trivalent Gd^{3+}, Sm^{3+} and Y^{3+} cations increases the affinity of the surface for water compared to the stoichiometric surfaces. Adsorption is strongest on the {100} surface and thus at low temperatures and high water partial pressures there is a high {100} surface area relative to the {111}. Furthermore, comparing surfaces with equal oxygen stoichiometries, Reduced and Doped surfaces shows that dopants decrease the affinity of the {111} and {110} surfaces for water while increasing the affinity of the {100} for water. Consequently, dopants increase the temperature and pressure range where the {100} surface is stabilised.

5 The Influence of Carbonates on the Catalytic Activity of Doped CeO_2 Surfaces

At the time of writing the contents of this chapter have been submitted for peer review at the Journal of Physical Chemistry C.

5.1 Background

As the issue of global warming caused by the increase of anthropogenic CO_2 levels in the atmosphere is currently under worldwide scrutiny [185]. This opens the potential to utilize CO_2 within carbon recycling either contributing to reduce the environmental impact or to useful chemicals' production[186, 187]. Catalytically activated CO_2 conversion provides a significant avenue of research and industrial scope. However the activation of such a stable molecule poses energy-related challenges, i.e. the use of high temperatures in the catalytic processes. The design and engineering of catalyst based on materials is therefore of primary importance for realizing optimal and efficient CO_2 conversion.

As materials come in contact with CO_2, the understanding of the interaction between surfaces and CO_2 from the surrounding environment is the first step towards addressing CO_2 conversion, i.e. the adsorption of CO_2 on the materials' surfaces. Here, the bonding of CO_2 at the materials' surfaces becomes the first process that

requires control as it will define the activation of the molecule towards catalysis. Nevertheless, there are challenges to overcome, such as the formation of surface – carbonate species, alterations to the particle morphology and removal of CO_2 from the surface.

The formation of carbonates at the surface on the adsorption of CO_2 is observed for many materials, e.g. yttria stabilized zirconia (YSZ) [188], ZrO_2 [188], MgO [189], $BaTiO_3$ [190], TiO_2 [191, 192, 193, 194], Fe_2O_3 [195, 196, 197] and Al_2O_3 [198]. Of particular interest is cerium oxide (CeO_2) due to the wide range of applications that result in direct contact between its surfaces and CO_2 [34, 199]. For example, CeO_2 comes into contact with CO_2 when used in both three-way catalysts and soot oxidation catalysts [43, 200], where it oxidizes unburnt hydrocarbons and oxidizes CO to CO_2. CeO_2 is used in the water gas shift reaction [201, 202], where H_2O + CO $\rightarrow$ H_2 + CO_2. The dry reforming process is another application [203, 204] where the interaction between the surface and the gas is a conceivable way to provide an oxidant for organic reactions and would yield CO as a syngas for further synthesis. All these applications hold the key to understanding and defining a wider picture of the interaction of CO_2 with CeO_2 and thus avenues to control and tune the conversion.

Although CO_2 adsorption at the surfaces of ceria has been studied, the nature of surface intermediates has not been fully explored. In some cases it has been reported that surface carbonates are responsible for the reduction in the activity of ceria surfaces in several catalytic processes [205, 206, 207, 208], i.e. carbonate poisoning. Both experimental and computational work have confirmed that carbonate species can form [209, 210, 211, 212] at the surface [213, 214], but findings seems to be somehow complicated by the claims of a morphology dependent effect. Furthermore, the effect of dopants has not been considered,

In this chapter, a computational analysis of the associatively adsorbed carbon dioxide molecules (carbonate CO_3 species) with the most important low index surfaces of CeO_2 and doped CeO_2 is discussed, with the aim of defining a relationship between

the adsorption of CO_2 at CeO_2 surfaces and the morphology of the nanoparticle.

5.2 Calculation Details

Carbon dioxide adsorption on the stoichiometric surface of ceria, referred to as Ce(IV) surfaces, reduced surfaces, where an oxygen vacancy has been introduced to the surface, referred to as Ce(III) and doped surfaces, referred to as M^{3+}, where M is Sm, Gd and Y has been considered in this chapter.

The number of potential configurations for adsorbed carbon dioxide on surfaces of ceria is extremely large and many have been proposed in the literature[209]. The associative adsorption of CO_2 on the surfaces of ceria as been studied i.e. CO_2 molecules adsorbed through a surface oxygen to form a carbonate (CO_3^{2-}) species (figure 5.1). We have also studied sub-stoichiometric surfaces of ceria, here, an oxygen vacancy is introduced, which leaves two electrons that localize and reduce two cerium atoms from Ce^{4+} to Ce^{3+}; these surfaces are referred to as reduced surfaces in this article. For reduced surfaces, configurations were constructed to ensure that a CO_3 oxygen fills the vacancy. In some configurations where a carbonate was set at the start of the calculation, the surface oxygen-carbon bond was found to break but the CO_2 molecule remained loosely bound to the surface: these configurations are referred to as 'molecular CO_2' in this chapter. Several configurations for each carbon dioxide coverage were then computed, but only the most stable one is reported.

In order to investigate the adsorption geometry, four concentrations of CO_2 were investigated: 0.13, 0.25, 0.38 and 0.51 CO_2/nm^2 on the {111}; 0.12, 0.23, 0.35 and 0.47 CO_2/nm^2 on the {110}; and 0.17, 0.33, 0.50 and 0.67 CO_2/nm^2 on the {100}. These concentrations correspond to 1, 2, 3 and 4 CO_2 species on each surface. In each case, different adsorption geometries were investigated and corresponded to monodentate, bidentate and tridentate adsorption configurations. In reality, hydroxyls/water will also exist at these surfaces and thus an interaction of these species with carbon dioxide is likely. Temperature Programmed Desorption experiments have shown that the stability of water and carbon dioxide on these surfaces is not

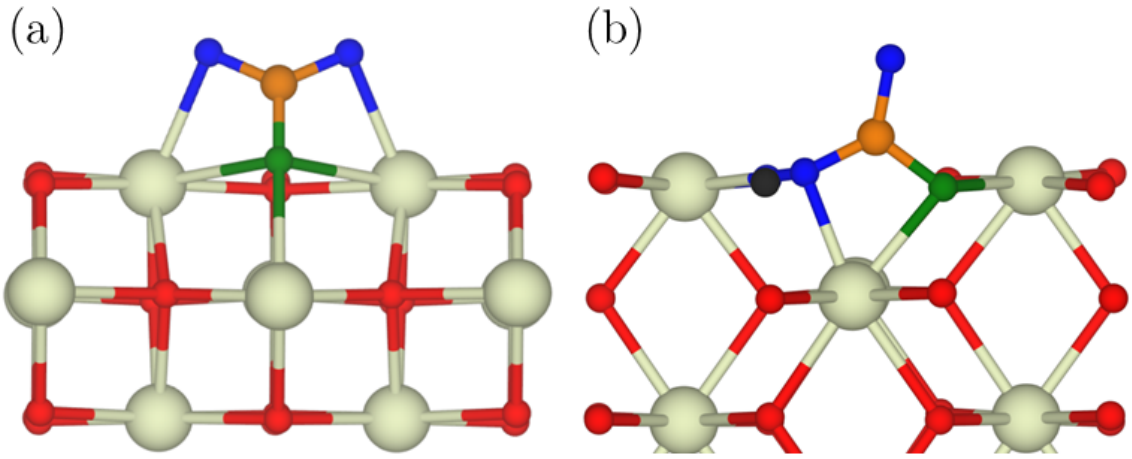

Figure 5.1: Schematic illustrating associative adsorption on stoichiometric (a) and reduced (b) ceria. For clarity, oxygen, cerium, carbon, oxygen vacancies are shown in red, cream, orange and black respectively. The oxygen of the CO_2 molecule are shown in blue and the surface oxygen that the carbon bonds to is shown in green.

identical and that carbon dioxide adsorbed as a carbonate can persist in the absence of water[164, 209, 212, 215]. A study on the co-sorption of water and carbon dioxide represents a possible future avenue of research.

The DFT calculations, surface models and the analysis methods are the same as those outlined in chapter 3.

5.3 Carbon Dioxide Adsorption at CeO_2 Surfaces

5.3.1 Adsorption Geometry

At the lowest concentration of CO_2, tridentate adsorption is favoured on all surfaces, however there are slight differences between the {100} and the {110}/{111} surfaces. On the {100} surface the carbonate ion lies "flat", with each of the three oxygen bridging between two surface cerium atoms. This arrangement is in agreement with Albrecht et al. who studied carbonate at the {100} surface and found that CO_3^{2-} exists as a flat lying, tridentate species [212]. The surface oxygen rearranges slightly to accommodate the carbonate (Figure 5.2). The rearrangement of the {100} oxygen sub-lattice has been reported in other studies of polyanion adsorption, e.g.

phosphates[1] [132]. In contrast on the {110} and {111} surfaces a carbonate lies at an angle with the carbonate oxygen coordinated to two surface cerium atoms (Figure 5.2). The adsorption geometry on the {111} surface is in agreement with Hahn et al [213].

Tridentate adsorption geometry is energetically favoured at the two lowest CO_2 concentrations (Figure 5.2) whereas a mixture of adsorption geometries becomes favoured at higher CO_2 concentrations as steric effects between molecules become important. This sheds light on the proposition that carbonates exist either as a mixture of flat lying and upright, slightly tilted, or that the entire carbonate population is lying flat [212]. Our results indicates that at high concentrations the carbonates will exist as a mixture of tilted and flat lying carbonates, but at low concentrations the entire population is flat lying.

On the {110} and {100} surfaces all carbonates remain intact whereas on the {111} surface at a concentration of 0.51 CO_2/nm^2 there is a mixture of molecularly adsorbed CO_2 and carbonate species (CO_3^{2-}). This is in agreement with Hahn et al., who predicted that at higher concentrations of CO_2 there are chains of physiosorbed CO_2 molecules opposed to chemisorbed CO_3^{2-} [212].

On the reduced surfaces the most stable configurations are those that maximize the surface coordination of the cerium atoms. On stoichiometric surfaces carbonates can be monodentate adsorbed, this is unlikely on reduced surface. It was found that some monodentate configurations switched geometry during the minimization to bidentate or tridentate, further indicating that the surface species will adsorb by promoting those configurations with higher surface coordination.

The average bond length between the carbonate oxygen and surface cerium atoms is smallest for monodentate adsorption configurations (2.17 Å) and longest for tridentate configurations (2.5 Å). This shows that the surface is capable of recovering its oxygen coordination by increasing the numbers of slightly weaker, longer bonds.

[1]Phosphate adsorption will be discussed in Chapter 6

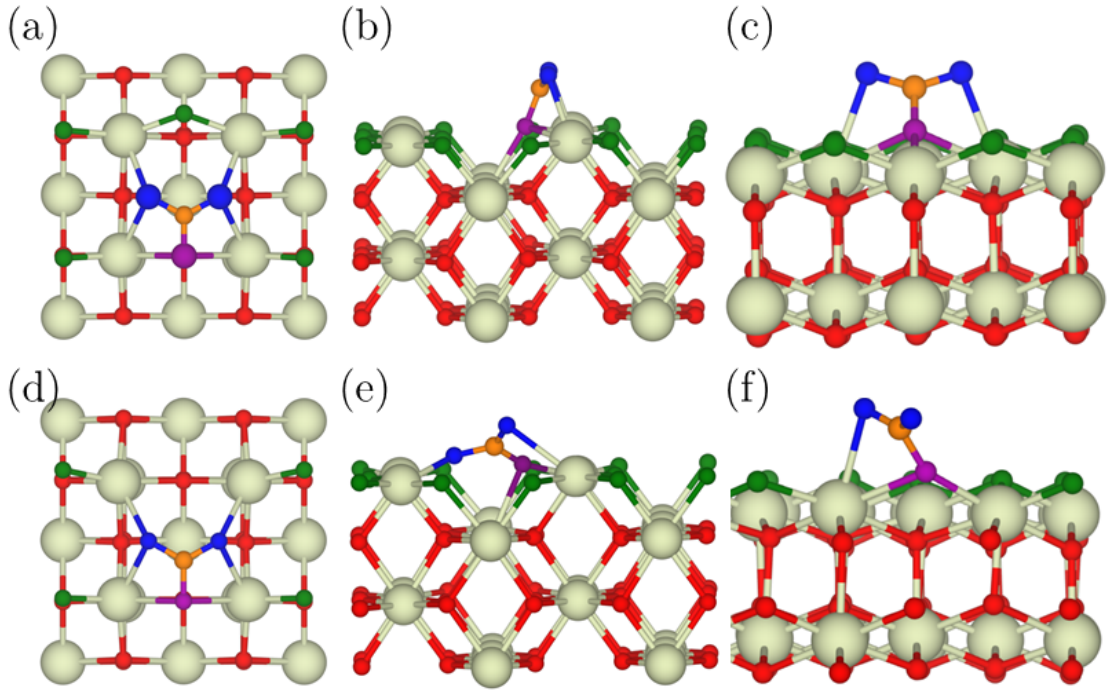

Figure 5.2: Adsorption geometry for a single carbonate molecule on the stoichiometric {100}, {110} and {111} (A, B, C) and reduced {100}, {110} and {111} (D, E, F) surfaces. The {100} surface is shown from above the surface plane and the {110} and {111} surfaces are shown from the side. For clarity, cerium, oxygen, surface oxygen and carbon atoms are displayed in cream, red, green and orange. Oxygen from the CO_2 molecule are shown in blue and the surface oxygen bonded to the CO_2 molecule are shown in purple.

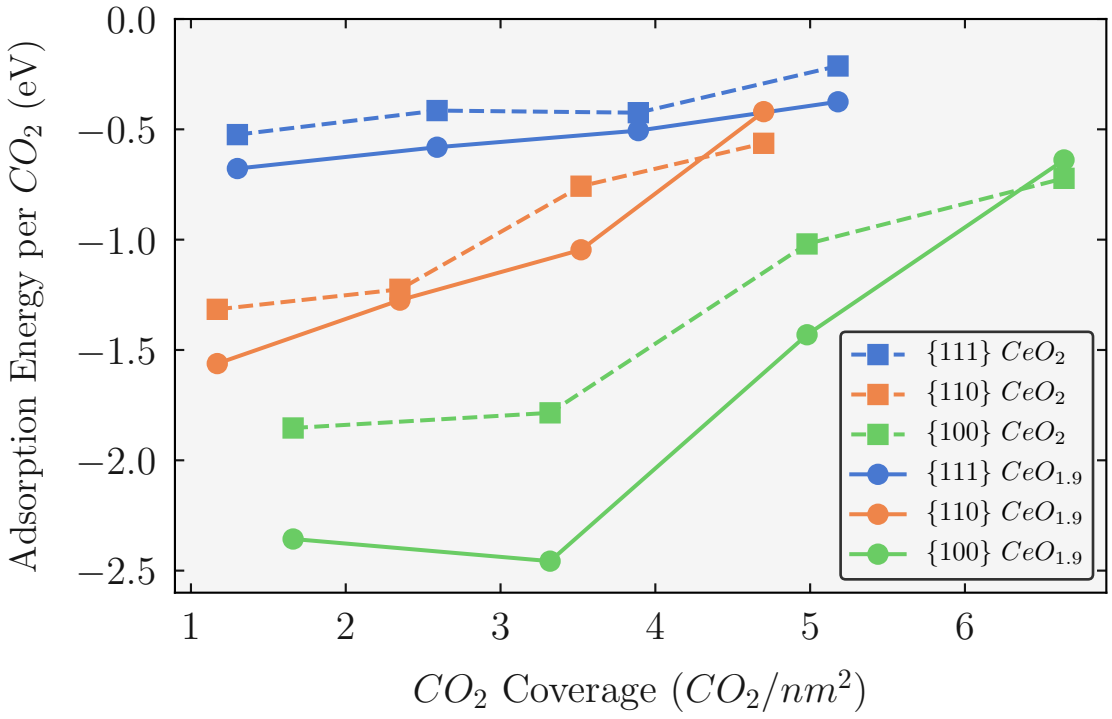

Figure 5.3: Adsorption energies for CO_2 adsorbing as a carbonate molecule on the stoichiometric (Squares) and reduced (Circles) CeO_2 surfaces. The {111}, {110} and {100} surfaces are shown in blue, orange and green.

5.3.2 Adsorption Energy

The strength of the adsorption energy of CO_2 follows the order {100} > {110} > {111} at all concentrations for both the stoichiometric and reduced surfaces (figure 5.3). The strength of the adsorption and order of stability of the adsorption energies can be explained by the surface cerium coordination. Cerium at the {111} is 7 fold coordinated, whereas 6 fold coordinated on the {100} {110}. The stronger adsorption energies for the {110} and {100} surfaces is due to the surface cerium regaining coordination from 6 – 7/8 depending on the concentration of CO_2. The Ce atoms at the {111} surface are already 7 fold coordinated and thus there is less energetic gain in regaining coordination.

At the lowest coverage, the adsorption energy on the {111} is -0.53 eV, which is in good agreement with that calculated by Hahn et al [213]. Cheng et al. calculated the adsorption energy of CO_2 on the {110} surface and concluded that it was physiosorbed as molecularly adsorbed CO_2 and did not form a carbonate. This is in

contrast to these results which find that CO_2 can form a carbonate on the {110} [214]. The much stronger interaction between the {100} and CO_2 is supported by Albrecht et al. [212] who calculated an adsorption energy for flat lying CO_3 of -1.93 eV, which is in good agreement with our calculated adsorption energy of -1.87 eV.

The adsorption energy is more favourable on the reduced compared to the stoichiometric surfaces, this is because the reduction of CeO_2 involves the removal of surface oxygen, this reduces the cerium coordination. CO_2^{2-} species introduce two oxygen atoms to the surface which increase the surface coordination of the cerium atoms and thus there is a strong bind.

5.3.3 Surface Phase Diagrams

To define ceria surface stability in the presence of adsorbed CO_2, surface phase diagrams CO_2 partial pressure of CO_2 as a function of temperature were generated. Figure 5.4 shows the CO_2 partial pressure vs temperature phase diagrams for each surface, where the different regions of the diagrams represent the most stable surface composition (i.e. those with the lowest surface energy).

On the stoichiometric surfaces, CO_2 will desorb from the {111} first, followed by the {110} and then the {100} at any given pressure (Figure 5.4). The introduction of oxygen vacancies greatly increases the temperature range that adsorbed carbonate is stable on the surfaces. This is due to the surface healing effect where CO_3^{2-} species at the surface allow the surface cerium to regain their partial coordination (Figure 5.3). As seen in previous section, the adsorption energies for 3 and 4 carbonate species are quite weak compared to 1 and 2 carbonate species, as a result the 3 and 4 carbonate "phases" do not appear in the phase diagram (with the exception of the reduced {110} surfaces). At low T (blue region) the surfaces are partially covered with carbonate molecules, whereas at high T (red region) carbonate molecules are not stable at the surface and thus are not present.

The atmospheric CO_2 pressure at 298 K is marked on each phase diagram in Fig-

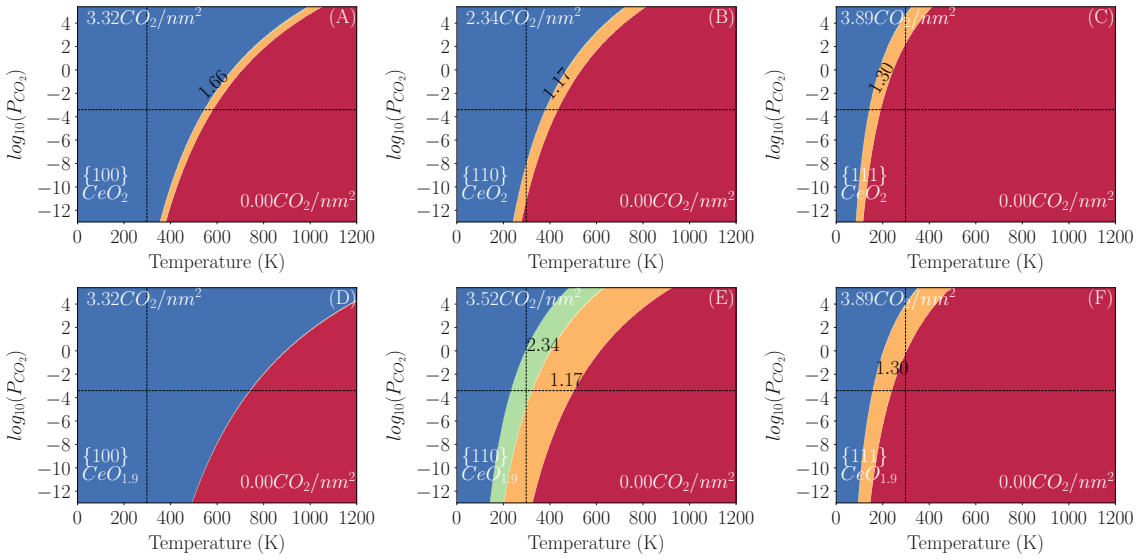

Figure 5.4: CO_2 partial pressure vs temperature phase diagrams for the stoichiometric {100} (A), {110} (B), {100} (C) and the reduced {100} (D), {110} (E) and {111} (F) surfaces. The CO_2 coverage (CO_2/nm^2) of each phase is added to the phase diagram. The atmospheric carbon dioxide pressure at 298 K has been marked with dashed black lines.

ure 5.4 in order to highlight the state of the surfaces when samples interact with the atmosphere. Under these conditions carbonates will not form on either the stoichiometric or reduced {111} surface, so an octahedral nanoparticle, left in the atmosphere will remain free of carbonate species. In contrast, both the {110} and {100} surfaces (Stoichiometric and reduced) when exposed to the atmosphere, will suffer from carbonate deposition at the surface. Taken together this shows that nanoparticles containing all three of these surfaces (Nanospheres) or just the {100} and {111} (Truncated Octahedra) will have different surface compositions if exposed to the atmosphere.

5.3.4 Desorption Temperature

Based upon the pressure vs temperature phase diagrams, the temperature of desorption for carbonate species at the {111}, {110} and {100} surfaces as a function of CO_2 partial pressure were calculated (Figure 5.5). The desorption temperatures represent the transition between a bare surface and a surface with adsorbed CO_2. These can be compared to the experimental values measured via temperature programmed desorption experiments for the low index surfaces of ceria. On all surfaces,

the carbonate is more stable on the reduced surface compared to the stoichiometric surface and this can be attributed to the oxygen vacancy healing effect discussed in the previous section.

Senanayake and Mullins reported weakly bound CO_2 on the {111}, which start desorbing at 150 K with only a small amount of carbonate at 200 K [209]. Ultra-high vacuum conditions (1.33^{-11} bar) are used for temperature programmed desorption temperatures. Based upon the predicted desorption temperatures, CO_2 is removed at 127 K on the {111} under these conditions. Removal of CO_2 at low temperatures on the {111} is also reported by Staudt et al who could not detect any CO_2 on the {111} surface at 300 K [216]. Also, Senanayake et al determined that carbonates were removed from the {111} surface of CeOx/Au on heating to 300 K [217]. These observations are consistent with the calculated desorption temperatures as only at high CO_2 pressures are there carbonates persisting beyond 300 K.

Carbonate is bound much more strongly on the {100} and thus the desorption temperatures are much higher (Figure 5.5). Albrecht et al,. found that carbonate species on the {100} are stable up to 600 K for stoichiometric ceria and 700 K for partially reduced ceria ($CeO_{1.7}$) under ultra-high vacuum conditions [212]. We predict under these conditions that CO_2 will desorb by 450 K on stoichiometric ceria and 550 K on reduced ceria. It is worth noting that our reduced ceria model is $CeO_{1.916}$ which not as oxygen deficient as the experimental samples. Furthermore, we have only considered CO_3^{2-} species at the surface and in reality, depending on the pH, a wide range of carbonate species can exist and the distinction is not made in the experiments.

5.3.5 Effect on Reduction

Reduction temperatures for the bare surfaces were calculate in chapter 3 and calculated in the presence of water in the previous chapter. In this section, the reduction temperature in the presence of CO_2 has been calculated (figure 5.6). For all surfaces, carbon dioxide at the surface lowers the temperature at which oxygen can desorb from the surface. The severity of this change is different depending on the surface, the desorption temperature {111} surface is lowered by the smallest amount while

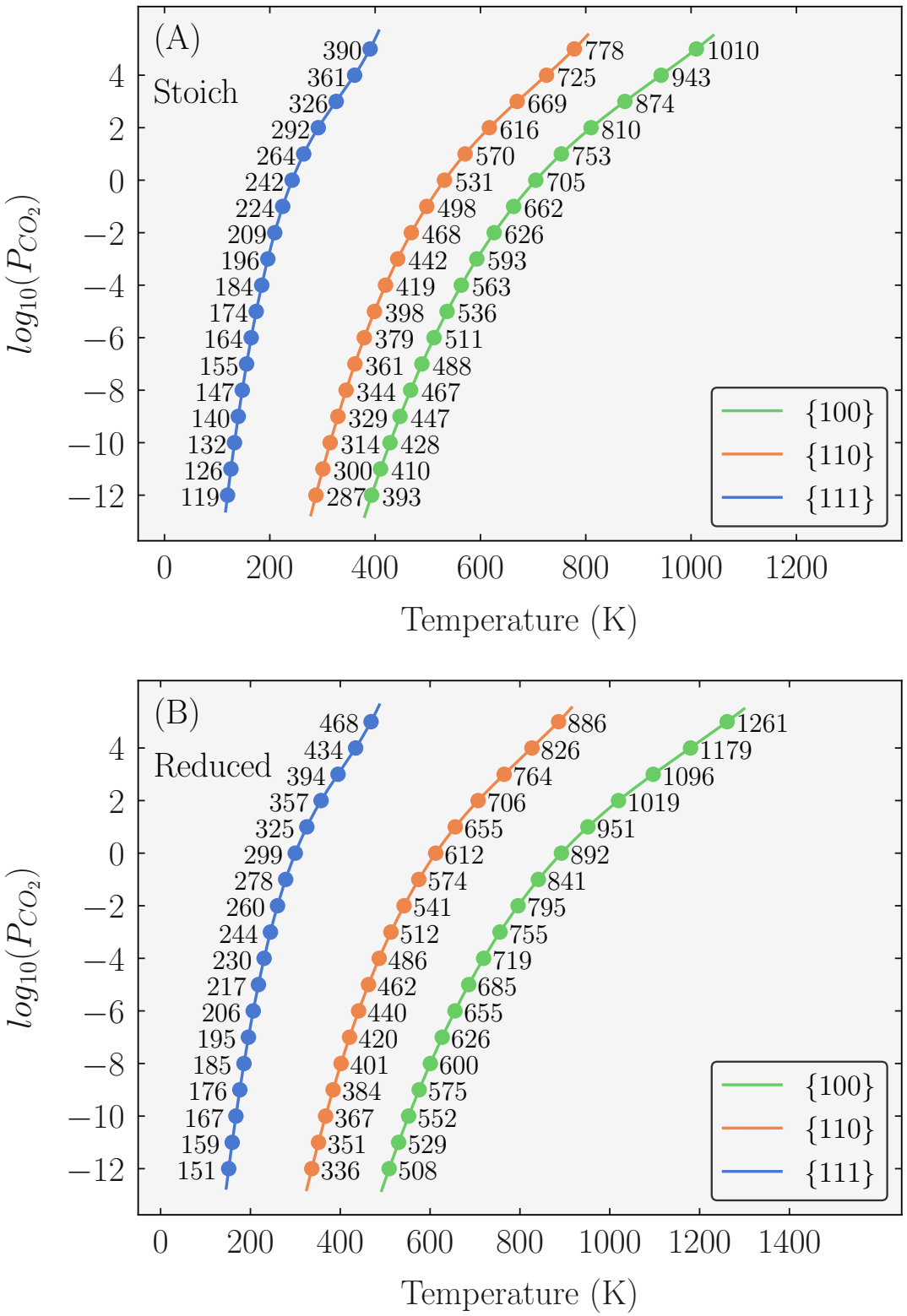

Figure 5.5: Temperature of desorption for the stoichiometric (A) and reduced (B) surfaces. The {111}, {110} and the {100} surfaces are shown in blue, orange and green. The temperature of desorption at pressures ranging from -12 $\log_{10}(P_{CO_2})$ (bar) to 5 $\log_{10}(P_{CO_2})$ (bar) in increments of 1 are marked at the corresponding locations on the plots.

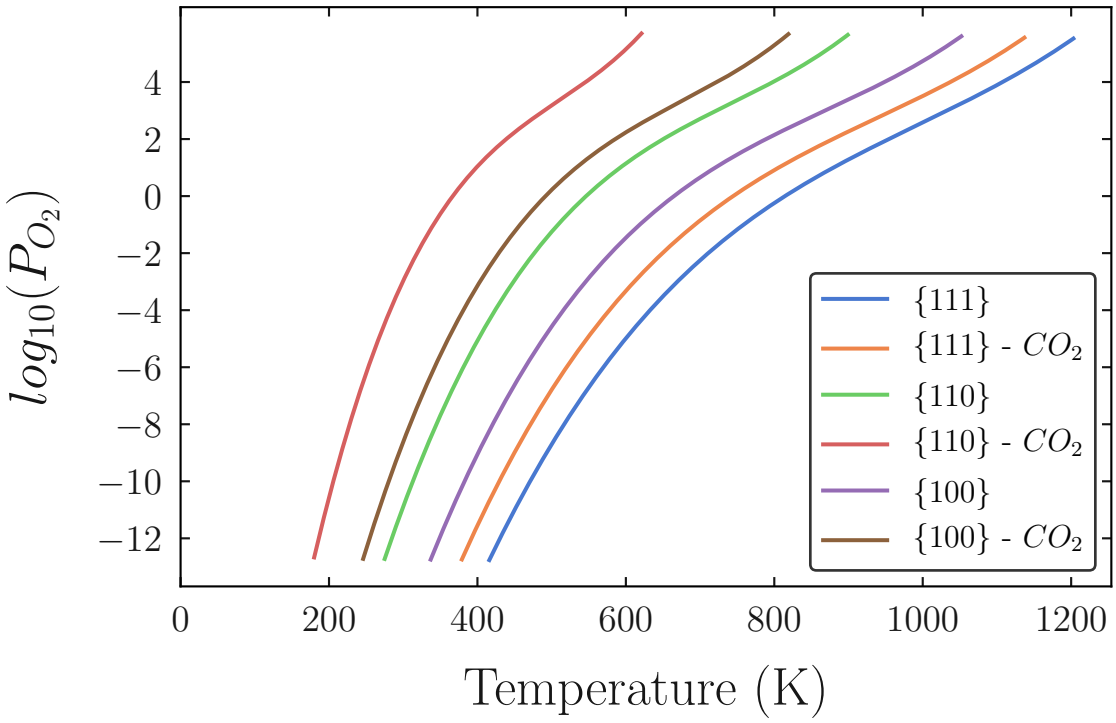

Figure 5.6: Desorption temperature for oxygen (Reduction temperature) on the bare {111}, {110}, {100} (Blue, green and purple lines) and the carbonated {111}, {110}, {100} (Orange, red and brown lines)

the {110}/{100} is lowered by a larger amount. The lowering of the reduction temperature is likely due to the ability of carbon dioxide to heal the coordination of the surface cerium atoms. The extra oxygen from the carbon dioxide adsorbs at surface cerium sites, and this lowers the impact to the surface cerium coordination of losing an oxygen, thus oxygen can desorb easier.

5.3.6 Predicted Particle Morphology

Based upon the surface energies calculated in section 3.3, Wulff plots have been constructed as a function of temperature and CO_2 partial pressure for the stoichiometric and reduced surface systems (Figure 5.7). These plots illustrate the relative stability of the surfaces in the presence of CO_2. The {111} surface is the most stable surface and the particle morphology, based upon the surface energies at 0 K from DFT is octahedral displaying the {111} surface. When a molecule adsorbs at a surface, it lowers the surface energy of that surface, thus, when carbonate is present at the surface it lowers the surface energy. There is a significant difference between the

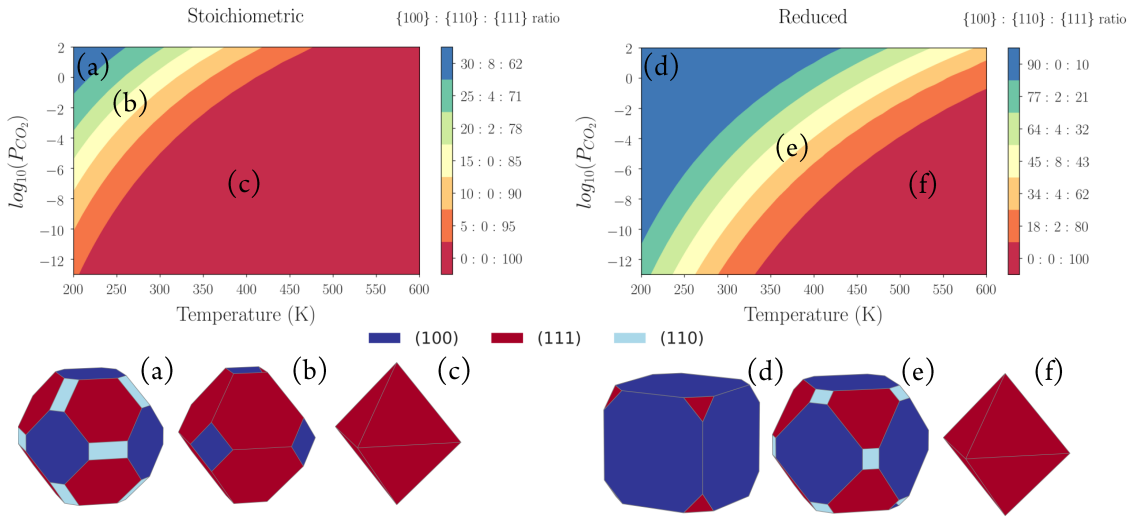

Figure 5.7: Particle morphology phase diagram for the stoichiometric and reduced surfaces. Wulff constructions are shown for the stoichiometric and reduced surfaces. These correspond to a {100}:{110}:{111} ratio of 35:12:63 (a), 15:0:85 (b) and 0:0:100 (c) for the stoichiometric surface and 90:0:10 (d), 45:12:43 (e) and 0:0:100 (f) for the reduced surface. For clarify the {111}, {110} and {100} facets are shown in red, light blue and dark blue respectively.

stability of carbonate on the three surfaces and the change in the surface energies as a result can be analysed via the Wulff construction.

The desorption temperature curves for each surface has been overlaid on to each plot. These illustrate the regions of the morphology phase diagram where each surface is being stabilized by carbonate species. For example, on stoichiometric surface the {111} surface has very low desorption temperatures whereas the {100} surface has comparatively high desorption temperatures, the region of the phase diagrams between these lines is the region where the surface energy of the {100} is being lowered by carbonate species while the {111} is not (this means that in this region the particle morphology the {100} is covered in carbonates whereas the {111} is not). This lowering of one surface energy relative to another is why adsorbed species are able to affect the morphology significantly.

Using ultra high vacuum conditions as a reference point (i.e. below 10^{-10} bar pCO_2), for stoichiometric ceria, there is a clear preference for octahedral nanoparticles at temperatures above 210 K. However with increasing pressure, the nanoparticle area

is increasingly made up of {100} and {110} surfaces.

Using ultra high vacuum conditions as a reference point, for reduced surfaces octahedral nanoparticles are formed above 310 K. High pressures of CO_2, low temperatures and reduced ceria are a conceivable combination to generate highly reactive nanocubes. It is interesting to note that corners of nanocubes (Figure 5.7) are truncated by {111} surfaces; this seems to be in line with the findings that there is a minimum size of associated with this truncation.

5.4 Carbon Dioxide Adsorption at Doped Surfaces

In this section, the associative adsorption of CO_2 on doped surfaces of CeO_2 will be discussed. As with the stoichiometric and reduced surfaces discussed in the previous section, the adsorption energies, phase diagrams, desorption temperatures and particle morphologies have been generated and will be discussed within the context of catalysis with cerium oxide.

5.4.1 Adsorption Energy

The associative CO_2 adsorption energy is shown in Figure 5.8. The adsorption energy at low coverage is found by evaluating the energy of an isolated carbonate species at the surface. The CO_2 adsorption energy follows the order {100} < {110} < {111} on all surfaces, i.e the order of stability of the bare surfaces, with the least stable surface ({100}) having the strongest adsorption energy.

The surface containing oxygen vacancies (Reduced Ce(III) or Doped M(III) surface) have a stronger affinity for associative CO_2 than the stoichiometric surfaces, which contain no oxygen vacancies. This is due to the vacancy itself, the introduction of a vacancy reduces the coordination of the surface cerium atoms, the introduction of the adsorbed CO_2 species allows the surface to recover its partial coordination and as with OH groups in the previous chapter, the CO_2 heals the vacancy.

At the lowest coverage, dopants decrease the affinity of the {111} and {100} surfaces for CO_2 whereas they increase the affinity of the {110} when compared to the reduced surfaces which have an equal concentration of oxygen vacancies. This difference is small for the {111} and {100} surface but significant for the {110}. On all surfaces the Sm^{3+} doped surface is most similar to the reduced surfaces in terms of energy and Ce - O - C bond lengths. This is likely due to the atomic radii of the dopants and Ce(III). Sm^{3+} is the closest in radii to Ce(IV), whereas Y^{3+}, which is the most contrasting compared to the reduced surface and has the biggest difference in radii.

The associative CO_2 adsorption energy is shown in Figure 5.8 as a function of coverage. The general trend is that the adsorption energy becomes less favourable as coverage increases, with the exception of the {100} and {111} surfaces between 1.66 - 3.32 and 2.59 - 3.89 CO_2/nm^2 respectively. The decrease in energy on the {100} is due to the surface coordination of cerium atoms, at a coverage of 3.32 the surface reconstructs and there is a symmetrical arrangement of oxygen and carbonate species which allows the surface cerium to almost completely regain 8 fold coordination. Generally however, as the coverage increases, particularly at the highest coverage, the repulsion between carbonates offsets the increase in surface coordination.

5.4.2 Phase Diagrams

In order to infer the stability of carbonates at the surface under catalytic operating conditions, phase diagrams for each surface as a function of CO_2 partial pressure and temperature were generated and the phase boundary between adsorbed CO_2 and the bare surface is shown in figure 5.9. When compared with the stoichiometric surfaces, the oxygen vacancy containing surfaces (CeIII and MIII) cause a large increase in the stability of carbonate at the surface. As discussed in the previous section, there is an increase in the pressure/temperature range where carbonate is stable on each surface. The dopants promote a slight increase in the region on the {100} surface and a large increase on the {110} surface. In contrast, the dopants have a minimal effect on the {111} surface although cause a small decrease in the

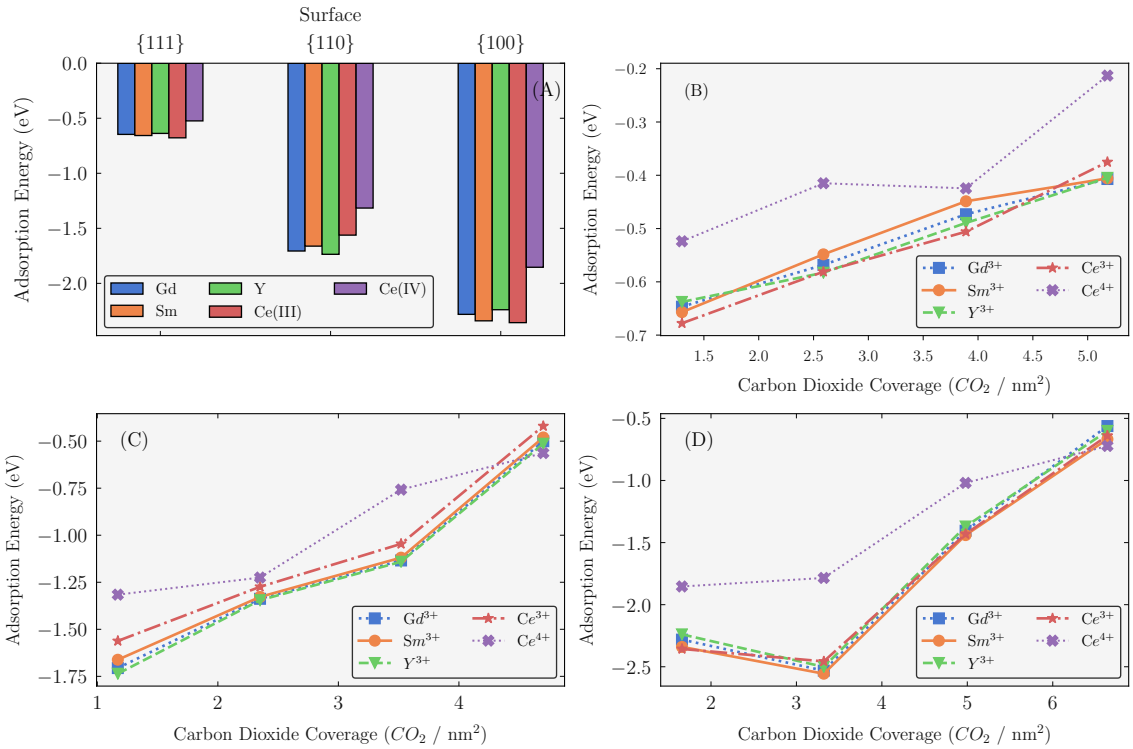

Figure 5.8: (A) Adsorption energies for carbon dioxide on the low index surfaces of ceria for a coverage of 1.66, 1.17 and 1.30 CO_2/nm^2 for associative CO_2 on the {111}, {110} and {100}. Ce(IV), Ce(III), Sm^{3+}, Gd^{3+}, Y^{3+} are denoted by blue, orange, green, red and purple bars, respectively. (B, C, D) Adsorption energy (eV) per CO_2 as a function of coverage for (B) {111}; (C) {110}; (D) {100}; for Gd^{3+} doped (blue squares), Sm^{3+} doped (orange circles), Y^{3+} doped (green triangles), Ce(III) (red stars) and Ce(IV) (purple crosses) ceria.

stability.

5.4.3 Desorption Temperature

The desorption temperature, which is defined as the point where the free energy of the bare surface is equal to that of a carbonated surface can be evaluated from the phase diagrams. To date there are no experimental studies on the desorption temperature of CO_2 on the doped surfaces of ceria.

The difference between the desorption temperature of the M^{3+} doped and stoichiometric surfaces is shown in Figure 5.10 and the difference between the desorption temperature on the reduced surfaces and doped surfaces is shown in Figure 5.10. These were calculated as $T_{M^{3+}\text{ - surface}}$- $T_{\text{stoichsurface}}$ and $T_{\text{doped surface}}$- $T_{\text{reduced surface}}$ respectively. Introducing dopants and reduction of the surface (controlled oxygen partial pressure) are two ways of modifying the oxygen stoichiometry of the surface. The reduced and doped surface have an equal concentration of oxygen vacancies, thus the variable at the surface is the cation, e.g. Gd^{3+} vs Ce^{3+}.

Reduction of the {111} surface increases the temperature where adsorbed CO_2 is stable and present, compared with doping the surface (Figure 5.10). In contrast, doping the {110} {100} surfaces increases the temperature range where CO_2 is stable, compared with reducing the surface. Unlike the hydrated surfaces, dopants have a very small impact on the desorption temperatures. On the {111} and {100} surfaces the difference between desorption temperatures is negligible ($< 10\,K$ and $< 25\,K$ at all pressures for the {111} and {100} respectively.). The difference is slightly greater on the {110} surface (30 - 50 K depending on pressure) but not to the same extent as with hydrated surfaces.

5.4.4 Predicted Particle Morphology

As in the previous chapter, the particle morphology for each system as a function of CO_2 partial pressure and temperature has been calculated. Figure 5.11 shows the morphology phase diagrams for each surface system. There is a driving force at low temperature towards morphologies with a large {100} area, whereas a low ratio

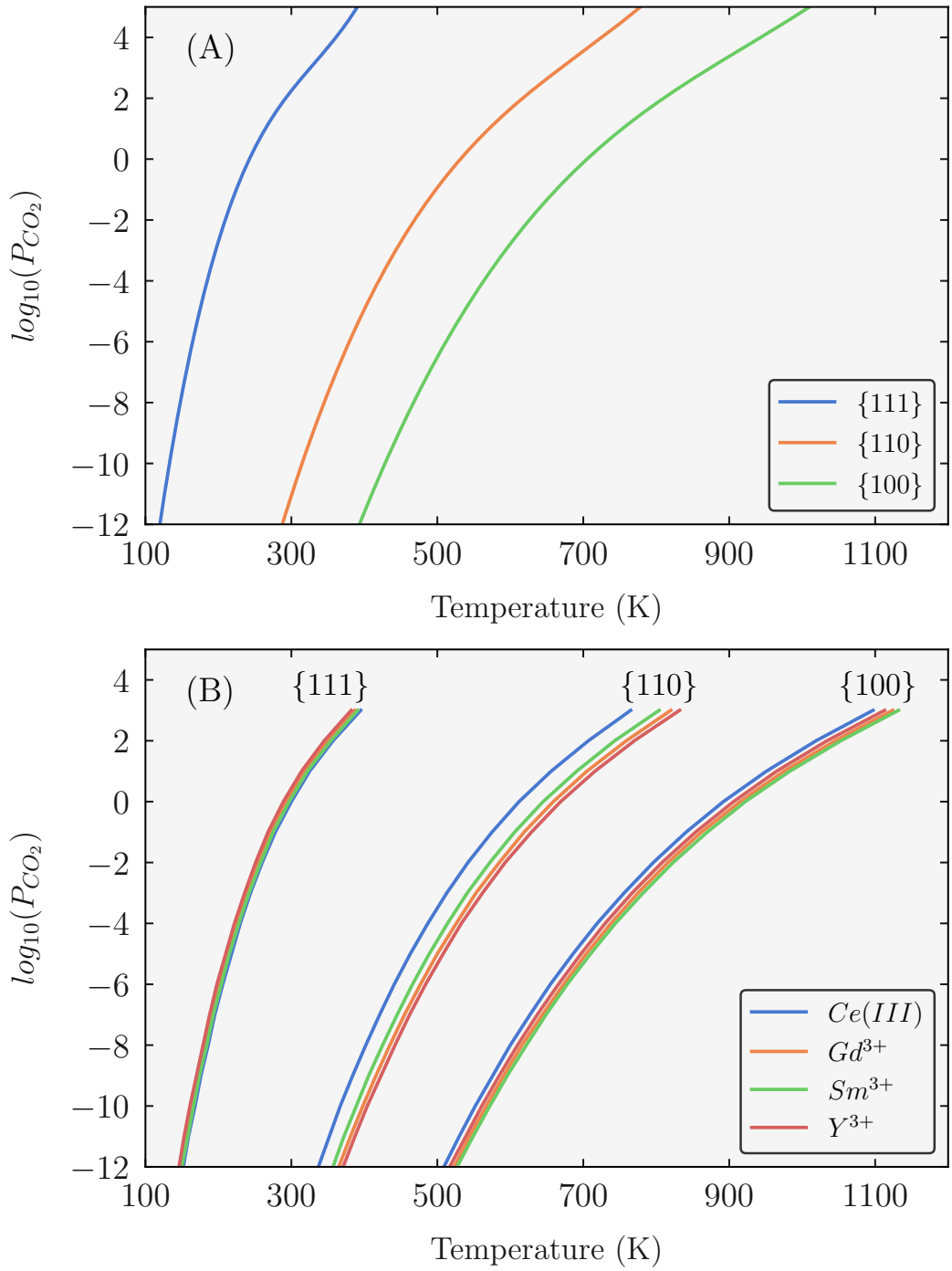

Figure 5.9: The phase boundary between bare and carbonated surfaces as a function of CO_2 partial pressure and temperature. (A) CO_2 desorption temperatures at different partial pressures of CO_2 on stoichiometric {111} (Blue), {110} (Orange) and {100} (Green) surfaces (CeIV), (B) Desorption temperatures for CO_2 on the reduced (Ce(III)), Sm^{3+}, Gd^{3+} and Y^{3+} surfaces (Blue, orange, green and red lines) surfaces. The desorption regions are labelled for each surface.

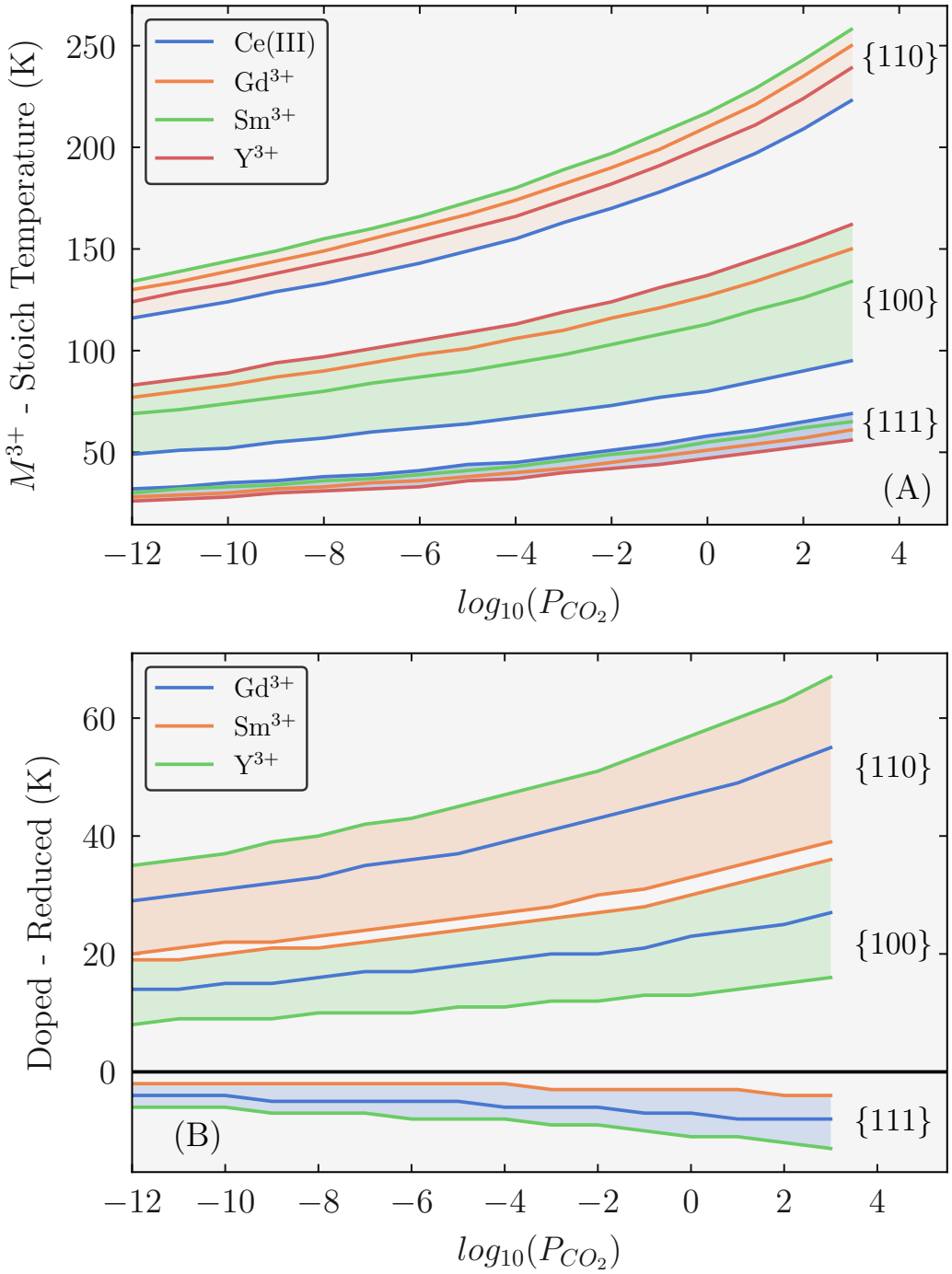

Figure 5.10: (A) The difference in desorption temperatures for doped surfaces compared to stoichiometric surfaces, calculated as $T_{M^{3+}\text{ - surface}}$- $T_{stoichsurface}$. The reduced (Ce(III)), Gd^{3+} doped, Sm^{3+} doped and Y^{3+} doped surfaces are shown in blue, orange, green and red, respectively. (B) The difference in desorption temperature between doped surfaces and reduced surfaces, calculated as $T_{\text{doped surface}}$- $T_{\text{reduced surface}}$. Gd^{3+}, Sm^{3+} and Y^{3+} are denoted by the blue, orange and green lines. The blue, orange and green shaded areas correspond to the {111}, {110} and {100} datasets.

at high temperature and low pressure. The dopants cause a small increase in the temperature / pressure range where the {100} surface is expressed. This is greatest on the Y^{3+} doped surfaces.

Due to the increased stability of CO_2 on the doped {100} surfaces, {100} surfaces are predicted to be present (Forming truncated octahedral) under more extreme conditions than for undoped reduced surface containing Ce^{3+}. For example, our results suggest that doped octahedral nanoparticles, used at ultra-high vacuum (-10 log_{10}) at 360 K, will truncate to express {100} surfaces, whereas undoped reduced (Ce^{3+} containing) surfaces thermodynamically will not. Whereas in contrast, nanocubes used at high temperatures, will be driven towards {111} bearing octahedral nanoparticles.

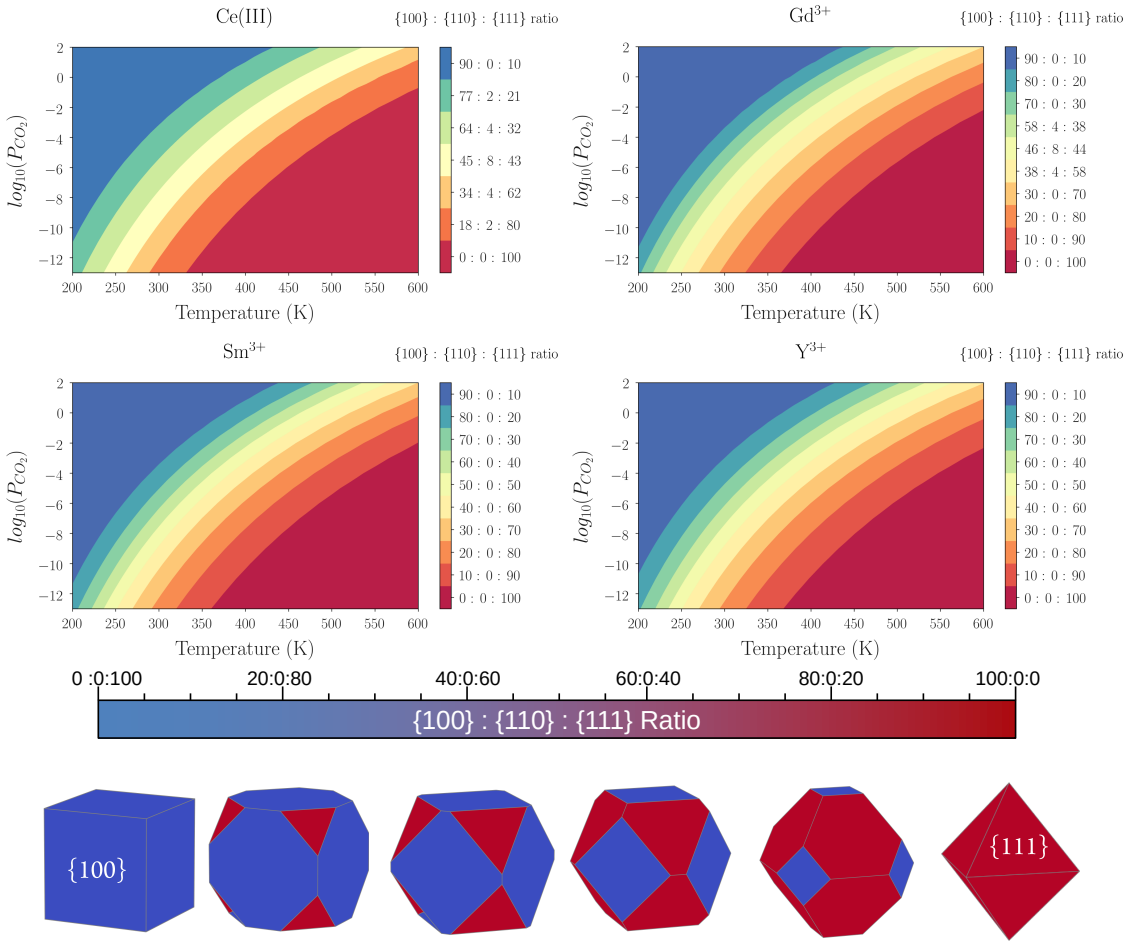

Figure 5.11: Ratio between the {100}, {110} and {111} surface areas as a function of temperature and pressure for the stoichiometric system. For visual clarity, nanoparticles corresponding to these ratios are shown. The ratio between the {100} and {111} reduced, Gd^{3+}, Sm^{3+} and Y^{3+} doped systems as a function of temperature and pressure are shown. It should be noted that the {110} surface does not appear under these conditions for the doped systems and has thus not been included. Predicted particle morphologies across a range of surface area rations are shown for visualization of these ratios.

5.5 Discussion

The performance of nanoceria catalysts in the form of nanoparticles is influenced by the surface morphology, composition and stoichiometry of the exposed facets [34]. This has been shown in recent times, where research has focused on the effect of the different exposed facets on different catalytic processes [218, 219, 220]. As individual catalytic application is optimized by a specific morphology, then it is important to reach the nanoparticle optimal design before implementing the material in the catalytic process.

In this chapter, it has been shown that the interaction of carbon dioxide with CeO_2 strongly affects the relative surface stability and can be visualized through the calculation of the equilibrium particle morphology, however this strategy neglects kinetic considerations. The surface stability as a function of surface composition (e.g. stoichiometric, reduce and carbonated surfaces), pressure and temperature has been predicted, and presented in simple phase diagrams. These diagrams make it easy to forecast those surfaces that would be preferred for a specific catalytic process either in terms of surface stoichiometry or surface carbonation. The calculations suggest that oxidation of the surface removes / hinders the adsorption of carbonates from/to the surface, as the reduced surfaces have considerably higher desorption temperatures compared to stoichiometric surfaces (up to 200 K). Oxygen vacancies are reactive sites and are often desirable in catalytic reactions, however carbon dioxide interact so strongly with the vacancies that the catalyst may lose its efficiency. It is clear that efficiency may be restored as the temperature increase (and CO_2 desorbs). However, this comes at a higher cost as more energy consumption is required to remove CO_2 form reduced compared to stoichiometric surface. (Fig 5)

Ceria is used in the water gas shift reaction (WGSR). Here the redox reactions proceeds via a stable carbonate intermediate, the coverage of which was dependent on the surface Ce^{3+} concentration [221]. Because the reduced surfaces have a considerably stronger interaction with carbonates compared to the stoichiometric surfaces and given that Ce^{3+} concentration is dependent on the concentration of oxygen va-

cancies, it can be inferred that the experimental observations of Feng et al., is to be attributed to the strong interaction between CO_2 and the oxygen vacancies.

In industrial processes like Fischer-Tropsch synthesis, methanol synthesis or hydroformylation, a well defined $H_2/CO/CO_2$ ratio is needed for operation [202]. Or in order to be used for ammonia synthesis, hydrogenation reactions or as possible energy vector in combination with PEMFC, H_2 must contain very low amounts of CO in order to minimize poisoning of the various catalysts employed [202]. The water gas shift reaction when combined with preferential oxidation (PROX) is the most promising way to purify H_2 steam from CO poisoning. Ceria based catalysts are employed in low temperature WGSR (500 - 600 K). The reaction is dependent on the formation of formates or carbonates at the surface, these decompose into CO_2 and H_2 [34]. Pt/CeO_2 catalysts suffer from deactivation by carbonate deposition when there is CO_2 within the reaction chamber [43]. It was proposed that carbonate formation reduces the concentration of surface OH groups which are a key component of the reaction. Water dissociation is considerably stronger at oxygen vacancy sites [163], thus a possible explanation for the deactivation is that carbonate groups form a strong complex at the oxygen vacancy sites, blocking the reactive sites for water splitting to occur.

Using surface phase diagrams, the equilibrium morphology of nanoparticles as a function of temperature and CO_2 partial pressure have been evaluated. This strategy shows not only the morphology of the nanoparticles but also the composition of the surfaces expressed in the nanoparticle. At specific conditions of temperature and partial pressure, surfaces behave in different ways towards carbonates, some will be preferably carbonated and some will not. Although, this is a thermodynamic strategy, and kinetic factors are not included, it is clear that there will be a thermodynamic driving force for a nanoparticle to evolve into its most energetically stable/favourable conformation and composition. Thus perhaps, optimal nanoparticles shapes may be selected for specific catalytic applications beforehand using such computationally derived morphology phase diagrams. As the exposed surfaces have a big impact on the stability of carbonates at the nanoparticle, for example

nanocubes, bearing the {100} surface will support carbonate molecules across a much wider temperature range than morphologies displaying {110} or {111} surfaces (i.e. octahedra). This method could potentially be applied to any material and catalytic process that see carbonates as either welcomed or unwanted adsorbed species.

These calculations only consider the adsorption of dry CO_2, i.e. CO_2 in the absence of water. In reality there is likely competition between CO_2 and H_2O at the surface because there are limited adsorption sites. An avenue for future exploration would be to consider both the adsorption of CO_2 and H_2O at the surface. Comparison between this chapter and the results of the previous chapter indicates that water is more likely to adsorb than CO_2 on the {111}/{100} surfaces and CO_2 is more likely on the {110} surface, based purely on the comparison of adsorption energies. Further study into the interaction between water and carbon dioxide at the surface is needed.

5.6 Conclusions

Initially the work in this chapter was limited to associative adsorption of carbon dioxide on the surfaces of CeO_2 and explored how carbonates at the surface affected the relative stability of the three surfaces. It was found that there were vast differences in the adsorption behaviour between the three surfaces, with the {100} surface being stabilised vastly more than the {111} surface. As a result of the different adsorption energies, the {100} surface is stabilised and expressed in the particle morphology across a much wider temperature and pressure range compared with water in chapter 5. Reducing or doping the surface with trivalent Gd^{3+}, SM^{3+} and Y^{3+} cations increases the affinity of the surface for carbon dioxide compared to the stoichiometric surface. When comparing surfaces with equal oxygen stoichiometries (Doped and Reduced) there is very little change in the adsorption energy and thus the morphology.

6 The Interaction between Phosphate Anions and CeO_2 Surfaces

The contents of this chapter have been previously published by the author as part of this PhD project and can be found at the following reference, Molinari, M.; Symington, A. R.; Sayle, D. C.; Sakthivel, T. S.; Seal, S.; Parker, S. C., Computer-Aided Design of Nanoceria Structures as Enzyme Mimetic Agents: The Role of Bodily Electrolytes on Maximizing Their Activity. ACS Applied Bio Materials **2019**, 2 (3), 1098-1106. This chapter includes the work conducted by the author and does not include any work carried out by collaborators. Notably, molecular dynamics simulations and experimental analysis which aid in the conclusions of this work, carried out by Dr Dean Sayle and Prof Sudipta Seal, have been omitted but can be found in the referenced article.

In the previous three chapters, the surfaces of cerium oxide have been explored with dopants, water and carbon dioxide. The interaction between the surfaces and phosphate anions is considered as it presents an interesting research avenue, both in terms of the environment e.g. removal of phosphate anions from water supplies and in a biomedicine e.g. nanozymes. Cerium oxide is part of a group of nanoparticles or nanozymes being trialled in a biomedical context. In this chapter, DFT calculations have been used to address the interaction between the surfaces of cerium oxide and phosphate anions, under different oxygen and hydrogen stoichiometries.

6.1 Background

There is correlation between the development of many diseases and oxidative stress which evolves from the accumulation of highly reactive oxygen species (ROS) due to an insufficient buffering by the antioxidant defence [222, 223]. ROS can oxidize cell constituents such as lipids, proteins, and DNA, thus damaging cells structures and compromising their functions [224]. The induced oxidative stress has been related to chronic inflammations, cancer, neurodegenerative and immune-deficient disorders [225, 226].

Nanotechnologies, such as the usage of metal oxide nanomaterials, are one of many promising routes to control oxidative stress, by inducing apoptosis of damaged cells [227]. CeO_2, has high oxygen storage capacity and redox activity that arise from the easy conversion between oxidised CeO_2 and oxygen-deficient CeO_{2-x} and in recent years ceria has been explored in the fields of biology and medicine [199, 228, 229]. Ceria has earned the name of nanozyme, i.e. metal oxide nanomaterials that display enzyme-mimetic activity [227, 230, 231], and perhaps its most important enzyme-mimetic activities are indeed those related to the suppression of ROS. Ceria acts to reduce the amount of ROS in a cell by acting as a radical scavenger through its high oxygen storage capacity and redox chemistry. Ceria surface defects, i.e. oxygen vacancies and Ce^{3+} ions, are believed to be responsible for the materials radicals scavenging activity, including superoxide dismutase (SOD) and catalase. The latter are some of the most important enzymes to that regulate the concentration of superoxide anion radicals, O_2^- [232, 233, 234, 235], and hydrogen peroxide, H_2O_2 [235, 236, 237, 238, 239, 240].

Possible applications of ceria span from a protective agent against radiation-induce cellular damage [241], anti-inflammatory/antioxidant [240, 242, 243, 244] agents, growth promoter of stem cell [245], protection agents in cardiovascular disease [246, 247], and to a detection agent of cancer biomarkers [248, 249]. Most importantly, ceria can be exploited in therapy of oxidative stress-induced diseases, such as retinal degeneration [250], and neuroprotection [251, 252, 253], including Alzheimer's

disease [254]. However the treatment of oxidative stress through antioxidant therapy has drawn clinical attention. Whereas the quest is to find antioxidant agents able to mimic enzyme activities related to radical scavenging, antioxidant therapy is still under clinical scrutiny as ROS are required in physiological cellular functions. For this reason the antioxidant agent should cause apoptosis of damaged cells by inducing ROS production, or suppress ROS overproduction restoring the balance in the cellular environment. As clinical activity is focussed more on the physiological response of cells in the presence of ceria, the design and engineering of the material to act selectively towards the many and competing enzyme-mimetic activities can really benefit from atom-level information coming from modelling, particularly in light of ceria biological role [234, 240, 255, 256], and toxicity [255, 256, 257, 258] (e.g. non-toxic for normal (stromal) cells and cytotoxic to squamous tumour cells [259]).

The design and engineering of ceria as nanozyme will need to take into account the interaction of the material with the components of biological media. The cellular environment is a complex medium, and whereas cellular cytoplasm has neutral pH, subcellular organelles display a variety of pH. Asati showed that negatively charged ceria localizes in lysosome (pH 4.8) [249], although as surface charge becomes more positive it is released into the cytosol (pH 7.4) and localise in the mitochondria or endoplasmic reticulum [254]. Targeting different organelles will therefore require an understanding of the many factors such as particle size and morphology [236], Ce^{4+}/Ce^{3+} ratio, buffer species [237], pH conditions [260], and biomolecules and polymers [232], that modulate the enzyme mimetic activities of ceria.

Phosphate anions have been shown to alter the ROS scavenging ability of ceria, [232, 233, 260]. In this chapter the role of phosphate anions, a common inorganic anion present in biological media, at the surfaces of ceria has been investigated using DFT calculations. The interaction between phosphate and different surface compositions has been considered and discussed within the literature to provide a possible explanation for the alteration of the properties of ceria in the presence of phosphate.

6.2 Calculation Details

In the previous chapters on cerium oxide surfaces the slab method was used. In this method, it is preferable to have that the top and bottom surfaces are identical so as to be able to characterise each bonding interaction. However, due to the complexity of the calculations in this chapter, where phosphate anions, surface oxygen concentration and surface hydroxylation are all varied, the surface method has been explored. The surface method involves fixing the bottom two layers of the configuration, allowing electronic relaxation but not ionic relaxation. Thus no species are added to the "second" surface and the need for two identical surfaces is removed. The issue is that only the relative energies can be compared because it has to be assumed that the electrostatic energy contribution from the bottom, un-relaxed surface is removed. The surfaces were modelled at a constant volume using 6 repeat crystal layers (24 CeO_2 units) with a 15 Å vacuum gap perpendicular to the surface.

In the previous surface chapters the surface models were evaluated with DFT, using a PBE+U approach. The models in this chapter are evaluated using the PBEsol+U approach because this functional gave better agreement in terms of surface energy and reduction energy when compared to other theoretical and experimental work [136, 154, 163] (Table 6.1).

Table 6.1: Comparison of the surface and reduction energies using the PBE and PBEsol functional.

Surface	Surface Energy Jm^{-2}		Reduction Energy eV	
	PBEsol	PBE	PBEsol	PBE
{111}	0.85	0.89	2.63	2.03
{110}	1.23	1.30	1.83	1.52
{100}	1.72	1.78	1.99	2.06

Depending on the pH, phosphate can exist as PO_4^{3-}/ HPO_4^{2-}/ $H_2PO_4^-$ / H_3PO_4. Under biological conditions phosphate exists either as HPO_4^{2-} or $H_2PO_4^-$. Both species have been simulated in this chapter and it was found that$H_2PO_4^-$ was the most stable in most cases, and in those where it was not, a hydrogen atom dissociated from the $H_2PO_4^-$ to give the HPO_4^{2-} configuration. Thus, in the results section the

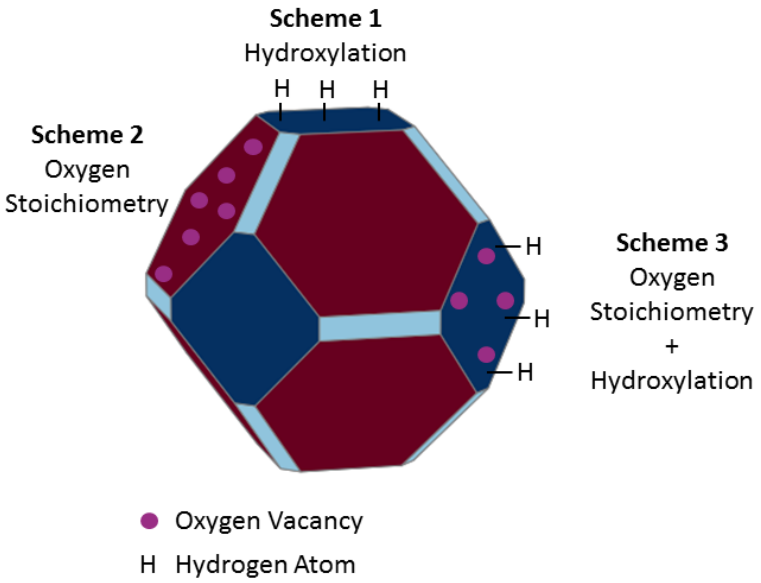

Figure 6.1: Schematic of the three surface states that were modelled. Scheme 1 considers a stoichiometric surface where the level of reduction (Ce^{3+} concentration increases due to the increase in surface hydrogen concentration. Scheme 2 considers a surface where the level of reduction (Ce^{3+}) concentration increases due to the decrease in oxygen stoichiometry. Scheme 3 considers a surface that contains oxygen vacancies, where the level of reduction (Ce^{3+}) concentration increases due to the increase in surface hydrogen concentration.)

data for $H_2PO_4^-$ has been presented and the data for HPO_4^{2-} can be found in the appendix. In the calculations, H_3PO_4 was used as a reference state for the reaction energy calculations.

For each scheme, information on the preferential affinity of phosphates and ceria surfaces is provided by calculating the strength of the interaction, with more negative energy terms indicating the strongest interaction. There are three variables which are being controlled in these calculations, surface hydrogen coverage, oxygen coverage and cerium (III) coverage (which are defined as the percentage of each species per surface CeO_2 unit (figure 6.1). For each surface composition several possible orientations of the phosphate anion and surface hydrogen were computed and the lowest energy configuration is reported in this chapter.

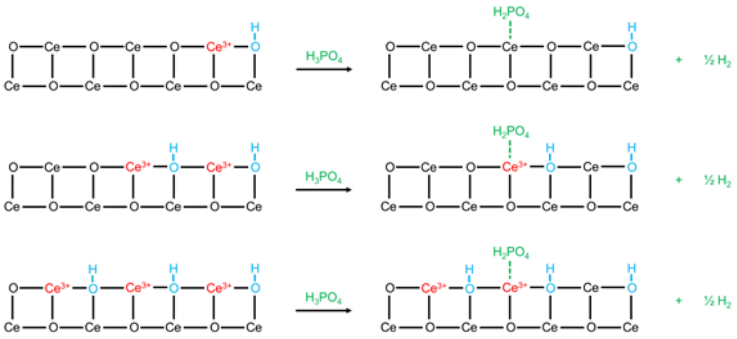

Figure 6.2: Schematic illustrating the adsorption schemes used in scheme 1. The hydrogen concentration increases while the oxygen stoichiometry and phosphate concentration remain constant.

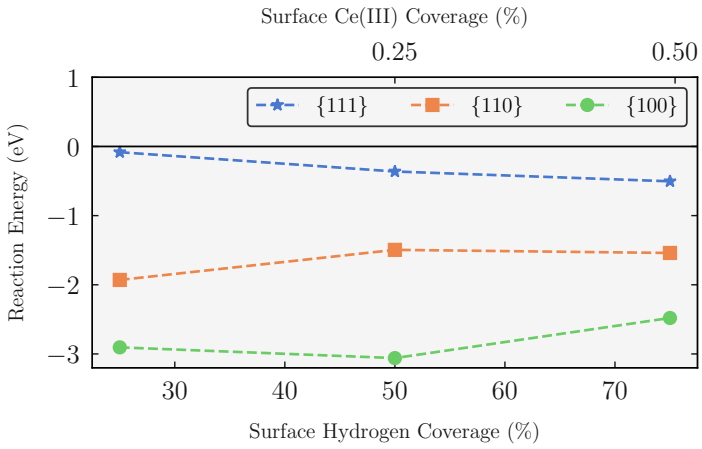

Figure 6.3: The reaction energy for phosphate adsorption on the stoichiometric {111} (blue), {110} (orange) and {100} (green) surfaces with varying hydrogen and Ce^{3+} concentration.

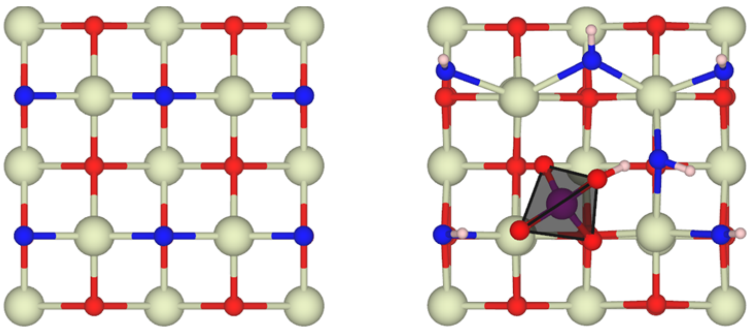

Figure 6.4: Surface structure of the stoichiometric {100} surface and the {100} surface with a surface OH group and an adsorption phosphate anion. Cerium, oxygen, phosphorus, hydrogen and surface oxygen are shown in cream, red, purple, white and blue

6.3 Hydroxylated CeO_2 Surfaces

In this scheme the ratio Ce^{4+}/Ce^{3+} in ceria is governed by the concentration of surface hydrogen species in the form of hydroxyl groups (OH%) and not by the surface oxygen sub-stoichiometry (i.e. there are no surface oxygen vacancies). As the concentration of surface OH groups increases, the surface Ce^{3+} concentration (Ce^{3+} %) increases. The interaction energy of phosphate is presented in Figure 6.3 as a function of OH% and Ce^{3+}%. The magnitude of the energy terms provides the order of stability of phosphate adsorption, and more negative energy terms contribute more towards the stabilization of the surface upon phosphate adsorption. The adsorption of phosphate is more favourable on the {100} surface followed by the {110} and {111} surfaces, when both the Ce^{3+} % and OH% are used as descriptors.

Across all three surfaces at all OH% and Ce^{3+}%, the phosphate adsorbs with bidentate or tridentate geometry Figure 6.5. This allows surface Ce atoms to recover partially on the {110} and {100}, and fully on the {111} surface, their coordination. The {111} surface consists of 7 fold coordinated surface Ce atoms, whereas the {100} and the {110} have 6 fold coordinated surface Ce atoms. These structural features provide a basic explanation of the different stabilization of ceria surfaces upon adsorption of phosphates, with the most under-coordinated surfaces (i.e. {100} and {110}) gaining the greatest stabilization compared to the {111} surface.

Of particular note is the behaviour of the {100} surface upon phosphate adsorption. Whereas, the surface oxygen sublattice of the {111} and {110} surfaces remains ordered upon phosphate adsorption, there is a large reconstruction on the {100} surface, which maximises the bonding network between surface Ce atoms and the phosphate (Figure 6.5). This is due to the extreme flexibility of the surface oxygen network on the {100} surface which can easily accommodate adsorbed species. This flexibility was also noted for carbon dioxide in the previous chapter.

Although all surfaces display a favourable adsorption energy of phosphate, the {111} surface is the only surface of ceria that shows a consistent decrease in adsorption energy ($\tilde{0}.5\,\mathrm{eV}$) with increasing OH% and Ce^{3+} % surface coverage, compared to the {110} and {100} surfaces where there is a decrease in favourability of about $0.4\,\mathrm{eV}$ across the coverage range.

The adsorption of phosphate on the {110} surface becomes less favourable in the middle range of OH% and Ce^{3+}% concentrations and then plateaus at high surface coverage. This is due to a lengthening of the bonds between the surface Ce ions and the adsorbed phosphate (Ce-OP) from 2.31 Å at the lowest concentration to 2.43 Å at the highest concentrations. Similarly, on the {100} surface there is a decrease in energy of adsorption at higher concentrations due to an increase in the hydrogen bonding network amongst the surface oxygen species and the surface OH% groups, whereas the hydrogen bonding network between the surface species and the adsorbed phosphate remains constant. The strengthening of the hydrogen bonding within the surface species causes a small increase in the Ce-OP bond lengths. The longest Ce-PO bond length increases from 2.55 Å to 2.66 Å . This indicates that on the {110} and {100} surfaces, Ce-OP bonding is a contributing factor governing the strength of adsorption.

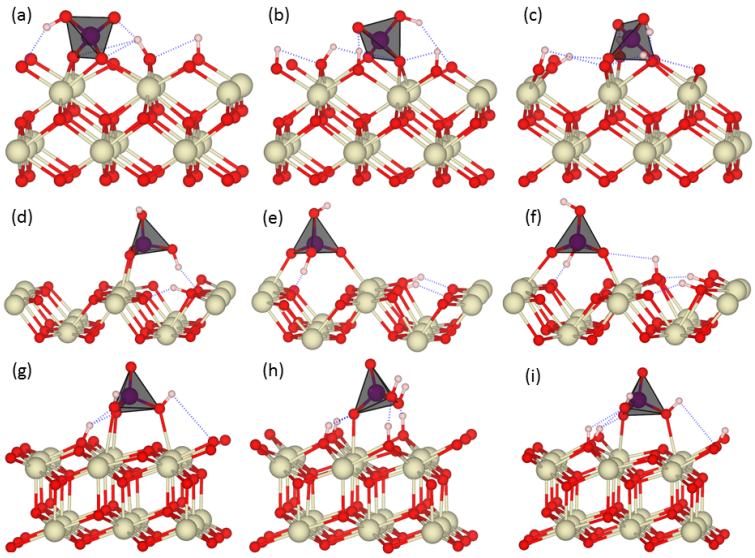

Figure 6.5: Adsorption geometry for $H_2PO_4^-$ the {100} (a, b, c), {110} (d, e, f) and {111} (g. h. i) surfaces with increasing hydrogen coverage. Cerium, oxygen, phosphorus and hydrogen atoms are shown in cream, red, purple and white and hydrogen bonds are shown with dashed blue lines. The polyhedra has been drawn on the phosphate for clarity.

6.4 CeO_{2-x} Surfaces

In this scheme the ratio Ce^{4+}/Ce^{3+} is governed by the surface oxygen stoichiometry (i.e. there is no hydroxylation of the surface). As the surface oxygen vacancy concentration increases (V_o %), the surface Ce^{3+} % increases.

Across all surfaces at all V_o%, the phosphate adsorbs with tridentate geometry (Figure 6.8). During minimisation a hydrogen atom leaves the phosphate anion and adsorbs on a nearby oxygen, suggesting that the dissociative adsorption of $H_2PO_4^-$ (i.e. HPO_4^{2-} and H adsorbed onto a surface oxygen) is barrier less in terms of energy on sub stoichiometric surfaces. The phosphate adsorbs so as to fill the

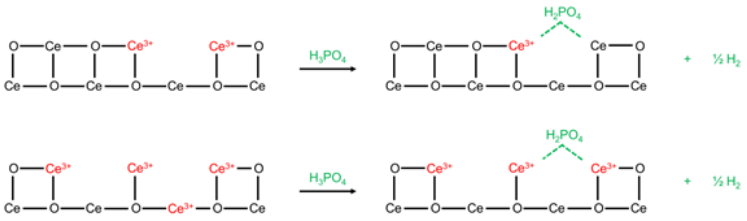

Figure 6.6: Schematic illustrating the adsorption schemes used in scheme 2. The oxygen stoichiometry decreases while the phosphate concentration remains constant.

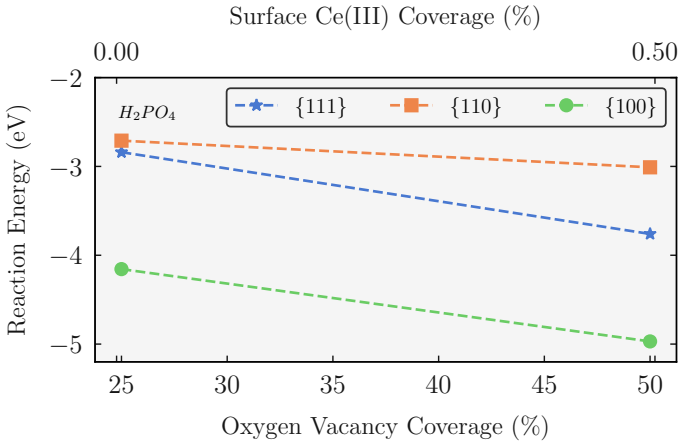

Figure 6.7: The reaction energy for phosphate adsorption on the {111} (blue), {110} (orange) and {100} (green) surfaces at varying oxygen stoichiometry and varying Ce^{3+} concentration.

vacant coordination sites caused by oxygen vacancies.

On each surface, at each Ce^{3+}%, the Ce-OP bonding network remains unchanged and so does the length of Ce-OP bonds. The decrease in adsorption energy can be explained by the under coordinated Ce surface atoms. The average coordination of Ce decreases as the Vo% increases. Phosphate anions allow surface Ce to partially recover their oxygen coordination environment.

The interaction energy of phosphate adsorption is presented in Figure 6.7 as a function of Ce^{3+}% and the concentration of oxygen vacancies at the surface. The adsorption of phosphate becomes more favourable when Vo% and Ce^{3+}% increase. The adsorption of phosphate is more favourable on the {100} surface followed by the {111} and {110} surfaces, when both Ce^{3+}% and V_o% are used as descriptors. The {100} is an intrinsically defective surface and so increasing coverage of surface oxygen vacancies causes a large de-stabilisation of the surface. Due to the oxygen sub-stoichiometry, the {100} surface is stabilised by phosphate anions to a much greater extent than for the {110} and {111} surfaces.

The {111} surface is stabilised to a greater extent relative to the {110} surface. The reduction of the {111} surface is the most energetically unfavourable, (1.98

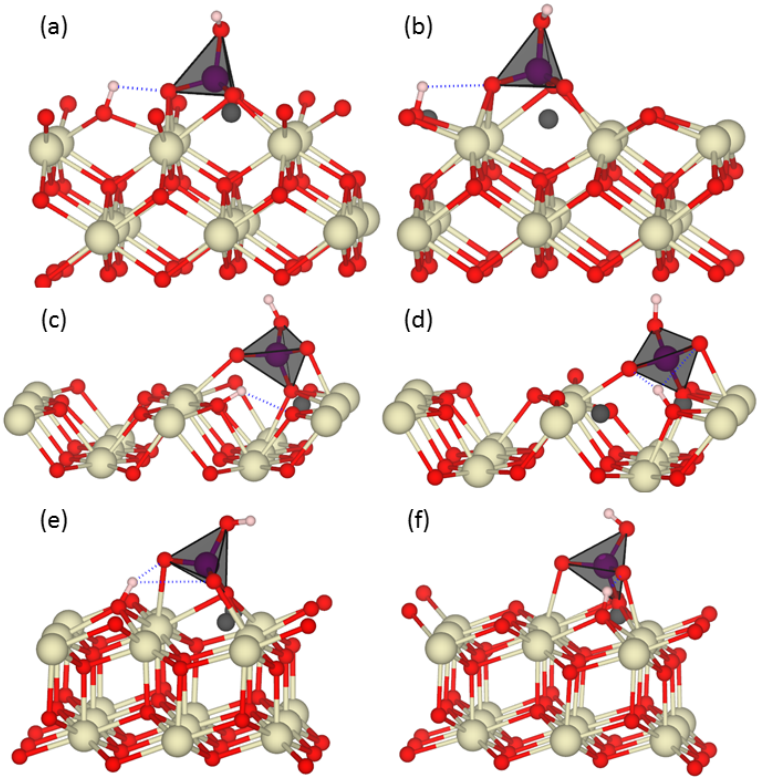

Figure 6.8: Adsorption geometry for $H_2PO_4^-$ the {100} (a, b), {110} (c, d) and {111} (e, f) surfaces with decreasing oxygen stoichiometry. Cerium, oxygen, phosphorus and hydrogen atoms are shown in cream, red, purple and white and hydrogen bonds are shown with dashed blue lines. The polyhedra has been drawn on the phosphate for clarity.

eV) and the reduction of the {110} surface the least energetically unfavourable, (1.07 eV). The phosphate heals the oxygen vacancies at the surface and this is more energetically favourable on the {111} than the {110}. This is because the {110} surface, as evidenced by the smaller reduction energy is more energetically stable with oxygen vacancies than the {111}. Unlike the in scheme 1, there is a relationship between the strength of phosphate adsorption and Ce^{3+} concentration due to oxygen stoichiometry. This suggests that the oxygen stoichiometry is an important factor that controls the strength of phosphate adsorption.

The oxygen sub-lattice of the {110} and {111} surfaces remains ordered however the {100} surface undergoes a small reconstruction to maximise the bonding network between the surface cerium and the phosphate anion (figure 6.8).

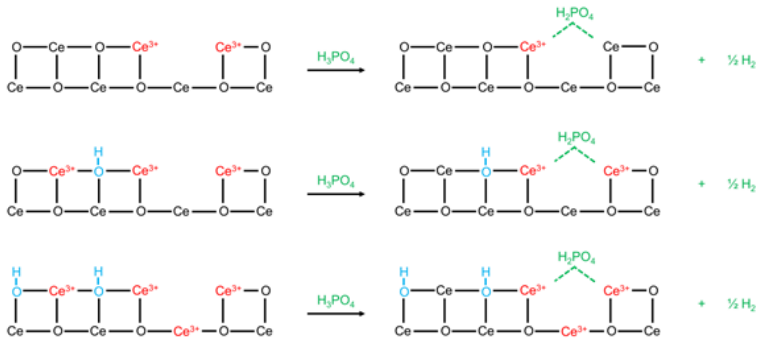

Figure 6.9: Schematic illustrating the adsorption schemes used in scheme 3. The hydrogen concentration increases while the oxygen stoichiometry, while sub-stoichiometric and phosphate concentration remain constant.

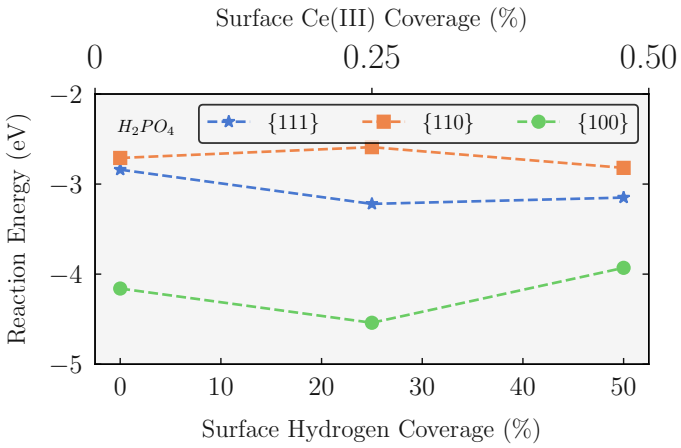

Figure 6.10: The reaction energy for phosphate adsorption on the {111} (blue), {110} (orange) and {100} (green) surfaces at constant, but sub-stoichiometric oxygen stoichiometry, varying hydrogen concentration and varying Ce^{3+} concentration.

6.5 Hydroxylated CeO_{2-x} Surfaces

In scheme 3 the ratio Ce^{4+}/Ce^{3+} is governed by the concentration of surface hydroxyl groups and the surface oxygen stoichiometry, i.e. there are both surface oxygen vacancies V_o% and surface hydroxylation OH%. However the V_o% and thus the oxygen stoichiometry of the surface is constant, and thus this scheme demonstrates the effect of increasing surface hydroxylation upon phosphate adsorption on oxygen deficient surfaces. The Ce^{3+} % changes due to increasing surface hydroxyl groups OH%.

The adsorption of phosphate is more favourable on the {100} surface followed by the

{111} and {110} surfaces, when both the Ce^{3+}% and OH% are used as descriptors. On the {110} surface, an increase in OH% groups and thus Ce^{3+}% results in a net decrease of 0.1 eV between the lowest and highest concentrations. There is no change in Ce-OP bonding but there is a more developed hydrogen bonding network between the surface and adsorbed phosphate, which accounts for this small decrease in adsorption energy.

On both the {111} and {100} surfaces there is a similar trend. An increase in OH% results in a decrease in interaction energy of 0.3 eV for both surfaces between 0 and 0.25 OH/CeO_2 unit. In both cases there is no change in cerium phosphate bonding but there is an increase in hydrogen bonding concentration which can account for this decrease. However a further increase in OH% from 0.25 to 0.5 OH/CeO_2 unit is accompanied by an increase in adsorption energy (0.05 eV for the {111} and 0.5 eV for the {100}). This is due to a reduction in cerium phosphate bonding as well as a general lengthening of Ce-OP bonds. This can be attributed as in scheme 1 to the increase in hydrogen concentration which causes an increase in hydrogen bonds at the expense of Ce-OP bonding. Crucially however there is clear separation between the 3 surfaces, demonstrating a clear order of stability.

Across all surfaces at all OH%, the phosphate adsorbs in an oxygen vacancy (Figure 6.11). $H_2PO_4^-$ adsorbs dissociatively as $H_2PO_4^-$ and OH. This allows for the surface cerium atoms to partially recover the oxygen coordination environment on the {111}, {110} and {100} surfaces. The order of stability presented in scheme 2 is also seen in scheme 3 and can be rationalised in the same manner. The intrinsically defective {100} surface is stabilised to a greater extent by phosphate anions, while the {111} surface is easier to oxidise than the {110} surface. As seen in sections 3.2 and 3.3, the oxygen sub lattice of the {100} surface undergoes reconstruction upon phosphate adsorption with the {111} and {110} surfaces remain ordered. This reconstruction maximises the coordination of surface cerium cations which partially regain coordination (7/8 fold coordinated) and surface hydrogen bonding between the phosphate anion and the surface as well as between surface hydroxyl groups and surface oxygens.

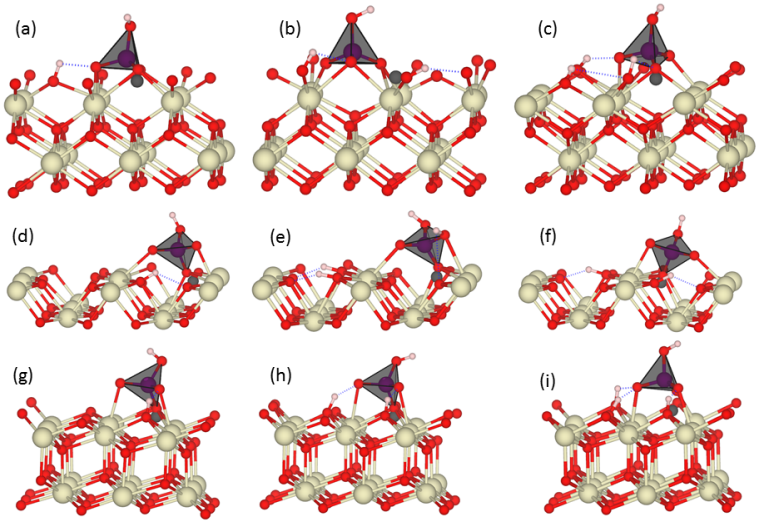

Figure 6.11: Adsorption geometry for $H_2PO_4^-$ the {100} (a, b, c), {110} (d, e, f) and {111} (g. h. i) surfaces with increasing hydrogen coverage. Cerium, oxygen, phosphorus and hydrogen atoms are shown in cream, red, purple and white and hydrogen bonds are shown with dashed blue lines. The polyhedra has been drawn on the phosphate for clarity.

6.6 Discussion

In this chapter, three different surface variables were studied in relation to the strength of interaction between the phosphate and the surface.

1. Surface OH concentration - The concentration of OH groups at the surface had a small effect on the interaction between phosphate and thus surface. The hydrogen bonding network therefore plays an important role in the interaction energy.

2. Surface oxygens stoichiometry - The surface oxygen stoichiometry has a significant impact on the interaction energy. Specifically, the surfaces without oxygen vacancies have a smaller interaction when compared to the surfaces with vacancies.

3. Surface Ce^{3+} concentration - Does not influence the interaction in a meaningful way. The scheme involving oxygen vacancies shows that the interaction does increase with increase Ce^{3+} concentration, however on surfaces without vacancies there is no change in adsorption with increasing Ce^{3+} (Scheme 1).

The catalytic activity of ceria is strongly dependent on the morphology and thus control over morphology becomes an important aspect of materials engineering. This will include control of surface composition, surface charge (i.e. oxidation state of surface Ce atoms), hydroxylation, defect chemistry (i.e. oxygen deficiency) and adsorbed species. The interaction of ceria with electrolyte species present in biological media is still largely overlooked and given the abundance of inorganic anions in biological systems, it is likely that cytoplasmic and nucleoplasmic concentration of these inorganic species will affect the exploitation of ceria catalysis. In recent years, modelling has been largely used to capture the atomistic details of the structure and properties of ceria, and linked to experimentation. [261, 262, 263].

Ceria can prevent cellular damage due to oxidative stress, i.e. an uncontrolled increase in reactive oxygen species (ROS). Both the superoxide and hydrogen peroxide are within such species. Whereas in the cellular environment, ROS are controlled by enzymes superoxide dismutase (SOD) and catalase, it is not the case when degenerative diseases prevail. SOD enables the dismutation of superoxide anion radicals, $O_2^{-\cdot}$, (equations 6.1/6.2) [232, 233, 234, 235] and catalase the degradation of hydrogen peroxide, H_2O_2 (equations 6.3/6.4)[235, 236, 237, 238, 239]. Despite of $O_2^{-\cdot}$ being highly reactive, excess H_2O_2 is believed to have a more toxic potential as it is the substrate for the Fenton reaction that generates hydroxyl radicals, the most destructive reactive oxygen species [264]. Ceria has also been suggested to act as oxidase [248, 249], and as hydroxyl radical scavenger [250, 251] although there is still some controversy [234]. Peroxo radicals have been predicted to be abundant both on oxidized and reduced surfaces showing the oxygen buffering activity of ceria [219] and hydroxyl radical scavenging has been shown to be dependent on the Ce^{3+} content at the surface [265].

$$O_2^{*-} + SOD - Ce^{4+} \rightarrow O_2 + SOD - Ce^{3+} \tag{6.1}$$

$$O_2^{*-} + 2H^+ SOD - Ce^{3+} \rightarrow H_2O_2 + SOD - Ce^{4+} \tag{6.2}$$

$$H_2O_2 + Catalase - Ce^{3+} \rightarrow H_2O_2 + Catalase - (O - Ce^{4+}) \quad (6.3)$$

$$H_2O_2 + Catalase - (O - Ce^{4+}) \rightarrow H_2O_2 + O_2 + Catalase - Ce^{3+} \quad (6.4)$$

Scheme 1. Physiological reactions of ROS in the presence of ceria. (1) Superoxide dismutase. It is a disproportionation reaction where Ce active sites react with two superoxide ions: one is oxidized to molecular oxygen and the other is reduced to hydrogen peroxide (equation 6.1). 6.2 Catalase. It is a disproportionation reaction where Ce active sites react with two hydrogen peroxide molecules: one is reduced to water (equation 6.3) and the other is oxidized to water and molecular oxygen (equation 6.4).

The most efficient superoxide scavenging (SOD) is exhibited by ceria with high level of Ce^{3+} [232, 233, 260]. On the other hand, Ce^{4+} rich ceria has stronger catalase activity and appears to be independent of morphology, i.e. nanorods and nanocubes [236]. Exposure to phosphates has been shown to poison the SOD activity [265], but it does not seems to affect catalase activity [237]. It has been shown that at high concentration of phosphates, there is no driving force to form cerium phosphate on Ce^{4+} compared to Ce^{3+} rich ceria [237, 238]. This suggests a strong affinity of phosphates to Ce^{3+}, which may block the inter-conversion $Ce^{3+} <-> Ce^{4+}$. Upon transformation (CeO_2 to $CePO_4$), unlike catalase activity, SOD activity is inhibited. This implies that there may be alternative mechanisms for catalase, triggered when phosphates are adsorbed[235], or $CePO_4$ can catalyse catalase.

Modelling results show that, phosphates bind strongly at oxygen vacancy / Ce^{3+} sites. The consequence here is that any enzyme mimetic activity that is more likely catalysed by Ce^{3+}, like SOD, will be inhibited by the presence of phosphates as these anions will directly sequestrate the reactive site. This is supported by experiments which say that unlike Ce^{3+} rich ceria, Ce^{4+} rich ceria does not have strong affinity

for phosphate [237, 238]. They showed that at equimolar amounts (i.e. high concentration) of phosphate buffer, Ce^{3+} rich ceria also transforms in cerium phosphate ($CePO_4$) unlike Ce^{4+} rich ceria [237]. The precipitation of $CePO_4$ has been see in vitro test [237, 238, 266] and in roots cell of cucumber plants, where Ce accumulated both as CeO_2 and $CePO_4$. These results cannot comment on the formation of $CePO_4$ as this will require modelling techniques that can capture the evolution of the surface in time, and higher concentration of phosphates. These calculations only shed light on the early stage of phosphate adsorption. These calculations indicate that there is a strong affinity of ceria with phosphates, in particular on the {100} surface. It has been shown that this surface strongly reconstructs its outer layer to accommodate the phosphate anion. Nanocubes will therefore see their enzyme mimetic activity shot down in the presence of phosphates independently from the surface composition. On the other hand nano-octahedra with a high concentration of OH groups will offer greater resistance to phosphate adsorption; the interaction energy is the weakest and thus a small energy would be needed to remove the phosphate (Scheme 1).

The exploitation of the enzyme mimetic activity of ceria depends strongly on the nanoscale structure and chemistry of its surfaces. DFT modelling has provided atomistic insights into the strength of phosphate adsorption, a constituent part of biological media that can hinder the biological exploitation of ceria based enzymes mimetics.Oxygen deficient ceria interacts strongly with phosphate anions compared to hydroxylated ceria. However this interaction depends strongly on surface structure. Specially, whether nanoceria consist of {111}, {110} or {100} surfaces.

As the strongest interaction occurs between {100} surfaces and phosphate due to a large surface reconstruction, the data suggests that ceria nanocubes bind phosphate strongly, which will inhibit Ce^{4+}/Ce^{3+} redox and nanozyme activity to a greater extent compared to ceria nano-octahedra comprising {111} surfaces, as these display much weaker interactions with phosphate. The simulations provide a prescription for high phosphatase mimetic activity - the nanomaterial should have polyhedral or cuboidal morphology to maximise exposure of CeO_2 {100} surfaces and comprise

a high concentration of Ce^{3+} and oxygen vacancies; the pH should be adjusted in preparation of the nanotheraputic, or encapsulated to maintain a local environment (in vivo), to provide a high HO- concentration.

6.7 Conclusions

This chapter focussed on how cerium oxide surfaces, with differing surface compositions affected the adsorption of phosphate anions. Oxygen deficient ceria interacts strongly with phosphate anions compared to hydroxylated ceria. However this interaction depends strongly on surface structure. Specially, whether nanoceria consist of {111}, {110} or {100} surfaces. The strongest interaction occurs between {100} surfaces and phosphate due to a large surface reconstruction, which suggests that ceria nanocubes bind phosphate strongly, which will inhibit $Ce^{4+/Ce3+}$ redox and nanozyme activity to a greater extent compared to ceria nano-octahedra comprising {111} surfaces, as these display much weaker interactions with phosphate.

7 Fluorite Grain Boundary Structure

The contents of this chapter have been previously published by the author as part of this PhD project and can be found at the following references, A.R.Symington, M. M., N.A.Brincat, N.R.Williams and S.C.Parker Defect Segregation Facilitates Oxygen Transport at Fluorite UO_2 Grain Boundaries. Philosophical Transactions of the Royal Society of London. Series A: **2019** and A.R. Symington, S.; Marco, M.; Joel, S.; Ji, W.; Stephen Charles, P., The role of dopant segregation on the oxygen vacancy distribution and oxygen diffusion in CeO_2 grain boundaries. Journal of Physics: Energy **2019**.

Fluorite structured ceramic materials, such as ceria (CeO_2) and UO_2, have attracted considerable attention for energy applications in the last three decades. CeO_2 has high ionic conductivity and is being investigated as a SOFC electrolyte material. Whereas UO_2 has been at the forefront of the nuclear industry for the last century. Ionic transport in polycrystalline materials is a common research question for both materials. In SOFCs the electrolyte must have high ionic conductivity so the oxygen conductivity of CeO_2 is of crucial importance to the operation of the device. UO_2 is the main fuel used in nuclear reactors and the oxygen conductivity is linked to the corrosion of the fuel. Both materials are polycrystalline and thus the transport properties within grain boundaries must be considered.

In this chapter, the grain boundaries of these two fluorite materials, uranium oxide (UO_2) and cerium oxide (CeO_2) will be discussed. While they share a parent structure, they have vast differences in their underlying chemistry, redox chemistry

and uses. Despite these differences, previous modelling and experimental work suggests that these materials have very similar grain boundary structures. Thus, in this chapter the grain boundary structures of each material have been generated, and their properties analysed. Molecular mechanics calculations have been used to evaluate the structure of the grain boundaries and molecular dynamics simulations have been applied in order to determine how the structure evolves with time and temperature. Furthermore, as oxygen transport is crucial for their respective applications, molecular dynamics simulations have been used to evaluate the oxygen transport at the grain boundary. A short literature review of grain boundaries in uranium oxide and cerium oxide will be presented first, followed by the calculation details and the results.

7.1 Background

Uranium oxide (UO_2) is a common polycrystalline material used in nuclear energy but it is challenging to work with due to its propensity for oxidation [267]. In UO_2 understanding oxygen transport is key to understanding the corrosion of the fuel. The fluorite lattice of UO_2 accommodates additional oxygen with little expansion up to around $UO_{2.5}$ stoichiometry but then undergoes a transition to a layered structure which is associated with a 36% volume increase [268, 269]. In a nuclear power plant this can cause swelling and eventually cracking of fuel rods, which can in turn release harmful contaminants into the environment [270]. Developing a fundamental understanding of oxygen transport properties in UO_2 can therefore be used to improve the efficiency, lifespan and, most importantly, safety of nuclear power plants. Furthermore, given the polycrystalline nature of UO_2, understanding how grain boundaries affects oxygen transport is also crucial.

The transport properties of grain boundaries have received some attention in recent years but the results have been contradictory. Using experimental techniques, Marin *et al,.* and Sabioni *et al,.* both reported no change in the oxygen transport properties at grain boundaries [271, 272]. Whereas, using molecular dynamics studies, Verwerft *et al,.* [273] and Arima *et al,.* [274] both report enhanced oxygen transport at grain

boundaries. The latter suggested that this effect was due to the misorientation angle of the grain boundaries. Further molecular dynamics studies by Vincent-Aublant *et al,.* and Williams *el al,.* have found enhanced diffusion within the grain boundary region at the atomic scale [275, 276].

Cerium oxide and other cerium oxide based compounds are promising electrolyte materials, capable of operating in the intermediate temperature range (770 - 1070 K). Cerium oxide is both thermally stable and exhibits appreciable ionic conductivity however this ionic conductivity is not high enough for effective usage in a SOFC device. Cerium oxide is consequently dependent on oxygen vacancies which act as charge carriers and improve ionic conductivity, however are linked with electronic conductivity and can contribute to short circuiting in the fuel cell. The most common way to increase the conductivity is to dope the material with di/trivalent cations which creates a charge compensating oxygen vacancy, removing the short circuit risk. Dopants can be accommodated readily into the structure up to significant concentrations without altering the fluorite structure.

The oxygen transport is key to understanding and improving the performance of the devices. While transport is relatively well understood in the bulk, focus has now shifted to the grain boundaries of cerium oxide. Feng et al studied the structure of several tilt grain boundaries using both experimental and theoretical methods and found that increased structural distortion at the grain boundary resulted in an increase in the oxygen vacancy concentration at the boundary. They found that the $\Sigma 5$ boundary had a high degree of structural distortion compared to the bulk and a high density of oxygen vacancies. This link between grain boundary structural disorder and oxygen reactivity is supported by An et al. Furthermore, oxygen vacancy segregation has been investigated using first principle calculations in the $\Sigma 3(111)$ boundary and it was found that oxygen vacancies migrate to the grain boundary core and this helps to stabilise the grain boundary. Grain boundaries have been shown to have a blocking effect to ionic transport across the boundary. This is considered to be due to the space charge effect, whereby segregation of charged defects to the grain boundary causes a reduction in ionic transport across

the boundary [277, 278, 279, 280]. Grain boundaries in other fluorite materials are well studied although there are contrasting interpretations. For example,there are studies stating that it is generally accepted that diffusion along grain boundaries is faster than in the bulk due to the higher defect concentrations and the reduced activation energy of oxygen hops [276, 281].

In this chapter, the grain boundary structures of UO_2 and CeO_2 have been generated and simulated with molecular dynamics.

7.2 Calculation Details

The potential model used to simulate grain boundaries of UO_2 and CeO_2 is from the work of Williams [276] and Sayle [122] and is based upon the potential model developed by Pedone [106]. There is debate in the literature as to whether more potential model parameters are required to model diffusion e.g. polarisability [56]. These models are considerably more computationally expensive than the rigid ion model used in this chapter. The DIPPIM model includes a term to account for the polarisability and has been used to model the transport properties of cerium oxide [282]. The oxygen diffusion coefficient calculated using this model better agrees with the experimental diffusion coefficient when compared to a rigid ion model, however the calculated activation energy is the same for both models. The crucial issue with these models is computational cost, the DIPPIM model is approximately 10 times slower than the rigid ion model and this limits the size of the simulation cells that can be studied and also, in a molecular dynamics sense, the number of steps that can be achieved. In this work, large simulation cells (10,000 atoms) are modelled for long simulation times (5,000,000 steps), thus it is impractical to use expensive models like DIPPIM.

Table 7.1: Potential parameters for the Morl potential model. The superscripts on the species represent the charges of the atoms.

Ion Pair	D_{ij} (eV)	B_{ij} (Å)	r_0 (Å)	A_{ij} (eV A^{12})
$O^{1.2}$ – $O^{1.2}$	0.041730	1.886824	3.189367	22
$U^{2.4}$ – $O^{1.2}$	0.083352	1.946417	2.946396	1
$Ce^{2.4}$ - $O^{1.2}$	0.098352	1.848592	2.930147	1

Table 7.2: Comparison of elastic constants and bulk moduli for uranium oxide

	Uranium Oxide					
Property	This work	Experiment	Catlow	Grimes	Morelon	Arima
a = b= c	5.47	5.47	5.52	5.46	5.45	5.46
B/GPa	209.0	209.0	211.8	272.9	125.0	217.8
C_{11}/GP	386.4	389.3	434.4	524.2	216.9	436.1
C_{12}/GP	102.9	118.7	100.4	147.3	79.1	108.7
C_{44}/GP	88.1	59.7	57.4	89.2	78.5	101.6
	Cerium Oxide					
Property	This work	Experiment	Conesa	Goldsby	Kanchana	Sevic
a = b= c	5.41	5.41	5.41	5.41	5.43	5.45
B/GPa	197	204	263.3	277.4	184	217
C_{11}/GP	404.0	403.0	504.0	455.0	392.7	390
C_{12}/GP	94.0	105.0	143.0	188.7	138.1	130
C_{44}/GP	83.4	143.0	143.0	81.5	96.5	82

Uranium oxide and cerium oxide have a cubic, fluorite lattice with an experimental lattice parameter of 5.47 and 5.41 Å respectively. The lattice parameters and elastic constants were simulated using the morl potential and compared with other theoretical [274, 283, 284, 285, 286, 287, 288] and experimental [134, 289] work.

Grain boundary configurations were generated using the METADISE code according to the energy scan method described in Chapter 2. The low energy configuration generated from these scans was then simulated with molecular dynamics. The simulation cells are described in Table 7.3, grain boundary widths were determined based on the changed in atomic density on going from the bulk to the grain boundary.

All molecular dynamics simulations (MD) are performed using the DLPOLY code [290]. The scanning process gives grain boundary structures at 0 K and is thus not representative of the operating conditions in a nuclear reactor, catalytic cycle, fuel cell etc. Thus, the simulation cells were annealed from low temperature (300 K) to high temperatures (3000 K) in order to generate a structure that was stable across a large temperature range. The annealing process was carried out using the NPT ensemble across a temperature range of 300 - 3000 K in increments of 300 K. Molecular dynamics simulations were completed using a timestep of 1 fs with an 8.5 Å cutoff. The system was equilibrated for 1ns using the NPT ensemble and transport behaviour was evaluated using the NVT ensemble across across a temperature range

of 2000 - 3000 K (at 250 K intervals) for 5 ns. Configurational and statistical data was recorded every 250 fs.

Table 7.3: Total number of atoms in each grain boundary supercell.

Grain Boundary	Number of Atoms	GB Width (Å)
Σ3(111)	8640	20.00
Σ5(210)	7680	21.00
Σ5(310)	7680	20.00
Σ9(221)	5760	20.00
Σ11(311)	7200	20.00
Σ19(331)	7200	17.00

The activation energy for oxygen transport was calculated from the Arrhenius equation,

$$k = Ae^{\frac{-Ea}{k_B T}} \tag{7.1}$$

where k is the rate constant, T is the temperature, A is the pre-exponential factor, E_a is the activation energy and k_B is the Boltzmann constant.

7.3 Grain Boundary Scans

In this work 6 low index tilt grain boundaries of both UO_2 and CeO_2 were generated and studied, namely, the Σ3(111), Σ11(311), Σ5(210), Σ5(310), Σ9(221) and the Σ19(331). These were chosen because they have been observed experimentally.

Using the METADISE code, structural scans were performed of one grain relative to the other. At each point in this theoretical grid a full minimisation was performed. These scans are visualised in Figure 7.1 and they highlight the interface stability vs grain displacement. For clarity, each point in the energy surface plots represents a different grain boundary structure, arising from the combination of two identical surfaces.

The low energy GB structure was taken from these scans. These structures show

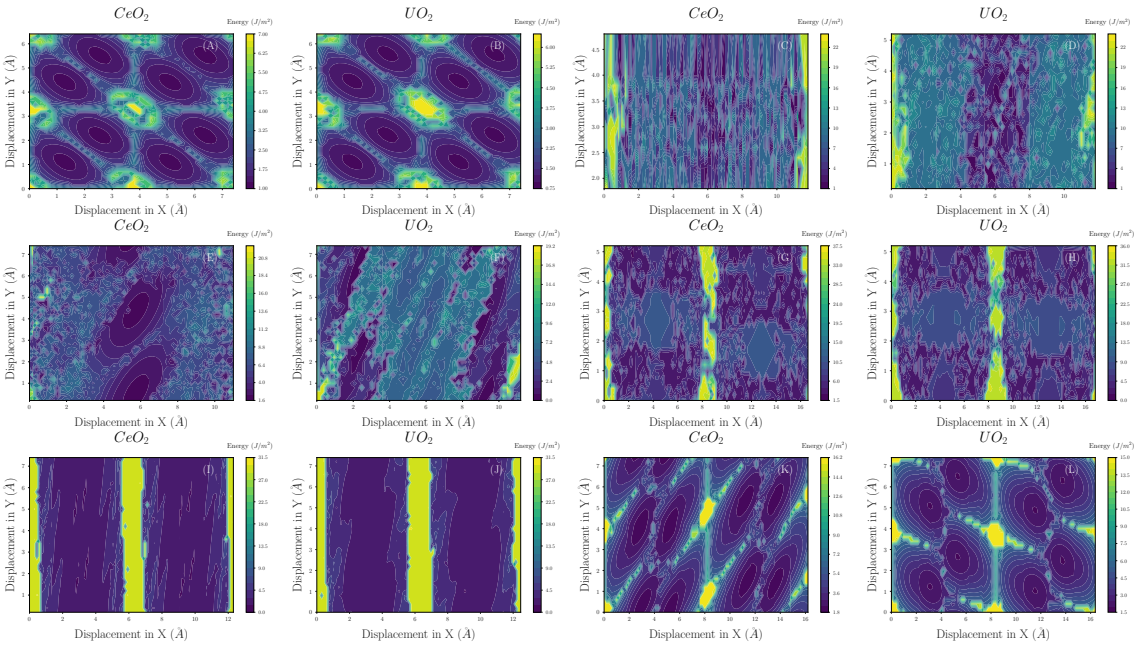

Figure 7.1: Grain boundary scans for CeO_2 and UO_2 $\Sigma3(111)$ (A/B), $\Sigma5(210)$(C/D), $\Sigma9(221)$ (E/F), $\Sigma5(310)$ (G/H), $\Sigma11(311)$ (I/J) and $\Sigma19(331)$ (K/L) grain boundaries. Yellow and blue areas denote areas of high and low energy.

strong resemblance to experimental structures of CeO_2, and doped ZrO_2 [291]. The grain boundary energies of these structures are shown in Figure 7.2. The low σ GB values of the $\Sigma3$ and $\Sigma9$ boundaries indicate the presence of high concentrations of these boundaries in UO_2 polycrystals in line with experimental SEM analysis of UO_2 samples [292].

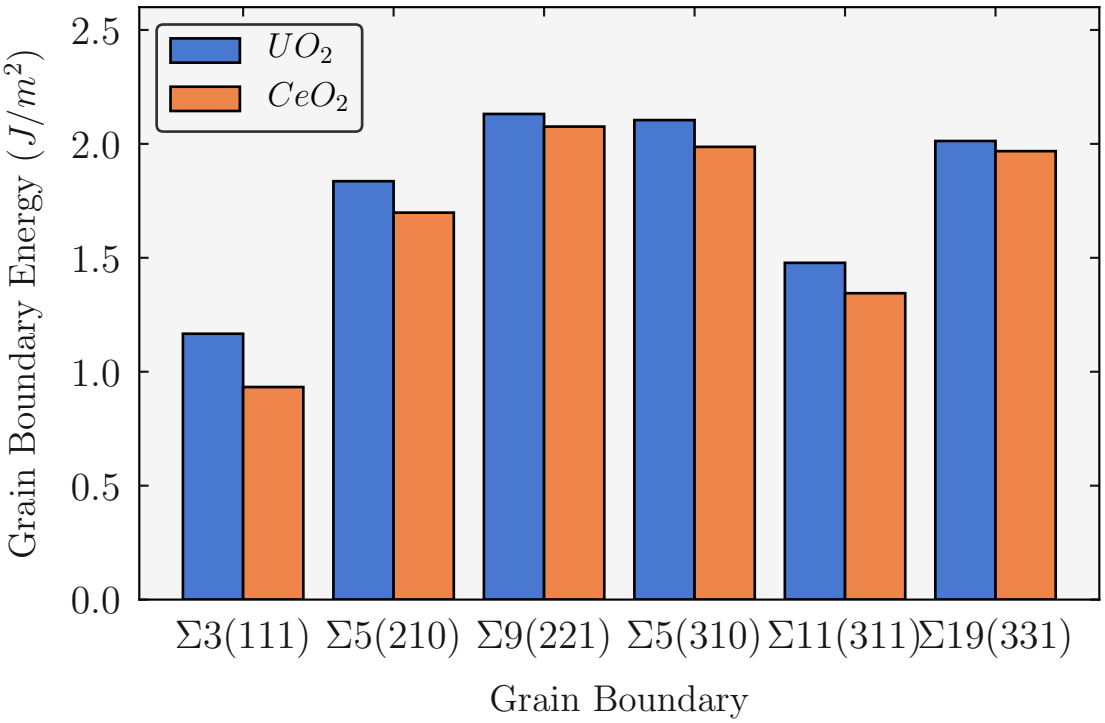

Figure 7.2: Grain boundary energy for CeO_2 (Orange), and UO_2 (Blue.) in Jm^{-2}

7.4 Dynamics

7.4.1 Structure

The lowest energy grain boundary structures generated from the scanning process were simulated using molecular dynamics. It was found that there are no significant structural differences between the two materials and thus the results in this section apply to both UO_2 and CeO_2. The grain boundary cation structure following structural annealing with molecular dynamics are shown in Figure 7.3 at low (900 K) and high (2000 K) temperatures for UO_2.

There is little change between the structure predicted by energy minimisation and the structure post annealing for the Σ3(111) and Σ11(311) boundaries however the other 4 structures undergo some alterations.

There is a structural alteration in the Σ5(210) grain boundary that occurs during the annealing process. At low temperatures ($<$ 2000 K) the structure resembles

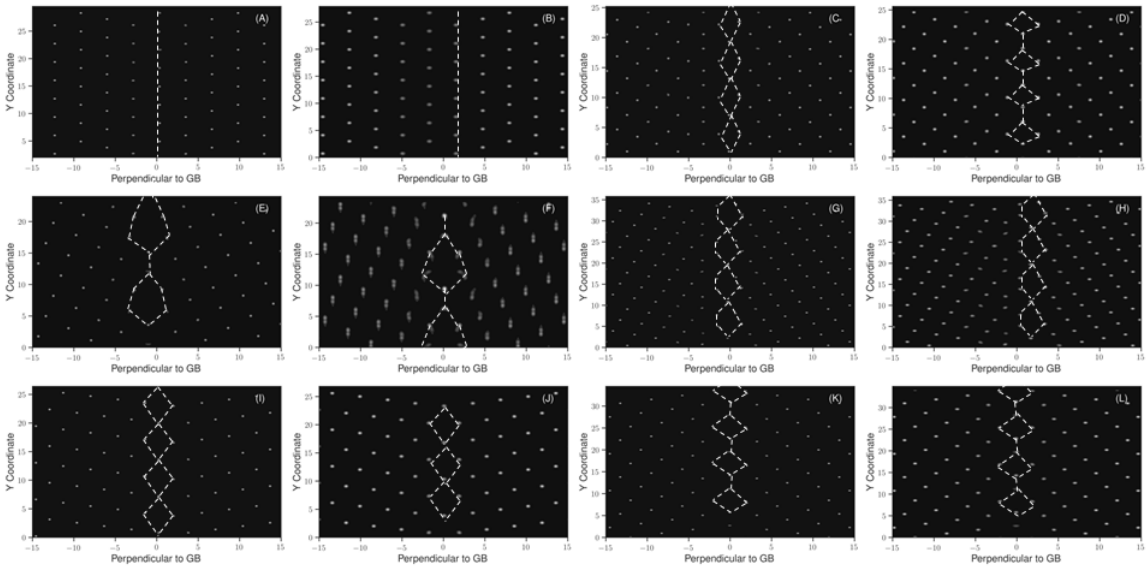

Figure 7.3: Centre of mass of all cations displayed every 0.5 ps for 1ns at 900 K and 2000 K for the Σ3(111) (A/B), Σ5(210)(C/D), Σ9(221) (E/F), Σ5(310) (G/H), Σ11(311) (I/J) and Σ19(331) (K/L) grain boundaries.

that predicted by energy minimisation, but once this temperature is exceeded an alteration occurs (Figure 7.3 C/D). This can be explained by examining the energy surface (Figure 7.1 C/D) for the Σ5(210) boundary. The energy landscape is complicated with lots of low energy regions, separated by relatively small energy barriers. As the structure is heated it is able to change structure by jumping over these energy barriers.

The structure of the Σ9(221), Σ5(310), and Σ19(331) boundaries alter slightly during the annealing and once shifted, remain stable across the temperature range studied (1000 - 3000 K). Although in the case of the Σ9(221) there is some migration of the cation arrays that occurs parallel to the grain boundary (Figure 7.3 F). Figure 7.3 presents the grain boundaries centred at 0 on the x axis, thus it does not show any grain boundary movement perpendicular to the plane. The Σ9(221), Σ5(210) and the Σ5(310) boundaries all undergo some movement (5-10 Å) perpendicular to the boundary plane.

The atomic densities are shown for all 6 boundaries in Figure 7.4 to highlight the structural change that occurs between the bulk and the grain boundary.

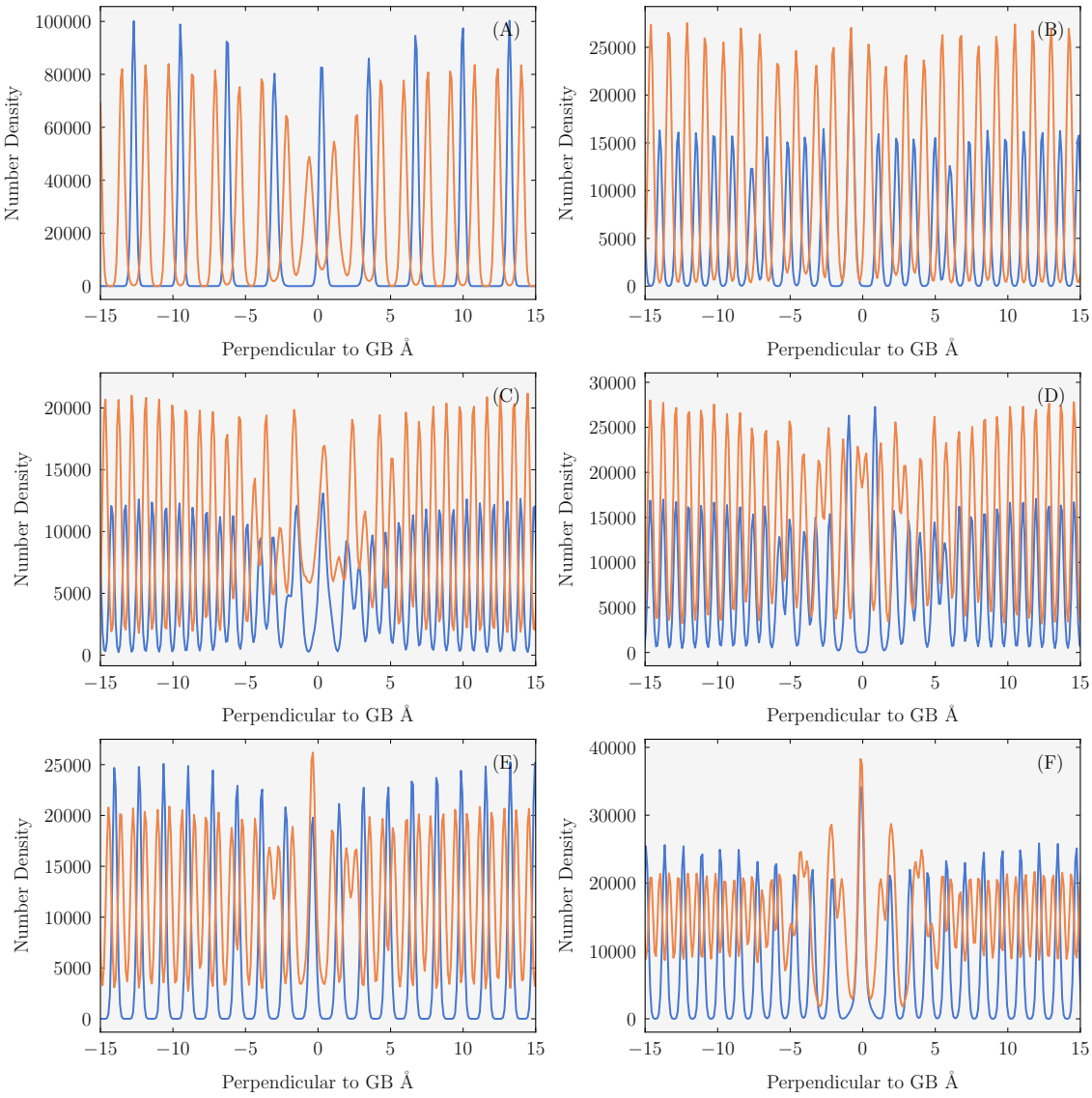

Figure 7.4: Oxygen (Orange lines) and uranium (Blue lines) number density perpendicular to the grain boundary (GB at 0) for the Σ3(111) (A), Σ5(210) (B), Σ9(221) (C), Σ5(310) (D), Σ11(311) (E) and Σ19(331) (F) grain boundaries.

7.4.2 Grain Boundary Mobility

It was found that the two grains that come together to form the Σ11(311) boundary of both UO_2 and CeO_2, move relative to one another i.e. the two grains slide across one another. This can be explained by examining the grain boundary scans for the Σ11(311) boundary (Figure 7.1 I,J). The low energy "trenches" that run in the Y direction illustrate that there is minimal energy barrier for the grains to move in that direction. Thus when heat is applied during a molecular dynamics simulation, the grains are able to move along this energy landscape.

Grain boundary sliding occurs in the Σ11(311) boundary at temperatures exceeding 2700 K. Grain boundary sliding was confirmed by viewing the trajectories in VMD and diffusion coefficients were calculated for the grains moving in the y direction. While small, they are significantly higher that those calculated for other grain boundaries and are in the range 0.04 - 0.05 x $10^{-9}m/s^2$ between 2700 - 3000 K.

7.4.3 Grain Boundary Transport

CeO_2 grain boundaries are slightly more diffuse that the UO_2 grain boundaries. In both materials, it was found that the diffusion enhancement in stoichiometric boundaries follows the order Σ3(111) > Σ9(221) > Σ19(331) > Σ11(311) > Σ5(310) > Σ5(210). There is a significant difference in the diffusion coefficient of the grain boundaries, with a 1 order of magnitude difference between the lowest value of 0.049 x $10^{-9}m/s^2$ obtained for the Σ5(210) (UO_2) and the highest value of 0.53 x $10^{-9}m/s^2$ found for the Σ3(111) (UO_2) for UO_2 at 2500 K. The activation energies were calculated from the Arrhenius equation as shown in Figure 7.5. These are displayed for all datasets in figure 7.6.

The low diffusivity of the Σ5 grain boundaries can be explained by examining the cation density at the grain boundary compared to the bulk region (figure 7.6). The Σ3(111), Σ9(221), Σ19(331) and Σ11(311) boundaries all see a decrease in the cation density, defined as the total number of cations per $Å^3$ in the grain boundary. In contrast, the two Σ5 grain boundaries have an increase in cation density. Simply,

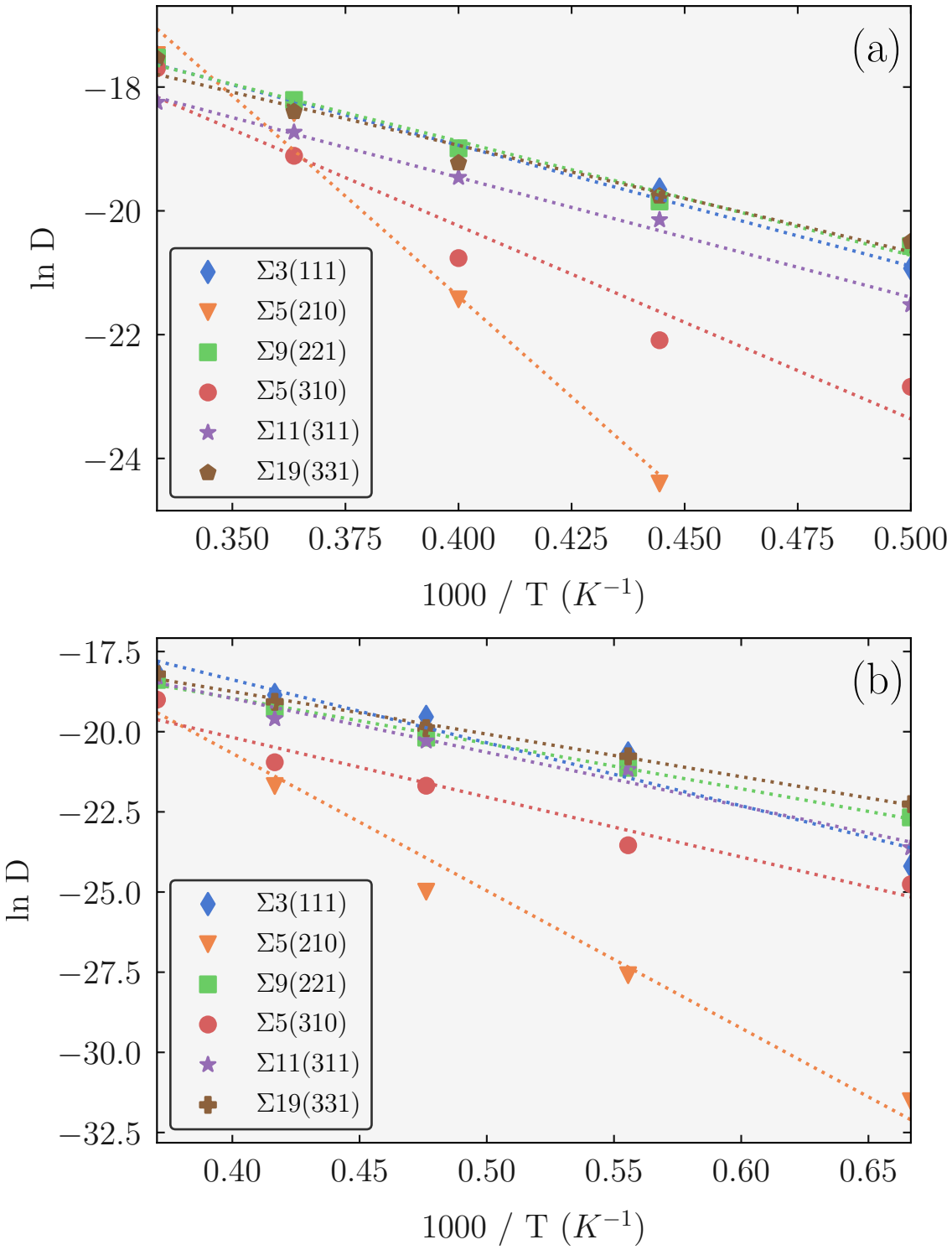

Figure 7.5: Arrhenius plots for the Σ3(111) (blue), Σ5(210) (orange), Σ9(221) (green), Σ5(310) (red), Σ11(311) (purple) and Σ9(331) (brown) grain boundaries in uranium oxide (a) and cerium oxide (b).

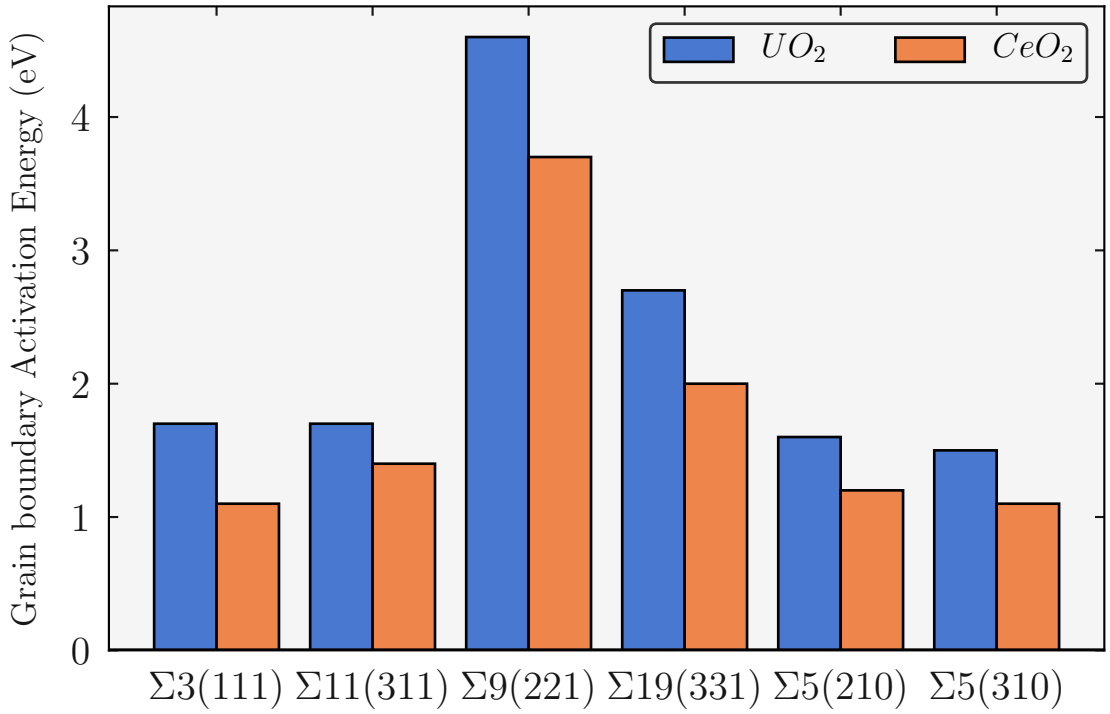

Figure 7.6: Activation energy for oxygen diffusion in the grain boundary of CeO_2 (Orange), and UO_2 (Blue.)

there is less space for oxygen to move around in the Σ5 grain boundaries and so diffusivity is small.

7.4.4 Electrostatic Potential

The electrostatic potential as a function of distance either side (-15 Å - 15 Å) of the grain boundary core, positioned at 0 Å is shown in Figure 7.8. The lattice polarization is illustrated by the x projection of the mean electrostatic potential (red dashed line). The sharp oscillations along X are due to the oppositely changed planes of cations (U or Ce) and anions (O). The polarization field is seen more clearly from a running average of the electrostatic potential, calculated across a distance equal to one lattice spacing (blue solid line). Generally there are quite substantial differences between the profiles of different grain boundaries. Some structures of the electrostatic potential at the core of the grain boundary that extend into the grain interior; this is hardly visible in the Σ3(111) whereas it is significant in the Σ5(310).

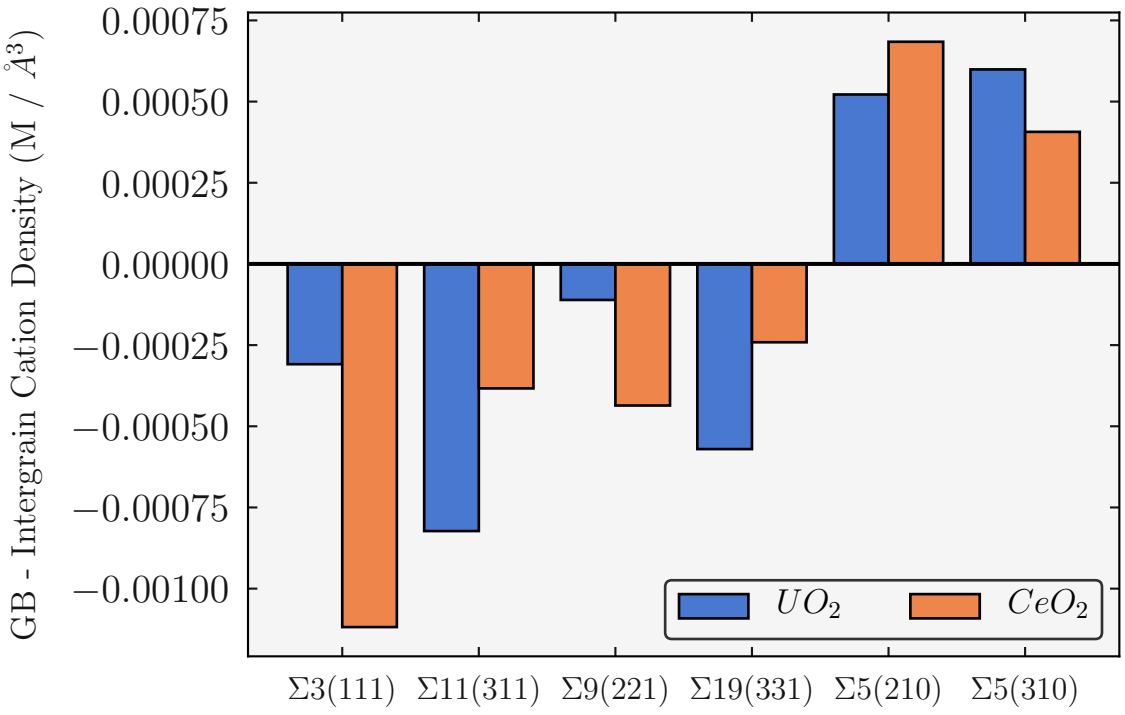

Figure 7.7: Difference between the cation density in the bulk region and the grain boundary region for CeO_2 (Orange), and UO_2 (Blue) grain boundaries. For clarity, positive values indicate a grain boundary which is more dense than the bulk.

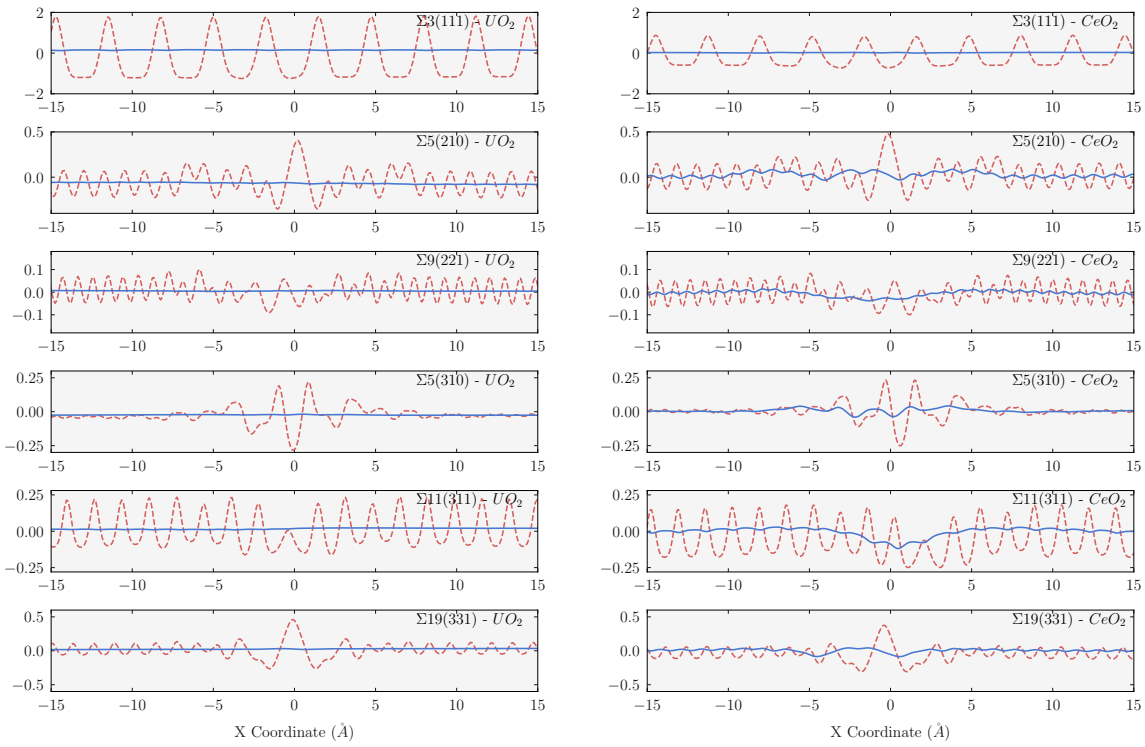

Figure 7.8: Red dashed lines: Poisson potentials calculated from molecular dynamics simulations as a function of distance from the grain boundary plane (-15 - + 15 Å) at 2000 K. Blue solid lines: running average potentials over one lattice spacing.

7.5 Conclusions

In this chapter, fluorite grain boundaries of both UO_2 and CeO_2 have been generated using energy minimisation and simulated across a large temperature range using molecular dynamics. It was found that the energy minimisation gives virtually identical grain boundary structures, with similar energies. The UO_2 grain boundaries were all slightly lower in energy compared to the CeO_2 grain boundaries.

All grain boundaries were stable across the temperature range studied, albeit with some structural alterations occurring. The $\Sigma3(111)$ and $\Sigma11(311)$ boundaries remained similar to those predicted by energy minimisation, the $\Sigma9(221)$, $\Sigma19(331)$ and $\Sigma5(310)$ grain boundaries shift during thermal annealing but remained stable thereafter and the $\Sigma5(210)$ remained similar to the structure predicted by energy minimisation and undergoes a structure change at high temperatures. The $\Sigma11(311)$ grain boundary is the least "solid" and the two grains are able to slide across one another at high temperatures, this was predicted by the energy minimisation calculations and confirmed by the molecular dynamics simulations.

Between temperatures of 2000 - 3000 K the $\Sigma3(111)$, $\Sigma9(221)$, $\Sigma19(331)$ and $\Sigma11(311)$ grain boundaries significantly increase the oxygen diffusion that is occurring in both materials. In contrast, the $\Sigma5$ grain boundaries are bulk like in terms of diffusion at temperatures below 2400 K. Cerium oxide is slightly more diffuse than uranium oxide, with slightly lower activation energies in each boundary. There is a link between the grain boundary structure and the transport properties, grain boundaries with lower cation density compared to the bulk are more diffuse than those with an increased density, which have poor transport properties. Finally, the electrostatic potential has been calculated across the grain boundaries and there is a clear difference between the bulk and the grain boundary.

The structure of grain boundaries in these two materials is remarkably similar and thus it can be predicted that the structure of all fluorite boundaries will be similar. It is apparent that while the grain boundaries studied in this chapter represents a

good starting point in the study of polycrystalline materials, there is not enough information to establish a "grain boundary rule" or common framework to describe the properties of polycrystalline materials.

8 Fission Products in UO_2 Grain Boundaries

The contents of this chapter have been published by the author as part of this PhD project and can be found at the following reference, A.R.Symington, M. Molinari, N.A.Brincat, N.R.Williams and S.C.Parker, Defect Segregation Facilitates Oxygen Transport at Fluorite UO_2 Grain Boundaries. *Philos. Trans. R. Soc. A*, 377(2152): 20190026, 2019. doi: 10.1098/rsta.2019.0026..

In chapter 5, a structural defect (grain boundaries) was discussed within the context of structure and oxygen transport. UO_2 as well as being polycrystalline also contains high levels of chemical defects, which are non-stoichiometric cations and anions. Chemical defects can be introduced to the fuel in three common ways, as defects during fuel fabrication, as a poison to alter the properties of the fuel, and as fission products from the atom splitting in the reactor. Chemical impurities are well studied in bulk UO_2, however the effect of impurities segregated at grain boundaries remains poorly studied in the literature.

8.1 Background

UO_2 pellets are formed and sintered at 2000 K under a reducing atmosphere before being loaded into tubes of a zirconium alloy. During this process impurities are incorporated into the lattice, the concentration and type of impurity is dependent upon the fabrication method used. For example dry fabrication processes result in

increased Fe, Cr, Cu and Ni impurities. There are standard impurity thresholds set to ensure that the total impurity concentration within the fuel is within a safe level, however there are still high concentrations of specific elements within the fuel.

Iron cations are a common impurity, widely reported within UO_2 at high concentrations (100 – 180 ppm) [293] and attributed to fuel pellet sintering with steel equipment at high temperatures 1750° [272, 293, 294, 295, 296, 297, 298, 299, 300, 301, 302, 303]. Fe is thought to affect the activation energy for grain growth. Comparison of grain growth in two samples: natural fuel and enriched fuel which had 35 ug/g and 100-300 ug/g Fe respectively shows that the enriched fuel has a slower rate of grain growth compared to the natural fuel. Two studies have identified Fe precipitates at UO_2 grain boundaries. In one it is proposed that Fe at the grain boundary acts as a nucleus for the deposition of solid fission products [301]. In another example several samples from different fabrication sites were analysed and found to have 100 ppm – 158 ppm Fe [293]. To date however, research into Fe in UO_2 and specifically UO_2 grain boundaries is limited. At this stage is has been established that Fe can be found in meaningful concentrations in UO_2 and that it is reported to segregate to grain boundaries. No studies have determined the effect it has on the performance or the corrosion of the fuel.

UO_2 is often doped with neutron absorbers in order to reduce the reactivity of the fuel and improve safety, e.g. Gadolinium. The enrichment of uranium to increase the amount of fissile U^{235} must be compensated with the introduction of neutron absorbers (Poisons) in order to mediate the reaction. Gadolinium is one such material that can be added. It is an excellent poison material because it has a high neutron cross section coupled with a burn rate similar to U^{235} depletion. Some fuels are now designed with Gd poison with up to 4% of Gd by weight. Research has focused on the structure of the fuel following the sintering process [304] and on the depletion of Gd inside the reactor. There is however a lack of information on how the Gd affects corrosion of the fuel. Gd_2O_3 doped UO_2 has recently been investigated computationally and found to significantly increase the oxygen diffusivity of bulk UO_2 [305], furthermore, Th doped UO_2 has also been studied and found to have higher

diffusivity [306, 307, 308, 309, 310].

The most common defects are fission products, which are produced during the burning of UO_2. There are a wide variety of fission products and they can be grouped into four categories based upon their chemical state. They can exist as volatile fission products (Kr, Xe, Br, I); metallic precipitates (alloys); ceramic precipitates (oxides based on Rb, Cs, Ba, Zr, Nb, Mo, Te); and oxides dissolved in the fuel (Sr, Zr, Nb, Y, La, Ce, Pr, Nd, Pm, Sm) [311].

Noble gases Helium[312], Xenon [273, 313, 314, 315, 316, 317, 318], Krypton [319] are insoluble in UO_2 and therefore appear within fuel solely due to the fission process. Typically these gases migrate to grain boundaries, pre-existing pores or dislocations where they collect and eventually form bubbles. This leads to swelling of the fuel which can negatively affect the structural and mechanical properties of the fuel. Furthermore, grain boundaries provide a route through which gas can leak to the interface between the fuel and fuel rod which can lead to the cracking of the fuel rod and damage the structural integrity of the rod. Furthermore one of these studies showed that Xe enhances the diffusion of O and U[313].

Solid state fission products such as caesium [320, 321, 322], strontium [323, 324], lanthanum [325, 326], barium [327, 328] etc. are all found in UO_2, formed in meaningful quantities from the radioactive decay of uranium and they are incredibly toxic. There are three types of fission product, grey phase, solid solution and white phase. Some fission products precipitate out of solution in the form of a complex oxide. The main components of this "grey phase" vary with fuel composition and where/how it was made but the main constituents are Ba, Zr, Cs, Nb, Te, Sr, Mo and Rb. These form perovskite structures such as $Ba_{1-x-y}Sr_xCs_y$, $BaZrO_3$ and (U, Pu, Ln, Zr, Mo)O_3. Grey phase precipitates have been known to form in LWR fuels after experiencing higher than normal operating temperatures. Cs in UO_2 with a high O to U ratio forms Cs_2UO_4, however due to the volatility of Cs it is found in small concentration in the grey phase. Cs has been shown to corrode zircalloy forming Cs_3ZrO_3, it will also react with stainless steel to form Cs_3CrO_4.

Fission products are also found in solid solution, these include Sr, Y and the lanthanide cations Ce, Nd, Eu, La, Y, Pm, Sm and Gd. These remain in the fuel and do not precipitate to the grey phase. Ce and Zr have different solubility's in UO_2; CeO_2 in concentrations in excess of usual concentrations caused by fission has been shown to be completely soluble in UO_2 while ZrO_2 is only soluble above 1500 K. CeO_2 precipitates have a negative effect on the thermal conductivity, phase stability and the performance of the fuel. Ce fission products are also of particular interest due Ce fission products being an analogue for plutonium, owing to similar oxidation behaviour and a similar ionic radius [329]. Any remaining fission products precipitate out of solution into a "white phase", which is comprised of metallic elements e.g. Mo, Te, Ru, Rh, Pd, Ag, Cd and Pd.

There is significant evidence, both experimental and theoretical, which shows that impurities segregate to UO_2 grain boundaries [330, 331] as well as other fluorite boundaries [332]. Hiernaut *et al,.* found that fuel oxidation enhanced the segregation of non-soluble fission products from the bulk to the boundaries [333]. Insoluble fission gases such as Xe migrate to grain boundaries where they form bubbles [292, 334], Xe can undergo further chain decay leading to other stable fission products e.g. La/Gd^{3+} has been shown to segregate to the grain boundaries, resulting in an increase in oxygen conductivity [335]. Recognising the potential significance of this in this work the combination of chemical impurities (Fission products and fabrication impurities) within extended structural defects (Grain Boundaries) and the effect that this combination has on the oxygen transport properties of UO_2 has been investigated.

Despite the importance of grain boundaries (GBs) and fission products, their combined effect on the oxygen transport properties of UO_2 remains poorly understood and a number of important questions remain. Using large scale molecular dynamics (MD), the effects of some common impurities (M = Fe^{3+}, Gd^{3+} and La^{3+}) on the oxygen diffusivity at grain boundaries in UO_2 have been explored, and these findings have been discussed within the broader context of the literature.

Table 8.1: Potential parameters for the Morl potential model. The superscripts on the species represent the charges of the atoms.

Ion Pair	D_{ij} (eV)	B_{ij} (Å)	r_0 (Å)	A_{ij} (eVA^{12}
$O^{1.2}$ – $O^{1.2}$	0.041730	1.886824	3.189367	22
$U^{2.4}$ – $O^{1.2}$	0.083352	1.946417	2.946396	1
$Fe^{1.8}$ – $O^{1.2}$	0.029584	2.575402	2.559207	3
$Gd^{1.8}$ – $O^{1.2}$	0.028451	2.057296	3.074956	3
$La^{1.8}$ – $O^{1.2}$	0.070053	1.3984	3.382429	3

Table 8.2: Comparison of elastic constants for iron oxide

Property	This work	Tucek	Pedone (Exp)	Pedone (Theory)
a = b	5.03	4.97	5.03	4.95
c	13.74	13.43	13.75	13.42
$\alpha = \beta$	90	90	90	90
γ	120	120	120	120

8.2 Calculation Details

The potential model used in this chapter is the same as in chapter 7 with the addition of a description of the Gd - O, Fe - O and La - O interactions. These extra interactions were taken from the model of Pedone et al., [106].

Iron oxide has a rhombohedral crystal structure. The lattice parameters calculated using the morl potential compare well with other theoretical [106] and experimental [106, 336] work.

Gadolinium oxide has a cubic crystal structure. The lattice parameters calculated using the morl potential compare well with other theoretical [106] experimental [106, 337] work.

Lanthanum oxide has a rhombohedral crystal structure. The lattice parameters calculated using the morl potential compare well with other theoretical [338, 339,

Table 8.3: Comparison of elastic constants for gadolinium oxide

Property	This work	Templeton	Pedone (Exp)	Pedone (Theory)
a = b = c	10.76	10.81	10.81	10.80
$\alpha = \beta\gamma$	90	90	90	90

Table 8.4: Comparison of elastic constants and bulk moduli for lanthanum oxide

Property	This work	Dordevic	Manoilova (Exp)	Manoilova (Theory)	Li
a = b	4.02	3.91	3.39	3.95	3.33
c	5.79	6.09	6.14	6.14	6.15
$\alpha = \beta$	90	90	90	90	90
γ	120	120	120	120	120

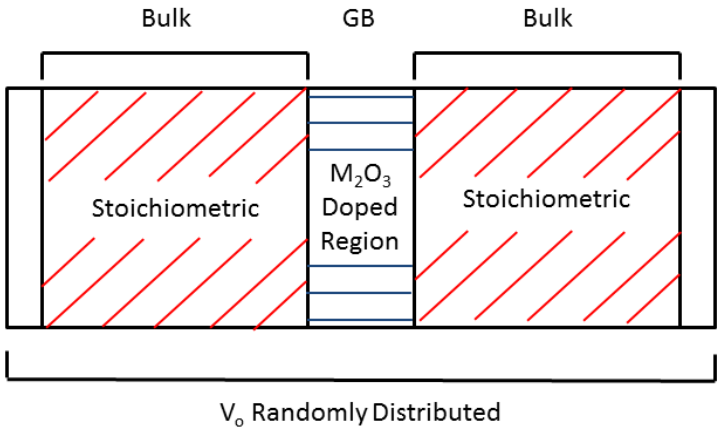

Figure 8.1: Schematic illustrating the model configuration for grain boundary and doping scheme.

340] and experimental [339] work.

In order to study the effect of impurities, impurities were introduced to the grain boundary structures discussed in chapter 5. Cation impurities (Fe^{3+}, Gd^{3+} and La^{3+}) were substituted onto uranium lattice sites up to a concentration of 1% and were distributed randomly within the grain boundary region (Figure 8.1). This low concentration was chosen to establish whether even a small concentration of dopants will affect oxygen transport, i.e. early stage of corrosion. These models are constructed under the approximation that impurities segregate at the boundary as suggested by experiment [291, 341]. A single distribution of dopants is not necesarily representative, so five doped configurations were generated for each grain boundary and the data presented in this chapter is the average for these five configuraitons. Oxygen vacancies were introduced randomly to maintain charge neutrality throughout the entire structure. Oxygen vacancies reached their equilibrium distribution within the NPT MD simulation, this was confirmed by examining the evolution of the oxygen stoichiometry over time. Oxygen vacancies distributed during the early

Table 8.5: Total number of atoms in each grain boundary supercell and the total number of dopants and oxygen vacancies added.

Grain Boundary	Number of Atoms	GB Width (Å)	Number of Species	
			M^{3+}	V_o
Σ3(111)	8640	20.00	30	15
Σ11(311)	7200	20.00	24	12
Σ5(210)	7680	21.00	26	13
Σ5(310)	7680	20.00	26	13
Σ9(221)	5760	20.00	20	10
Σ19(331)	7200	17.00	24	12

stages of the NPT simulation and this distribution persisted for the duration of the simulation. During these simulations there was minimal cation diffusion and thus, the distribution of impurities remained similar to the starting distribution.

All molecular dynamics simulations (MD) are performed using the DLPOLY code [290]. MD simulations of 5 ns were completed using a timestep of 1 fs with an 8.5 Å cutoff. Dopants were added to the simulation cells discussed in chapter 7 and the system was equilibrated for 1ns using the NPT ensemble. Transport behaviour was evaluated using the NVT ensemble across a temperature range of 2000 - 3000 K (at 250 K intervals) for 5 ns. Configurational and statistical was recorded every 250 fs. The size of each simulation cell and total number of defects are shown in Table 8.5.

Tracer-diffusion data for O within grain boundaries was obtained from a regional mean squared displacement (MSD). The calculation of the MSD only takes into account those segments of atom trajectories for oxygen species that pass within the grain boundary region. Residence time was used to evaluate the average length of time that an oxygen atom spends in contact with each cation (U^{4+} and M^{3+}).

8.3 Doped Grain Boundary Structure

All stoichiometric structures discussed in chapter 7 were doped following the doping scheme illustrated in Figure 8.1. In order provide some information on the segregation of impurities, configurations where all impurities are located within the bulk region of the structure were generated. The difference in energy between the two

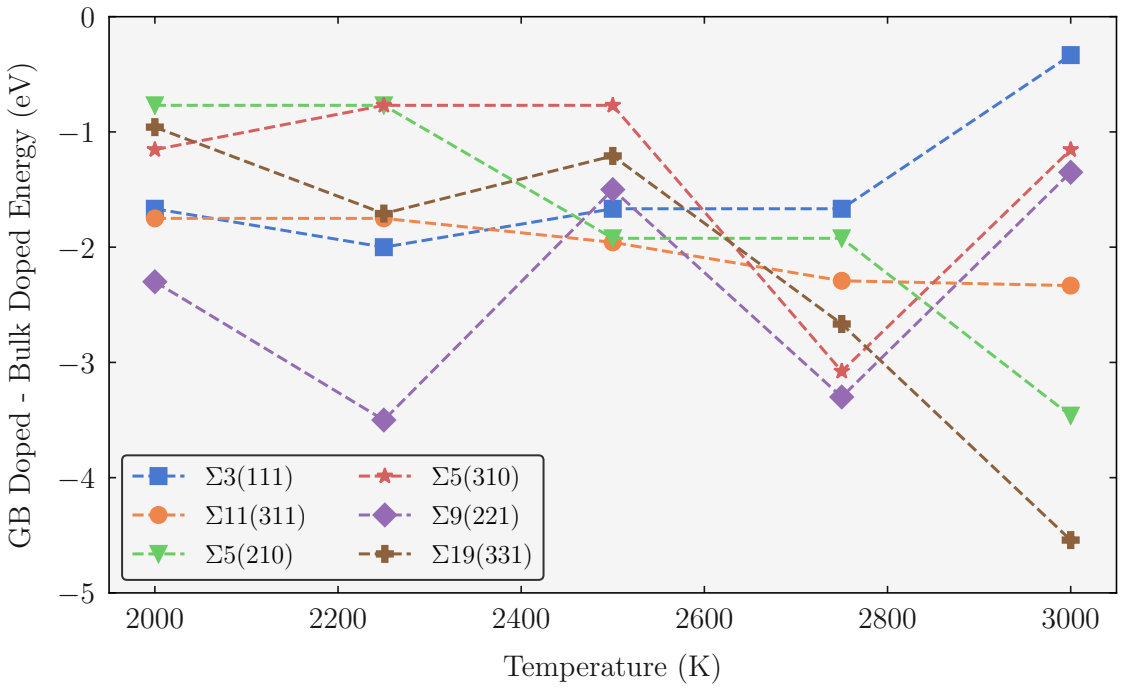

Figure 8.2: Energy difference between dopants in the doped GB structure and doped bulk structure, calculated by subtracting the energy of the bulk region doped structure from that of the GB doped structure.

dopant schemes was calculated in order to confirm that segregation is energetically feasible. All energies differences are negative, showing that segregation is energetically feasible (Figure 8.2).

Doping does not cause any significant structural change with increasing temperature in the Σ3(111), Σ9(221), Σ19(331) and Σ11(311) boundaries. In contrast the presence of impurities promotes an alteration to the structure of the Σ5(210) grain boundary and a partial structural change in the Σ5(310) grain boundary. Figure 8.3 depicts the time averaged two dimensional density profiles of the centre of mass of the cations (U^{4+}/M^{3+}) in the Σ5 grain boundaries at different temperatures. A structural change has been previously reported in the Σ5(210) GB in stoichiometric UO_2 and occurs within a temperature range of 2400 K – 2600 K [276]; when the structure is doped the transition occurs between 1700 K – 2000 K. In the Σ5(310) the partial structural change occurs above 2500 K for the doped boundary but it has not been reported in the case of stoichiometric UO_2.

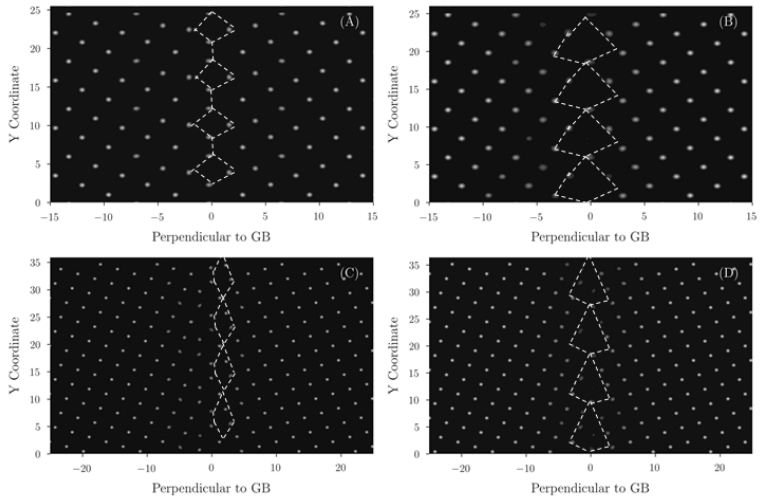

Figure 8.3: (a, b) Time averaged two dimensional density profiles of the centre of mass of the cations (U^{4+}/M^{3+}) displayed every 0.5 ps at different temperatures for a 1% Fe^{3+} doped $\Sigma5(210)$ and (c, d) $\Sigma5(310)$ grain boundaries. The white dots denote the U arrays parallel to the grain boundary plane. Patterns have been drawn to aid visibility.

The energy map for the two $\Sigma5$ boundaries is relatively complicated with many structural configurations within the low energy areas (Figure 7.1). These structural changes as a function of temperature show that impurities stabilise metastable grain boundary configurations, which may not be accessible at low temperature when the structure is stoichiometric.

8.4 Oxygen Vacancy Segregation

Oxygen vacancies were randomly distributed throughout the entire system (Figure 8.1). During the NPT MD simulations, the oxygen vacancies, which are mobile species, reached their equilibrium position within the doped structure. To quantify the segregation of oxygen vacancies within the doped grain boundary region the reduction in oxygen concentration for all grain boundaries has been evaluated.

Residence time analysis, i.e. the average time spent by an oxygen atom within the coordination sphere of a cation impurity at the boundaries was used to evaluate the interaction between cations and oxygen(figure 8.4). It was found that oxygen resides longest close to U^{4+} then $La^{3+} > Gd^{3+} > Fe^{3+}$ (Figure 8.6) which again follows the atomic radii of the impurity cations. The average coordination number within the

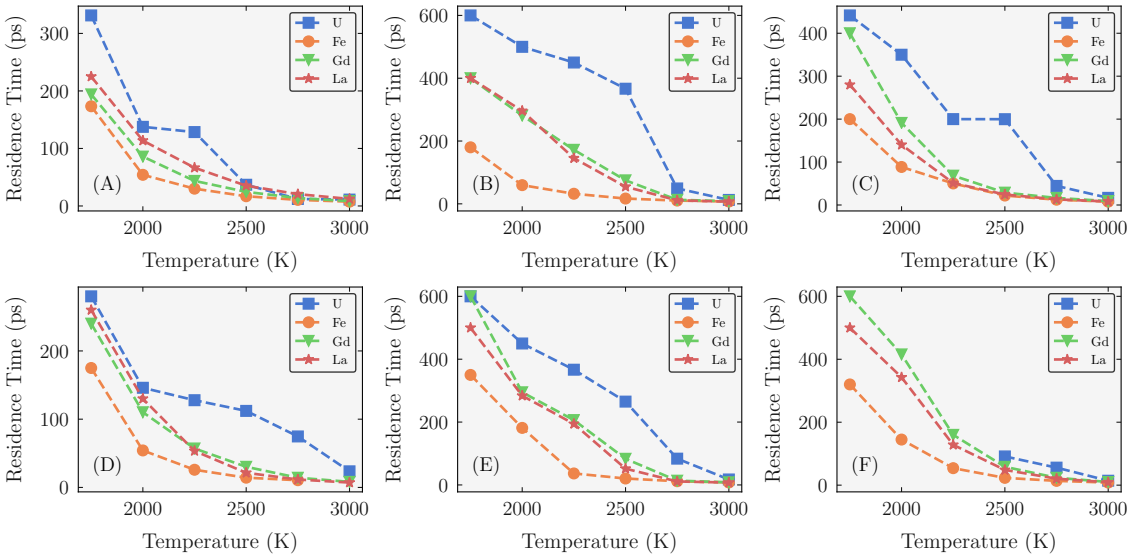

Figure 8.4: Average residence time in the first shell (0 - 3 Å) of oxygen with U, Fe, Gd and La (Blue, orange, green and red lines) as a function of temperature for the Σ3(111) (A), Σ5(210) (B), Σ9(221) (C), Σ5(310) (D), Σ11(311) (E) and Σ19(331) (F).

first coordination shell (0 – 3 Å from the impurity) and second coordination shell (3 – 6 Å from the impurity) are shown in Figure 8.5. Fe^{3+} in particular has a significantly lower average CN within the first coordination shell. In contrast Fe has a higher average CN within the second shell. M^{3+} defect clusters have been observed experimentally in other M_2O_3 doped UO_2 This is also been seen for doped CeO_2 and linked to the difference in ionic radii of the dopants La^{3+}, Gd^{3+}, Fe^{3+} (1.061, 0.958, 0.645 Å respectively) compared to the host cation U^{4+} (0.89 Å) [342].

The percentage increase in V_o concentration within the grain boundary region of each structure is presented as a function of temperature (Figure 8.7). There is a common behaviour for our grain boundaries considered whereby there is an increase in V_o concentration in the grain boundary region. The Σ5(310), Σ9(221), Σ19(331) and Σ11(311) boundaries show a 1.5-2.5% increase in vacancy concentration in the full grain boundary region regardless of the type of impurity up to a temperature of 2750 K where the oxygen sublattice becomes significantly mobile. To separate the effects of the grain boundary and the impurities the oxygen stoichiometry of the stoichiometric structures with that of the bulk doped structures mentioned in Figure 8.1 are compared and there is no change in the oxygen concentration at the boundary.

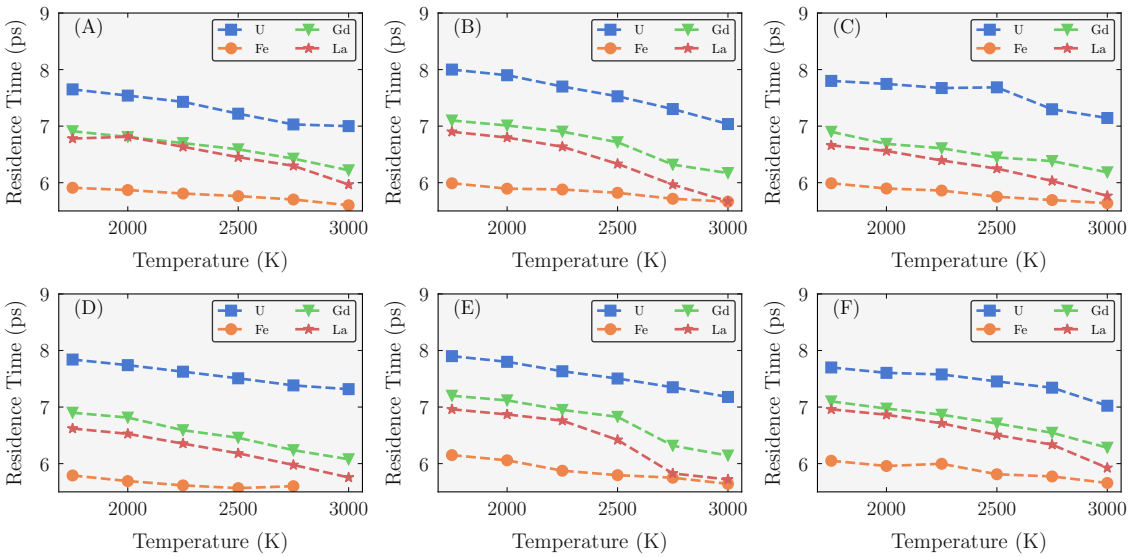

Figure 8.5: Average coordination number, in the first shell (0 - 3 Å) of U, Fe, Gd and La (Blue, orange, green and red lines) with oxygen as a function of temperature for the Σ3(111) (A), Σ5(210) (B), Σ9(221) (C), Σ5(310) (D), Σ11(311) (E) and Σ19(331) (F).

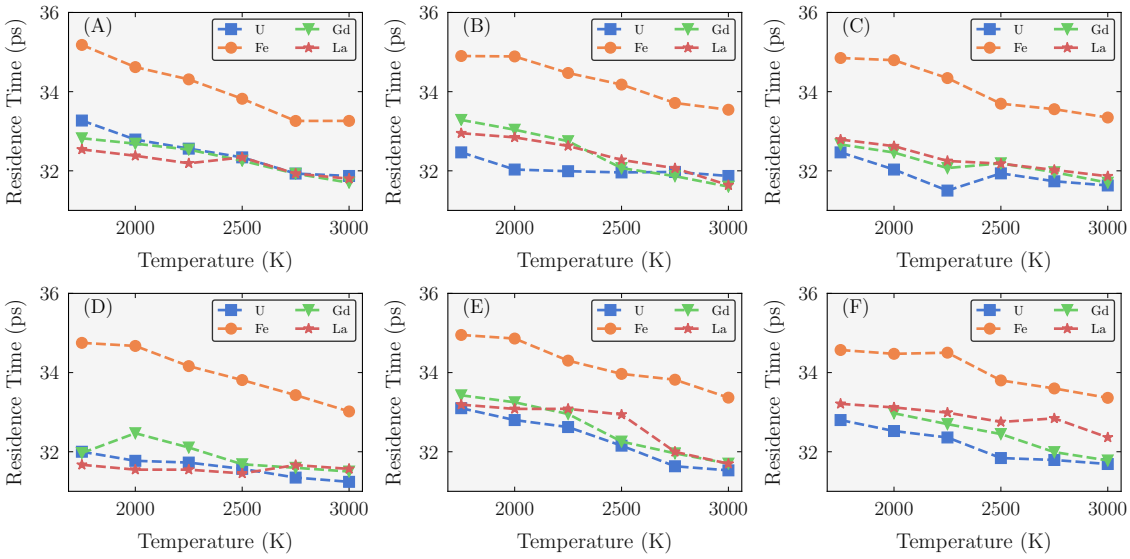

Figure 8.6: Average coordination number, in the second shell (3 - 6 Å) of U, Fe, Gd and La (Blue, orange, green and red lines) with oxygen as a function of temperature for the Σ3(111) (A), Σ5(210) (B), Σ9(221) (C), Σ5(310) (D), Σ11(311) (E) and Σ19(331) (F)

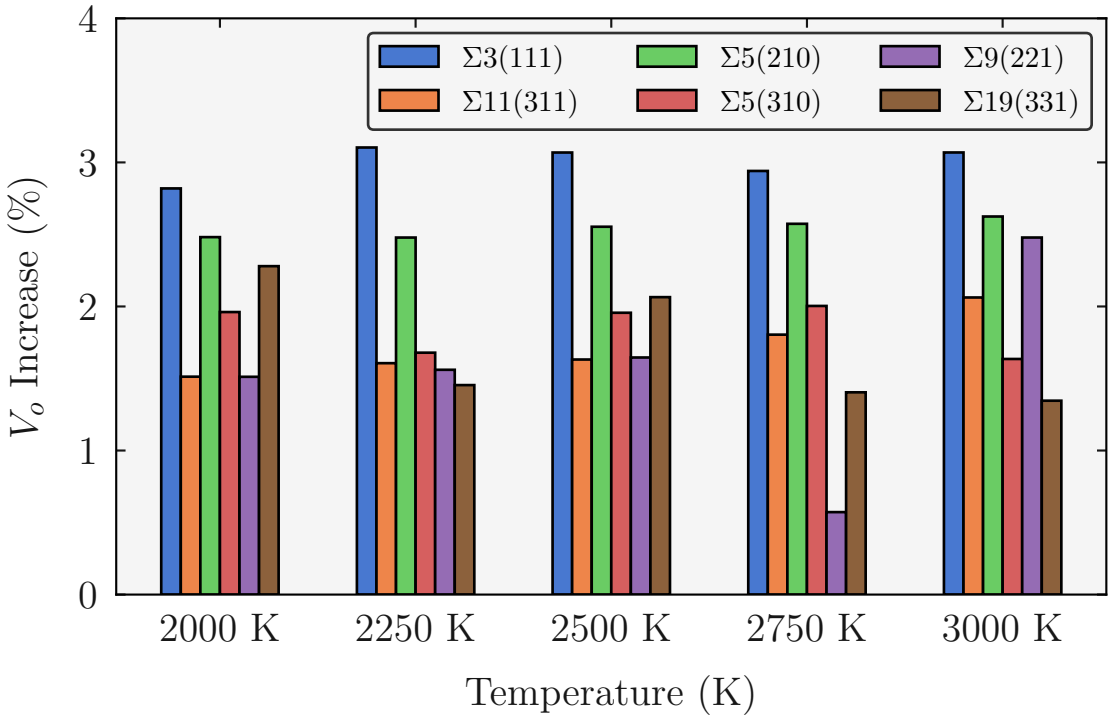

Figure 8.7: Oxygen vacancy concentration within each grain boundary between 2000 – 3000 K.

This indicates that it is the impurities driving the segregation behaviour in UO_2. V_o segregation at grain boundaries is generally accepted for fluorite structures, e.g. Gadolinium doped ceria (GDC) and Yttria stabilised zirconia (YSZ), in line with the space charge theory [279]. Arora *et al.,* studied the energetics of V_o within UO_2 grain boundaries and found vacancy segregation favourable when compared to the bulk material [343]. Several other studies have reported oxygen vacancy segregation within doped grain boundary systems [344, 345, 346, 347, 348]. This represents the first time that impurity promoted oxygen vacancy segregation at the grain boundaries has been proposed in UO_2.

8.5 Oxygen Diffusion at Grain Boundaries

Modelling results show that impurities significantly increase the oxygen transport within the grain boundaries. This behaviour is consistent with other studies investigating the effect of space charge on transport [280].

The diffusion of stoichiometric grain boundaries is discussed in chapter 7 but recapped here. It was found that the diffusion enhancement in stoichiometric boundaries follows the order $\Sigma3(111) > \Sigma9(221) > \Sigma19(331) > \Sigma11(311) > \Sigma5(310) > \Sigma5(210)$ at a representative temperature of 2500 K. There is a significant difference in the diffusion coefficient of the grain boundaries,with a 1 order of magnitude difference between the lowest value of 0.049 x $10^{-9}m/s^2$ obtained for the $\Sigma5(210)$ and the highest value of 0.53 x $10^{-9}m/s^2$ found for the $\Sigma3(111)$ at 2500 K.

Impurity cations further increase the diffusion within the grain boundary with Fe^{3+} having a greater effect than La^{3+} and Gd^{3+}. The increase corresponds to 0.1 x $^{-9}m/s^2$ for the $\Sigma3(111)$, $\Sigma9(221)$, $\Sigma19(331)$, $\Sigma11(311)$ boundaries and 0.5 x $10^{-9}m/s^2$ for the $\Sigma5(210)$ and $\Sigma5(310)$ boundaries. The large increase in the $\Sigma5$ series is due to the $\Sigma5$ structural changes discussed in section 8.3 (Figure 8.3).

The calculated activation energy for a 1% concentration of M^{3+} doped bulk UO_2 is 2.4 eV. While this is the activation energy of a UO_{2-x} system and a comparison should be treated with caution, the activation energy of stoichiometric UO_2calculated experimentally - 2.60 eV should be noted [349]. The activation energies have been calculated from Arrhenius plots (figure 8.8).

For clarity, only the activation energies for oxygen diffusion within the grain boundary region(Figure 8.9) are presented. There is a general decrease in activation energy (Ea) from the stoichiometric bulk (2.4 eV) to the grain boundaries with the exception of the $\Sigma5(210)$ and $\Sigma5(310)$ boundaries. The stoichiometric $\Sigma3(111)$ / $\Sigma11(311)$ and $\Sigma9(221)$ / $\Sigma19(331)$ boundaries have similar Ea – 1.7 and 1.6 eV, which is approximately half that of the bulk region. Fe^{3+} and Gd^{3+} cause a small decrease in Ea in the $\Sigma3(111)$ boundary while La^{3+} has no effect. With the exception of Fe^{3+} in the $\Sigma11(311)$ boundary, impurities cause a small increase in Ea in the $\Sigma9(221)$, $\Sigma19(331)$ and $\Sigma11(311)$ grain boundaries compared to their stoichiometric counterparts. So while the impurities are promoting increased diffusivity, the activation energy is for the most part unchanged or slightly increased.

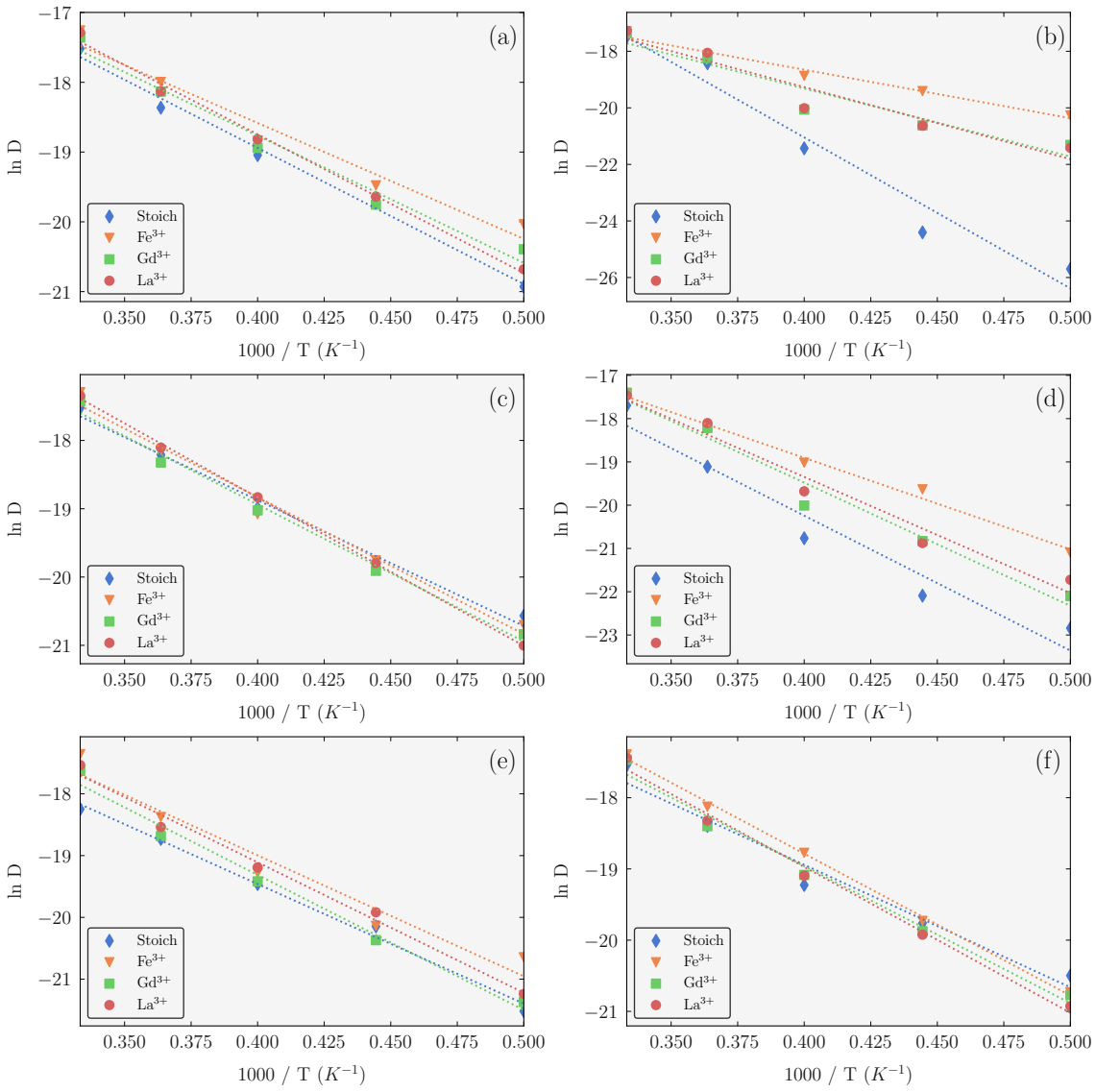

Figure 8.8: Arrhenius plots for the Σ3(111) (a), Σ5(210) (b), Σ9(221) (c), Σ5(310) (d), Σ11(311) (e) and Σ9(331) (f) grain boundaries. Data for the stoichiometric, iron doped, gadolinium doped and lanthanum doped configurations are plotted in blue, orange, green and red.

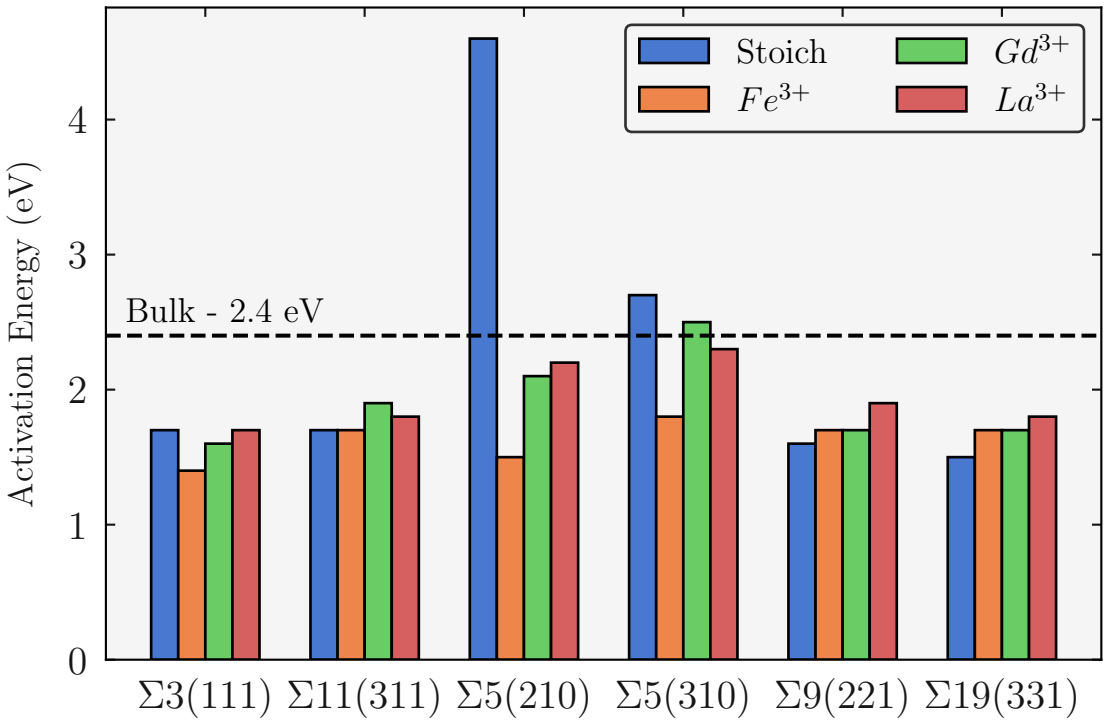

Figure 8.9: Activation energies for the stoichiometric (blue), Fe^{3+} (green), Gd^{3+} (red) and La^{3+} (purple) doped grain boundary regions compared to the activation energy of oxygen diffusion in 1% M^{3+} doped bulk UO_2 (2.4 eV)

As discussed in chapter 7, the stoichiometric Σ5 boundaries have a particularly high Ea, 4.3 and 2.7 eV for the Σ5(210) and Σ5(310) respectively, highlighting the poor transport properties of these boundaries. This has was attributed to the increased cation density at the boundary compared to the bulk. Upon the introduction of impurities there is a large decrease in the *Ea* for the Σ5(210) boundary and a modest decrease for the Σ5(310) boundary, which is due to the structural change discussed in section 7.4.1.

Upon introduction of impurities there is a decrease in the cation density at the Σ5 boundaries due to a small increase in grain boundary width (Figure 8.10).Relating the cation density at the grain boundary to the transport properties of boundaries provides a possible explanation for the blocking nature of the Σ5.

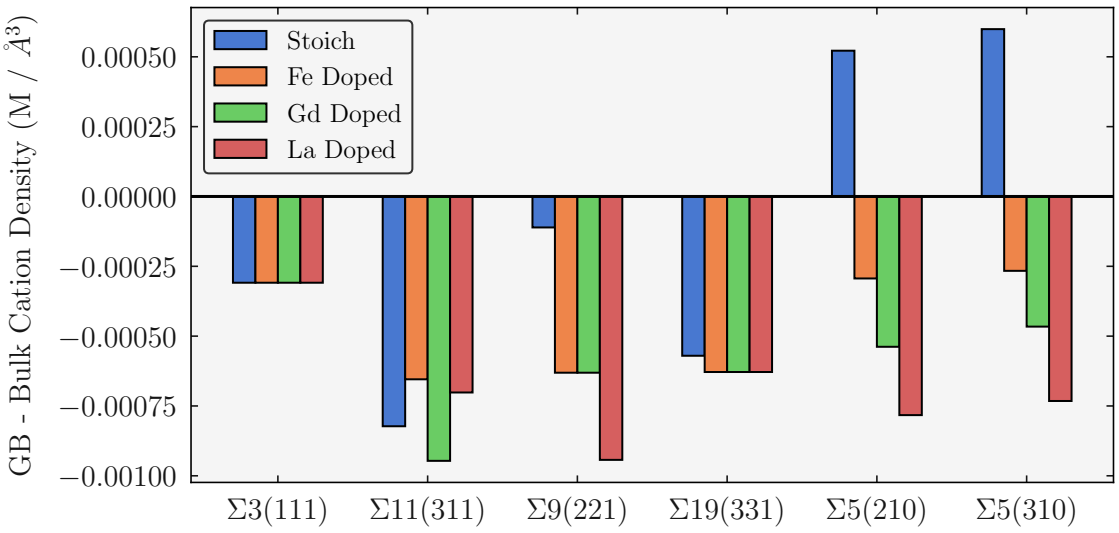

Figure 8.10: Cation density difference between the bulk region and the grain boundary region.

8.6 Electrostatic Potential

The electrostatic potential as a function of distance either side (-15 Å 15 Å) of the grain boundary core, positioned at 0 Å is shown in figure 8.11. The lattice polarization is illustrated by the x projection of the mean electrostatic potential (red dashed line). The sharp oscillations along X are due to the oppositely charged planes of cations (U or Ce) and anions (O). The polarization field is seen more clearly from a running average of the electrostatic potential, calculated across a distance equal to one lattice spacing (blue solid line).

The doped grain boundaries have a slightly lower potential at the boundary relative to the stoichiometric structures. This is due to the distribution of oxygen vacancies within the system. The doped grain boundaries have full segregation of both dopants and oxygen vacancies, thus, there is a reduction in charge density at the grain boundary relative to the bulk region and so the potential is smaller.

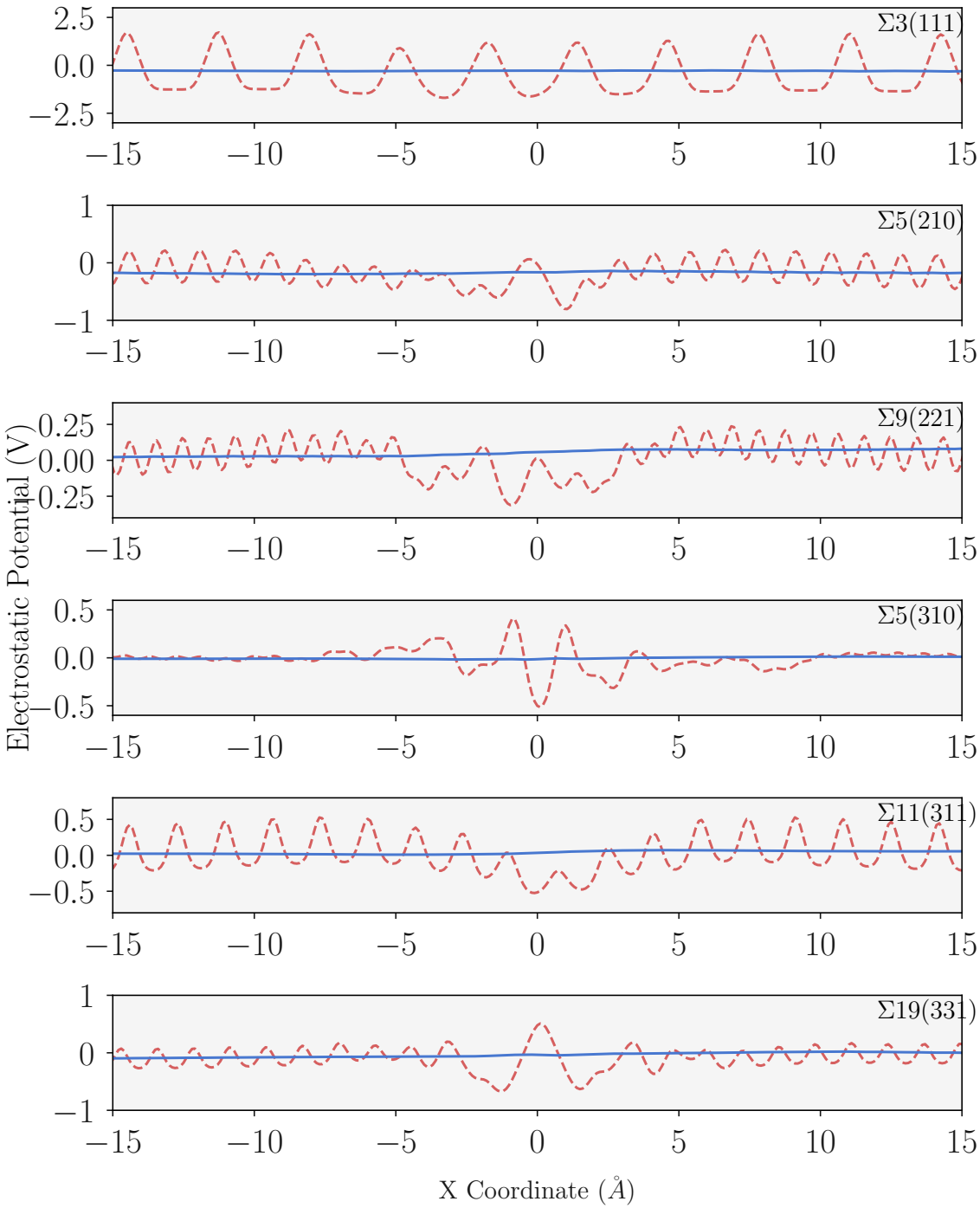

Figure 8.11: Red dashed lines: Poisson potentials calculated from molecular dynamics simulations as a function of distance from the grain boundary plane (-15 - + 15 Å) at 2000 K. Blue solid lines: running average potentials over one lattice spacing.

8.7 Discussion

The early stage of segregation of impurities at grain boundaries was studied, and it was demonstrated that even at a concentration as low as 1%, there is segregation of oxygen vacancies and an increase of local oxygen diffusion that will impact the oxygen storage capacity of the fuel and so the availability of oxygen to enter the corrosion process. These results demonstrate that the impurity content of UO_2 can have important implications for the corrosion of nuclear material.

This work illustrates the importance of the pre reactor stage of the fuel cycle. Fe^{3+} is a potentially avoidable impurity that is found in all fuels as a result of the fuel pellet sintering. It has been shown that the amount of Fe within the fuel pellets can be reduced by different fabrication processes, e.g. high levels of Fe are characteristic of fuel produced by dry chemical conversion compared to other methods such as the water or gas flame methods [293]. Fabrication plants typically have a purity limit (generally 1250 ppm [350]). Given that impurities segregate to the grain boundaries [280, 331], there will be high local concentrations of impurity within the grain boundaries, opposed to an homogeneous distribution of the impurity in the grain interiors.Based upon these results, sintering methods that minimise the inclusion of Fe within the UO_2 pellet are crucial to increasing the safety and lifetime of the fuel. Unlike Fe^{3+}, our results add further evidence to previous experimental and theoretical studies that Gd^{3+} enhances the oxygen transport within the fuel and thus the corrosion. The state of the grain boundaries within irradiated UO_2 has also been studied. The presence of La^{3+} in UO_2 is unavoidable as it forms through fission chain decay within the reactor [351]. These results show that La^{3+} will increase the corrosion through oxygen diffusion and in the case of the $\Sigma 5$ boundaries cause structural changes. Experimental studies of post reactor fuel should pay careful attention to La^{3+} concentration within the spent fuel as its presence could indicate unstable grain boundary systems.

These results can be expected to be applicable to the wider field of fluorite grain boundaries. While it is accepted that transport along grain boundaries is higher

than bulk transport, transport across the grain boundaries is blocked by the space charge effect. The space charge effect is well documented in CeO_{2-x} and doped zirconia and is due to the segregation of charged defects to the grain boundary [278, 279, 280] . This causes a blocking effect of transport across the boundary. Our results show that the M^{3+} cations present at the boundary strongly attract oxygen vacancies (Figures 8.4, 8.5, 8.6 and 8.7), pulling them to the boundary where they will remain trapped and facilitate high levels of oxygen transport along the boundary and thereby increase the rate of corrosion. Kubo et al has seen a similar effect in UO_2 whereby at Gd^{3+} concentrations at or exceeding 10 wt%, a potential barrier for the migration of electron holes formed [335].

8.8 Conclusions

This chapter focused on how fission products at uranium oxide grain boundaries affects the oxygen transport and thus corrosion of the material. It was found that the segregation of these defects to the grain boundary was energetically favourable and thus segregation of fission products will occur over time. Oxygen vacancies follow the fission products and thus segregate to the fission products, facilitating increased oxygen diffusion in those regions.

9 Defect Segregation and Oxygen Transport in CeO_2 Grain Boundaries

The contents of this chapter have been previously published by the author as part of this PhD project and can be found at the following reference, A.R. Symington, M. Molinari, J. Statham.;J. Wu, S. C. Parker, The role of dopant segregation on the oxygen vacancy distribution and oxygen diffusion in CeO_2 grain boundaries. *J Phys Energy*, 1(1): 042005, 2019. doi: 10.1088/2515-7655/ab28b5.

9.1 Background

Fluorite structured ceramic materials, including ceria (CeO_2) and doped zirconia (ZrO_2), have attracted considerable attention for energy applications in the last three decades due to their high ionic conductivity [352, 353]. These ionic conductors find use as solid electrolytes in solid state electrochemical devices such as solid oxide fuel cells (SOFC) [126, 354, 355]. However the widespread use of such devices is hindered by material issues relating to high operating temperatures [356]. Lanthanide doped ceria materials, i.e. Ln^{3+} ions like gadolinium, exhibit excellent oxygen conductivity due to the introduction of excess ionic carriers (oxygen vacancies). These doped materials, particularly gadolinium doped ceria (GDC), allow for slower material degradation as the diffusion of oxygen occurs at lower operating temperatures (1000 - 1200 K) [127, 356, 357],with further improvement obtained through a reduction of

particle size [358, 359]. Thus demonstrating that the microstructure plays a key role in the material properties.

Polycrystalline GDC, similar to other doped oxides, shows defect segregation to the grain boundaries (GBs), which has been observed experimentally and is detrimental to material properties [29, 360]. As defects, particularly dopants, segregate and accumulate at the GBs, they may contribute to an increase in grain boundary resistance to the transport of oxygen. This results in a reduction in the conductivity of polycrystals compared to single crystals [29, 345, 361, 362]. It is therefore critically important to understand and ultimately control the processes that occur at these interfaces and how they affect the materials properties.

The degradation associated with dopant segregation at grain boundaries in GDC has been studied theoretically to elucidate the atomistic details relating to the mechanism [363]. A hybrid Monte Carlo-molecular dynamics (MD) revealed that Gd^{3+} segregation to the GBs is a thermodynamically favourable process, [364] and driven by a high oxygen vacancy concentration at the GBs. However, this study was only limited to the $\Sigma5(310)/[001]$ tilt grain boundary in GDC. Dholabhai et al. combined MD and density functional theory to study three symmetric GDC GBs, namely the $\Sigma3(111)/[110]$ tilt GB, $\Sigma5(310)/[001]$ tilt GB and $\Sigma5(001)$ Θ=36.87 twist GB [55], finding that GBs have different segregation behaviour, and that the stability of dopant-vacancy clusters at GBs was heavily dependent on the local structure and dopant arrangements at the GBs.

9.2 Calculation Details

The potential model used in this chapters is the same as in chapter 7 and 8. In order to study the effect of gadolinium dopants, dopants were introduced to the grain boundary structures discussed in chapter 7. Three concentrations of Gd^{3+}, 10%, 16% and 30% were substituted to Ce^{4+} cations. These percentages represent the concentration of dopants over the overall number of Ce^{4+} cations in the simulation cell.

Different doping schemes were studied; GB doped - which are Gd^{3+} doped CeO_2 nanolayered structures with 10, or 16% random substitution of Gd^{3+} localized within the grain boundary regions; e.g. 10% GB doped represents a configuration with 10% Gd^{3+} randomly distributed within the grain boundary regions (these represent a degraded SOFC device) . Random doped - which are Gd^{3+} doped CeO_2 nanolayered structures with 10, 16 or 30% substitution of Gd^{3+} randomly distributed through the entire structure, i.e. both bulk and grain boundary region; e.g. 10% random doped represents a configuration with 10% Gd^{3+}+ randomly distributed within the entire structure (these represent a freshly prepared device). 30% GB doped configurations cannot be formed within this model as there are not enough Ce^{4+} cations within the grain boundary regions to accommodate 30% Gd^{3+} substitution. Stoichiometric structures were also simulated as a control, referred to as CO.

Oxygen vacancies were introduced randomly to maintain charge neutrality throughout the entire structure. Oxygen vacancies reached their equilibrium distribution within the NPT MD simulation, this was confirmed by examining the evolution of the oxygen stoichiometry over time. Oxygen vacancies distributed during the early stages of the NPT simulation and this distribution persisted for the duration of the simulation. During these simulations there was minimal cation diffusion and thus, the distribution of impurities remained similar to the starting distribution. A single distribution of dopants is not necesarily representative, so five doped configurations were generated for each grain boundary and the data presented in this chapter is the average for these five configuraitons. Configurational and statistical was recorded every 250 fs.

All molecular dynamics simulations (MD) are performed using the DLPOLY code [290]. MD simulations of 5 ns were completed using a timestep of 1 fs with an 8.5 Å cutoff. Dopants were added to the simulation cells discussed in chapter 7 and the system was equilibrated for 1ns using the NPT ensemble. Transport behaviour was evaluated using the NVT ensemble across across a temperature range of 2000 - 3000 K (at 250 K intervals) for 5 ns. The size of each simulation cell and total number of defects are shown in Table 9.1.

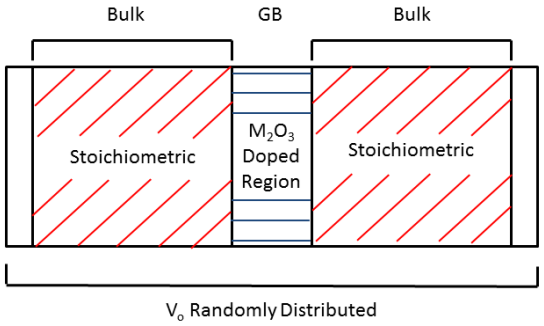

Figure 9.1: Schematic illustrating the model configuration for grain boundary and doping scheme.

Table 9.1: Total number of atoms in each grain boundary supercell and the total number of dopants added.

Grain Boundary	Number of Atoms	Number of Species		
		10% Gd^{3+}	16% Gd^{3+}	30% Gd^{3+}
Σ3(111)	8640	288	460	864
Σ5(210)	7680	256	410	768
Σ5(310)	7680	256	410	768
Σ9(221)	5760	192	308	576
Σ11(311)	7200	240	384	720
Σ19(331)	7200	240	384	720

Tracer-diffusion data for O within grain boundaries was obtained from a regional mean squared displacement (MSD). The calculation of the MSD only takes into account those segments of atom trajectories for oxygen species that pass within the region of interest e.g. the grain boundary. Residence time analysis was used to evaluate the average length of time that an oxygen atom spends in contact with each cation (Ce^{4+} and M^{3+}).

9.3 Doped Grain Boundary Structure

Molecular dynamics simulations have been used to evaluate the impact of temperature and dopant concentration on the energetics of Gd segregation.

In this case by comparing the GB doped models where all the dopants are in the GBs, to the random doped models where Gd^{3+} dopants are randomly distributed throughout the entire structure. The difference in configurational energy between the two schemes (10% and 16% concentrations) is shown in figure 9.2. The data

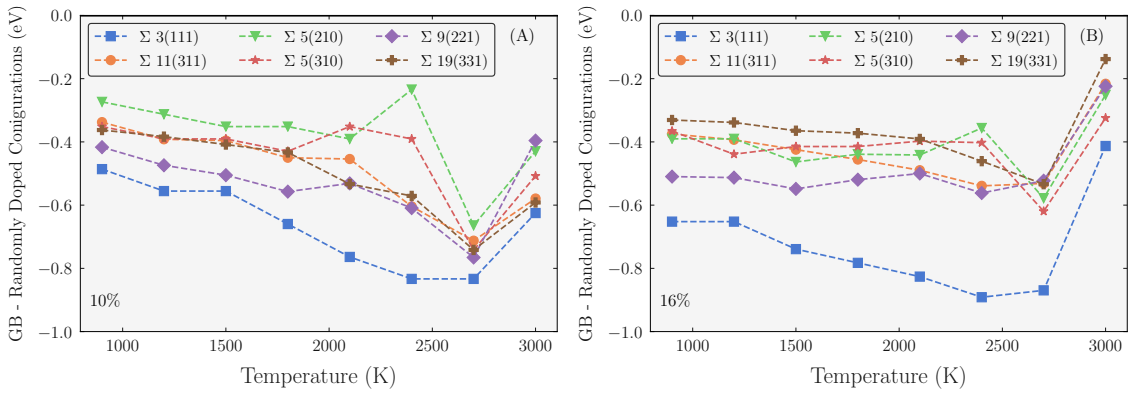

Figure 9.2: Energy difference between the 10% randomly doped and 10% GB doped (A) configurations and 16% randomly doped and 16% GB doped (B) configurations per Gd^{3+} ion.

indicates that the energetic contribution favours Gd^{3+} segregation at the GBs rather than random distribution in all models evaluated. This is in line with experimental evidence [292, 365]. Increasing temperature increases segregation energies until about 2700K, beyond which the grain boundaries start to melt.

On random introduction of Gd^{3+} ions over the entire simulation cell (random doped configurations) the stoichiometric grain boundary structures are retained. However, when Gd^{3+} was segregated within the grain boundary regions (GB doped configurations), there are significant structural rearrangements during the annealing (Figure 9.3). The presence of impurities promotes an alteration to the structure of the $\Sigma5(210)$ with similar structural changes reported for stoichiometric UO_2 in the previous chapter, but not yet for GDC. However previous studies on Gd^{3+} segregation in GDC are based on a static GB model of undoped CeO_2, [55, 364] where the GB structure of GDC is visualised as a dilute solution of 0K point defects in the parent CeO_2.

The concentration of Gd in the GB doped models is relatively high, thus may not be representative of many experimental studies. However these results are the first that show that high concentrations of Gd can cause an alteration in grain boundary structure, which may impact those experimental sample of doped nanoceria with high concentration of Gd [359]. A possible explanation for these structural rearrangements is that the dopants stabilise metastable grain boundary configurations

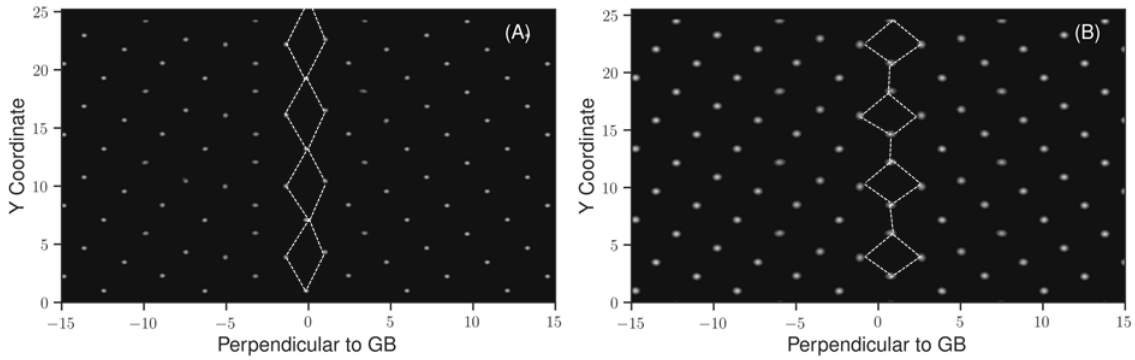

Figure 9.3: Time averaged 2D density profiles of the centre of mass of the cations (Ce^{4+} /Gd^{3+}) displayed every 0.5 ps at 2100 K for the stoichiometric and 16% GB doped $\Sigma5(210)$ structures. The white dots denote the cation arrays parallel to the grain boundary plane. Patterns have been drawn to aid visibility.

at higher temperatures, which may be energetically inaccessible under stoichiometric conditions, although these structures may be present in the potential energy surfaces presented in Figure 7.1. It is worth noting that the GDC material is used at relatively high temperatures (600 - 1000 K or higher) [291] in thermochemical devices, thus the GB structures are likely to change over time. Therefore, the segregation triggered structural transformations is likely to be important in the study of the long-term degradation behaviour of GDC.

9.4 Oxygen Vacancy Segregation

The distribution of oxygen vacancies (V_o) within the doped configurations as the V_o concentration within the two regions per Å ^{3} i.e. the bulk and the grain boundary (GB) regions has been calculated (Figure 9.4). In the GB doped configurations there is almost complete depletion of V_o in the bulk region and complete segregation of V_o to the GB region. In all randomly doped configurations, where the Gd^{3+} concentration is constant with depth, there is still a small increase in the concentration of V_o per Å ^{3} at the grain boundaries. Thus indicating that while the dopants strongly attract oxygen vacancies, there is still a contribution from the grain boundary. This was not found in the previous chapter on uranium oxide, however in this chapter considerable larger concentrations are being studied. Furthermore, this effect seems to increase as the concentration of Gd increases, thus at the low concentrations studied in the previous chapter (1%) there may be less of an effect. If the GB structure

was not a driving force for V_o segregation, then there would have been an equal or greater concentration of V_o in the bulk region of the random doped configurations. In effect, in the random doped configurations, the grain boundary and the dopant Gd^{3+} in the bulk are in competition for oxygen vacancies.

The average cation-oxygen coordination number (CN) within the first coordination shell (3 Å from the cation) as a function of temperature (Figure 9.6) show that Ce^{4+} is surrounded by a greater number of oxygen ions on average compared to Gd^{3+}. This is a common feature within the grain boundary structures, doping schemes and configurations studied. This is evidence that there is a stronger interaction between Gd^{3+} and V_o compared to Ce^{4+} and V_o.

The formation of this first nearest neighbour Gd^{3+} - V_o clustering has been reported in the literature [53] for bulk cerium dioxide and in the previous chapter for UO_2. For the random doped configurations, the oxygen CN of Ce^{4+} , either in the bulk or in the grain boundary, decreases as the concentration of Gd^{3+} increases from 10 to 30%. The oxygen CN of Ce^{4+} in the grain boundary region of GB doped configurations follows the same trend, although the difference between 10% and 16% Gd^{3+} doping is less prominent. The same pattern applies to the oxygen CN of Gd^{3+} in both random and GB doped configurations, which is due to the decrease of the total oxygen ions available in the simulation cells.

Residence time analysis, i.e. the average time spent by an oxygen atom within the first coordination sphere of a cation was used to define the preferential affinity to oxygen with Ce^{4+} or Gd^{3+}. On average, it was found that oxygen resides longest closer to Ce^{4+} than Gd^{3+} (Figure 9.5). This supports the stronger interaction between oxygen vacancies and Gd^{3+}. The residence time decreases with increasing temperature as the diffusion of oxygen becomes more predominant. At high temperature the residence time for both Ce^{4+} and Gd^{3+} converge to the same value. It is also evident from the data that all the grain boundaries, i.e. extended defects, behave in a similar way, and have a marginal effect on the time oxygen resides close to a cation, i.e. for Gd^{3+} a point defect. Based upon these observations, two key

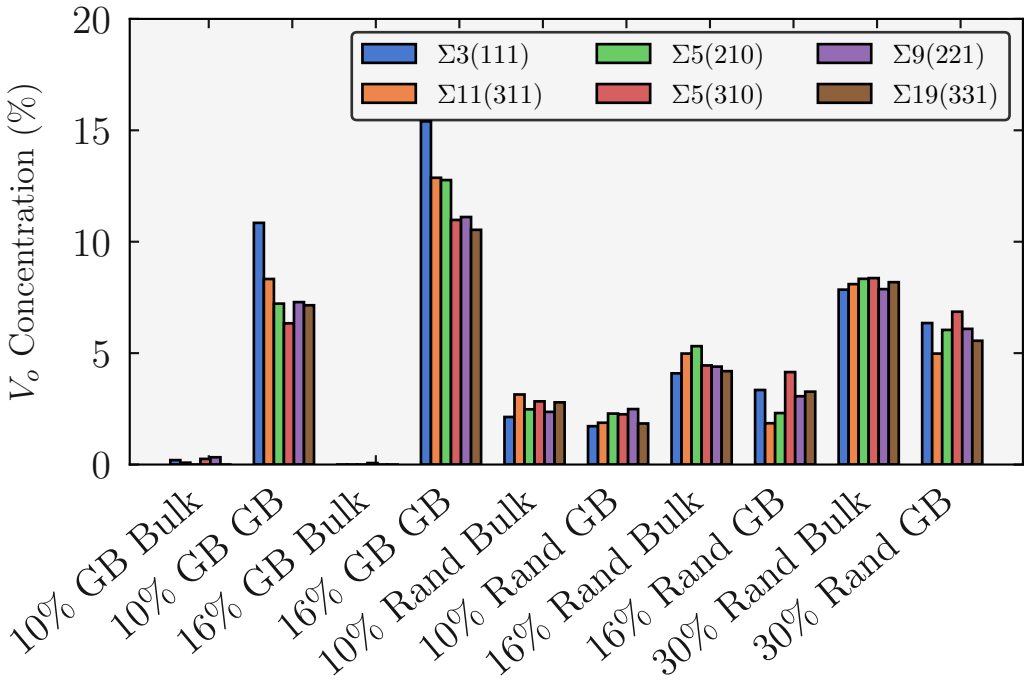

Figure 9.4: Oxygen vacancy distribution within the bulk and GB regions of each configuration at a representative temperature of 2100 K.

points are inferred. First, there is a strong interaction between Gd^{3+} and V_o, which causes oxygen vacancies to distribute partially due to the distribution of the Gd^{3+}. This is not surprising given that the effective charges of Gd^{3+} and V_o are -1 and +2 respectively. Secondly, grain boundaries themselves have a strong interaction with oxygen vacancies and cause some V_o to segregate to the boundary despite uniform distributions of Gd^{3+}.

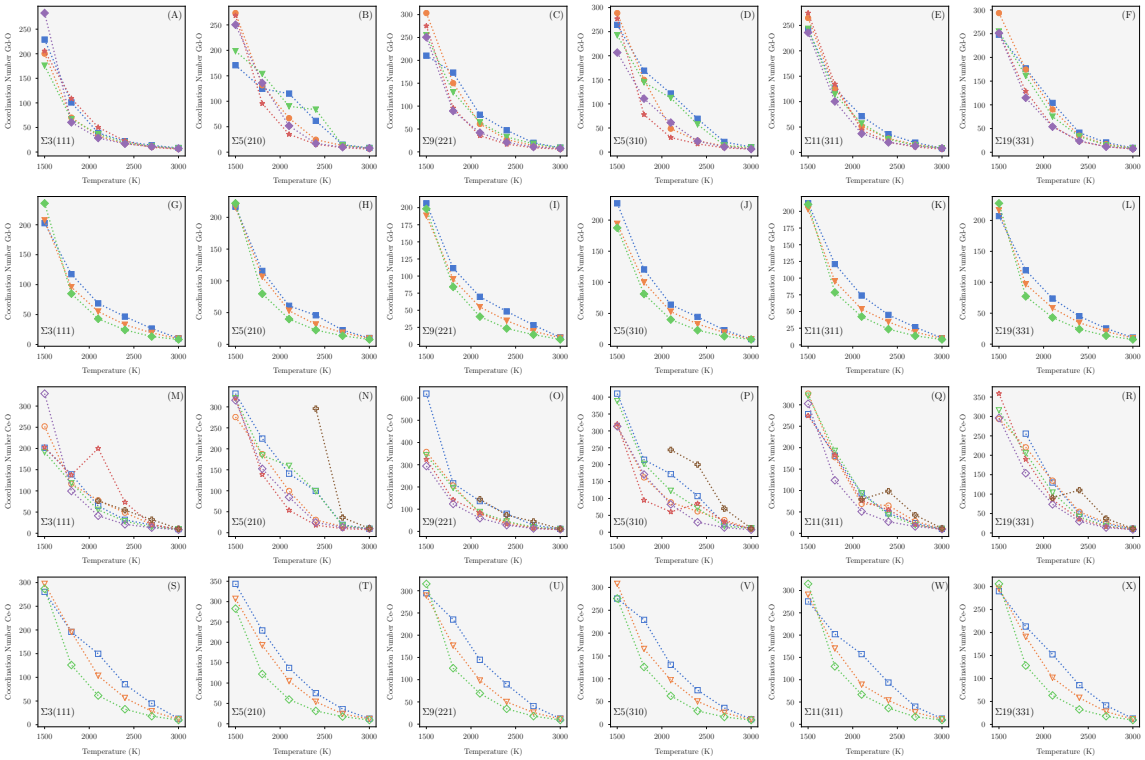

Figure 9.5: Residence time for oxygen with Gd in the GB doped configurations (Σ3(111), Σ5(210), Σ9(221), Σ5(310), Σ11(311), Σ19(331)) (A-F), oxygen with cerium in the GB doped configurations (Σ3(111), Σ5(210), Σ9(221), Σ5(310), Σ11(311), Σ19(331)) (G-L), oxygen with Gd in the bulk doped configurations (Σ3(111), Σ5(210), Σ9(221), Σ5(310), Σ11(311), Σ19(331)) (M - R) and oxygen with Ce in the bulk doped configurations (Σ3(111), Σ5(210), Σ9(221), Σ5(310), Σ11(311), Σ19(331)) (S-X)

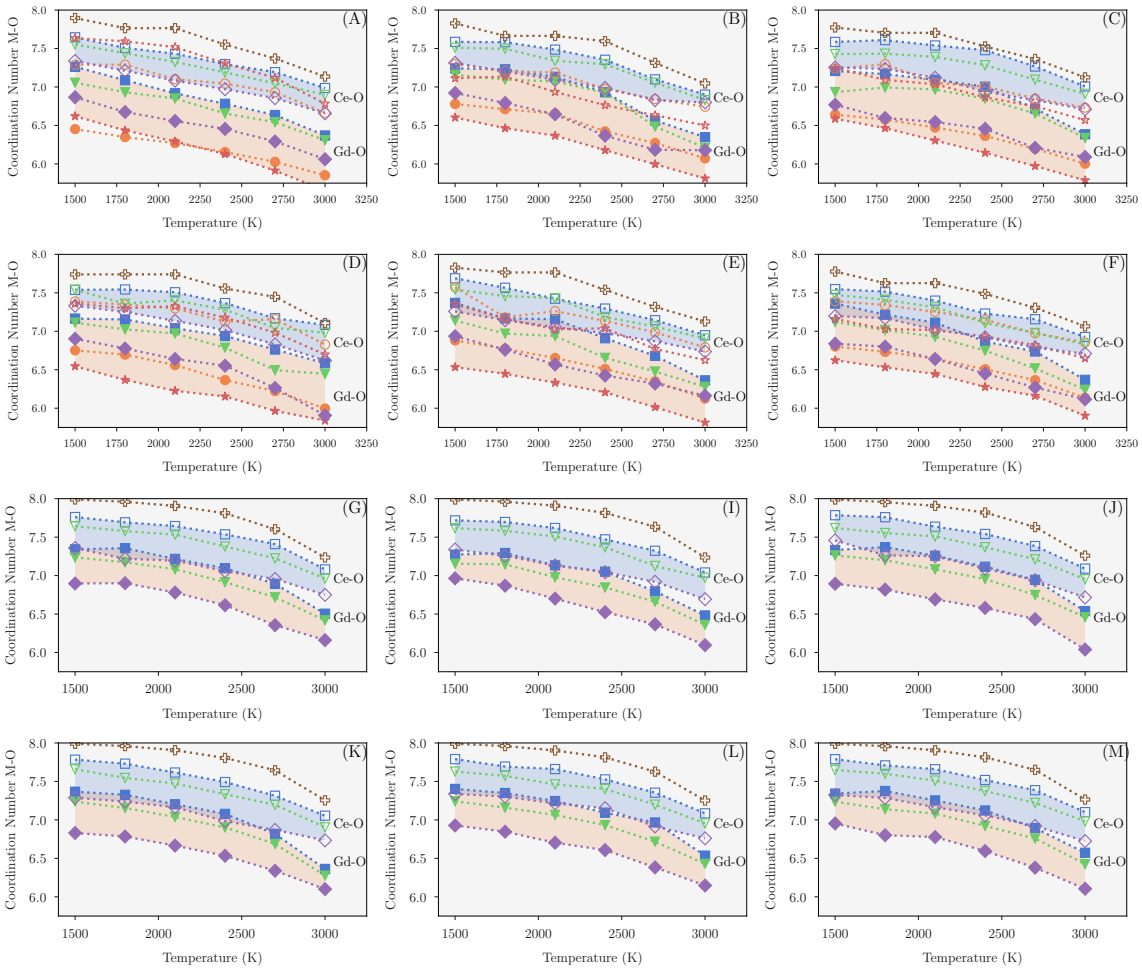

Figure 9.6: Coordination number as a function of temperature for the GB (A-F) Σ3(111), Σ5(210), Σ9(221), Σ5(310), Σ11(311), Σ19(331) grain boundaries and bulk (G-M) Σ3(111), Σ5(210), Σ9(221), Σ5(310), Σ11(311), Σ19(331) grain boundaries.

9.5 Oxygen Diffusion at Grain Boundaries

The presence of dopants was found to significantly increase the oxygen transport along the grain boundary. This is illustrated with a typical 1ns trajectory of 3 oxygen atoms (1 in the grain boundary and two in the bulk) for three different grain boundary simulations, for example a time averaged density of diffusing species (oxygen) shows that in GB doped configurations, enhanced diffusion is localised to the grain boundary, with no change in diffusion in the bulk when compared with the stoichiometric structure (Figure 9.7). In contrast, in randomly doped configurations there is significant diffusion in both the grain boundary and bulk (Figure 9.7C). Both observations can be rationalised by examining the oxygen vacancy distribution. Randomly doped configurations have a more uniform distribution of V_o, albeit with a slightly higher concentration in the grain boundary, throughout the structure. This more even distribution of charge carriers facilitates diffusion throughout. In GB doped configurations V_o have all localised in the grain boundary leaving few hopping sites in the bulk, as it is for stoichiometric configurations.

As the bulk and the grain boundary regions display such different behaviour, the two regions were treated separately. Considering the grain boundary regions for all the grain boundary configurations, our data does not show significant variation in the magnitude of the diffusivity. As the concentration of Gd^{3+} increases, the diffusivity increases for all configurations.

In the GB doped configurations, there is a small concentration of oxygen vacancies in the bulk, thus, activation energies could not be collected from the bulk due to the lack of diffusion events that occurred in the GI. Activation energies could be calculated for the 10, 16 and 30% randomly doped configurations as there is a suitably high concentration of oxygen vacancies throughout the GI (figure 9.8). The activation energy in the bulk regions was calculated to be 0.8, 0.9 and 1.0 eV. Grain boundary regions generally have a slightly increased activation energy compared with the bulk (Figure 9.9). The $\Sigma3(111)$, $\Sigma11(311)$, $\Sigma5(210)$ and $\Sigma9(221)$ randomly doped configurations have a similar but slightly larger activation energy

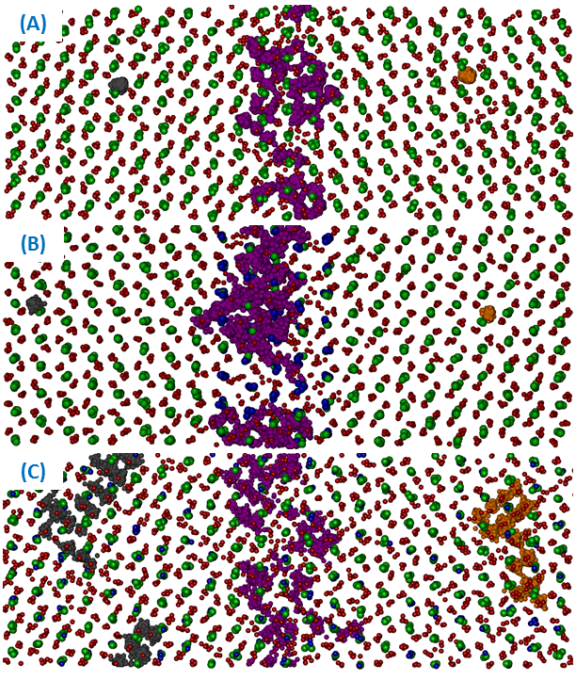

Figure 9.7: Shows the superimposition of a snapshot of the grain boundary and the bulk regions of (A) stoichiometric (CO), (B) 10% GB and (C) 30% random doped $\Sigma 3(111)$ configurations. For clarity Oxygen, Cerium and Gadolinium are shown in red, green and blue. To illustrate the effect of the grain boundary on diffusion, the full trajectory across 1 ns for a single oxygen atom has been shown for one oxygen in the grain boundary region (purple) and one in the bulk either side of the boundary (grey and orange).

at the GB compared with the bulk regions whereas the Σ5(310) and Σ19(331) randomly doped configurations have a much larger activation energy in the bulk regions compared with the GB. With the exception of the Σ19(331) grain boundary the randomly doped configurations have lower activation energies that the GB doped configurations. This highlights that the specific local micro-structure of these materials can have a large effect on transport properties. This is in line with experimental predictions that grain boundary regions reduce the conductivity of the material.

The stoichiometric Σ5(210) has the highest activation energy, followed by the stoichiometric Σ5(310), indicating that these grain boundaries may be strongly blocking oxygen transport. However upon the introduction of dopants there is a large decrease in the Ea for both grain boundaries to values similar to all other grain boundaries.

A possible explanation for the low diffusivity in the Σ5 boundaries relates to the cation density at the boundary compared with the bulk region. It was found that in the stoichiometric Σ3, Σ9, Σ11 and Σ19 boundaries there is a slight decrease in cation density, whereas in the Σ5 boundaries there is an increase in cation density (Figure 9.10). Upon introduction of impurities there is a decrease in the cation density at the boundary due to a slight widening of the boundary region (Figure 9.10). The contribution of the cation density at the grain boundary to the transport properties of boundaries provides a possible explanation for the strong blocking nature of the stoichiometric Σ5.

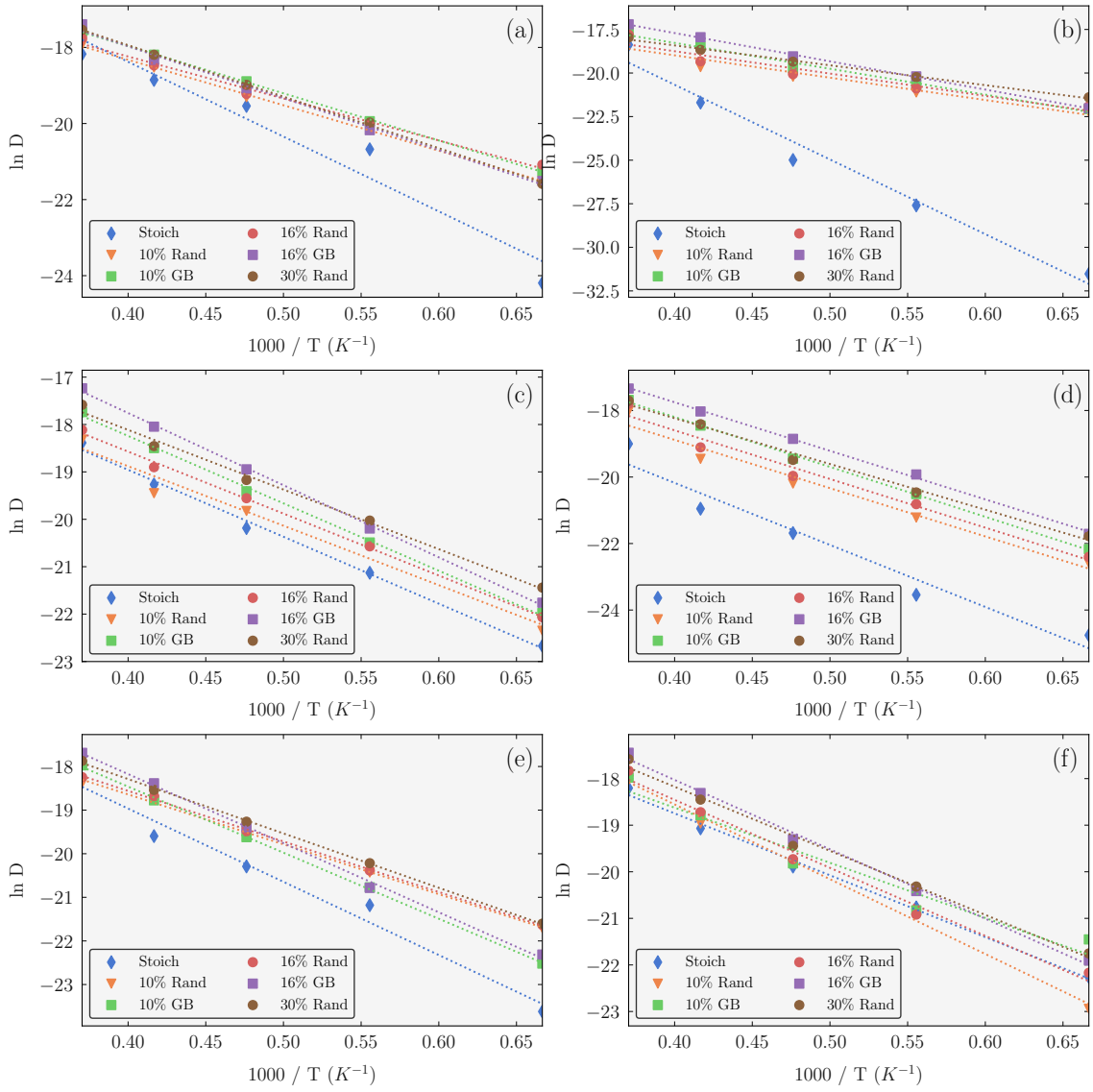

Figure 9.8: Arrhenius plots for the Σ3(111) (a), Σ5(210) (b), Σ9(221) (c), Σ5(310) (d), Σ11(311) (e) and Σ9(331) (f) grain boundaries. Data for the stoichiometric, 10% random, 10% GB, 16% random, 16% GB and 30% random are plotted in blue, orange, green, red, purple and brown.

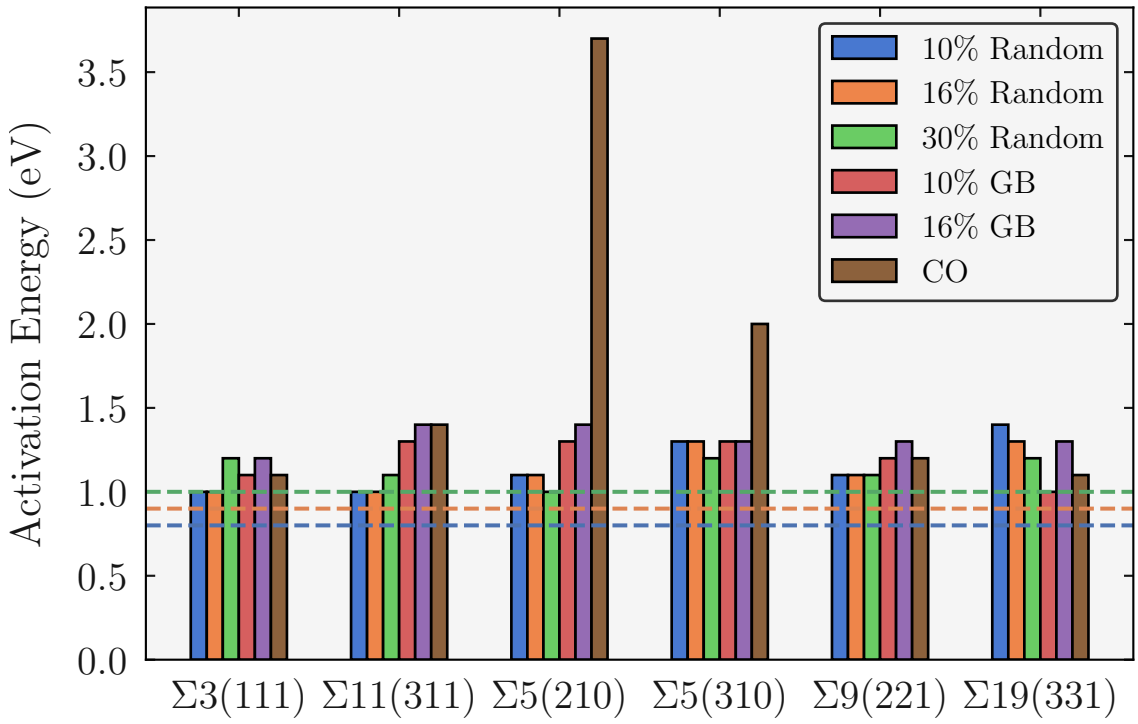

Figure 9.9: Activation energies for oxygen diffusion in the grain boundary regions for all the nanolayer configurations. The calculated bulk activation energies for the 10, 16 and 30% randomly doped configurations are denoted by blue, orange and green horizontal lines.

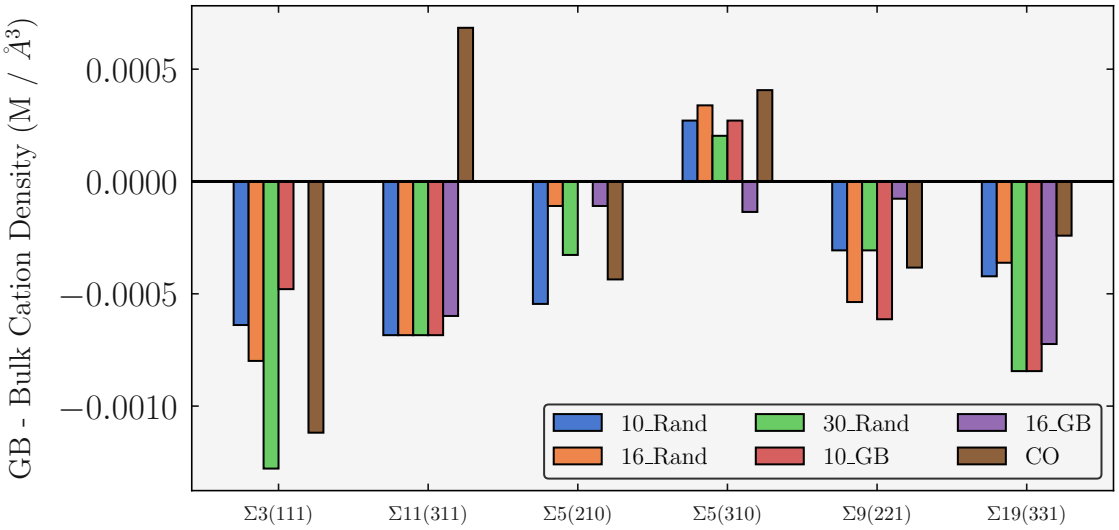

Figure 9.10: Cation density difference between the bulk region and the grain boundary region for all configurations studied.

9.6 Electrostatic Potential

The electrostatic potential was calculated as a function of distance either side (15 Å 15 Å) of the grain boundary core positioned at 0 Å (Figure 9.12), for each grain boundary within each scheme (stoichiometric CO, doped grain boundary region (GB doped configurations) and randomly doped grain boundary and bulk regions (randomly doped configurations)). The lattice polarization is illustrated by the X projection of the mean electrostatic potential (Figure 9.12 - red dashed line). The sharp oscillations along X are due to the oppositely charged planes of Ce^{4+}/Gd^{3+} and O^{2-}. The polarization field is seen more clearly from a running average of the electrostatic potential, calculated across a distance equal to one lattice spacing (Figure 9.12 - blue solid line). Generally there are quite substantial differences between the profiles of different grain boundaries. Some structures show disruption of the electrostatic potential at the core of the grain boundary that extend into the bulk; this is hardly visible in the $\Sigma3(111)$ whereas it is significant in the $\Sigma5(310)$.

It was found that GB doped configurations have a slightly lower potential at the boundary relative to the stoichiometric structures (Figure 9.12), which is in contrast with the randomly doped configurations, which generally have a slightly larger potential. This is due to the distribution of oxygen vacancies within the systems. The random doped configurations have an constant distribution of Gd^{3+} throughout but an uneven distribution of V_o (i.e. the average V_o density is greater in the bulk compared to the GB regions, 9.4), thus there is a greater net positive charge at the GB relative to the GI. In contrast the GB doped configurations display segregation of both Gd^{3+} and almost all V_o at the grain boundaries, thus there is a reduction in charge density at the GB region relative to the bulk and so the potential is smaller (Figure 9.12).

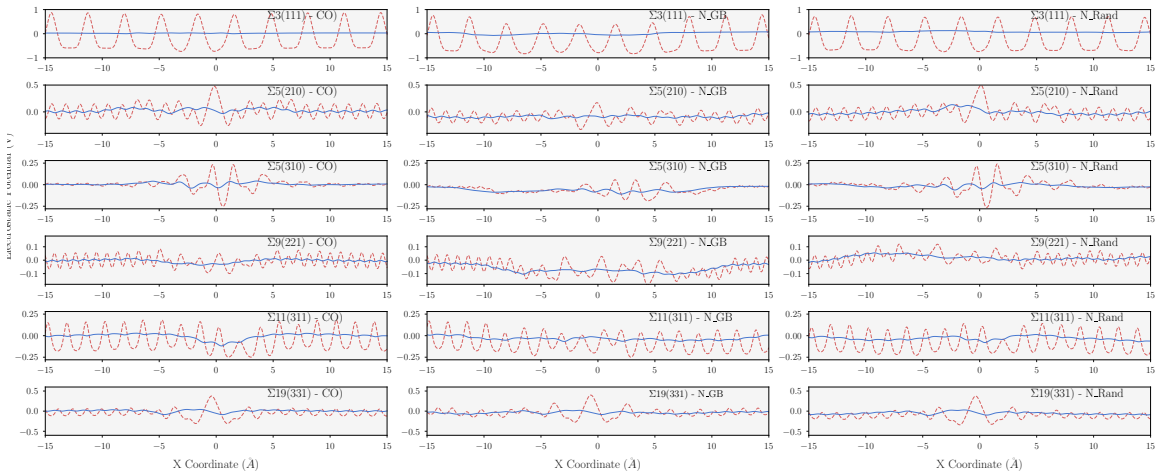

Figure 9.11: Red dashed lines: Poisson potentials calculated from molecular dynamics simulations as a function of distance from the grain boundary plane (-15 - 15 Å) at 2100] K for the stoichiometric, 10% GB and 10% random doped configurations. Blue solid lines: running average potentials over one lattice spacing.

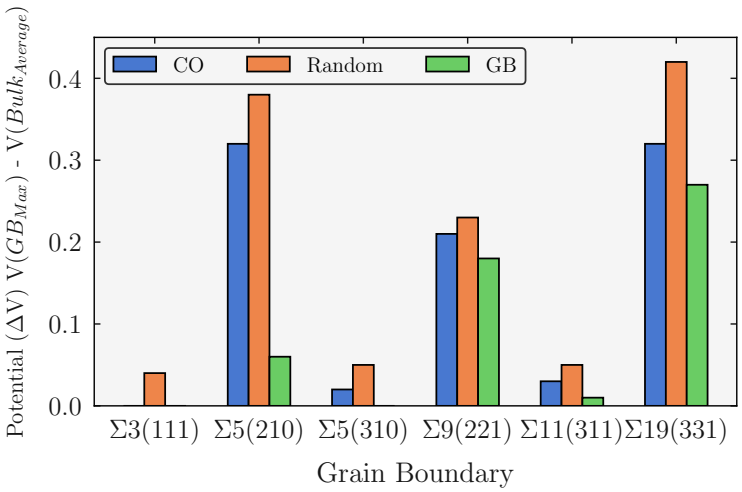

Figure 9.12: Difference between the average electrostatic Poisson potential at the bulk and at the grain boundary core for the stoichiometric CO (Blue), random doped (Orange) and GB doped (Green) configurations for all grain boundary structures.

9.7 Discussion

All calculations, both molecular mechanics and molecular dynamics, show that grain boundaries are sinks for gadolinium and oxygen vacancy segregation (Figures 9.2, 9.4, 9.5 and 9.6) although the oxygen vacancies (V_o), segregation depends on GBs local structure. This observation agrees with the findings of Dholabhai et al, where the defect energy is found to be sensitive to the local environment, i.e. the GB [55]. The segregation of V_o was also found to be dependent on distance from the grain boundary core by Allen et al [128] to a depth of approximately 1.5 nm. This is similar to that found from EELS, which revealed an enhanced oxygen vacancy and gadolinium concentration in first 2-4 nm from the GB and is assumed to be the effective width of the space charge layer [345].For a information the reader can refer to more detailed papers [29, 280].

A key result is that although grain boundaries are sinks for oxygen vacancies, dopant segregation may play a much greater role in their segregation. All GB doped configurations, where all Gd^{3+} was segregated in the grain boundary regions see a complete depletion of V_o in their bulk regions (Figure 9.2, 9.4, 9.5 and 9.6), which is in line with previous experimental reports [29, 128, 279, 366]. Whereas in randomly doped configurations, where there is an equal amount of Gd^{3+} in the bulk, a significant amount of oxygen vacancies do not segregate to the grain boundary. Therefore, as devices degrade over time and the Gd^{3+} concentration decreases in the bulk and increases in the grain boundaries, there will be a depletion of charge carriers in the bulks and thus an overall decrease in conductivity.

As there is accumulation of V_o in the grain boundary, oxygen diffusion increases due to the increase of charge carriers. However, visual inspection has shown that this is limited to the GB region, hence the high oxygen diffusion remains parallel to the grain boundary plane (Figure 9.9). Although the oxygen diffusion in GB regions is much higher than in the bulk regions, the activation energies are higher due to the energy required for an oxygen to leave the coordination sphere of an already undercoordinated cation atom. A higher activation energy for oxygen diffusion in

GB was measured by Avila-Paredes et al., for heavily Gd doped [367].The activation energies for oxygen in our bulk regions (Figure 9.9) are in line with experiments with heavily doped Gd samples (30%) having the highest Ea. As the dopant concentration decreases so does Ea [173, 332, 368, 369]. These results can be used to interpret the blocking effect of grain boundaries in GDC. Generally this blocking behaviour has been quantitatively described using the space charge layer model, which sees a positive electrostatic potential at the grain boundary core due to segregation of oxygen vacancies and oxygen vacancy depletion (space charge layers SCL) adjacent to the core; this induces a reduction in ionic conductivity [173, 278, 370, 371]. It is energetically favourable for large quantities of Gd^{3+} to segregate to the grain boundary, along with the majority of charge carriers (V_o). This depletion of charge carriers in the bulks results in the blocking effect of grain boundaries as diffusion is limited to the grain boundary planes (i.e. parallel to the GB plane). The simulated potential maps show this same behaviour for a number of grain boundaries, i.e. with a positive core potential along with depletion zones.

Positive space-charge potentials of 0.3 V have been obtained for polycrystalline ceria which is in good agreement with some of those calculated in this chapter [372]. Furthermore the blocking grain boundary effects depend also on temperature and the dopant content and type [373, 374, 375]. When the temperature is high enough, the grain boundary resistance appears to become negligible in comparison to the grain resistance, although this behaviour varies with dopant types and concentrations (usually 15 mol% regardless of the dopant type). Samples of heavily doped cerium oxides, prepared by Spark Plasma Sintering in the form of a high density (>98%) body with grain size of 15 nm, showed no grain boundary blocking effect and moreover the conductivity was demonstrated to be purely ionic [359].

9.8 Conclusions

In this chapter simulations on two different GDC systems were conducted, namely GB doped configurations (i.e. dopants segregated at the grain boundaries) which is an analogue for a degraded solid electrolyte of a SOFC device, and randomly

doped configurations (i.e. dopants randomly distributed between grain boundaries and bulks) which is an analogue for a freshly made material. It was found that segregation of Gd^{3+} to the grain boundaries is a thermodynamically favourable process and thus the randomly doped configurations will degrade into the GB doped configurations over time. Furthermore, as the oxygen vacancies are strongly attracted to Gd^{3+} the resulting high concentrations of Gd_2O_3 at the GB doped grain boundaries lead to a reduction in bulk oxygen transport and this transport is limited to the grain boundaries. Counter to this, it was found that a more uniform distribution of Gd^{3+} allows transport to occur in the bulks as well as in the grain boundaries as oxygen vacancies can also reside close to Gd^{3+} dopants in the bulk. Thus segregation of dopants over time is a significant factor in the blocking effect of grain boundaries in GDC, which was evaluated in terms of electrostatic potential.

10 Understanding Defect Distribution in UO_2 with Monte Carlo Simulations

10.1 Background

In general, understanding the distribution of atoms within a material is of crucial importance to understanding the material properties. For example, in battery or SOFC materials, the distribution of charge carriers has a massive impact on the conductivity of the material. In another example, the distribution of Li and La cations in lithium lanthanum titanate has been shown to have a significant impact on the conductivity of the material [129], with more disordered systems being more conductive [376, 377, 378]. Furthermore, in chapter 9, the distribution of Gd^{3+} in cerium oxide grain boundaries was shown to have a significant effect on the oxygen diffusivity of the system. In this example, "segregation" of Gd^{3+} to the interface prompted a decrease in conductivity in the grains of the material due to the segregation of charge carrying oxygen vacancies to the grain boundary.

In this thesis dopants/defects at surfaces and grain boundaries have been investigated, and the effect that these have on the material properties have been quantified. However in these examples, the distribution of the defects and dopants has been (in the case of the grain boundary chapters) random and (in the case of the surface chapters) based on the Ewald summation. In the case of the grain boundaries an average

energy difference was taken between randomly doped configurations and the segregated configurations and this was shown to be negative, indicating that segregation is energetically favourable. In chapters 4 - 6, the defect ordering energies indicated that surface segregation was favourable. Furthermore, defect segregation to interfaces is a common theme in the literature and the segregation of dopants to interfaces is shown in a range of materials [379, 380, 381, 382, 383, 384, 385, 386, 387, 388, 389, 390] as well as in CeO_2 [29, 345, 361, 362] and UO_2 [330, 331].

Defect clustering, grain boundary segregation and surface segregation has been studied with Monte Carlo in cerium oxide previously in several studies and it has been shown that there is a driving force for Gd^{3+} clustering and segregation to interfaces [380, 381, 382, 383]. In these examples Monte Carlo swap moves between Gd^{3+} and Ce were used to understand the distribution of Gd^{3+} within the material. To date no such study has been performed on uranium oxide or on polycrystalline surfaces and given the highly defective nature of uranium oxide, the distribution of defects, especially harmful fission products, is of crucial concern. There are important questions regarding segregation to the surface of the material, putting harmful products in potential contact with the environment.

In this chapter, Monte Carlo simulations have been used to study the distribution of dopants at the surfaces, grain boundaries and polycrystalline surfaces of Gd^{3+} doped UO_2. The aim of this chapter is to understand how extended structural defects affect the segregation of dopants in the material and to understand how "competition" between different structural defects effects the segregation behaviour of Gd^{3+}. For example, when studying the surfaces and grain boundaries there is only one interface to consider. In the case of polycrystalline surfaces (which will be refered to as T-Interfaces), there are three distinct extended structural defects, the surface, the grain boundary and the junction between them. Until now, most computational studies of segregation using Monte Carlo have only considered a single structural defect, however in nature there will be different structural defects with different segregation behaviours.

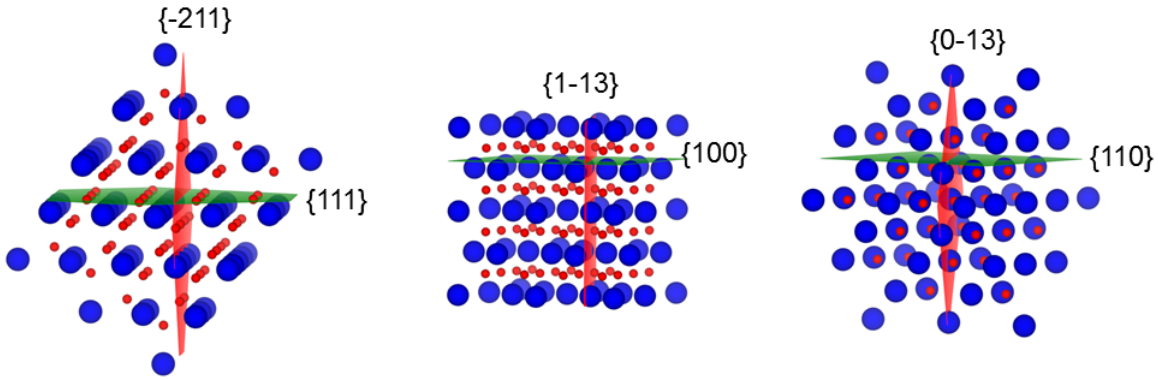

Figure 10.1: Bulk uranium oxide with the Miller planes that make up the T-interfaces in this study highlighted.

10.2 Calculation Details

A total of 9 configurations were used in this work. T-Interfaces which consist of the Σ3(211) tilt GB || {111}, Σ11(311) tilt GB || {110} and Σ5(310) tilt || {100} have been generated. The {111}, {110}, {100} surfaces and Σ3(211), Σ11(311) and Σ5(310) grain boundaries (Which all make up the T-Interfaces) have also been generated. This section has been split into two subsections, one will deal with the generation of the configurations and one will outline the Monte Carlo procedure.

10.2.1 Model Generation

The grain boundary and surface structures were generated using the METADISE code [153] as outlined in the methodology chapter. T-Interfaces were generated by introducing a vacuum gap to a grain boundary configuration perpendicular to the surface of interest. If the surface is flat, a grain boundary can terminate at the surface with a surface - grain boundary angle between 1 - 179 degrees. In this study only grain boundaries that terminate perpendicular to the surface plane have been studied (i.e. the angle between the surface and the grain boundary planes is 90). There is a finite number of planes that have this relationship and these were found manually using the crystal plane tool in VESTA. It was found that the Σ3(211), Σ11(311) and Σ5(310) grain boundaries terminate at the {111}, {110} and {100} surfaces respectively. This relationship can be visualised in figure 10.1 and the final structures can be visualised in figure 10.3.

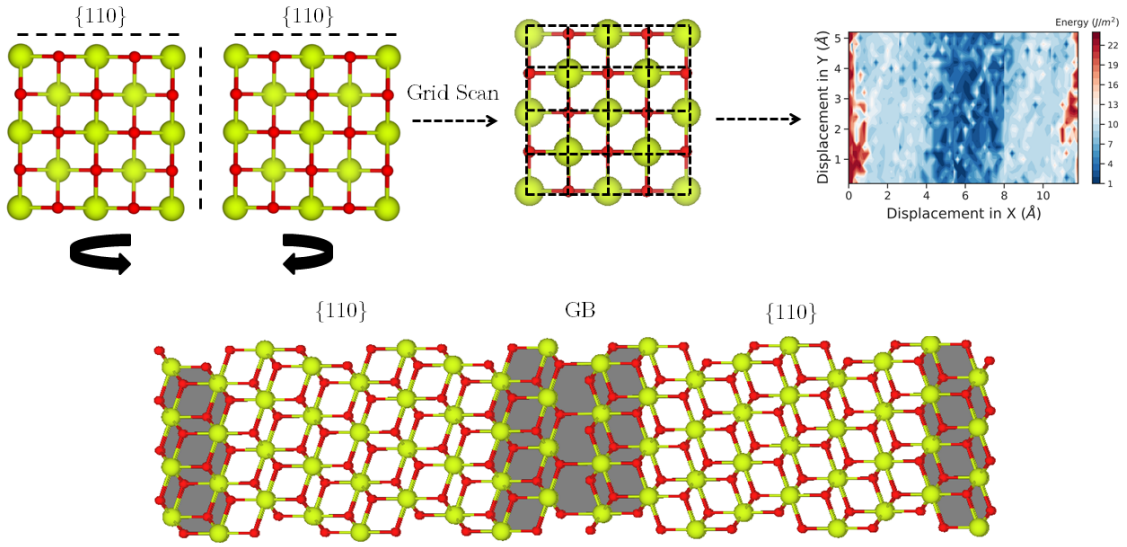

Figure 10.2: Schematic representation of T-Interface generation. Bulk crystals are reoriented so that the surface of interest is perpendicular to the grain boundary. A scan of the two grains is then performed and a low energy structure chosen.

All structures were thermally annealed using molecular dynamics between 300 - 2000 K over 10 ns. The grain boundaries were annealed using the NPT ensemble and the surfaces / T-Interfaces were annealed using the NVT ensemble.

Table 10.1: Total number of atoms in each grain boundary supercell and the total number of dopants and oxygen vacancies added.

Configuration	Number of Atoms
{111}	2304
{110}	3456
{100}	4608
Σ3(211)	2880
Σ5(310)	7680
Σ11(311)	7200
Σ3(211) - {111}	2880
Σ5(310) - {100}	7680
Σ11(311) - {110}	7200

10.2.2 Simulation Procedure

Gadolinium was introduced randomly to the starting configurations up to a concentration of 10% Gd^{3+} / U^{4+} substitutions. Gadolinium has a formal charge of 3+ and uranium has a formal charge of 4+, thus introduction of Gd^{3+} to the configuration results in a charged system. To account for this in chapters 8 and 9, oxygen vacan-

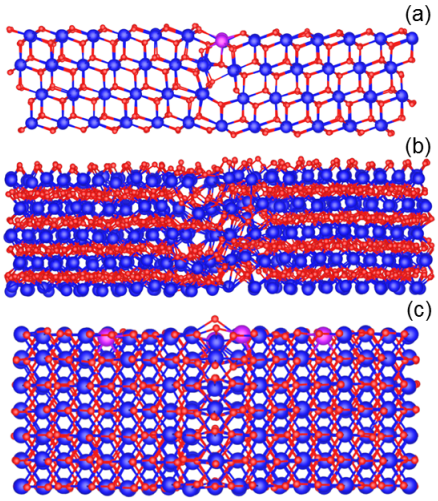

Figure 10.3: Structure of the Σ3(211) grain boundary with {111} surface, the Σ5(310) grain boundary with the {100} and the Σ11(311) grain boundary with the {110} surface and the

cies were added to account for the excess charge of the system. Oxygen vacancies represent a challenging problem to solve in Monte Carlo. Ideally, oxygen vacancies would be introduced to the system and the MC simulations could be run, with swaps between U^{4+} and Gd^{3+}. However in reality, the Gd^{3+} will quickly segregate to the oxygen vacancies and remain trapped there for the simulation because the smaller charge of the Gd^{3+} is happier than the U^{4+}. This results in an incredibly low swap acceptance rate and means billions of steps are required to generate enough statistics. Furthermore, if the oxygen vacancies do not move then the results of the simulation may not be representative anyway. A strategy that has been employed in the literature is to introduce "dummy atoms" as oxygen vacancies and swap these "oxygen vacancies" with oxygen atoms [380, 381, 383, 391]. However the codes that were used in these studies are unpublished. In this chapter the oxygen vacancy problem was treated by averaging and adding the excess charge to the uranium atoms in the system. No explicit oxygen vacancies were introduced to the system and the excess charge was accounted for by altering the charge of the atoms in the simulation. There are a number of ways that the charge can be "smeared" across the system, the excess charge could averaged across and added to the uranium, taken away from the oxygen or added/taken away from uranium and oxygen atoms. The alteration to the uranium charge as a function of Gd^{3+} concentration (up to 50 %)

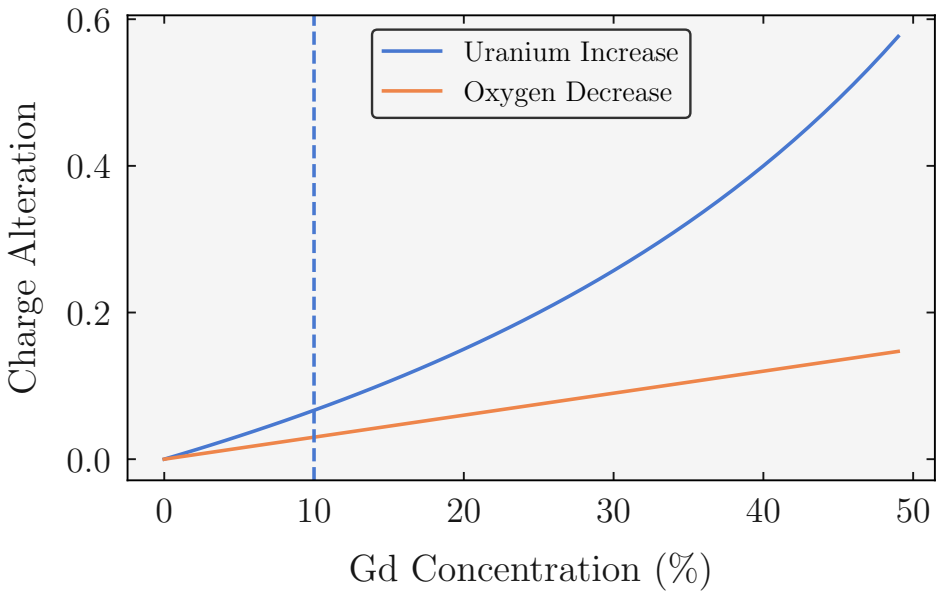

Figure 10.4: Schematic illustrating the relationship between Gd^{3+} unit cell concentration and the alteration to charge. The maximum Gd^{3+} concentration studied in this chapter (10 %) is marked with a dashed line.

is shown in figure 10.4. Two schemes were tested and the results are presented in section 10.3. Configurational and statistical was recorded every 10,000 steps so as to ensure that each sampled configurations was statistically different.

All Monte Carlo simulations were performed using the DL_MONTE code [391]. Monte Carlo simulations were employed within the NVT ensemble at temperatures of 500, 1000 and 1500 K. Two MC moves were used. Swap moves between Gd^{3+} and U^{4+} cations were used to study the segregation behaviour of Gd^{3+}, these moves allow Gd^{3+} to move unphysical distances and large numbers of configurations can be sampled. Translation moves were used for Gd^{3+}, U^{4+} and O atoms to allow system relaxations over time. Simulations were run for 300,000,000 steps and the acceptance rate for U^{4+} - Gd^{3+} swaps was 1%.

Following the Monte Carlo calculations, oxygen vacancies were added to configurations with an equilibrium distribution of Gd^{3+} (Taken from the MC calculations). These configurations were then simulated with molecular dynamics in order to determine the oxygen distribution. Molecular dynamics simulations were carried out in the NVT ensemble for 2 ns, using a timestep of 1fs and an 8.5 Å cutoff.

When discussing the segregation behaviour of these systems a different names will be used to describe distinct regions within the structure, namely;

- Surface - The layer of $U_{2-x}Gd_xO_2$ that is exposed to the vacuum gap of the simulation cell. i.e. the topmost layer of the structure.
- Grain Boundary - The central 10 Å region that separates two grains.
- T-Interface - The point where the surface and grain boundary meet.
- Bulk - The region of the $U_{2-x}Gd_xO_2$ structures that retain bulk properties.
- Sub-Surface - The region that separates the surface and the bulk, surface and T-Interface, grain boundary and bulk and grain boundary and T-Interface. This region is unique to the bulk because, while the coordination environment is identical to that of the bulk, this region is close enough to the interface to be influenced by it.

10.3 Charge Balance Schemes

Two methods were tried to account for the excess charge in the configuration and overcome the issue of Gd trapping:

- Scheme 1 - the charge was average across and added to the uranium atoms
- Scheme 2 - the charge was averaged across and taken away from the oxygen atoms.

Uranium undergoes oxidation from 4+ to 6+ [392, 393] as it undergoes oxidation. Without oxygen vacancies, these systems are essentially UO_{2+x} systems and within the context of the UO_{2+x} system, the charge would be accounted for with oxidation of the uranium atoms i.e. these smulations are equivelant to oxidising conditions.

Thus one way to account for the charge associated with the Gd^{3+} dopants is to average across and add the charge to the uranium atoms. However, in theory, at high concentrations of Gd^{3+} (figure 10.4), the charge on the uranium will be very high and thus this may introduce a driving force for the Gd^{3+} to segregate to the less coordinated interfaces, because the higher charge of the uranium will be more energetically stable with a higher coordination (bulk).

Scheme 2 is the second option investigated and in this case the charge was averaged across and removed from the oxygen atoms. There are more oxygen atoms and thus the charge is averaged over more atoms and the impact on individual interactions smaller. However the reduction of the oxygen charge in response to a higher oxygen stoichiometry makes less sense within the context of the UO_{2+x} system. Both of these schemes were investigated for the surface segregation calculations.

Figure 10.5 shows the Gd^{3+} number density in the 1% Gd^{3+} doped {111}, {110}, {100} and 10% Gd^{3+} doped {111}, {110} and {100} surfaces for both schemes. At low concentrations of Gd^{3+} (1%) after 300,000,000 steps and 30,000,000 accepted swaps, there is an identical Gd^{3+} distribution for both schemes. At high concentrations (10%), there is a very small deviation between the two schemes. When the charge is removed from the oxygen there is a slightly larger preference for Gd^{3+} to segregate to the bulk compared to when the charge is added to the uranium and vice versa with the surface. This is likely due to the higher charge of the uranium atoms in scheme 1 being more energetically favourable in the bulk where there is more oxygen, compared to the undercoordinated surfaces.

Without oxygen vacancies, these systems are essentially UO_{2+x} systems. Uranium oxide is prone to oxidation and the 5+ and 6+ oxidation states are found as UO_2 oxidises through various higher oxides (U_2O_5 and U_3O_8) to UO_3. Higher oxidation states of uranium have been reported in the literature and U^{5+} has been shown to be stable in the fluorite structure [394]. It has been shown in Gd^{3+} doped UO_2 that Gd^{3+} doping does lead to an increase in oxygen vacancy concentration, but that oxidation of U^{4+} does occur [395] Furthermore, analysis of Gd^{3+} doped UO_2 has

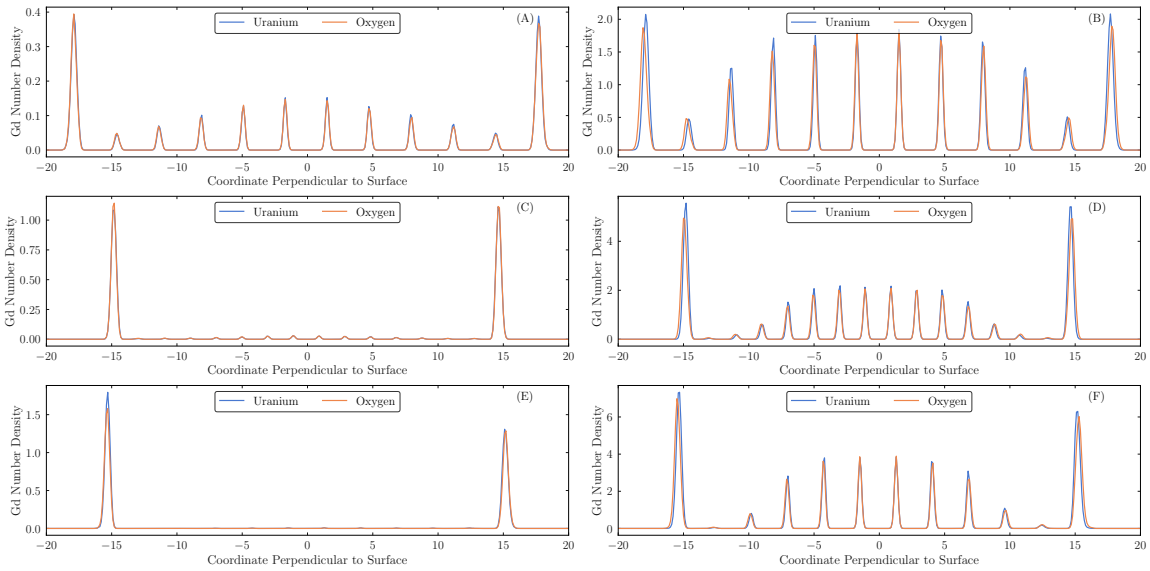

Figure 10.5: Average gadolinium distribution perpendicular to the surface in the 1% and 10% doped {111} (A, B), {110} (C, D), and {100} (E, F) surfaces. For clarity, the surfaces of the slab are o the extreme left and right of each plot. The Gd^{3+} number density for the system with the excess charge added to the oxygen atoms and uranium atoms are shown in blue and orange respectively.

shown the presence of U^{5+} and U^{6+} [396].

Based upon these results scheme 1 was chosen to account for the charge. This is because, within the concentration range studied there is a minimal difference in terms of Gd^{3+} distribution between the two scheme and because higher oxidation states are common for uranium within the UO_x system. Thus, in all subsequent calculations, the excess charge in the system was averaged across and added to the uranium atoms.

10.4 Surface Segregation

There are three distinct segregation regions in each of the surfaces which can be visualised by the Gd^{3+} number densities displayed for each surface in figure 10.6. Surface layer which corresponds to the first UO_2 layers, Sub-surface layer which corresponds to 1-3 UO_2 layers, Bulk in the centre, sitting between the sub-surface layers (located at 0 Å in the three surfaces displayed in figure 10.6).

There is a clear driving force for Gd^{3+} atoms to segregate to the surface, followed by

the bulk and then the sub-surface. The {100} and {110} surfaces behave in a similar manner while the {111} behaves slightly differently. There is a clear preference for Gd^{3+} segregation to the {110} and {100} surfaces with almost no segregation occurring to the sub-surface. In contrast in the {111} system there is preference for surface segregation but the difference between the surface and bulk concentrations is not as extreme as in the other surfaces. Furthermore there is some segregation to the sub - surface.

This can be explained by the uranium - oxygen coordination at the surface. Uranium at the {111} surface is formally 7 fold, whereas it is only 6 fold for the other two surfaces. Gadolinium is a 3+ ion in these simulations and energetically has a thermodynamic preference for a lower oxygen coordination. Thus in the more undercoordinated {110} and {100} surfaces there is a driving force for the Gd^{3+} to segregate there. This effect is lessened in the {111} system due to the higher coordination at the surface.

The segregation of Gd^{3+} in the three surfaces was studied across a concentration range between 1 and 10% Gd^{3+}. Figure 10.7 shows the concentration of Gd^{3+} in each region (surface, sub-surface and bulk) across this unit cell concentration range at 500, 1000 and 1500 K. The {110} and {100} surfaces are similar, with a significant preference for Gd^{3+} surface segregation, followed by the bulk and then the sub-Surface. The trend is also true on the {111} surface although the difference between the three regions is less pronounced. Sub-Surface depletion of dopants is reported in the literature [397].

In this work the highest Gd^{3+} concentration studied was 10%. Within this concentration range the surface saturation point has not been identified, ie. the point where the surface cannot hold anymore Gd^{3+} atoms and the regional concentration would level off with increasing Gd^{3+} cell concentration.

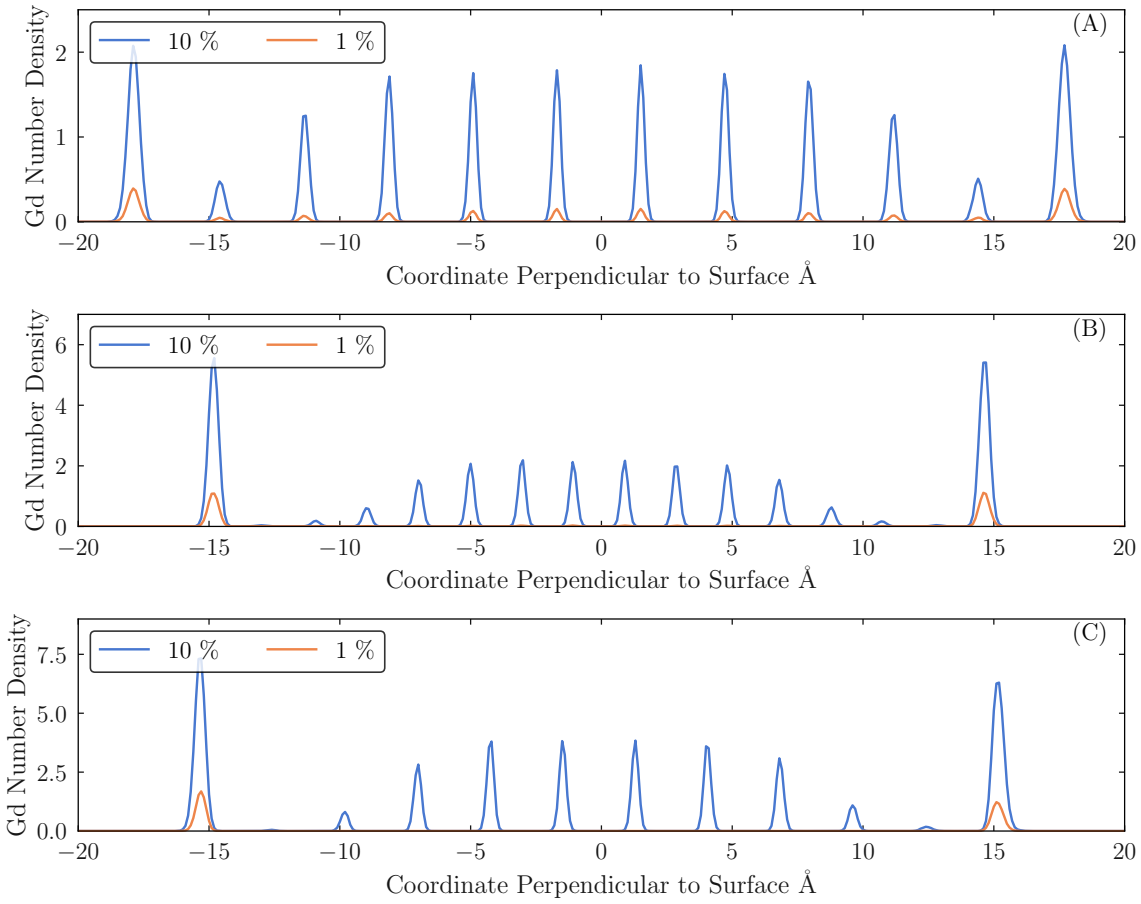

Figure 10.6: Average gadolinium distribution perpendicular to the surface in the {111} (A), {110} (B) and {100} (C) surfaces. For clarity, the surfaces of the slab are on the extreme left and right of each plot. The lowest (1%) and largest (10%) concentrations have been plotted in orange and blue respectively.

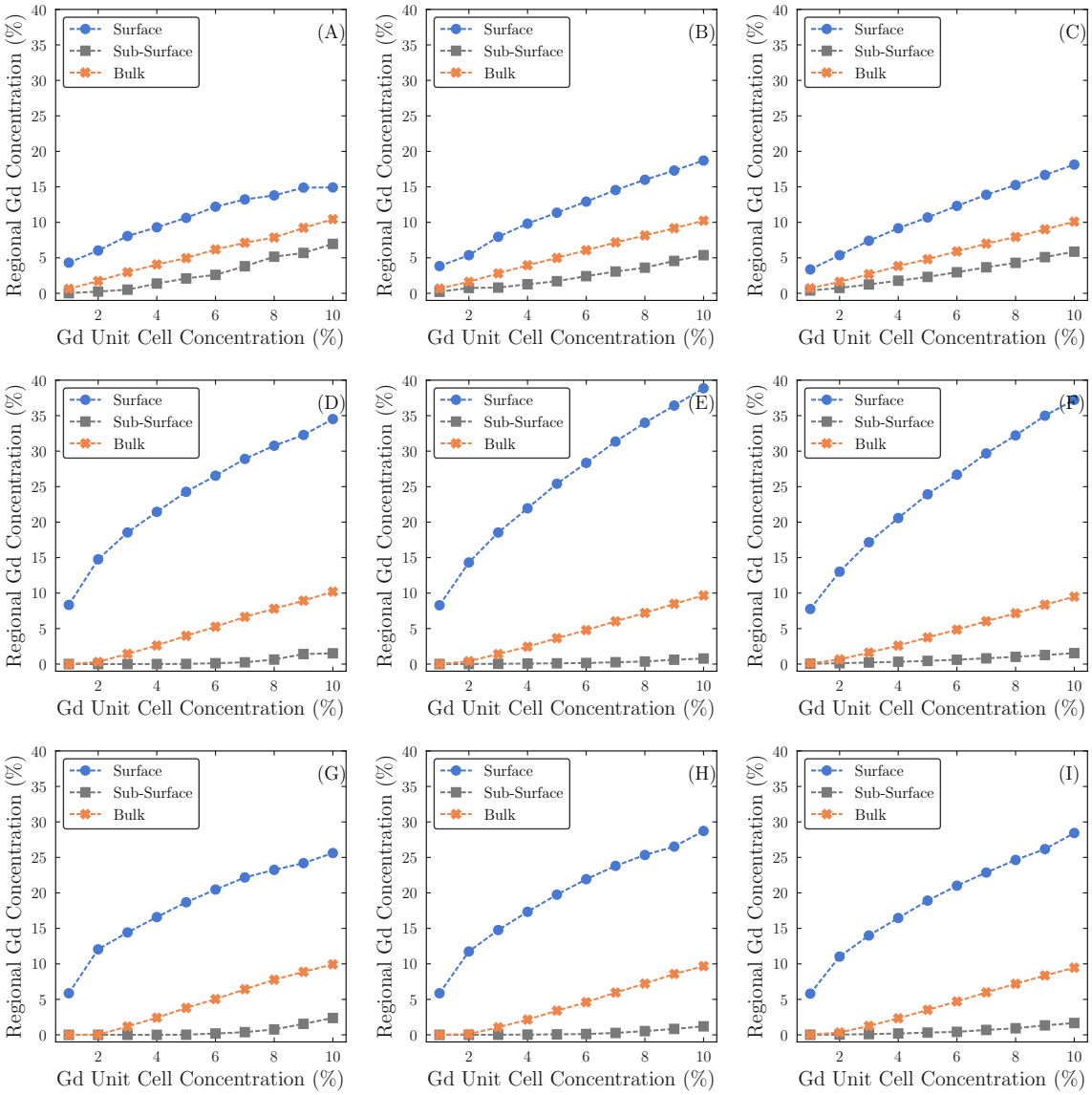

Figure 10.7: Gadolinium distribution in the {111} surface at 500, 1000 and 1500 (A,B and C), the {110} surface at 500, 1000 and 1500 K (D, E and F) and the {100} surface at 500, 1000 and 1500 K (G, H and I)

10.5 Grain Boundary Segregation

As with the surfaces, there are three distinct regions in the grain boundary configurations, although unlike the surfaces the differences between the systems is much more pronounced. In each grain boundary structure there is a clear difference in segregation behaviour between the grain boundary core, the "sub-surface" (Or space charge layer) that links the core to the bulk and the bulk. There is a clear preference for segregation to the grain boundary core, followed by the bulk and then the sub-surface. This is most pronounced in the $\Sigma3(211)$ grain boundary and least pronounced in the $\Sigma11(311)$ grain boundary. The Gd^{3+} density profiles at the grain boundary are not symmetric, this is because the grain boundary structures are not symmetric in terms of oxygen coordination. For example, the $\Sigma5(310)$ (figure 10.8B) has a pronounced peak on the right of the grain boundary, this corresponds to a layer of cations with a smaller oxygen coordination number.

The regional concentration as a function of Gd^{3+} unit cell concentration for the grain boundaries, is remarkably different to that of the surfaces. In all cases, across the concentration range, Gd^{3+} segregates preferentially to the grain boundary, bulk and sub-surface. The $\Sigma3(211)$ grain boundary has the most pronounced segregation effect to the grain as there is a large difference between the grain boundary Gd^{3+} concentration and the bulk / sub-surface. In contrast there is only a very small difference between the three regions in the $\Sigma5(310)$ and $\Sigma11(311)$ grain boundaries. In the $\Sigma5(310)$ system the three regional concentrations increase linearly with increasing total Gd^{3+} concentration, whereas in the $\Sigma11(311)$ the three regional concentrations increase sharply at low total Gd^{3+} concentrations and then they level off at high total Gd^{3+} concentration. The difference between the behaviour of the $\Sigma3(211)$ GB and the other two GBs is due to the cation coordination at the boundary. In the $\Sigma3(211)$, cations to the left and right of the central core cation layer are 7 fold coordinated and Gd segregation occurs at high concentrations. This is shown in figure 10.8 A, there are two peaks to the left and right of the central layer. In contrast, the cation sites in the $\Sigma5(310)$ and $\Sigma11(311)$ grain boundaries are all 8 fold coordinated and thus there is less of a thermodynamic driving force

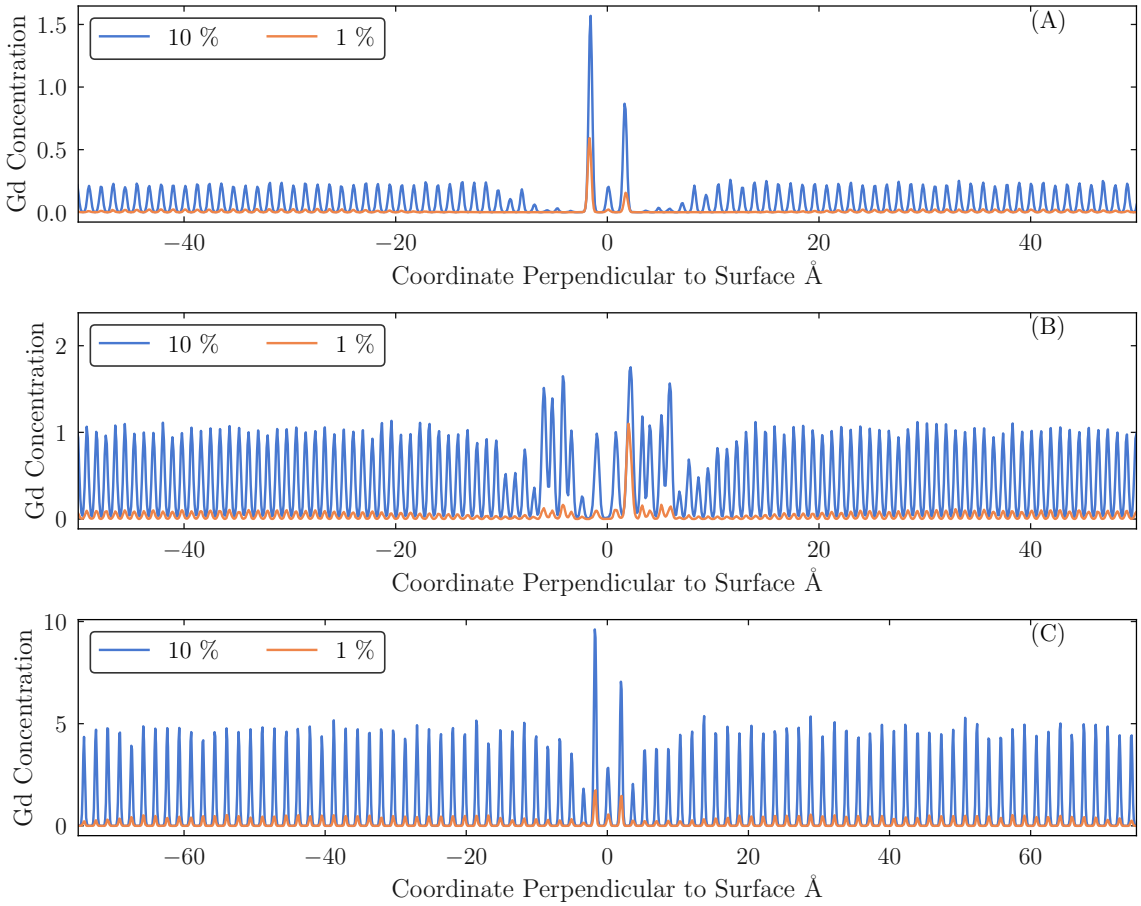

Figure 10.8: Average gadolinium distribution perpendicular to the grain boundary in the Σ3(211) (A), Σ5(310) (B) and Σ11(311) (C) grain boundaries. For clarity, the grain boundary is located at the centre each plot. The lowest (1%) and largest (10%) concentrations have been plotted in orange and blue respectively.

for segregation.

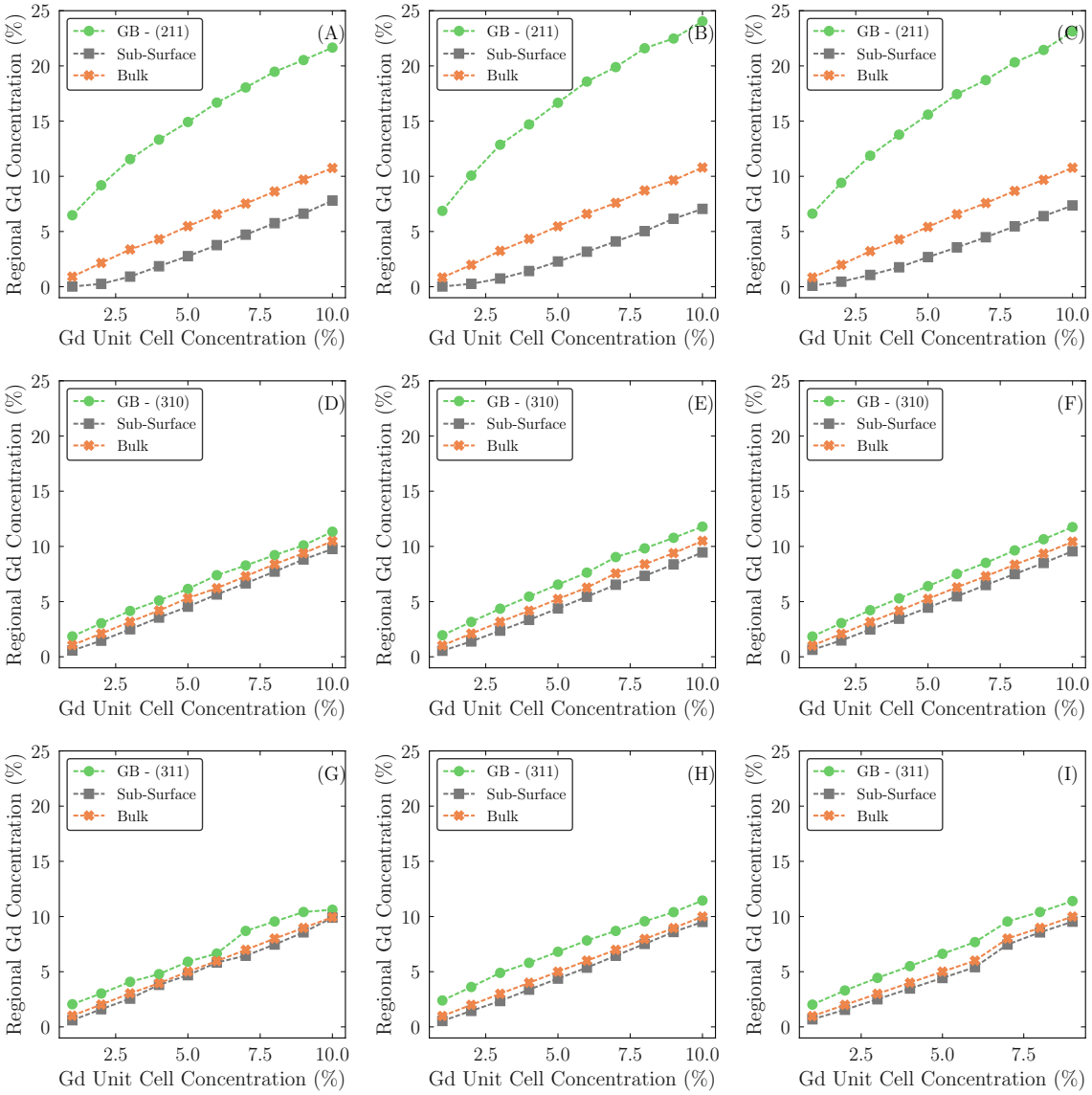

Figure 10.9: Gadolinium distribution at the {111} grain boundary at 500, 1000 and 1500 K (A,B and C), the {211} grain boundary at 500, 1000 and 1500 K (D, E and F) the {311} grain boundary at 500, 1000 and 1500 K (G, H and I) and the {210} grain boundary at 500, 1000 and 1500 K (J, K and L)

10.6 T-Interface Segregation

Combining interfaces to form T-Interfaces has interesting effects on the segregation behaviour. Regional Gd^{3+} concentration follows the order T-Interface > Surface > Grain Boundary > Bulk > Sub-Surface from highest to lowest in terms of Gd^{3+} concentration. This is illustrated in figure 10.10, where there brighter regions show the areas of high concentration and the darker regions, areas of low concentration. The three structures show similar behaviour in terms of the overall trends but there are differences relating to the degree of segregation.

The $\Sigma3(211)$ / {111} structure has very clearly defined regions, with distinct separation between them. The order of segregation is very clear from the brightness of the heatmap. The $\Sigma5(310)$ / {100} shows much greater segregation to the T junction and surface compared to the GB and bulk, which look similar in terms of brightness. The $\Sigma11(311)$ / {110} structure shows a huge preference for segregation to the T junction, followed by the surface, with the bulk and GB being comparably low in terms of Gd^{3+} concentration. Interestingly, there is a depletion region that separates the different interfaces of the structure from the bulk.

The segregation behaviour has been quantified at all concentrations in Figure 10.11. The concentration of Gd^{3+} in the surface and T-Junction increases sharply at the lower concentrations and begins to level off at the higher concentrations. Inc contrast the bulk, grain boundary and sub surface concentrations increases bluntly at lower concentrations and then sharply at the higher concentrations. If the full 0 - 100% concentration range was studied, at some point the concentration of each region would meet.

The grain boundary regions in the $\Sigma5(310)$ / {100} and $\Sigma11(311)$ / {110} structures behave very similar to the bulk and the segregation in these structures is dominated by the surface and T. In contrast the grain boundary in the $\Sigma3(211)$ / {111} structure behaves in a similar manner to the surface. This can be explained by the coordination of cations in the structure. The {111} surface is 7 fold coordinated

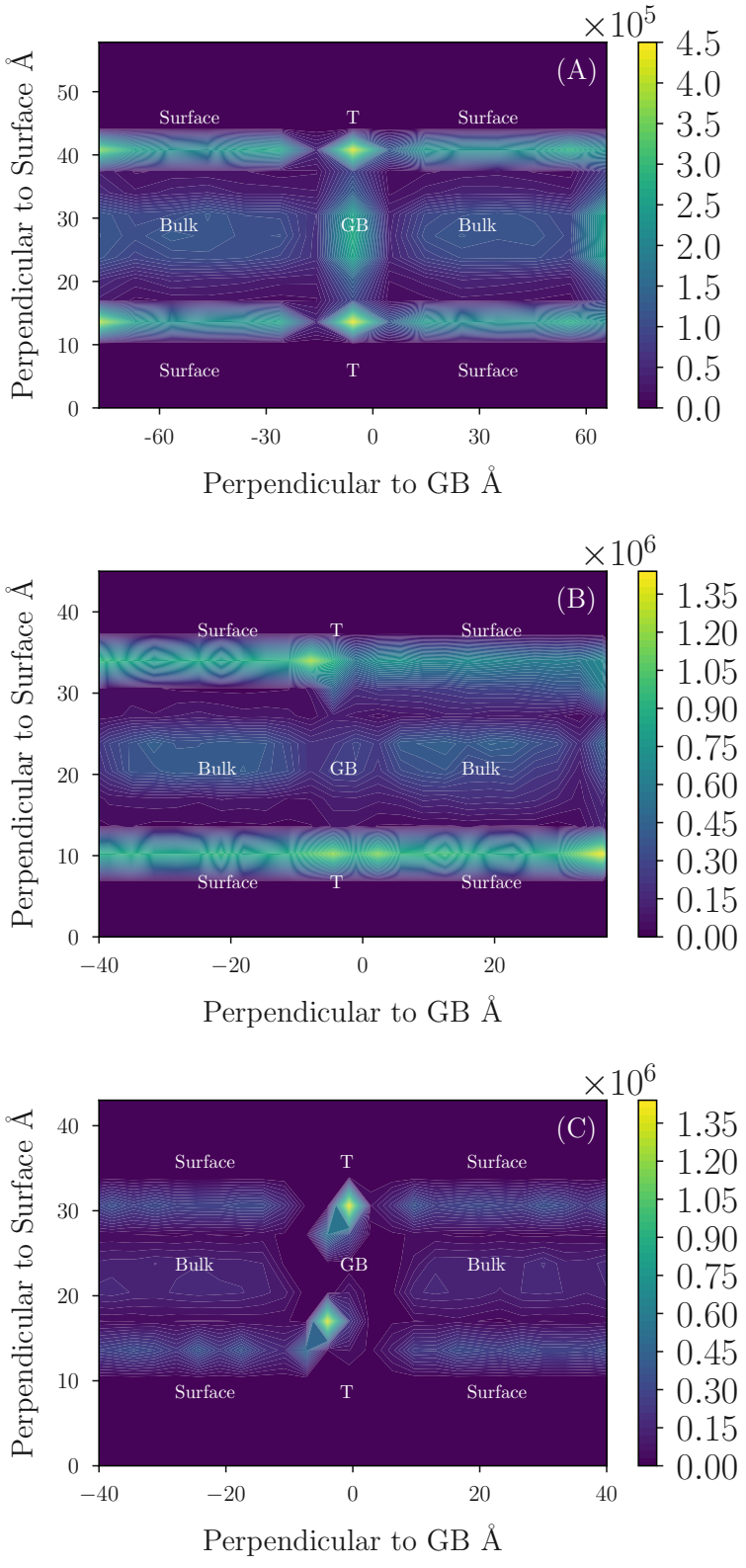

Figure 10.10: Gadolinium distribution in the {111} surface, Σ3(211) T-Interface (A), {110} surface, Σ11(311) T-Interface (B) and {100} surface, Σ5(310) T-Interface (C) in two dimensions. Regions with high concentration are shown in blue and regions with low concentration are shown in white.

whereas the {110} and {100} surfaces are 6 fold coordinated. In these two surfaces it is more energetically favourable for the 4+ uranium atoms to be swapped to the bulk and the 3+ gadolinium atoms to segregate to the surface. In the Σ3(211) / {111}, the higher surface coordination reduces the driving force for Gd^{3+} segregation to the surface to some degree. Thus segregation occurs to the region that is "next in line" in terms of solubility - the grain boundary.

The different "sub-surface" regions were not separated out depending on their location and where treated as a single region. An interesting avenue of research would be to investigate if the concentration in the grain boundary - bulk sub-surface is different to the T-Interface - grain boundary sub-surface.

The bulk Gd^{3+} concentration averaged across the 9 configurations are shown in figure 10.12 along with errorbars. There is a small but consistent variation at in the bulk concentration. The T-Interface configurations give rise to most of the error in the bulk concentration in figure 10.12. This is possibly due to the size of the simulation cells, the T-Interface configurations have a large interface region, the slab method and PBCs means that there are two surface regions and two grain boundary regions. Thus the simulation cells may not be large enough to give a large enough bulk region.

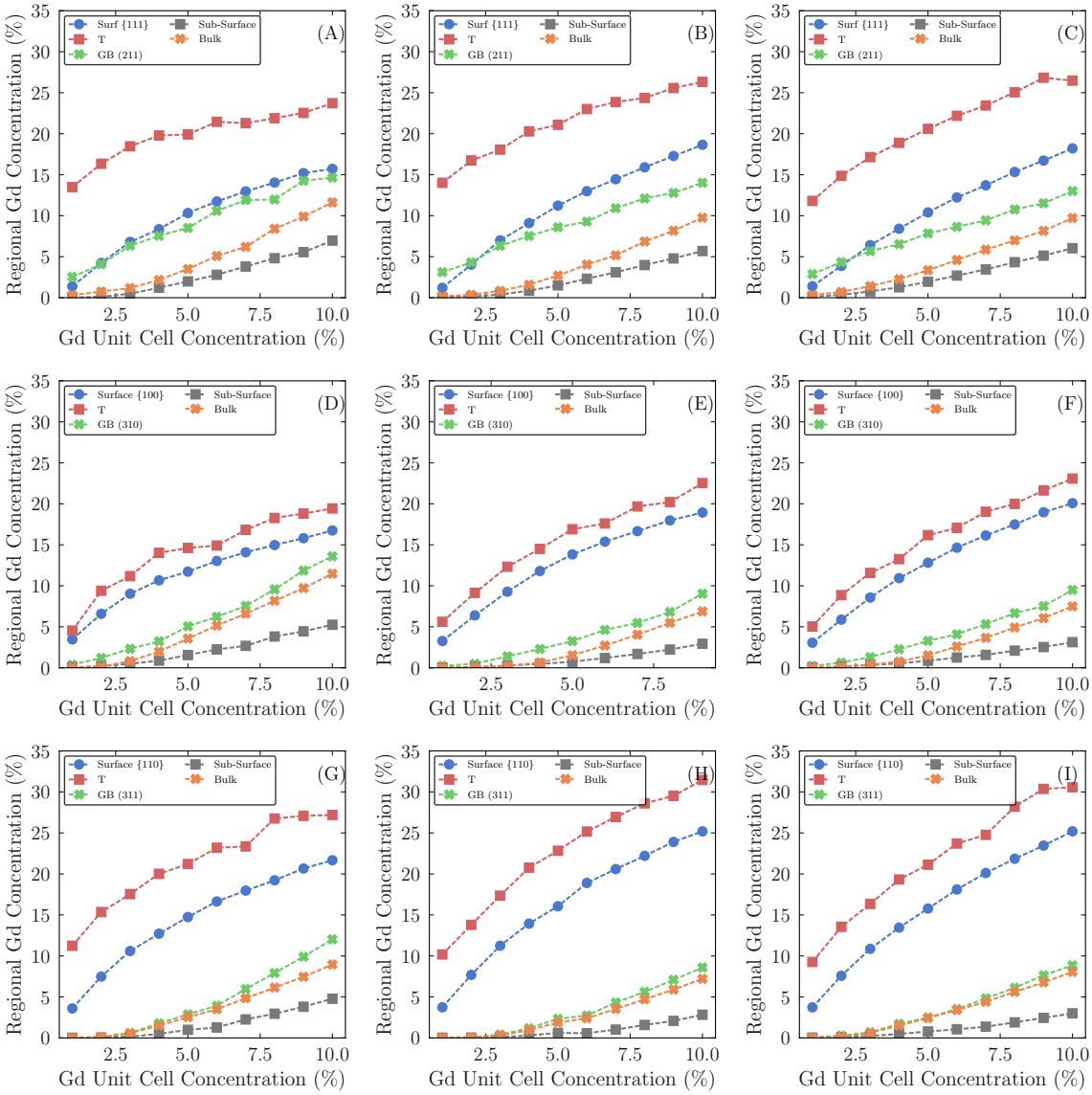

Figure 10.11: Gadolinium distribution in two dimensions showing the grain boundary and surface in the Σ3(211) GB / {111} surface (A), Σ5(310) GB / {100} surface (B) and Σ11(311) GB / {110} (C). For clarity, the grain boundary is located at the centre each plot.

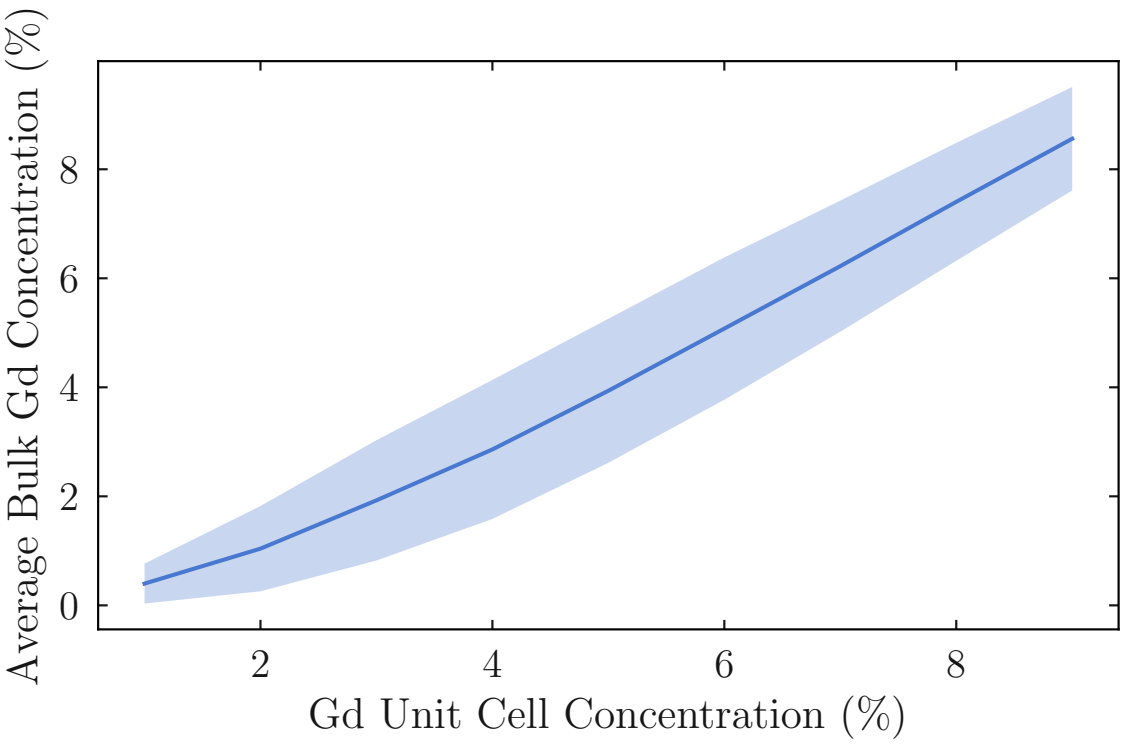

Figure 10.12: Average bulk concentration across the 9 configurations. The shaded regions show the standard errors calculated from the standard deviation of the mean.

10.7 Oxygen Vacancy Segregation

Once an equilibrium distribution of Gd^{3+} was calculated from Monte Carlo calculations, oxygen vacancies were introduced and these structures were simulated with molecular dynamics in order to establish an equilibrium oxygen vacancy distribution. The change in oxygen stoichiometry in the different regions was calculated alongside the average cation coordination number in order to establish if oxygen vacancies segregate to the different regions.

In the surface structures oxygen vacancies segregate preferentially to the surface, followed by the bulk and then the sub surface. This is in line with the relative concentrations of Gd^{3+} in each region and the average coordination number which shows that the Gd^{3+} in each system has a lower average CN than the uranium. Furthermore, based upon the results in chapters 9 and 10, it is clear than oxygen vacancy segregation is predicted to be controlled at least in part by the dopants distribution.

This trend also holds for the grain boundary structures and oxygen vacancies segregate to the grain boundary followed by the bulk and then the depletion. As discussed in chapter 9, defect segregation to the grain boundaries, has been observed experimentally and is detrimental to material properties [29, 360]. As dopants, segregate and to the grain boundaries, they may contribute to an increase in grain boundary resistance to the transport of oxygen. This results in a reduction in the conductivity of polycrystals compared to single crystals [29, 345, 361, 362]. The reason for this reduction in conductivity is likely due to the space charge effect [370], wherein oxygen vacancies segregate to the grain boundary core and deplete in the regions adjacent to the grain boundary core. Thus there is a depletion of charge carriers either side of the boundary and transport across the boundary is hindered. Our results show clearly segregation of Gd_2O_3 to the grain boundary and some depletion in the adjacent regions.

The T-Interface structures are much more complicated. In all three structures there is 3-5% increase in the oxygen vacancy concentration in each of the three interface regions. This indicates that in these highly defective structures the vacancies are more evenly distributed.

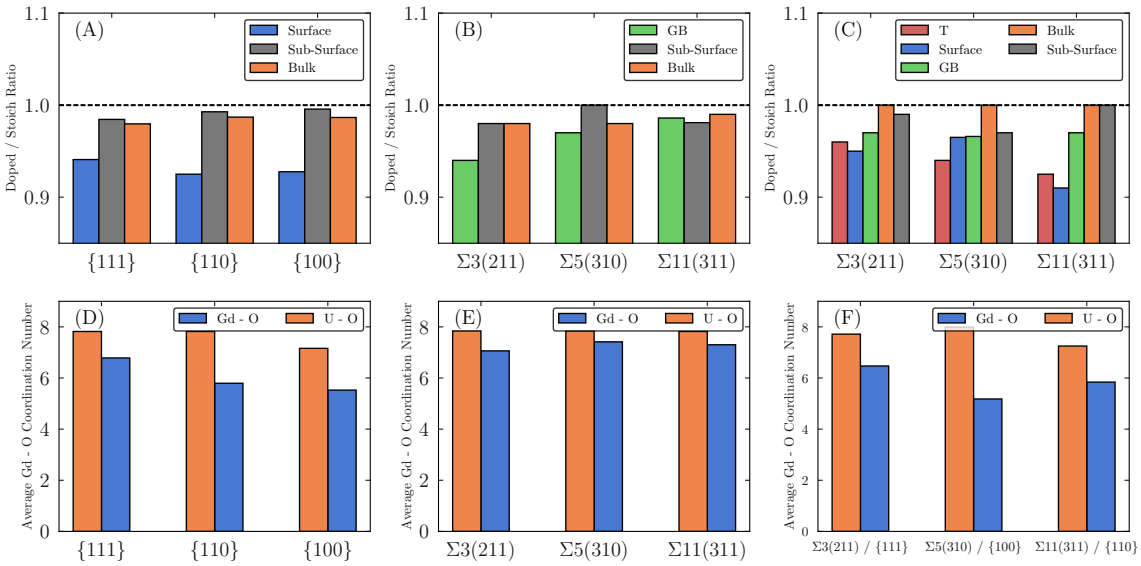

Figure 10.13: Ratio of oxygen concentration between the doped and stoichiometric structures (%) for each region of the surfaces (A), grain boundaries(B) and T-Interfaces (C) at a temperature of 1000 K and a Gd^{3+} concentration of 5 %. Cation - Oxygen coordination number in the surfaces (D), grain boundaries(E) and T-Interfaces (F) at a temperature of 1000 K and a Gd^{3+} concentration of 5 %

10.8 Conclusions

In this chapter Monte Carlo simulations have been used to study the distribution of Gd^{3+} in $U_{1-x}Gd_xO_{2-x}$. Three extended structural defects were studied, namely, surfaces, grain boundaries and T-Interfaces. Cation coordination seems to play a large role in the segregation of Gd^{3+} in these interfaces. The {110} and {100} surfaces are less coordinated than the {111} surface and thus in these surfaces there is a greater degree of segregation of Gd^{3+} to the surface, compared to the {111}. Cation coordination also plays a role in the segregation behaviour of grain boundaries. The Σ5(310) and Σ11(311) boundaries cations are approximately 7-8 fold coordinated and thus the segregation behaviour is less extreme compared to the surface, with appreciable concentrations of Gd^{3+} segregating to the bulk and sub-surface regions. Whereas in the Σ3(211) boundary the cations are 6 fold coordinated and there is considerably more segregation to the grain boundary relative to the bulk and sub surface. When surfaces and grain boundaries are combined, the cation coordination again seems to drive the segregation behaviour. The Σ3(211) / {111} interface has the least defective surface and most defective grain boundary studied. Thus there are comparable levels of segregation to the surface and grain boundary.

The T-Interface is the most defective and under coordinated part of the structure and thus there is more segregation occurring there. The other two systems contain more defective surfaces and more stable grain boundaries, thus the segregation is driven by the surface and T-Interface.

11 Conclusions and Future Work

The main focus of this thesis is to improve our understanding the effect of defects in fluorite oxides. Structural defects (Surfaces, grain boundaries and T-Interfaces), chemical defects (Dopants) and environmental defects (Molecules such as water) have been investigated in two common fluorite oxides, CeO_2 and UO_2. Chapter 5 and 6 describe, using density functional theory the adsorption of water and carbon dioxide at the surfaces of cerium oxide doped with trivalent cations and discuses the effect of this interaction on the particle morphology. Chapter 7 describes, using density functional theory, the adsorption of phosphate anions at surfaces of cerium oxide with varying oxygen and hydrogen stoichiometry. Chapter 8 describes, using molecular dynamics simulations, the structural and transport properties of fluorite CeO_2 and UO_2 grain boundaries and Chapters 9 and 10 describes the effect of dopants on the properties of these grain boundaries. Finally, chapter 11 describes, using Monte Carlo simulations, the effect of interfaces on the segregation of dopants with uranium oxide. The aim of this chapter is to draw together the conclusions from each of these areas and suggest future work that could be carried out, before drawing some general conclusions for the entire project and thesis.

Water Adsorption at CeO_2 Surfaces

Initially the work in this chapter was limited to water adsorption at stoichiometric surfaces of CeO_2 and explored how the adsorption of water affected the relative stability of the three surfaces. It was found that each surface has a different interaction with water and adsorbed water molecules have a modest impact on the morphol-

ogy of ceria. Adsorbed water at low temperatures and high water partial pressures promotes a change of surface stability and the more reactive, less stable {100} and {110} surfaces are stabilised relative to the {111} and are consequently expressed in the particle morphology. Reducing the surface or doping the surface with trivalent Gd^{3+}, Sm^{3+} and Y^{3+} cations increases the affinity of the surface for water compared to the stoichiometric surfaces. Adsorption is strongest on the {100} surface and thus at low temperatures and high water partial pressures there is a high {100} surface area relative to the {111}. Furthermore, comparing surfaces with equal oxygen stoichiometries, Reduced and Doped surfaces shows that dopants decrease the affinity of the {111} and {110} surfaces for water while increasing the affinity of the {100} for water. Consequently, dopants increase the temperature and pressure range where the {100} surface is stabilised.

This work could be extended in a number of ways. Firstly, dopant concentration effects have been ignored and only one concentration of dopant was considered, thus a logical extension of this work would be to increase the dopant concentration and evaluate the effect that it has on water adsorption. This work was aimed at understanding how water adsorption effects the morphology of ceria. Only the three most common surfaces of ceria were investigated. One of the key findings of this work was that water can stabilise the less stable, more reactive surfaces with respect to the more stable surfaces and thus cause them to be expressed in the morphology. Further study could investigate how water adsorption on other surfaces affects their stability relative to the more stable surfaces.

Carbon Dioxide at CeO_2 Surfaces

Initially the work in this chapter was limited to associative adsorption of carbon dioxide on the surfaces of CeO_2 and explored how carbonates at the surface affected the relative stability of the three surfaces. It was found that there were vast differences in the adsorption behaviour between the three surfaces, with the {100} surface being stabilised vastly more than the {111} surface. As a result of the different adsorption energies, the {100} surface is stabilised and expressed in the particle

morphology across a much wider temperature and pressure range compared with water in chapter 5. Reducing or doping the surface with trivalent Gd^{3+}, SM^{3+} and Y^{3+} cations increases the affinity of the surface for carbon dioxide compared to the stoichiometric surface. When comparing surfaces with equal oxygen stoichiometries (Doped and Reduced) there is very little change in the adsorption energy and thus the morphology.

This work could be extended in a number of ways, as with chapter 5, only a single dopant concentration has been investigated and thus increasing the dopant concentration is a logical extension to this work. Studying different surface terminations is again a good avenue to explore as the adsorption of carbon dioxide will have different effects on the stability of each surfaces.

The adsorption of carbon dioxide on its own is only likely to occur under carefully controlled experimental conditions and thus there is likely going to be competition at the surface with water. Thus, a possible extension to this work would be to investigate the adsorption of both water and carbon dioxide at the surface in order to determine if there is competition between the two for adsorption sites, and if so, which species the surface has a stronger affinity for. In chapter 5, molecular dynamics calculations of nanoparticle evolution in the presence of water, performed by collaborators at the University of Kent were discussed. Due to time constraints this was not undertaken for the carbon dioxide, however it presents a clear avenue for future work.

Phosphate at CeO_2 Surfaces

This chapter focussed on how cerium oxide surfaces, with differing surface compositions affected the adsorption of phosphate anions. Oxygen deficient ceria interacts strongly with phosphate anions compared to hydroxylated ceria. However this interaction depends strongly on surface structure. Specially, whether nanoceria consist of {111}, {110} or {100} surfaces. The strongest interaction occurs between {100} surfaces and phosphate due to a large surface reconstruction, which suggests that

ceria nanocubes bind phosphate strongly, which will inhibit $Ce^{4+/Ce3+}$ redox and nanozyme activity to a greater extent compared to ceria nano-octahedra comprising {111} surfaces, as these display much weaker interactions with phosphate.

Due to the complexity of the surfaces, the surface method was used. This meant that the phase diagrams and the particle morphology could not be evaluated. The calculations could be repeated with care using the slab method, or a method could be developed to generate phase diagrams from the surface method calculations. Furthermore, only a single concentration of phosphate was studied and in reality there will be multiple phosphate anions at the surface, interacting with both the surface and with each other.

Fluorite Grain Boundary Structure

This focused on the structure of the grain boundary of two materials, uranium oxide and cerium oxide. Going forward a larger sample size is needed to better understand the transport properties of not just fluorite materials, but polycrystalline materials in general. One approach would be to generate a large numbers of polycrystalline simulation cells with varying grain size using Voronoi tessellations. These would then be taken and simulated with molecular dynamics to determine their transport properties in order to build a dataset with the transport properties of thousands of polycrystals with different combinations of grain boundaries. This dataset would then be employed within a machine learning model to predict the properties of a much larger dataset, consisting of millions of polycrystals. There are several hurdles that need to be overcome to achieve this, simulating thousands of polycrystalline models with molecular dynamics is feasible with current computational power but represents a significant amount of computational power. Furthermore, a method to describe a polycrystal that can be used to relate properties of the polycrystal e.g. diffusion coefficient or activation energy to the structure (and thus the internal microstructure) of the polycrystal. For example, properties like the density, dimensionality or the variance in the bond lengths or atomic volumes within the structure are properties that are used in current ML models to characterise a structure and

represent a possible avenue to explore.

Oxygen transport at UO_2 and CeO_2 Grain Boundaries

Chapter 8 focused on how fission products at uranium oxide grain boundaries affects the oxygen transport and thus corrosion of the material. It was found that the segregation of these defects to the grain boundary was energetically favourable and thus segregation of fission products will occur over time. Oxygen vacancies follow the fission products and thus segregate to the fission products, facilitating increased oxygen diffusion in those regions.

Chapter 9 focussed on how gadolinium dopants at cerium oxide grain boundaries affected the oxygen transport of the material. It was found that segregation of Gd^{3+} to the grain boundaries is a thermodynamically favourable process and thus the randomly doped configurations will degrade into the grain boundary doped configurations over time. Furthermore, as the oxygen vacancies are strongly attracted to Gd^{3+} the resulting high concentrations of Gd_2O_3 at the doped grain boundaries lead to a reduction in grain interior oxygen transport and this transport is limited to the grain boundaries. Counter to this, we find that a more uniform distribution of Gd^{3+} allows transport to occur in the grain interiors as well as in the grain boundaries as oxygen vacancies can also reside close to Gd^{3+} dopants in the grain interior. Thus segregation of dopants over time is a significant factor in the blocking effect of grain boundaries in GDC, which was evaluated in terms of electrostatic potential.

Chapter 9 built on chapter 8 by considering different dopant distribution schemes and different dopant concentrations however it did not consider a distribution of dopants that was at thermodynamic equilibrium. The concept of studying dopant distribution was discussed in chapter 10 and the studies conducted in chapters 8 and 9 would benefit from studying the distribution of dopants using Monte Carlo. The tools that were utilised in chapter 10 were not available when the work was being conducted for chapters 8 and 9 which is why this was not performed during this project. This represents and avenue of future work for both chapters 8 and 9.

Furthermore, defects in uranium oxide are wide ranging and thus combinations of fission products are inevitable, a useful avenue to explore would be investigate how different combinations of impurities effect the properties of the material. Likewise, in cerium oxide, different trivalent dopants have been used to improve the transport properties and thus different dopants could be studied.

Dopant Segregation to UO_2 Interfaces

This chapter focussed on how gadolinium dopants segregate to different interfaces in uranium oxide, and for the first time introduces the concept of polycrystalline surfaces. It was found that dopants readily segregate to the surfaces and grain boundaries of uranium oxide when looked at in isolation. When combined (In I-Interfaces), dopants prefer to segregate to the surface and T-interface before segregating to the grain boundary and then to the bulk and sub surface regions.When oxygen vacancies were introduced they segregate to the Gd.

This chapter represents an early study on the effect of T-Interfaces on the properties of oxide surfaces. In the future more interfaces should be generated in order to increase the sample size and thus make the predictions more universal. The method for dealing with the oxygen vacancies needs to be addressed further. In this work, the charge was added to the uranium atoms, in the future, a method to allow oxygen vacancies to be added to the system should be tried. For example. other studies have used dummy atoms in place of oxygen vacancies and swaps were performed between these dummy atoms and the oxygen atoms. This approach could be utilised in the future in order to cope with the poor swap rates that are associated with oxygen vacancies in Monte Carlo simulations. It would be interesting to determine if this method would give a different result to the charge smearing approach used in this work. Furthermore, the T-Interface configurations used in this work gave a slightly smaller bulk Gd concentration that the surfaces and grain boundaries. In future, larger simulation cells could be used to see if this is due to the size of the configurations.

Thesis Conclusions

In this thesis structural (Surfaces, Grain boundaries and T-Interfaces) and chemical impurities were studied in two metal oxides, UO_2 and CeO_2. The ultimate goal was to understand how a combination of these defects affects the properties of each material. The ultimate conclusion of this thesis is that there is a complicated relationship between structural defects and chemical defects and that in real systems, the effect of both combined, must be considered. In the final chapter, the segregation of Gd to the interfaces of UO_2 was discussed. There is a thermodynamic driving force for dopants to segregate to the surfaces, thus the influence of dopants on the adsorption properties of materials must be considered. For example in this thesis the adsorption of atmospheric and environmental molecules on the surfaces of CeO_2 was discussed, it was found that the strength of adsorption was altered by the presence of dopants at the surface. Another example in this thesis related to grain boundaries, in grain boundaries it was found that defects at the boundary alter the transport properties and structure of both UO_2 and CeO_2.

In conclusion the work presented in this thesis has explored the interplay between chemical defects and structural defects in uranium oxide and cerium oxide for a wide array of applications. This work has demonstrated how defects control the important properties of CeO_2 and UO_2. Through the use of theoretical calculations, it was possible to gain a greater understanding of the formation, stability and structure of these defects, what external factors influence them, and how they determine the chemistry of both materials. Furthermore, through the use of computational modelling it was possible to predict new properties, which will aid future research.

References

[1] M. Roser and E. Ortiz-Ospina. Global rise of education. *Our World in Data*, 3(7), 2019. https://ourworldindata.org/global-rise-of-education.

[2] A. Kressig. Global power plant database. *Global Energy Observatory*, 358(7): 191–212, 2018. http://datasets.wri.org/dataset/globalpowerplantdatabase.

[3] D. Luthi, M. Le Floch, B. Bereiter, T. Blunier, J. M. Barnola, D. U. R. Siegenthaler, J. F. H. Jouzel, K. Kawamura, and T. F. Stocker. High-resolution carbon dioxide concentration record 650,000-800,000 years before present. *Nature*, 7183(7):379–382, 2008. doi: 10.1038/nature06949.

[4] J. A. Higgins, A. V. Kurbatov, N. E. Spaulding, E. Brook, D. S. Introne, L. M. Chimiak, Y. Yan, P. A. Mayewski, and M. L. Bender. Atmospheric composition 1 million years ago from blue ice in the allan hills, antarctica. *Proceedings of the National Academy of Sciences*, 112(22):6887–6891, 2015. doi: 10.1073/pnas.1420232112.

[5] B. D. Santer, K. E. Taylor, T. M. L. Wigley, T. C. Johns, P. D. Jones, D. J. Karoly, J. F. B. Mitchell, A. H. Oort, J. E. Penner, V. Ramaswamy, M. D. Schwarzkopf, R. J. Stouffer, and S. Tett. A search for human influences on the thermal structure of the atmosphere. *Nature*, 382(7):39–46, 1996. doi: 10.1038/382039a0.

[6] G. C. Hegerl, H. von Storch, K. Hasselmann, B. D. Santer, U. Cubasch, and P. D. Jones. Detecting greenhouse-gas-induced climate change with an optimal

fingerprint method. *Journal of Climate*, 9(10):2281–2306, 1996. doi: 10.1175/1520-0442.

[7] V. Ramaswamy, M. D. Schwarzkopf, W. J. Randel, B. D. Santer, B. J. Soden, and G. L. Stenchikoy. Anthropogenic and natural influences in the evolution of lower stratospheric cooling. *Science*, 311(5764):1138–1141, 2006. doi: 10.1126/science.1122587.

[8] B. D. Santer, M. F. Wehner, T. M. L. Wigley, R. Sausen, G. A. Meehl, K. E. Taylor, C. Ammann, J. Arblaster, W. M. Washington, J. S. Boyle, and W. Bruggemann. Contributions of anthropogenic and natural forcing to recent tropopause height changes. *Science*, 301(5632):479–483, 2003. doi: 10.1126/science.1084123.

[9] J. Jouzel and V. Masson-Delmotte. EPICA Dome C Ice Core 800KYr deuterium data and temperature estimates, 2007.

[10] J. Hansen, M. Sato, R. Ruedy, K. Lo, D. W. Lea, and M. Medina-Elizade. Global temperature change. *Proceedings of the National Academy of Sciences*, 103(39):14288–14293, 2006. doi: 10.1073/pnas.0606291103.

[11] E. Rignot, Jeremie Mouginot, Bernd Scheuchl, Michiel van den Broeke, Melchior J. van Wessem, and Mathieu Morlighem. Four decades of antarctic ice sheet mass balance from 1979 - 2017. *Proceedings of the National Academy of Sciences*, 116(4):1095–1103, 2019. doi: 10.1073/pnas.1812883116.

[12] Artic sea ice minimum. https://climate.nasa.gov/vital-signs/arctic-sea-ice/, 2018. Accessed: 2019-09-24.

[13] J. R. Khusnutdinova, N. P. Rath, and L. M. Mirica. Stable mononuclear organometallic pd(iii) complexes and their c-c bofnd formation reactivity. *Journal of the American Chemical Society*, 132(21):7303–7305, 2010. doi: 10.1021/ja103001g.

[14] T. M. Boichuk and S. N. Orlik. Effect of no, SO_2, and O_2 on the conversion of nitrous oxide on iron-containing zeolite catalysts. *Theoretical and Experimental Chemistry*, 42(4):250–254, 2006. doi: 10.1007/s11237-006-0048-x.

[15] S. Y. Christou and A. M. Efstathiou. Efficient in-situ regeneration method of the catalytic activity of aged twc. *Topics in Catalysis*, 42(1):415–419, 2007. doi: 10.1007/s11244-007-0216-9.

[16] D. M. Alongi. Carbon sequestration in mangrove forests. *Carbon Management*, 3(3):313–322, 2012. doi: 10.4155/cmt.12.20.

[17] J. E. Lovelock and C. G. Rapely. Ocean pipes could help the earth to cure itself. *Nature*, 449(7):403, 2007. doi: doi.org/10.1038/449403a.

[18] A. Spolaor, P. Vallelonga, G. Cozzi, J. Gabrieli, C. Varin, N. Kehrwald, P. Zennaro, C. Boutron, and C. Barbante. Iron speciation in aerosol dust influences iron bioavailability over glacial-interglacial timescales. *Geophysical Research Letters*, 40(8):1618–1623, 2013. doi: 10.1002/grl.50296.

[19] Nasa details earthquake effects on the earth. https://www.jpl.nasa.gov/news/news.php?feature=716, 2019. Accessed: 2019-01-08.

[20] H. Cai, S. Piccolroaz, J. Huang, Z. Liu, F. Liu, and M. Toffolon. Quantifying the impact of the three gorges dam on the thermal dynamics of the yangtze river. *Environmental Research Letters*, 13(5):054016, 2018. doi: 10.1088/1748-9326/aab9e0.

[21] M. T. Islam, N. Huda, A.B. Abdullah, and R. Saidur. A comprehensive review of state of the art concentrating solar power (csp) technologies: Current status and research trends. *Renewable and Sustainable Energy Reviews*, 91(7):987 – 1018, 2018. doi: 10.1016/j.rser.2018.04.097.

[22] B. Parida, S. Iniyan, and R. Goic. A review of solar photovoltaic technologies. *Renewable and Sustainable Energy Reviews*, 15(3):1625 – 1636, 2011. doi: 10.1016/j.rser.2010.11.032.

[23] S.P.S. Badwal and K. Foger. Solid oxide electrolyte fuel cell review. *Ceramics International*, 22(3):257 – 265, 1996. doi: 10.1016/0272-8842(95)00101-8.

[24] L. Blum, W. A. Meulenberg, H. Nabielek, and R. Steinberger-Wilckens. Worldwide sofc technology overview and benchmark. *International Journal of Applied Ceramic Technology*, 2(6):482–492, 2005. doi: 10.1111/j.1744-7402.2005.02049.x.

[25] D. J. L. Brett, A. Atkinson, N. P. Brandon, and S. J. Skinner. Intermediate temperature solid oxide fuel cells. *Chem. Soc. Rev.*, 37(7):1568–1578, 2008. doi: 10.1039/B612060C.

[26] J. B. Goodenough. Oxide-ion electrolytes. *Annual Review of Materials Research*, 33(1):91–128, 2003. doi: 10.1146/annurev.matsci.33.022802.091651.

[27] J. S. Ping. Development of lanthanum strontium manganite perovskite cathode materials of solid oxide fuel cells: a review. *Journal of Materials Science*, 43(21):6799–6833, 2008. doi: 10.1007/s10853-008-2966-6.

[28] Z. Li, M. Behruzi, L. Fuerst, and D. Stover. Crystalline structure and electrical conductivity of bulk-sintered and plasma-sprayed $La_{1-x}Sr_xMnO_{3-y}$ with $0 < x < 0.9$. *ECS Proceedings Volumes*, 1993-4(7):171–179, 1993. doi: 10.1149/199304.0171PV.

[29] X. Guo and R. Waser. Electrical properties of the grain boundaries of oxygen ion conductors: Acceptor-doped zirconia and ceria. *Progress in Materials Science*, 51(2):151 – 210, 2006. doi: 10.1016/j.pmatsci.2005.07.001.

[30] J. Molenda, K. Swierczek, and W. Zajac. Functional materials for the it-sofc. *Journal of Power Sources*, 173(2):657 – 670, 2007. doi: 10.1016/j.jpowsour.2007.05.085.

[31] A. J. Jacobson. Materials for solid oxide fuel cells. *Chemistry of Materials*, 22 (3):660–674, 2010. doi: 10.1021/cm902640j.

[32] H. Yokokawa, N. Sakai, T. Horita, and K. Yamaji. Recent developments in solid oxide fuel cell materials. *Fuel Cells*, 1(2):117–131, 2001. doi: 10.1002/1615-6854.

[33] J. Mizusaki, Y. Yonemura, H. Kamata, K. Ohyama, N. Mori, H. Takai, H. Tagawa, M. Dokiya, K. Naraya, T. Sasamoto, H. Inaba, and T. Hashimoto.

Electronic conductivity, seebeck coefficient, defect and electronic structure of nonstoichiometric $La_{1-x}Sr_xMnO_3$. *Solid State Ionics*, 132(3):167 – 180, 2000. doi: 10.1016/S0167-2738(00)00662-7.

[34] T. Montini, M. Melchionna, M. Monai, and P. Fornasiero. Fundamentals and catalytic applications of CeO_2-based materials. *Chemical Reviews*, 116(10): 5987–6041, 2016. doi: 10.1021/acs.chemrev.5b00603.

[35] T. Huang and J. Li. Effect of Bi_2O_3 content on characteristics of Bi_2O_3-GDC systems for direct methane oxidation. *Journal of Power Sources*, 181(1):62 – 68, 2008. doi: 10.1016/j.jpowsour.2008.03.038.

[36] M.A. Henderson, C.L. Perkins, M.H. Engelhard, S. Thevuthasan, and C.H.F. Peden. Redox properties of water on the oxidized and reduced surfaces of CeO_2(111). *Surface Science*, 526(1):1 – 18, 2003. doi: 10.1016/S0039-6028(02)02657-2.

[37] Z. Yang, T. K. Woo, M. Baudin, and K. Hermansson. Atomic and electronic structure of unreduced and reduced CeO_2 surfaces: A first-principles study. *The Journal of Chemical Physics*, 120(16):7741–7749, 2004. doi: 10.1063/1.1688316.

[38] E. B. Lavik, I. Kosacki, H. L. Tuller, Y. M. Chiang, and J. Y. Ying. Nonstoichiometry and electrical conductivity of nanocrystalline CeO_{2-x}. *Journal of Electroceramics*, 1(1):7–14, 1997. doi: 10.1023/A:1009934829870.

[39] M. Nolan, S. C. Parker, and G. W. Watson. The electronic structure of oxygen vacancy defects at the low index surfaces of ceria. *Surface Science*, 595(1):223 – 232, 2005. doi: 10.1016/j.susc.2005.08.015.

[40] J. Wang, H. Chen, Z. Hu, M. Yao, and Y. Li. A review on the pd-based three-way catalyst. *Catalysis Reviews*, 57(1):79–144, 2015. doi: 10.1080/01614940.2014.977059.

[41] A.F. Diwell, R.R. Rajaram, H.A. Shaw, and T.J. Truex. In A. Crucq, editor, *The Role of Ceria in Three-Way Catalysts*, volume 71 of *Studies in Surface*

Science and Catalysis, pages 139 – 152. 1991. doi: 10.1016/S0167-2991(08)62975-4.

[42] T. Johnson. Vehicular emissions in review. *SAE Int. J. Engines*, 9(7):1258–1275, 2016. doi: 10.4271/2016-01-0919.

[43] S. Liu, X. Wu, D. Weng, and R. Ran. Ceria-based catalysts for soot oxidation: a review. *Journal of Rare Earths*, 33(6):567 – 590, 2015. doi: 10.1016/S1002-0721(14)60457-9.

[44] M. Boaro, S. Colussi, and A. Trovarelli. Ceria-based materials in hydrogenation and reforming reactions for CO_2 valorization. *Frontiers in Chemistry*, 7 (7):28, 2019. doi: 10.3389/fchem.2019.00028.

[45] J. A. Rodriguez, D. C. Grinter, Z. Liu, R. M. Palomino, and S. D. Senanayake. Ceria-based model catalysts: fundamental studies on the importance of the metal-ceria interface in co oxidation, the water-gas shift, CO_2 hydrogenation, and methane and alcohol reforming. *Chem. Soc. Rev.*, 46(7):1824–1841, 2017. doi: 10.1039/C6CS00863A.

[46] L. Vivier and D. Duprez. Ceria-based solid catalysts for organic chemistry. *ChemSusChem*, 3(6):654–678, 2010. doi: 10.1002/cssc.201000054.

[47] H. A. Miran, M. Altarawneh, Z. T. Jiang, H. Oskierski, M. Almatarneh, and B. Z. Dlugogorski. Decomposition of selected chlorinated volatile organic compounds by ceria (CeO_2). *Catal. Sci. Technol.*, 7(7):3902–3919, 2017. doi: 10.1039/C7CY01096F.

[48] Y. Zhang, Z. Li, L. Zhang, L. Pan, X. Zhang, L. Wang, F. Aleem, and J. Zou. Role of oxygen vacancies in photocatalytic water oxidation on ceria oxide: Experiment and dft studies. *Applied Catalysis B: Environmental*, 224(7):101 – 108, 2018. doi: 10.1016/j.apcatb.2017.10.049.

[49] O. Marina, C. Bagger, S. Primdahl, and M. Mogensen. A solid oxide fuel cell with a gadolinia-doped ceria anode: Preparation and performance. *Solid State Ionics*, 123(7):199–208, 2000. doi: 10.1016/S0167-2738(99)00111-3.

[50] D. Kim. Lattice parameters, ionic conductivities, and solubility limits in fluorite-structure MO_2 oxide [m = Hf^{4+}, Zr^{4+}, Ce^{4+}, Hf^{4+}, U^{4+}] solid solutions. *Journal of the American Ceramic Society*, 72(7):1415 – 1421, 2005. doi: 10.1111/j.1151-2916.1989.tb07663.x.

[51] D. A. Andersson, S. I. Simak, N. V. Skorodumova, I. A. Abrikosov, and B. Johansson. Optimization of ionic conductivity in doped ceria. *Proceedings of the National Academy of Sciences*, 103(10):3518–3521, 2006. doi: 10.1073/pnas.0509537103.

[52] D. Marrocchelli, S. R. Bishop, H. L. Tuller, and B. Yildiz. Understanding chemical expansion in non-stoichiometric oxides: Ceria and zirconia case studies. *Advanced Functional Materials*, 22(9):1958–1965, 2012. doi: 10.1002/adfm.201102648.

[53] S. Zha, C. Xia, and G. Meng. Effect of gd (sm) doping on properties of ceria electrolyte for solid oxide fuel cells. *Journal of Power Sources*, 115(1):44 – 48, 2003. doi: 10.1016/S0378-7753(02)00625-0.

[54] C. B. Gopal and A. van de Walle. Ab initio thermodynamics of intrinsic oxygen vacancies in ceria. *Phys. Rev. B*, 86(7):134117, 2012. doi: 10.1103/PhysRevB.86.134117.

[55] P. P. Dholabhai, J. A. Aguiar, L. Wu, T. G. Holesinger, T. Aoki, R. H. R. Castro, and B. P. Uberuaga. Structure and segregation of dopant-defect complexes at grain boundaries in nanocrystalline doped ceria. *Phys. Chem. Chem. Phys.*, 17(7):15375–15385, 2015. doi: 10.1039/C5CP02200B.

[56] M. Burbano, D. Marrocchelli, B. Yildiz, H. L. Tuller, S. T. Norberg, S. Hull, P. A. Madden, and G. W. Watson. A dipole polarizable potential for reduced and doped CeO_2 obtained from first principles. *Journal of Physics: Condensed Matter*, 23(25):255402, 2011. doi: 10.1088/0953-8984/23/25/255402.

[57] A. Gotte, D. Spangberg, K. Hermansson, and M. Baudin. Molecular dynamics study of oxygen self-diffusion in reduced CeO_2. *Solid State Ionics*, 178(25): 1421 – 1427, 2007. doi: 10.1016/j.ssi.2007.08.003.

[58] S. A. Acharya. The effect of processing route on sinterability and electrical properties of nano-sized dysprosium-doped ceria. *Journal of Power Sources*, 198(7):105 – 111, 2012. doi: 10.1016/j.jpowsour.2011.09.087.

[59] N. Bohr and J. A. Wheeler. The mechanism of nuclear fission. *Phys. Rev.*, 56 (7):426–450, 1939. doi: 10.1103/PhysRev.56.426.

[60] E.A.C. Crouch. Fission-product yields from neutron-induced fission. *Atomic Data and Nuclear Data Tables*, 19(5):417 – 532, 1977. doi: 10.1016/0092-640X(77)90023-7.

[61] E.A.C. Crouch. Bulletin of the atomic scientists index to vol. xviii, 1962. *Bulletin of the Atomic Scientists*, 18(10):46–48, 1962. doi: 10.1080/00963402.1962.11454440.

[62] G. R. Choppin. Technology for nuclear reprocessing: Present and future directions. *Separation Science and Technology*, 41(10):1955–1963, 2006. doi: 10.1080/01496390600745768.

[63] C. R. Edwards and A. J. Oliver. Uranium processing: A review of current methods and technology. *JOM*, 52(9):12–20, 2000. doi: 10.1007/s11837-000-0181-2.

[64] D. Olander. Nuclear fuels - present and future. *MRS Proceedings*, 1264(7): 1264–Z04–01, 2010. doi: 10.1557/PROC-1264-Z04-01.

[65] B. Cox. Pellet-clad interaction (pci) failures of zirconium alloy fuel cladding - a review. *Journal of Nuclear Materials*, 172(3):249 – 292, 1990. doi: 10.1016/0022-3115(90)90282-R.

[66] F. Gauthier-Lafaye, F. Weber, and H. Ohmoto. Natural fission reactors of Oklo. *Economic Geology*, 84(8):2286–2295, 1989. doi: 10.2113/gsecongeo.84.8.2286.

[67] Y. Funabashi and K. Kitazawa. Fukushima in review: A complex disaster, a disastrous response. *Bulletin of The Atomic Scientists - BULL ATOM SCI*, 68(7):9–21, 2012. doi: 10.1177/0096340212440359.

[68] J.N. Mathur, M.S. Murali, and K.L.Nash. Actinide partioning-a review. *Solvent Extraction and Ion Exchange*, 19(3):357–390, 2001. doi: 10.1081/SEI-100103276.

[69] M. Lenzen. Life cycle energy and greenhouse gas emissions of nuclear energy: A review. *Energy Conversion and Management*, 49(8):2178 – 2199, 2008. doi: 10.1016/j.enconman.2008.01.033.

[70] M. A. Rosen. Energy and exergy-based comparison of coal-fired and nuclear steam power plants. *Exergy, An International Journal*, 1(3):180 – 192, 2001. doi: 10.1016/S1164-0235(01)00024-3.

[71] N. Zainul, A.Majid, and W. Al-Areqi. Advantages of liquid fluoride thorium reactor in comparison with light water reactor. *AIP Conference Proceedings*, 1659(1):040001, 2015. doi: 10.1063/1.4916861.

[72] D.G Martin. The thermal expansion of solid UO_2 and (u, pu) mixed oxides - a review and recommendations. *Journal of Nuclear Materials*, 152(2):94 – 101, 1988. doi: 10.1016/0022-3115(88)90315-7.

[73] B. R. T. Frost. Chapter 2 - fuel types. In BRIAN R.T. FROST, editor, *Nuclear Fuel Elements*, pages 13 – 49. 1982. ISBN 978-0-08-020412-3. doi: 10.1016/B978-0-08-020412-3.50006-3.

[74] R. Dubourg, H. Austregesilo, C. Bals, M. Barrachin, J. Birchley, T. Haste, J.S. Lamy, T. Lind, B. Maliverney, C. Marchetto, A. Pinter, M. Steinbruck, J. Stuckert, K. Trambauer, and A. Vimi. Understanding the behaviour of absorber elements in silver-indium-cadmium control rods during pwr severe accident sequences. *Progress in Nuclear Energy*, 52(1):97 – 108, 2010. doi: 10.1016/j.pnucene.2009.09.012.

[75] V. D. Risovanyi, E. P. Klochkoy, and E. E. Varlashova. Hafnium and dysprosium titanate based control rods for thermal water-cooled reactors. *Atomic Energy*, 81(5):764–769, 1996. doi: 10.1007/BF02408175.

[76] P. A. Egelstaff. The scattering of thermal neutrons by moderators. *Nuclear Science and Engineering*, 12(2):250–259, 1962. doi: 10.13182/NSE62-A26065.

[77] T. Abram and S. Ion. Generation-IV nuclear power: A review of the state of the science. *Energy Policy*, 36(12):4323–4330, 2008.

[78] M.F. Lyons, R.F. Boyle, J.H. Davies, V.E. Hazel, and T.C. Rowland. UO_2 properties affecting performance. *Nuclear Engineering and Design*, 21(2):167 – 199, 1972. doi: 10.1016/0029-5493(72)90072-6.

[79] E. Schrodinger. An undulatory theory of the mechanics of atoms and molecules. *Phys. Rev.*, 28(7):1049–1070, 1926. doi: 10.1103/PhysRev.28.1049.

[80] M. Born and R. Oppenheimer. Zur quantentheorie der molekeln. *Annalen der Physik*, 389(20):457–484, 1927. doi: 10.1002/andp.19273892002.

[81] D. R. Hartree and W. Hartree. Self-consistent field, with exchange, for beryllium. *Proceedings of the Royal Society of London. Series A - Mathematical and Physical Sciences*, 150(869):9–33, 1935. doi: 10.1098/rspa.1935.0085.

[82] J. C. Slater. A simplification of the hartree-fock method. *Phys. Rev.*, 81(7): 385–390, 1951. doi: 10.1103/PhysRev.81.385.

[83] D. R. Hartree. The wave mechanics of an atom with a non-coulomb central field. part i. theory and methods. *Mathematical Proceedings of the Cambridge Philosophical Society*, 24(1):89–110, 1928. doi: 10.1017/S0305004100011919.

[84] V. Fock. Näherungsmethode zur lösung des quantenmechanischen mehrkörperproblems. *Zeitschrift für Physik*, 61(1):126–148, 1930. doi: 10.1007/BF01340294.

[85] J. C. Slater. The theory of complex spectra. *Phys. Rev.*, 34(7):1293–1322, 1929. doi: 10.1103/PhysRev.34.1293.

[86] L. H. Thomas. The calculation of atomic fields. *Mathematical Proceedings of the Cambridge Philosophical Society*, 23(5):542548, 1927. doi: 10.1017/S0305004100011683.

[87] P. A. M. Dirac. Note on exchange phenomena in the thomas atom. *Mathematical Proceedings of the Cambridge Philosophical Society*, 26(3):376–385, 1930. doi: 10.1017/S0305004100016108.

[88] P. Hohenberg and W. Kohn. Inhomogeneous electron gas. *Phys. Rev.*, 136(7): B864–B871, 1964. doi: 10.1103/PhysRev.136.B864.

[89] W. Kohn and L. J. Sham. Self-consistent equations including exchange and correlation effects. *Phys. Rev.*, 140(7):A1133–A1138, 1965. doi: 10.1103/PhysRev.140.A1133.

[90] A. D. Becke. Density-functional exchange-energy approximation with correct asymptotic behavior. *Phys. Rev. A*, 38(7):3098–3100, 1988. doi: 10.1103/PhysRevA.38.3098.

[91] J. P. Perdew and Y. Wang. Accurate and simple analytic representation of the electron-gas correlation energy. *Phys. Rev. B*, 45(7):13244–13249, 1992. doi: 10.1103/PhysRevB.45.13244.

[92] J. P. Perdew, K. Burke, and M. Ernzerhof. Generalized gradient approximation made simple. *Phys. Rev. Lett.*, 77(7):3865–3868, 1996. doi: 10.1103/PhysRevLett.77.3865.

[93] J. P. Perdew, A. Ruzsinszky, G. Csonka, O. A. Vydrov, G. E. Scuseria, L. A. Constantin, X. Zhou, and K. Burke. Restoring the density-gradient expansion for exchange in solids and surfaces. *Phys. Rev. Lett.*, 100(7):136406, 2008. doi: 10.1103/PhysRevLett.100.136406.

[94] V. I. Anisimov, F. Aryasetiawan, and A. I. Lichtenstein. First-principles calculations of the electronic structure and spectra of strongly correlated systems: the lda+u method. *Journal of Physics: Condensed Matter*, 9(4):767–808, 1997. doi: 10.1088/0953-8984/9/4/002.

[95] J. Hubbard and B. H. Flowers. Electron correlations in narrow energy bands. *Proceedings of the Royal Society of London. Series A. Mathematical and Physical Sciences*, 276(1365):238–257, 1963. doi: 10.1098/rspa.1963.0204.

[96] A. I. Liechtenstein, V. I. Anisimov, and J. Zaanen. Density-functional theory and strong interactions: Orbital ordering in mott-hubbard insulators. *Phys. Rev. B*, 52(7):R5467–R5470, 1995. doi: 10.1103/PhysRevB.52.R5467.

[97] M. C. Payne, M. P. Teter, D. C. Allan, T. A. Arias, and J. D. Joannopoulos. Iterative minimization techniques for ab initio total-energy calculations: molecular dynamics and conjugate gradients. *Rev. Mod. Phys.*, 64(7):1045–1097, 1992. doi: 10.1103/RevModPhys.64.1045.

[98] H. J. Monkhorst and J. D. Pack. Special points for brillouin-zone integrations. *Phys. Rev. B*, 13(7):5188–5192, 1976. doi: 10.1103/PhysRevB.13.5188.

[99] Volker Heine. The pseudopotential concept. *Solid State Physics*, 24(7):1 – 36, 1970. doi: 10.1016/S0081-1947(08)60069-7.

[100] P. E. Blochl. Projector augmented-wave method. *Phys. Rev. B*, 50(7):17953–17979, 1994. doi: 10.1103/PhysRevB.50.17953.

[101] M. Born and K. Huang. *Dynamical theory of crystal lattices*. Oxford classic texts in the physical sciences. Oxford, 1954.

[102] C. A. Coulomb. Premier memoire sur l'electricite et le magnetisme. *Histoire de l'Academie Royale des Sciences*, 358(7):569–577, 1788.

[103] C. A. Coulomb. Second memoire sur l'electricite et le magnetisme. *Histoire de l'Academie Royale des Sciences*, 358(7):578–611, 1788.

[104] D. Frenkel and B. Smit. *Understanding molecular simulation : from algorithms to applications. 2nd ed*, volume 50. 1996. doi: 10.1063/1.881812.

[105] A. Rahman. Correlations in the motion of atoms in liquid argon. *Phys. Rev.*, 136(7):A405–A411, 1964. doi: 10.1103/PhysRev.136.A405.

[106] A. Pedone, G. Malavasi, M. Menziani, C. Cristina, N. Alastair, and U. Segre. A new self-consistent empirical interatomic potential model for oxides, silicates, and silica-based glasses. *The Journal of Physical Chemistry B*, 110(24):11780–11795, 2006. doi: 10.1021/jp0611018.

[107] R. Fletcher and C. M. Reeves. Function minimization by conjugate gradients. *The Computer Journal*, 7(2):149–154, 1964. doi: 10.1093/comjnl/7.2.149.

[108] M. J. Norgett and R. Fletcher. Fast matrix methods for calculating the relaxation about defects in crystals. *Journal of Physics C: Solid State Physics*, 3 (11):L190–L192, 1970. doi: 10.1088/0022-3719/3/11/003.

[109] E. T. Jaynes. Information theory and statistical mechanics. *Phys. Rev.*, 106 (7):620–630, 1957. doi: 10.1103/PhysRev.106.620.

[110] W. C. Swope, H. C. Andersen, P. H. Berens, and K. R. Wilson. A computer simulation method for the calculation of equilibrium constants for the formation of physical clusters of molecules: Application to small water clusters. *The Journal of Chemical Physics*, 76(1):637–649, 1982. doi: 10.1063/1.442716.

[111] H. C. Andersen. Molecular dynamics simulations at constant pressure and/or temperature. *The Journal of Chemical Physics*, 72(4):2384–2393, 1980. doi: 10.1063/1.439486.

[112] S. Nose. A unified formulation of the constant temperature molecular dynamics methods. *The Journal of Chemical Physics*, 81(1):511–519, 1984. doi: 10.1063/1.447334.

[113] H. J. C. Berendsen, J. P. M. Postma, W. F. van Gunsteren, A. DiNola, and J. R. Haak. Molecular dynamics with coupling to an external bath. *The Journal of Chemical Physics*, 81(8):3684–3690, 1984. doi: 10.1063/1.448118.

[114] W. G. Hoover. Canonical dynamics: Equilibrium phase-space distributions. *Phys. Rev. A*, 31(7):1695–1697, 1985. doi: 10.1103/PhysRevA.31.1695.

[115] G. Bussi, D. Donadio, and M. Parrinello. Canonical sampling through velocity rescaling. *The Journal of Chemical Physics*, 126(1):014101, 2007. doi: 10.1063/1.2408420.

[116] M. Parrinello and A. Rahman. Polymorphic transitions in single crystals: A new molecular dynamics method. *Journal of Applied Physics*, 52(12):7182–7190, 1981. doi: 10.1063/1.328693.

[117] G. W. Watson, E. T. Kelsey, N. H. de Leeuw, D. J. Harris, and S. C. Parker. Atomistic simulation of dislocations, surfaces and interfaces in mgo. *J. Chem. Soc., Faraday Trans.*, 92(7):433–438, 1996. doi: 10.1039/FT9969200433.

[118] P. W. Tasker. The stability of ionic crystal surfaces. *Journal of Physics C: Solid State Physics*, 12(22):4977–4984, 1979. doi: 10.1088/0022-3719/12/22/036.

[119] A. R. Symington, J. Tse, M. Molinari, A. Marmier, and S. C. Parker. surfinpy: A surface phase diagram generator. *Journal of Open Source Software*, 4(34): 1210, 2019. doi: doi.org/10.21105/joss.01210.

[120] G. Wulff. Zur frage der geschwindigkeit des wachsthums und der auflosung der krystallflachen. *Crystalline Materials*, 34(7):449, 1901.

[121] M. A. Barteau. Organic reactions at well-defined oxide surfaces. *Chemical Reviews*, 96(4):1413–1430, 1996. doi: 10.1021/cr950222t.

[122] T. X. T. Sayle, S. C. Parker, and C. R. A. Catlow. Surface oxygen vacancy formation on CeO_2 and its role in the oxidation of carbon monoxide. *J. Chem. Soc., Chem. Commun.*, 358(7):977–978, 1992. doi: 10.1039/C39920000977.

[123] J. Paier, C. Penschke, and J. Sauer. Oxygen defects and surface chemistry of ceria: Quantum chemical studies compared to experiment. *Chemical Reviews*, 113(6):3949–3985, 2013. doi: 10.1021/cr3004949.

[124] P. Jasinski, T. Suzuki, and H. U. Anderson. Nanocrystalline undoped ceria oxygen sensor. *Sensors and Actuators B: Chemical*, 95(1):73 – 77, 2003. doi: 10.1016/S0925-4005(03)00407-6.

[125] B. Elyassi, N. Rajabbeigi, A. Khodadadi, S.S. Mohajerzadeh, and M. Sahimi. An yttria-doped ceria-based oxygen sensor with solid-state reference. *Sensors and Actuators B: Chemical*, 103(1):178 – 183, 2004. doi: 10.1016/j.snb.2004.04.117.

[126] V. V. Kharton, F. M. Figueiredo, L. Navarro, E. N. Naumovich, A. V. Kovalevsky, A. A. Yaremchenko, A. P. Viskup, A. Carneiro, F. M. B. Marques, and J. R. Frade. Ceria-based materials for solid oxide fuel cells. *Journal of Materials Science*, 36(5):1105–1117, 2001. doi: 10.1023/A:1004817506146.

[127] J. A. Kilner and M. Burriel. Materials for intermediate-temperature solid-oxide fuel cells. *Annual Review of Materials Research*, 44(1):365–393, 2014. doi: 10.1146/annurev-matsci-070813-113426.

[128] J. P. Allen, W. Grea, M. Molinari, C. Arrouvel, F. Maglia, and S. C. Parker. Atomistic modelling of adsorption and segregation at inorganic solid interfaces. *Molecular Simulation*, 35(7):584–608, 2009. doi: 10.1080/08927020902774570.

[129] A. Symington, M. Molinari, J. Statham, J. Wu, and S. C. Parker. The role of dopant segregation on the oxygen vacancy distribution and oxygen diffusion in CeO_2 grain boundaries. *Journal of Physics: Energy*, 1(4):042005, 2019. doi: 10.1088/2515-7655/ab28b5.

[130] H.C. Yao and Y.F.Yu Yao. Ceria in automotive exhaust catalysts: I. oxygen storage. *Journal of Catalysis*, 86(2):254 – 265, 1984. doi: 10.1016/0021-9517(84)90371-3.

[131] W. C. Chueh, C. Falter, M. Abbott, D. Scipio, P. Furler, S. M. Haile, and A. Steinfeld. High-flux solar-driven thermochemical dissociation of CO_2 and H_2O using nonstoichiometric ceria. *Science*, 330(6012):1797–1801, 2010. doi: 10.1126/science.1197834.

[132] M. Molinari, A. Symington, D. C. Sayle, T. S. Sakthivel, S. Seal, and S. C. Parker. Computer-aided design of nanoceria structures as enzyme mimetic agents: The role of bodily electrolytes on maximizing their activity. *ACS Applied Bio Materials*, 2(3):1098–1106, 2019. doi: 10.1021/acsabm.8b00709.

[133] A. S. Karakoti, N. A. Monteiro-Riviere, R. Aggarwal, J. P. Davis, R. J. Narayan, W. T. Self, J. McGinnis, and S. Seal. Nanoceria as antioxidant: Synthesis and biomedical applications. *JOM*, 60(3):33–37, 2008. doi: 10.1007/s11837-008-0029-8.

[134] J. C. Conesa. Computer modeling of surfaces and defects on cerium dioxide. *Surface Science*, 339(3):337 – 352, 1995. doi: 10.1016/0039-6028(95)00595-1.

[135] N. V. Skorodumova, M. Baudin, and K. Hermansson. Surface properties of ceo_2 from first principles. *Phys. Rev. B*, 69(7):075401, 2004. doi: 10.1103/PhysRevB.69.075401.

[136] M. Nolan, S. C. Parker, and G. W. Watson. Reduction of NO_2 on ceria

surfaces. *The Journal of Physical Chemistry B*, 110(5):2256–2262, 2006. doi: 10.1021/jp055624b.

[137] M. Nolan. Hybrid density functional theory description of oxygen vacancies in the CeO_2 (110) and (100) surfaces. *Chemical Physics Letters*, 499(1):126 – 130, 2010. doi: 10.1016/j.cplett.2010.09.016.

[138] H. Norenberg and J. H. Harding. The surface structure of CeO_2(001) single crystals studied by elevated temperature stm. *Surface Science*, 477(1):17 – 24, 2001. doi: 10.1016/S0039-6028(01)00700-2.

[139] Y. Lin, Z. Wu, W. Zili, J. Wen, K. R. Poeppelmeier, and L. D. Marks. Imaging the atomic surface structures of CeO_2 nanoparticles. *Nano Letters*, 14(1):191–196, 2014. doi: 10.1021/nl403713b.

[140] A. Trovarelli and J. Llorca. Ceria catalysts at nanoscale: How do crystal shapes shape catalysis? *ACS Catalysis*, 7(7):4716–4735, 2017. doi: 10.1021/acscatal.7b01246.

[141] I. Florea, C. Feral-Martin, J. Majimel, D. Ihiawakrim, C. Hirlimann, and O. Ersen. Three-dimensional tomographic analyses of CeO_2 nanoparticles. *Crystal Growth & Design*, 13(3):1110–1121, 2013. doi: 10.1021/cg301445h.

[142] R. Si and M. Flytzani-Stephanopoulos. Shape and crystal-plane effects of nanoscale ceria on the activity of au-CeO_2 catalysts for the water gas shift reaction. *Angewandte Chemie International Edition*, 47(15):2884–2887, 2008. doi: 10.1002/anie.200705828.

[143] H. X. Mai, L. D. Sun, M. Zhang, R. Si, W. Feng, H. P. Zhang, H. C. Liu, and C. H. Yan. Shape-selective synthesis and oxygen storage behavior of ceria nanopolyhedra, nanorods, and nanocubes. *The Journal of Physical Chemistry B*, 109(51):24380–24385, 2005. doi: 10.1021/jp055584b.

[144] S. Asahina, S. Takami, T. Otsuka, T. Adschiri, and O. Terasaki. Exploitation of surface-sensitive electrons in scanning electron microscopy reveals the formation mechanism of new cubic and truncated octahedral CeO_2 nanoparticles. *ChemCatChem*, 3(6):1038–1044, 2011. doi: 10.1002/cctc.201000348.

[145] C. Yang, X. Yu, S. Heiayler, A. Nefedov, S. Colussi, J. Llorca, A. Trovarelli, Y. Wang, and C. Wall. Surface faceting and reconstruction of ceria nanoparticles. *Angewandte Chemie International Edition*, 56(1):375–379, 2017. doi: 10.1002/anie.201609179.

[146] P. A. Crozier, R. Wang, and R. Sharma. In situ environmental tem studies of dynamic changes in cerium-based oxides nanoparticles during redox processes. *Ultramicroscopy*, 108(11):1432 – 1440, 2008. doi: 10.1016/j.ultramic.2008.05.015.

[147] D. O. Scanlon, B. J. Morgan, and G. W. Watson. The origin of the enhanced oxygen storage capacity of $Ce_{1-x}(Pd/Pt)_xO_2$. *Phys. Chem. Chem. Phys.*, 13 (7):4279–4284, 2011. doi: 10.1039/C0CP01635G.

[148] J. Kullgren, K. Hermansson, and C. Castleton. Many competing ceria (110) oxygen vacancy structures: From small to large supercells. *The Journal of Chemical Physics*, 137(4):044705, 2012. doi: 10.1063/1.4723867.

[149] J. F. Jerratsch, X. Shao, N. Nilius, H. J. Freund, C. Popa, M. V. Ganduglia-Pirovano, A. M. Burow, and J. Sauer. Electron localization in defective ceria films: A study with scanning-tunneling microscopy and density-functional theory. *Phys. Rev. Lett.*, 106(7):246801, 2011. doi: 10.1103/PhysRevLett.106.246801.

[150] Y. Namai, K. Fukui, and Y. Iwasawa. Atom-resolved noncontact atomic force microscopic observations of $CeO_2(111)$ surfaces with different oxidation states: Surface structure and behavior of surface oxygen atoms. *The Journal of Physical Chemistry B*, 107(42):11666–11673, 2003. doi: 10.1021/jp030142q.

[151] Y. Namai, K. Fukui, and Y. Iwasawa. Atom-resolved noncontact atomic force microscopic and scanning tunneling microscopic observations of the structure and dynamic behavior of $CeO_2(111)$ surfaces. *Catalysis Today*, 85(2):79 – 91, 2003. doi: 10.1016/S0920-5861(03)00377-8.

[152] S. Gritschneder and M. Reichling. Structural elements of $CeO_2(111)$ surfaces. *Nanotechnology*, 18(4):044024, 2006. doi: 10.1088/0957-4484/18/4/044024.

[153] G. W. Watson, S. C. Parker, and G. Kresse. Ab initio calculation of the origin of the distortion of α-pbo. *Phys. Rev. B*, 59(7):8481–8486, 1999. doi: 10.1103/PhysRevB.59.8481.

[154] P. R. L. Keating, D. O. Scanlon, and G. W. Watson. Intrinsic ferromagnetism in CeO_2: dispelling the myth of vacancy site localization mediated superexchange. *Journal of Physics: Condensed Matter*, 21(40):405502, 2009. doi: 10.1088/0953-8984/21/40/405502.

[155] Z. Han, L. Zhang, M. Liu, M. V. Ganduglia-Pirovano, and Y. Gao. The structure of oxygen vacancies in the near-surface of reduced CeO_2 (111) under strain. *Frontiers in Chemistry*, 7(7):436, 2019. doi: 10.3389/fchem.2019.00436.

[156] C. Zhang, A. Michaelides, D. A. King, and S. J. Jenkins. Oxygen vacancy clusters on ceria: Decisive role of cerium f electrons. *Phys. Rev. B*, 79(7): 075433, 2009. doi: 10.1103/PhysRevB.79.075433.

[157] C. T. Campbell and C. H. F. Peden. Oxygen vacancies and catalysis on ceria surfaces. *Science*, 309(5735):713–714, 2005. doi: 10.1126/science.1113955.

[158] L. Minervini, M. O. Zacate, and R. W. Grimes. Defect cluster formation in M_2O_3-doped CeO_2. *Solid State Ionics*, 116(3):339 – 349, 1999. doi: 10.1016/S0167-2738(98)00359-2.

[159] X. Aparicio, A. Roldan, and N. H. de Leeuw. Gadolinium-vacancy clusters in the (111) surface of gadolinium-doped ceria: A density functional theory study. *Chemistry of Materials*, 27(23):7910–7917, 2015. doi: 10.1021/acs.chemmater.5b02861.

[160] P. Martin, D. Spagnoli, A. Marmier, S. C. Parker, D. C. Sayle, and G. Watson. Application of molecular dynamics dl_poly codes to interfaces of inorganic materials. *Molecular Simulation*, 32(12-13):1079–1093, 2006. doi: 10.1080/08927020601013817.

[161] S. Kerisit, A. Marmier, and S. C. Parker. Ab initio surface phase diagram of the 1014 calcite surface. *The Journal of Physical Chemistry B*, 109(39): 18211–18213, 2005. doi: 10.1021/jp053489x.

[162] Q. Sun, K. Reuter, and M. Scheffler. Effect of a humid environment on the surface structure of $RuO_2(110)$. *Phys. Rev. B*, 67(7):205424, 2003. doi: 10.1103/PhysRevB.67.205424.

[163] M. Molinari, S. C. Parker, D. C. Sayle, and S. M. Islam. Water adsorption and its effect on the stability of low index stoichiometric and reduced surfaces of ceria. *The Journal of Physical Chemistry C*, 116(12):7073–7082, 2012. doi: 10.1021/jp300576b.

[164] D. R. Mullins, P. M. Albrecht, T. Chen, F. C. Calaza, M. D. Biegalski, H. M. Christen, and S. H. Overbury. Water dissociation on $CeO_2(100)$ and $CeO_2(111)$ thin films. *The Journal of Physical Chemistry C*, 116(36):19419–19428, 2012. doi: 10.1021/jp306444h.

[165] B. E. Tegner, M. Molinari, A. Kerridge, S. C. Parker, and N. Kaltsoyannis. Water adsorption on AnO_2 111, 110, and 100 surfaces (an = u and pu): A density functional theory + u study. *The Journal of Physical Chemistry C*, 121(3):1675–1682, 2017. doi: 10.1021/acs.jpcc.6b10986.

[166] N. Sakai, K. Yamaji, Y. P. Xiong, H. Kishimoto, T. Horita, and H. Yokokawa. Interaction between water and ceria-zirconia-yttria solid solutions. *Journal of Electroceramics*, 13(1):677–682, 2004. doi: 10.1007/s10832-004-5175-y.

[167] M. Mogensen, K. V. Jensen, M. Juhl, J. A. Grgensen, and S. Primdahl. Progress in understanding sofc electrodes. *Solid State Ionics*, 150(1):123 – 129, 2002. doi: 10.1016/S0167-2738(02)00269-2.

[168] S. Kumar and P. K. Schelling. Density functional theory study of water adsorption at reduced and stoichiometric ceria (111) surfaces. *The Journal of Chemical Physics*, 125(20):204704, 2006. doi: 10.1063/1.2400034.

[169] A. Kumar, S. Das, P. Munusamy, W. Self, D. R. Baer, D. C. Sayle, and S. Seal. Behavior of nanoceria in biologically-relevant environments. *Environ. Sci.: Nano*, 1(7):516–532, 2014. doi: 10.1039/C4EN00052H.

[170] M. Fronzi, S. Piccinin, B. Delley, E. Traversa, and C. Stampfl. Water adsorption on the stoichiometric and reduced $CeO_2(111)$ surface: a first-

principles investigation. *Phys. Chem. Chem. Phys.*, 11(7):9188–9199, 2009. doi: 10.1039/B901831J.

[171] M. B. Watkins, A. S. Foster, and A. L. Shluger. Hydrogen cycle on CeO_2 (111) surfaces: A density functional theory calculations. *The Journal of Physical Chemistry C*, 111(42):15337–15341, 2007. doi: 10.1021/jp071715s.

[172] A. Jeyaranjan, T. S. Sakthivel, M. Molinari, D. C. Sayle, and S. Seal. Morphology and crystal planes effects on supercapacitance of CeO_2 nanostructures: Electrochemical and molecular dynamics studies. *Particle & Particle Systems Characterization*, 35(10):1800176, 2018. doi: 10.1002/ppsc.201800176.

[173] D. Perez-Coll and G. C. Mather. Electrical transport at low temperatures in dense nanocrystalline gd-doped ceria. *Solid State Ionics*, 181(1):20 – 26, 2010. doi: 10.1016/j.ssi.2009.11.017.

[174] A. Kossoy, H. Cohen, T. Bendikov, E. Wachtel, and I. Lubomirsky. Water adsorption at the surface of pure and gd-doped ceria. *Solid State Ionics*, 194 (1):1 – 4, 2011. doi: 10.1016/j.ssi.2011.05.011.

[175] B. Chen, Y. Ma, L. Ding, L. Xu, Z. Wu, Y. Yuan, and W. Huang. Reactivity of hydroxyls and water on a CeO_2(111) thin film surface: The role of oxygen vacancy. *The Journal of Physical Chemistry C*, 117(11):5800–5810, 2013. doi: 10.1021/jp312406f.

[176] A. M. Hernandez-Gimenez, D. Lozano-Castello, and A. Bueno-Lopez. Effect of CO_2, H_2O and SO_2 in the ceria-catalyzed combustion of soot under simulated diesel exhaust conditions. *Applied Catalysis B: Environmental*, 148-149(7):406 – 414, 2014. doi: 10.1016/j.apcatb.2013.11.029.

[177] K. Krishna, A. Bueno-Lopez, M. Makkee, and J.A. Moulijn. Potential rare earth modified CeO_2 catalysts for soot oxidation: I. characterisation and catalytic activity with O_2. *Applied Catalysis B: Environmental*, 75(3):189 – 200, 2007. doi: 10.1016/j.apcatb.2007.04.010.

[178] D.B. Pal, R. Chand, S.N. Upadhyay, and P.K. Mishra. Performance of water

gas shift reaction catalysts: A review. *Renewable and Sustainable Energy Reviews*, 93(7):549 – 565, 2018. doi: 10.1016/j.rser.2018.05.003.

[179] D.L. Trimm. Minimisation of carbon monoxide in a hydrogen stream for fuel cell application. *Applied Catalysis A: General*, 296(1):1 – 11, 2005. doi: 10.1016/j.apcata.2005.07.011.

[180] T. Shido and Y. Iwasawa. Reactant-promoted reaction mechanism for water-gas shift reaction on rh-doped CeO_2. *Journal of Catalysis*, 141(1):71 – 81, 1993. doi: 10.1006/jcat.1993.1119.

[181] T. Shido and Y. Iwasawa. Regulation of reaction intermediate by reactant in the water-gas shift reaction on CeO_2, in relation to reactant-promoted mechanism. *Journal of Catalysis*, 136(2):493 – 503, 1992. doi: 10.1016/0021-9517(92)90079-W.

[182] G.S. Zafiris and R.J. Gorte. Evidence for low-temperature oxygen migration from ceria to rh. *Journal of Catalysis*, 139(2):561 – 567, 1993. doi: 10.1006/jcat.1993.1049.

[183] G.S. Zafiris and R.J. Gorte. Evidence for a second co oxidation mechanism on rh/ceria. *Journal of Catalysis*, 143(1):86 – 91, 1993. doi: 10.1006/jcat.1993.1255.

[184] Z. Wu, M. Li, and S. H. Overbury. On the structure dependence of co oxidation over CeO_2 nanocrystals with well-defined surface planes. *Journal of Catalysis*, 285(1):61 – 73, 2012. doi: 10.1016/j.jcat.2011.09.011.

[185] R. S. J. Tol. The Economic Impacts of Climate Change. *Review of Environmental Economics and Policy*, 12(1):4–25, 2018. doi: 10.1093/reep/rex027.

[186] J. Ma, N. Sun, X. Zhang, N. Zhao, F. Xiao, W. Wei, and Y. Sun. A short review of catalysis for CO_2 conversion. *Catalysis Today*, 148(3):221 – 231, 2009. doi: 10.1016/j.cattod.2009.08.015.

[187] A. Samanta, A. Zhao, G. K. Shimizu, P. Sarkar, and R. Gupta. Post-combustion CO_2 capture using solid sorbents: A review. *Industrial & Engineering Chemistry Research*, 51(4):1438–1463, 2012. doi: 10.1021/ie200686q.

[188] E. M. Kock, M. Kogler, T. Bielz, B. Klatzer, and S. Penner. In situ ft-ir spectroscopic study of CO_2 and co adsorption on Y_2O_3, ZrO_2, and yttria-stabilized Zr_2. *The Journal of Physical Chemistry C*, 117(34):17666–17673, 2013. doi: 10.1021/jp405625x.

[189] G Pacchioni. Physisorbed and chemisorbed CO_2 at surface and step sites of the mgo(100) surface. *Surface Science*, 281(1):207 – 219, 1993. doi: 10.1016/0039-6028(93)90869-L.

[190] J. M. Polfus, B. Yildiz, H. L. Tuller, and R. Bredesen. Adsorption of CO_2 and facile carbonate formation on $BaZrO_3$ surfaces. *The Journal of Physical Chemistry C*, 122(1):307–314, 2018. doi: 10.1021/acs.jpcc.7b08223.

[191] C. C. Yang, Y. H. Yu, B. van der Linden, J. C. S. Wu, and G. Mul. Artificial photosynthesis over crystalline TiO_2-based catalysts: Fact or fiction? *Journal of the American Chemical Society*, 132(24):8398–8406, 2010. doi: 10.1021/ja101318k.

[192] M. Kotobuki, R. Leppelt, D.A. Hansgen, D. Widmann, and R.J. Behm. Reactive oxygen on a au/TiO_2 supported catalyst. *Journal of Catalysis*, 264(1):67 – 76, 2009. doi: 10.1016/j.jcat.2009.03.013.

[193] P. Konova, A. Naydenov, Cv. Venkov, D. Mehandjiev, D. Andreeva, and T. Tabakova. Activity and deactivation of au/TiO_2 catalyst in co oxidation. *Journal of Molecular Catalysis A: Chemical*, 213(2):235 – 240, 2004. doi: 10.1016/j.molcata.2003.12.021.

[194] B. Schumacher, Y. Denkwitz, V. Plzak, M. Kinne, and R.J. Behm. Kinetics, mechanism, and the influence of H_2 on the co oxidation reaction on a au/TiO_2 catalyst. *Journal of Catalysis*, 224(2):449 – 462, 2004. doi: 10.1016/j.jcat.2004.02.036.

[195] M. M. Schubert, A. Venugopal, M. J. Kahlich, V Plzak, and R.J. Behm. Influence of H_2O and CO_2 on the selective co oxidation in H_2-rich gases over au/a-Fe_2O_3. *Journal of Catalysis*, 222(1):32 – 40, 2004. doi: 10.1016/j.jcat.2003.08.015.

[196] S.T. Daniells, A.R. Overweg, M. Makkee, and J.A. Moulijn. The mechanism of low-temperature co oxidation with au/Fe_2O_3 catalysts: a combined mossbauer, ft-ir, and tap reactor study. *Journal of Catalysis*, 230(1):52 – 65, 2005. doi: 10.1016/j.jcat.2004.11.020.

[197] A. Hakim, T. S. Marliza, S. Tengku, T. Abu, M. Najiha, W. Isahak, W. N. Roslam, R. M. Yusop, H. Mohamed, M. Wahab, and A. M. Yarmo. Studies on CO_2 adsorption and desorption properties from various types of iron oxides (feo, Fe_2O_3, and fe3o4). *Industrial and Engineering Chemistry Research*, 55 (29):7888–7897, 2016. doi: 10.1021/acs.iecr.5b04091.

[198] H. Wijnja and C.P. Schulthess. Atr-ftir and drift spectroscopy of carbonate species at the aged y-Al_2O_3/water interface. *Spectrochimica Acta Part A: Molecular and Biomolecular Spectroscopy*, 55(4):861 – 872, 1999. doi: 10.1016/S1386-1425(98)00236-4.

[199] X. Can. Cerium oxide nanoparticle: a remarkably versatile rare earth nanomaterial for biological applications. *Npg Asia Materials*, 6(7):191–212, 2014. doi: 10.1038/am.2013.88.

[200] A. Bueno-Lopez. Diesel soot combustion ceria catalysts. *Applied Catalysis B: Environmental*, 146(7):1 – 11, 2014. doi: 10.1016/j.apcatb.2013.02.033.

[201] T. L. LeValley, A. R. Richard, and M. Fan. The progress in water gas shift and steam reforming hydrogen production technologies a review. *International Journal of Hydrogen Energy*, 39(30):16983 – 17000, 2014. doi: 10.1016/j.ijhydene.2014.08.041.

[202] M. Capdevila-Cortada, G. Vile, D. Teschner, J. Perez-Ramirez, and N. Lopez. Reactivity descriptors for ceria in catalysis. *Applied Catalysis B: Environmental*, 197(7):299 – 312, 2016. doi: 10.1016/j.apcatb.2016.02.035.

[203] J.M. Lavoie. Review on dry reforming of methane, a potentially more environmentally-friendly approach to the increasing natural gas exploitation. *Frontiers in Chemistry*, 2(7):81, 2014. doi: 10.3389/fchem.2014.00081.

[204] N. A. K. Aramouni, J. G. Touma, B. A. Tarboush, J. Zeaiter, and M. N. Ahmad. Catalyst design for dry reforming of methane: Analysis review. *Renewable and Sustainable Energy Reviews*, 82(7):2570 – 2585, 2018. doi: 10.1016/j.rser.2017.09.076.

[205] X. Liu, W. Ruettinger, X. Xu, and R. Farrauto. Deactivation of pt/CeO_2 water-gas shift catalysts due to shutdown/startup modes for fuel cell applications. *Applied Catalysis B: Environmental*, 56(1):69 – 75, 2005. doi: 10.1016/j.apcatb.2004.04.026.

[206] C. H. Kim and L. T. Thompson. Deactivation of au/ceox water gas shift catalysts. *Journal of Catalysis*, 230(1):66 – 74, 2005. doi: 10.1016/j.jcat.2004.10.004.

[207] W. Deng and M. Flytzani-Stephanopoulos. On the issue of the deactivation of au-ceria and pt-ceria water-gas shift catalysts in practical fuel-cell applications. *Angewandte Chemie International Edition*, 45(14):2285–2289, 2006. doi: 10.1002/anie.200503220.

[208] M. Cargnello, C. Gentilini, T. Montini, E. Fonda, S. Mehraeen, M. Chi, M. Herrera-Collado, N. D. Browning, S. Polizzi, L. Pasquato, and P.Fornasiero. Active and stable embedded auCeO_2 catalysts for preferential oxidation of co. *Chemistry of Materials*, 22(14):4335–4345, 2010. doi: 10.1021/cm101499x.

[209] S. D. Senanayake and D. R. Mullins. Redox pathways for hcooh decomposition over CeO_2 surfaces. *The Journal of Physical Chemistry C*, 112(26):9744–9752, 2008. doi: 10.1021/jp8016425.

[210] T. Staudt, Y. Lykhach, N. Tsud, T. Skala, K.C. Prince, V. Matolin, and J. Libuda. Ceria reoxidation by CO_2: A model study. *Journal of Catalysis*, 275(1):181 – 185, 2010. doi: 10.1016/j.jcat.2010.07.032.

[211] Y. Lykhach, T. Staudt, R. Streber, M. P.A.Lorenz, A. Bayer, H. P. Steinruck, and J. Libuda. CO_2 activation on single crystal based ceria and magnesia/ceria model catalysts. *Eur. Phys. J. B*, 75(1):89–100, 2010. doi: 10.1140/epjb/e2010-00110-x.

[212] P. M Albrecht, D. Jiang, and D. R. Mullins. CO_2 adsorption as a flat-lying, tridentate carbonate on $CeO_2(100)$. *The Journal of Physical Chemistry C*, 118 (17):9042–9050, 2014. doi: 10.1021/jp501201b.

[213] K. R. Hahn, M. Iannuzzi, A. P. Seitsonen, and J. Hutter. Coverage effect of the CO_2 adsorption mechanisms on $CeO_2(111)$ by first principles analysis. *The Journal of Physical Chemistry C*, 117(4):1701–1711, 2013. doi: 10.1021/jp309565u.

[214] Z. Cheng, B. J. Sherman, and C. S. Lo. Carbon dioxide activation and dissociation on ceria (110): A density functional theory study. *The Journal of Chemical Physics*, 138(1):014702, 2013. doi: 10.1063/1.4773248.

[215] G. S. Herman, Y. J. Kim, S. A. Chambers, and C. H. F. Peden. Interaction of D_2O with $CeO_2(001)$ investigated by temperature-programmed desorption and x-ray photoelectron spectroscopy. *Langmuir*, 15(11):3993–3997, 1999. doi: 10.1021/la990094u.

[216] T. Staudt, Y. Lykhach, N. Tsud, T. Skala, K. C. Prince, V. Matolin, and J. Libuda. Electronic structure of magnesia-ceria model catalysts, CO_2 adsorption, and CO_2 activation: A synchrotron radiation photoelectron spectroscopy study. *The Journal of Physical Chemistry C*, 115(17):8716–8724, 2011. doi: 10.1021/jp200382y.

[217] S. D. Senanayake, D. Stacchiola, J. Evans, M. Estrella, L. Barrio, M. Perez, J. Hrbek, and J. A. Rodriguez. Probing the reaction intermediates for the water-gas shift over inverse ceox/au(111) catalysts. *Journal of Catalysis*, 271 (2):392 – 400, 2010. doi: 10.1016/j.jcat.2010.02.024.

[218] P. Sudarsanam, B. Hillary, D. K. Deepa, M. H. Amin, B. Mallesham, B. M. Reddy, and S. K. Bhargava. Highly efficient cerium dioxide nanocube-based catalysts for low temperature diesel soot oxidation: the cooperative effect of cerium- and cobalt-oxides. *Catal. Sci. Technol.*, 5(7):3496–3500, 2015. doi: 10.1039/C5CY00525F.

[219] W. Huang and Y. Gao. Morphology-dependent surface chemistry and catalysis

of CeO_2 nanocrystals. *Catal. Sci. Technol.*, 4(7):3772–3784, 2014. doi: 10.1039/C4CY00679H.

[220] D. Gamarra, A. Lopez Camara, M. Monte, S.B. Rasmussen, L.E. Chinchilla, A.B. Hungria, G. Munuera, N. Gyorffy, Z. Schay, V. Cortes Corberan, J.C. Conesa, and A. Martinez-Arias. Preferential oxidation of co in excess H_2 over cuo/CeO_2 catalysts: Characterization and performance as a function of the exposed face present in the CeO_2 support. *Applied Catalysis B: Environmental*, 130-131(7):224 – 238, 2013. doi: 10.1016/j.apcatb.2012.11.008.

[221] Z. A. Feng, M. L. Machala, and W. C. Chueh. Surface electrochemistry of CO_2 reduction and co oxidation on sm-doped CeO_{2-x}: coupling between Ce^{3+} and carbonate adsorbates. *Phys. Chem. Chem. Phys.*, 17(7):12273–12281, 2015. doi: 10.1039/C5CP00114E.

[222] D. Wulf. Free radicals in the physiological control of cell function. *Physiological Reviews*, 82(1):47–95, 2002. doi: 10.1152/physrev.00018.2001.

[223] R. S. Balaban, S. Nemoto, and T. Finkel. Mitochondria, oxidants, and aging. *Cell*, 120(4):483 – 495, 2005. doi: 10.1016/j.cell.2005.02.001.

[224] M. Valko, D. Leibfritz, J. Moncol, M.T.D. Cronin, M. Mazur, and J. Telser. Free radicals and antioxidants in normal physiological functions and human disease. *The International Journal of Biochemistry and Cell Biology*, 39(1):44 – 84, 2007. doi: 10.1016/j.biocel.2006.07.001.

[225] L. Tong, C. C. Chuang, S. Wu, and L. Zuo. Reactive oxygen species in redox cancer therapy. *Cancer Letters*, 367(1):18 – 25, 2015. doi: 10.1016/j.canlet.2015.07.008.

[226] P. T. Schumacker. Reactive oxygen species in cancer: A dance with the devil. *Cancer Cell*, 27(2):156 – 157, 2015. doi: 10.1016/j.ccell.2015.01.007.

[227] J. Wu, X. Wang, Q. Wang, Z. Lou, S. Li, Y. Zhu, L. Qin, and H. Wei. Nanomaterials with enzyme like characteristics (nanozymes): next-generation artificial enzymes. *Chem. Soc. Rev.*, 48(7):1004–1076, 2019. doi: 10.1039/C8CS00457A.

[228] S. Das, J. M. Dowding, K. E. Klump, J. F. McGinnis, W. Self, and S. Seal. Cerium oxide nanoparticles: applications and prospects in nanomedicine. *Nanomedicine*, 8(9):1483–1508, 2013. doi: 10.2217/nnm.13.133.

[229] C. Walkey, S. Das, S. Seal, J. Erlichman, K. Heckman, L. Ghibelli, E. Traversa, J. F. McGinnis, and W. T. Self. Catalytic properties and biomedical applications of cerium oxide nanoparticles. *Environ. Sci.: Nano*, 2(7):33–53, 2015. doi: 10.1039/C4EN00138A.

[230] A. Karakoti, S. Singh, J. M. Dowding, S. Seal, and W. T. Self. Redox-active radical scavenging nanomaterials. *Chem. Soc. Rev.*, 39(7):4422–4432, 2010. doi: 10.1039/B919677N.

[231] H. Dong, S. R. Du, X. Y. Zheng, G. M. Lyu, L. D. Sun, L. D. Li, P. Z. Zhang, C. Zhang, and C. H. Yan. Lanthanide nanoparticles: From design toward bioimaging and therapy. *Chemical Reviews*, 115(19):10725–10815, 2015. doi: 10.1021/acs.chemrev.5b00091.

[232] A. S. Karakoti, S. Singh, A. Kumar, M. Malinska, S. Kuchibhatla, K. Wozniak, W. T. Self, and S. Seal. Pegylated nanoceria as radical scavenger with tunable redox chemistry. *Journal of the American Chemical Society*, 131(40):14144–14145, 2009. doi: 10.1021/ja9051087.

[233] C. Korsvik, S. Patil, S. Seal, and W. T. Self. Superoxide dismutase mimetic properties exhibited by vacancy engineered ceria nanoparticles. *Chem. Commun.*, 358(7):1056–1058, 2007. doi: 10.1039/B615134E.

[234] E. G. Heckert, A. S. Karakoti, S. Seal, and W. T. Self. The role of cerium redox state in the sod mimetic activity of nanoceria. *Biomaterials*, 29(18): 2705 – 2709, 2008. doi: 10.1016/j.biomaterials.2008.03.014.

[235] I. Celardo, J. Z. Pedersen, E. Traversa, and L. Ghibelli. Pharmacological potential of cerium oxide nanoparticles. *Nanoscale*, 3(7):1411–1420, 2011. doi: 10.1039/C0NR00875C.

[236] T. Pirmohamed, J. M. Dowding, S. Singh, B. Wasserman, E. Heckert, A. S. Karakoti, J. S. King, S. Seal, and W. T. Self. Nanoceria exhibit redox state-

dependent catalase mimetic activity. *Chem. Commun.*, 46(7):2736–2738, 2010. doi: 10.1039/B922024K.

[237] S. Singh, T. Dosani, A. S. Karakoti, A. Kumar, S. Seal, and W. T. Self. A phosphate-dependent shift in redox state of cerium oxide nanoparticles and its effects on catalytic properties. *Biomaterials*, 32(28):6745 – 6753, 2011. doi: 10.1016/j.biomaterials.2011.05.073.

[238] R. Singh and S. Singh. Role of phosphate on stability and catalase mimetic activity of cerium oxide nanoparticles. *Colloids and Surfaces B: Biointerfaces*, 132(7):78 – 84, 2015. doi: 10.1016/j.colsurfb.2015.05.005.

[239] L. Kong, X. Cai, X. Zhou, L. L. Wong, A. S. Karakoti, S. Seal, and J. F. McGinnis. Nanoceria extend photoreceptor cell lifespan in tubby mice by modulation of apoptosis/survival signaling pathways. *Neurobiology of Disease*, 42(3):514 – 523, 2011. doi: 10.1016/j.nbd.2011.03.004.

[240] I. Celardo, M. De Nicola, C. Mandoli, J. Z. Pedersen, E. Traversa, and L. Ghibelli. Ce^{3+} ions determine redox-dependent anti-apoptotic effect of cerium oxide nanoparticles. *ACS Nano*, 5(6):4537–4549, 2011. doi: 10.1021/nn200126a.

[241] R. W. Tarnuzzer, J. Colon, S. Patil, and S. Seal. Vacancy engineered ceria nanostructures for protection from radiation-induced cellular damage. *Nano Letters*, 5(12):2573–2577, 2005. doi: 10.1021/nl052024f.

[242] S. M. Hirst, A. S. Karakoti, R. D. Tyler, N. Sriranganathan, S. Seal, and C. R. Reilly. Anti-inflammatory properties of cerium oxide nanoparticles. *Small*, 5 (24):2848–2856, 2009. doi: 10.1002/smll.200901048.

[243] X. Liu, W. Wei, Q. Yuan, X. Zhang, N. Li, Y. Du, G. Ma, C. Yau, and D. Ma. Apoferritin-CeO_2 nanotruffle that has excellent artificial redox enzyme activity. *Chem. Commun.*, 48(7):3155–3157, 2012. doi: 10.1039/C1CC15815E.

[244] L. Rubio, B. Annangi, L. Vila, A. Hernandez, and R. Marcos. Antioxidant and anti-genotoxic properties of cerium oxide nanoparticles in a pulmonary-like cell system. *Archives of Toxicology*, 90(2):269–278, 2016. doi: 10.1007/s00204-015-1468-y.

[245] C. Mandoli, F. Pagliari, S. Pagliari, G. Forte, P. Di Nardo, S. Licoccia, and E. Traversa. Stem cell aligned growth induced by CeO_2 nanoparticles in plga scaffolds with improved bioactivity for regenerative medicine. *Advanced Functional Materials*, 20(10):1617–1624, 2010. doi: 10.1002/adfm.200902363.

[246] J. Niu, A. Azfer, L. M. Rogers, X. Wang, and P. E. Kolattukudy. Cardioprotective effects of cerium oxide nanoparticles in a transgenic murine model of cardiomyopathy. *Cardiovascular Research*, 73(3):549–559, 2007. doi: 10.1016/j.cardiores.2006.11.031.

[247] F. Pagliari, C. Mandoli, G. Forte, E. Magnani, S. Pagliari, G. Nardone, S. Licoccia, M. Minieri, P. Di Nardo, and E. Traversa. Cerium oxide nanoparticles protect cardiac progenitor cells from oxidative stress. *ACS Nano*, 6(5):3767–3775, 2012. doi: 10.1021/nn2048069.

[248] A. Asati, S. Santra, C. Kaittanis, S. Nath, and J. M. Perez. Oxidase like activity of polymer-coated cerium oxide nanoparticles. *Angewandte Chemie International Edition*, 48(13):2308–2312, 2009. doi: 10.1002/anie.200805279.

[249] A. Asati, C. Kaittanis, S. Santra, and M. J. Perez. ph-tunable oxidase like activity of cerium oxide nanoparticles achieving sensitive fluorigenic detection of cancer biomarkers at neutral ph. *Analytical Chemistry*, 83(7):2547–2553, 2011. doi: 10.1021/ac102826k.

[250] J. Chen, S. Patil, S. Seal, and J. McGinnis. Rare earth nanoparticles prevent retinal degeneration induced by intracellular peroxides. *Nature Nanotechnology*, 1(7):142–150, 2006. doi: 10.1038/nnano.2006.91.

[251] M. Das, S. Patil, N. Bhargava, J. F. Kang, L. M. Riedel, S. Seal, and J. J. Hickman. Auto-catalytic ceria nanoparticles offer neuroprotection to adult rat spinal cord neurons. *Biomaterials*, 28(10):1918 – 1925, 2007. doi: 10.1016/j.biomaterials.2006.11.036.

[252] K. L. Heckman, W. DeCoteau, A. Estevez, K. J. Reed, W. Costanzo, D. Sanford, J. C. Leiter, J. Clauss, K. Knapp, C. Gomez, P. Mullen, E. Rathbun, K. Prime, J. Marini, J. Patchefsky, A. S. Patchefsky, R. K. Hailstone, and J. S.

Erlichman. Custom cerium oxide nanoparticles protect against a free radical mediated autoimmune degenerative disease in the brain. *ACS Nano*, 7(12): 10582–10596, 2013. doi: 10.1021/nn403743b.

[253] J. M. Downing, W. Song, K. Bossy, A. Karokoti, A. Kumar, A. Kim, B. Bossy, S. Seal, M. H. Ellisman, and G. Perkins. Cerium oxide nanoparticles protect against ab-induced mitochondrial fragmentation and neuronal cell death. *Cell Death and Differentitation*, 21(7):1622–1632, 2014. doi: 10.1038/cdd.2014.72.

[254] H. K. Kwon, M. Y. Cha, D. Kim, D. K. Kim, M. Soh, K. Shin, T. Hyeon, and I. Mook-Jung. Mitochondria targeting ceria nanoparticles as antioxidants for alzheimers disease. *ACS Nano*, 10(2):2860–2870, 2016. doi: 10.1021/acsnano.5b08045.

[255] A. Asati, S. Santra, C. Kaittanis, and J. M. Perez. Surface charge dependent cell localization and cytotoxicity of cerium oxide nanoparticles. *ACS Nano*, 4 (9):5321–5331, 2010. doi: 10.1021/nn100816s.

[256] L. Peng, X. He, P. Zhang, J. Zhang, Y. Li, J. Zhang, Y. Ma, Y. Ding, Z. Wu, Z. Chai, and Z. Zhang. Comparative pulmonary toxicity of two ceria nanoparticles with the same primary size. *International Journal of Molecular Sciences*, 15(4):6072–6085, 2014. doi: 10.3390/ijms15046072.

[257] T. Xia, M. Kovochich, M. Liong, L. Madler, B. Gilbert, S. H. Hi, J. I. Yeh, J. I. Zink, and A. E. Nel. Comparison of the mechanism of toxicity of zinc oxide and cerium oxide nanoparticles based on dissolution and oxidative stress properties. *ACS Nano*, 2(10):2121–2134, 2008. doi: 10.1021/nn800511k.

[258] R. A. Yokel, S. Hussain, S. Garantziotis, P. Demokritou, V. Castranova, and F. R. Cassee. The yin: an adverse health perspective of nanoceria: uptake, distribution, accumulation, and mechanisms of its toxicity. *Environ. Sci.: Nano*, 1(7):406–428, 2014. doi: 10.1039/C4EN00039K.

[259] L. Alili, M. Sack, A. S. Karakoti, S. Teuber, K. Puschmann, S. M. Hirst, C. M. Reilly, K. Zanger, W. Stahl, S. Das, S. Seal, and P. Brenneisen. Combined

cytotoxic and anti-invasive properties of redox-active nanoparticles in tumor-stroma interactions. *Biomaterials*, 32(11):2918 – 2929, 2011. doi: 10.1016/j.biomaterials.2010.12.056.

[260] L. Alili, M. Sack, A. S. Karakoti, S. Teuber, K. Puschmann, S. M. Hirst, C. M. Reilly, K. Zanger, W. Stahl, S. Das, S. Seal, and P. Brenneisen. Combined cytotoxic and anti-invasive properties of redox-active nanoparticles in tumor-stroma interactions. *Biomaterials*, 32(11):2918 – 2929, 2011. doi: 10.1016/j.biomaterials.2010.12.056.

[261] J.Kullgren, K. Hermansson, and P. Broqvist. Supercharged low-temperature oxygen storage capacity of ceria at the nanoscale. *The Journal of Physical Chemistry Letters*, 4(4):604–608, 2013. doi: 10.1021/jz3020524.

[262] G. Preda, A. Migani, K. M. Neyman, S. T. Bromley, F. Illas, and G. Pacchioni. Formation of superoxide anions on ceria nanoparticles by interaction of molecular oxygen with Ce^{3+} sites. *The Journal of Physical Chemistry C*, 115(13):5817–5822, 2011. doi: 10.1021/jp111147y.

[263] M. Huang and S. Fabris. Role of surface peroxo and superoxo species in the low-temperature oxygen buffering of ceria: Density functional theory calculations. *Phys. Rev. B*, 75(7):081404, 2007. doi: 10.1103/PhysRevB.75.081404.

[264] C. Walling. Intermediates in the reactions of fenton type reagents. *Accounts of Chemical Research*, 31(4):155–157, 1998. doi: 10.1021/ar9700567.

[265] Y. Xue, Q. Luan, D. Yang, X. Yao, and K. Zhou. Direct evidence for hydroxyl radical scavenging activity of cerium oxide nanoparticles. *The Journal of Physical Chemistry C*, 115(11):4433–4438, 2011. doi: 10.1021/jp109819u.

[266] S. Singh. Cerium oxide based nanozymes: Redox phenomenon at biointerfaces. *Biointerphases*, 11(4):04B202, 2016. doi: 10.1116/1.4966535.

[267] Y. Guerin, GS. Was, and SJ. Zinkle. Materials challenges for advanced nuclear energy systems. *MRS Bulletin*, 34(7):10, 2009.

[268] N. A. Brincat, M. Molinari, G. C. Allen, M. T. Storr, and S. C. Parker. Density functional theory calculations of defective UO_2 at U_3O_7 stoichiometry. *Journal*

of Nuclear Materials, 467(7):724, 2015. doi: doi.org/10.1016/j.jnucmat.2015.10.006.

[269] N. A. Brincat, M. Molinari, G. C. Allen, M. T. Storr, and S. C. Parker. Density functional theory investigation of the layered uranium oxides U_3O_8 and U_2O_5. *Dalton Transactions*, 44(7):2613, 2015. doi: doi.org/10.1039/c4dt02493a).

[270] P. Taylor, D. D. Wood, A. M. Duclos, and D. G. Owen. Formation of uranium trioxide hydrates on UO_2 fuel in airsteam mixtures near 200c. *Journal of Nuclear Materials*, 168(7):70, 1989. doi: doi.org/10.1016/0022-3115(89)90566-7.

[271] J. F. Marin and P. Contamin. Uranium and oxygen self-diffusion in UO_2. *Journal of Nuclear Materials*, 30(7):16, 1969. doi: doi.org/10.1016/0022-3115(69)90164-0.

[272] A.C.S. Sabioni, W.B. Ferraz, and F. Millot. Effect of grain-boundaries on uranium and oxygen diffusion in polycrystalline UO_2. *Journal of Nuclear Materials*, 278(2):364 – 369, 2000. doi: 10.1016/S0022-3115(99)00250-0.

[273] K. Govers and M. Verwerft. Classical molecular dynamics investigation of microstructure evolution and grain boundary diffusion in nano-polycrystalline UO_2. *Journal of Nuclear Materials*, 438(1):134 – 143, 2013. doi: 10.1016/j.jnucmat.2013.03.024.

[274] T. Arima, K. Yoshida, K. Idemitsu, Y. Inagaki, and I. Sato. Molecular dynamics analysis of diffusion of uranium and oxygen ions in uranium dioxide. *IOP Conference Series: Materials Science and Engineering*, 9(7):012003, 2010. doi: doi.org/10.1088/1757-899X/9/1/012003.

[275] E. Vincent-Aublant, J. M. Delaye, and L. Van Brutzel. Self-diffusion near symmetrical tilt grain boundaries in UO_2 matrix: A molecular dynamics simulation study. *Journal of Nuclear Materials*, 394(7):114, 2010. doi: doi.org/10.1016/j.jnucmat.2009.03.059.

[276] N. R. Williams, M. Molinari, S. C. Parker, and M. T. Storr. Atomistic investigation of the structure and transport properties of tilt grain bound-

aries of UO_2. *Journal of Nuclear Materials*, 458(10):45 – 55, 2015. doi: 10.1016/j.jnucmat.2014.11.120.

[277] Y. Lin, S. Fang, D. Su, K. S. Brinkman, and F. Chen. Enhancing grain boundary ionic conductivity in mixed ionic-electronic conductors. *Nature Communications*, 6(7):6824, 2015. doi: doi.org/10.1038/ncomms7824.

[278] X. Guo, W. Sigle, and J. Maier. Blocking grain boundaries in yttria-doped and undoped ceria ceramics of high purity. *Journal of the American Ceramic Society*, 86(1):77–87, 2003. doi: 10.1111/j.1151-2916.2003.tb03281.x.

[279] X. Guo, W. Sigle, J. Fleig, and J. Maier. Role of space charge in the grain boundary blocking effect in doped zirconia. *Solid State Ionics*, 154-155(10): 555 – 561, 2002. doi: 10.1016/S0167-2738(02)00491-5.

[280] R. A. De Souza. The formation of equilibrium space-charge zones at grain boundaries in the perovskite oxide $SrTiO_3$. *Phys. Chem. Chem. Phys.*, 11 (10):9939–9969, 2009. doi: 10.1039/B904100A.

[281] D. M. Duffy. Grain boundaries in ionic crystals. *Journal of Physics and Condensed Matter*, 19(7):4393, 1986. doi: doi.org/10.1088/0022-3719/19/23/005.

[282] A. K. Lucid and G. W. Watson. The importance of polarizability in the modeling of ionic diffusion in ceria. *IOP Conference Series: Materials Science and Engineering*, 169(7):012002, 2017. doi: 10.1088/1757-899x/169/1/012002.

[283] C. R. A. Catlow and J. S. Anderson. Point defect and electronic properties of uranium dioxide. *Proceedings of the Royal Society of London. A. Mathematical and Physical Sciences*, 353(1675):533–561, 1977. doi: 10.1098/rspa.1977.0049.

[284] N.D. Morelon, D. Ghaleb, J.M. DelMorelonye, and L. Van Brutzel. A new empirical potential for simulating the simulation of defects and their mobility in uranium dioxide. 2003.

[285] G. Brillant, F. Gupta, and A. Pasturel. Fission products stability in uranium dioxide. *Journal of Nuclear Materials*, 412(1):170 – 176, 2011. doi: 10.1016/j.jnucmat.2011.02.054.

[286] J. C. Goldsby. Basic elastic properties predictions of cubic uranium oxide using first-principles methods. *Journal of Ceramics*, 2013(7):4, 2013. doi: 10.1155/2013/323018.

[287] V. Kanchana, G. Vaitheeswaran, A. Svane, and A. Delin. First-principles study of elastic properties of CeO_2, tho2 and poo2. *Journal of Physics: Condensed Matter*, 18(42):9615–9624, 2006. doi: 10.1088/0953-8984/18/42/008.

[288] C. Sevik and T. Cagin. Mechanical and electronic properties of CeO_2, ThO_2, and Ce/ThO_2 alloys. *Phys. Rev. B*, 80(7):014108, 2009. doi: 10.1103/PhysRevB.80.014108.

[289] I. J. Fritz. Elastic properties of UO_2 at high pressure. *Journal of Applied Physics*, 47(10):4353–4358, 1976. doi: 10.1063/1.322438.

[290] W. Smith and T.R. Forester. Dl_poly2.0: A general-purpose parallel molecular dynamics simulation package. *Journal of Molecular Graphics*, 14(3):136 – 141, 1996. doi: 10.1016/S0263-7855(96)00043-4.

[291] B. Feng, T. Yokoi, A. Kumamoto, M. Yoshiya, Y. Ikuhara, and N. Shibata. Atomically ordered solute segregation behaviour in an oxide grain boundary. *Nature Communications*, 7(10):11079, 2016. doi: 10.1038/ncomms11079.

[292] P. V. Nerikar, D. C. Parfitt, L. A. C. Trujillo, D. A. Andersson, C. Unal, S. B. Sinnott, R. W. Grimes, B. P. Uberuaga, and C. R. Stanek. Segregation of xenon to dislocations and grain boundaries in uranium dioxide. *Phys. Rev. B*, 84(10):174105, 2011. doi: 10.1103/PhysRevB.84.174105.

[293] L. Pajo. 1 UO_2 fuel pellet impurities, pellet face roughness and n(18o)/n(16o) ratios, applied to nuclear forensic science, 2010.

[294] A.B. Auskern and J. Belle. Uranium ion self diffusion in UO_2. *Journal of Nuclear Materials*, 3(3):311 – 319, 1961. doi: 10.1016/0022-3115(61)90199-4.

[295] I.L.F. Ray, H. Thiele, and Hj. Matzke. Transmission electron microscopy study of fission product behaviour in high burnup UO_2. *Journal of Nuclear Materials*, 188(10):90 – 95, 1992. doi: 10.1016/0022-3115(92)90458-W.

[296] A.G. Evans and R.W. Davidge. The strength and fracture of stoichiometric polycrystalline UO_2. *Journal of Nuclear Materials*, 33(3):249 – 260, 1969. doi: 10.1016/0022-3115(69)90019-1.

[297] D. J. Wronkiewicz, J. K. Bates, T. J. Gerding, E. Veleckis, and B. S. Tani. Uranium release and secondary phase formation during unsaturated testing of UO_2 at 90c. *Journal of Nuclear Materials*, 190(10):107 – 127, 1992. doi: 10.1016/0022-3115(92)90081-U.

[298] J.B. Ainscough, B.W. Oldfield, and J.O. Ware. Isothermal grain growth kinetics in sintered UO_2 pellets. *Journal of Nuclear Materials*, 49(2):117 – 128, 1973. doi: 10.1016/0022-3115(73)90001-9.

[299] D. J. Wronkiewicz, J. K. Bates, S. F. Wolf, and E. C. Buck. Ten-year results from unsaturated drip tests with UO_2 at 90c: implications for the corrosion of spent nuclear fuel. *Journal of Nuclear Materials*, 238(1):78 – 95, 1996. doi: 10.1016/S0022-3115(96)00383-2.

[300] K.C. Radford and J.M. Pope. UO_2 fuel pellet microstructure modification through impurity additions. *Journal of Nuclear Materials*, 116(2):305 – 313, 1983. doi: 10.1016/0022-3115(83)90116-2.

[301] I.J. Hastings, J.A. Scoberg, and Kathy MacKenzie. Grain growth in UO_2: in-reactor and laboratory testing. *Journal of Nuclear Materials*, 82(2):435 – 438, 1979. doi: 10.1016/0022-3115(79)90026-6.

[302] R. F. Canon, J. T. Roberts, and R. J. Beals. Deformation of UO_2 at high temperatures. *Journal of the American Ceramic Society*, 54(2):105–112, 1971. doi: 10.1111/j.1151-2916.1971.tb12230.x.

[303] N. Kazuhiro and U. Katsumi. Thermal recovery of radiation defects and microstructural change in irradiated UO_2 fuels. *Journal of Nuclear Science and Technology*, 30(9):900–910, 1993. doi: 10.1080/18811248.1993.9734564.

[304] T. M. Aldazharov, Y. G. Rusin, Z. H V. Eremeeva, and T. A. Ryspaev. Preparation methods and production of initial materials to prepare gadolinium oxide pellets used in fabrication of composite uranium–gadolinium fuel.

Russian Journal of Non-Ferrous Metals, 58(3):292–296, 2017. doi: 10.3103/S1067821217030026.

[305] C.O.T. Galvin, M.W.D. Cooper, M.J.D. Rushton, and R.W. Grimes. Oxygen diffusion in gd-doped mixed oxides. *Journal of Nuclear Materials*, 498(10):300 – 306, 2018. doi: 10.1016/j.jnucmat.2017.10.036.

[306] M. W. D. Cooper, S. T. Murphy, P. C. M. Fossati, M. J. D. Rushton, and R. W. Grimes. Thermophysical and anion diffusion properties of UO_2. *Proceedings of the Royal Society A: Mathematical, Physical and Engineering Sciences*, 470 (2171):20140427, 2014. doi: 10.1098/rspa.2014.0427.

[307] J.L. Kloosterman. Application of boron and gadolinium burnable poison particles in UO_2 and pu/UO_2 fuels in htrs. *Annals of Nuclear Energy*, 30(17): 1807 – 1819, 2003. doi: 10.1016/S0306-4549(03)00134-8.

[308] M. Asou and J. Porta. Prospects for poisoning reactor cores of the future. *Nuclear Engineering and Design*, 168(1):261 – 270, 1997. doi: 10.1016/S0029-5493(96)01322-2.

[309] T. Wakabayashi and I. Minatsuki. Critical experiments on gadolinium poisoned cluster-type fuel assemblies in heavy water lattices. *Nuclear Science and Engineering*, 83(1):50–62, 1983. doi: 10.13182/NSE83-A17988.

[310] H.G. Riella, M. Durazzo, M. Hirata, and R.A. Nogueira. UO_2-Gd_2O_3 solid solution formation from wet and dry processes. *Journal of Nuclear Materials*, 178(2):204 – 211, 1991. doi: 10.1016/0022-3115(91)90387-M.

[311] H. Kleykamp. The chemical state of the fission products in oxide fuels. *Journal of Nuclear Materials*, 131(2):221 – 246, 1985. doi: 10.1016/0022-3115(85)90460-X.

[312] C. Ronchi and J.P. Hiernaut. Helium diffusion in uranium and plutonium oxides. *Journal of Nuclear Materials*, 325(1):1 – 12, 2004. doi: 10.1016/j.jnucmat.2003.10.006.

[313] B. L. Deng, X. F. Tian, J. Zhai, and Y. F. Hu. Effect of fission xe on diffusion of oxygen and uranium in UO_2: a molecular dynamics study. *Indian Journal of Physics*, 88(11):1183–1189, 2014. doi: 10.1007/s12648-014-0573-8.

[314] E. Moore, L. R. Corrales, T. Desai, and R. Devanathan. Molecular dynamics simulation of xe bubble nucleation in nanocrystalline UO_2 nuclear fuel. *Journal of Nuclear Materials*, 419(1):140 – 144, 2011. doi: 10.1016/j.jnucmat.2011.08.052.

[315] D.R. Olander and P. Van Uffelen. On the role of grain boundary diffusion in fission gas release. *Journal of Nuclear Materials*, 288(2):137 – 147, 2001. doi: 10.1016/S0022-3115(00)00725-X.

[316] C.T. Walker, P. Knappik, and M. Mogensen. Concerning the development of grain face bubbles and fission gas release in UO_2 fuel. *Journal of Nuclear Materials*, 160(1):10 – 23, 1988. doi: 10.1016/0022-3115(88)90003-7.

[317] U. Katsumi and K. Shinji. Fission gas release during post irradiation annealing of bwr fuels. *Journal of Nuclear Science and Technology*, 27(11):1002–1016, 1990. doi: 10.1080/18811248.1990.9731285.

[318] M. O. Tucker. Grain boundary porosity and gas release in irradiated UO_2. *Radiation Effects*, 53(3-4):251–255, 1980. doi: 10.1080/00337578008207120.

[319] L. E. Thomas. *Condensed-Phase Xenon and Krypton in UO_2 Spent Fuel*, pages 431–441. Number 10. Boston, MA, 1991. doi: 10.1007/978-1-4899-3680-6_37.

[320] C.T. Walker, C. Bagger, and M. Mogensen. Observations on the release of cesium from UO_2 fuel. *Journal of Nuclear Materials*, 240(1):32 – 42, 1996. doi: 10.1016/S0022-3115(96)00477-1.

[321] C.T. Walker and K. Lassmann. Fission gas and caesium gradients in single grains of transient tested UO_2 fuel: Results of an epma investigation. *Journal of Nuclear Materials*, 138(2):155 – 161, 1986. doi: 10.1016/0022-3115(86)90001-2.

[322] M. Akabori and K. Fukuda. Release behavior of cesium in irradiated (th, u)O_2. *Journal of Nuclear Materials*, 186(1):47 – 53, 1991. doi: 10.1016/0022-3115(91)90351-7.

[323] B.M. Jeffery. Microanalysis of inclusions in irradiated UO_2. *Journal of Nuclear Materials*, 22(1):33 – 40, 1967. doi: 10.1016/0022-3115(67)90106-7.

[324] A. A. Solomon. Influence of impurity particles on the fracture of UO_2. *Journal of the American Ceramic Society*, 55(12):622–627, 1972. doi: 10.1111/j.1151-2916.1972.tb13456.x.

[325] K. Minato, T. Ogawa, K. Fukuda, M. Shimizu, Y. Tayama, and I. Takahashi. Fission product behavior in triso-coated UO_2 fuel particles. *Journal of Nuclear Materials*, 208(3):266 – 281, 1994. doi: 10.1016/0022-3115(94)90336-0.

[326] D.R. O'boyle, F.L. Brown, and J.E. Sanecki. Solid fission product behavior in uranium-plutonium oxide fuel irradiated in a fast neutron flux. *Journal of Nuclear Materials*, 29(1):27 – 42, 1969. doi: 10.1016/0022-3115(69)90124-X.

[327] K. Minato, K. Sawa, T. Koya, T. Tomita, A. Ishikawa, C. A. Baldwin, W. A. Gabbard, and C. M. Malone. Fission product release behavior of individual coated fuel particles for high-temperature gas-cooled reactors. *Nuclear Technology*, 131(1):36–47, 2000. doi: 10.13182/NT00-A3103.

[328] B.T. Bradbury, J.T. Demant, P.M. Martin, and D.M. Poole. Electron probe micro-analysis of irradiated UO_2. *Journal of Nuclear Materials*, 17(3):227 – 236, 1965. doi: 10.1016/0022-3115(65)90166-2.

[329] M. Born and K. Huang. Dynamical theory of crystal lattices. *American Journal of Physics*, 23(7):474–474, 1955. doi: 10.1119/1.1934059.

[330] R.C. Ewing. Longterm storage of spent nuclear fuel. *Nature Materials*, 14 (10):252 – 257, 1985. doi: doi:10.1038/nmat4226.

[331] M. Hong, B. P. Uberuaga, S. R. Phillpot, D. A. Andersson, C. R Stanek, and S. B. Sinnott. The role of charge and ionic radius on fission product segregation to a model UO_2 grain boundary. *Journal of Applied Physics*, 113(13):134902, 2013. doi: 10.1063/1.4798347.

[332] J. Hugo, Avila-Paredes, and K. Sangtae. The effect of segregated transition metal ions on the grain boundary resistivity of gadolinium doped ceria: Alteration of the space charge potential. *Solid State Ionics*, 177(35):3075 – 3080, 2006. doi: 10.1016/j.ssi.2006.08.017.

[333] J.P. Hiernaut, T. Wiss, D. Papaioannou, R.J.M. Konings, and V.V. Rondinella. Volatile fission product behaviour during thermal annealing of irradiated UO_2 fuel oxidised up to U_3O_8. *Journal of Nuclear Materials*, 372 (2):215 – 225, 2008. doi: 10.1016/j.jnucmat.2007.03.174.

[334] A.B. Lidiard. Self-diffusion of uranium in UO_2. *Journal of Nuclear Materials*, 19(1):106 – 108, 1966. doi: 10.1016/0022-3115(66)90138-3.

[335] T. Kubo, S.Ishimoto, and T. K. Ama. Effects of gadolinium doping on electrical properties of UO_2 grain boundaries. *Journal of Nuclear Science and Technology*, 30(7):664–672, 1993. doi: 10.1080/18811248.1993.9734532.

[336] J. Tucek, L. Machala, S. Ono, A. Namai, M. Yoshikiyo, K. Imoto, T. Hokoro, S. T. Ohkoshi, and R. Zboril. Zeta-Fe_2O_3 - a new stable polymorph in iron(iii) oxide family. *Scientific reports*, 5(7):15091, 2015. doi: 10.1038/srep15091.

[337] D. H. Templeton and C. H. Dauben. Lattice parameters of some rare earth compounds and a set of crystal radii. *Journal of the American Chemical Society*, 76(20):5237–5239, 1954. doi: 10.1021/ja01649a087.

[338] V. Dordevic, Z. Antic, M. Nikolic, and M. Dramicanin. Comparative structural and photoluminescent study of Eu^{3+}-doped La_2O_3 and $La(OH)_3$ nanocrystalline powders. *Journal of Physics and Chemistry of Solids*, 75(7):765456, 2013. doi: 10.1016/j.jpcs.2013.10.004.

[339] O. Manoilova, S. Podkolzin, B. Tope, J. Lercher, E. Stangland, J. Goupil, and B. Weckhuysen. Surface acidity and basicity of La_2O_3, laocl, and $LaCl_3$ characterized by ir spectroscopy, tpd, and dft calculations. *The Journal of Physical Chemistry B*, 108(7):87657, 2004. doi: 10.1021/jp040311m.

[340] B. Li and H. Metiu. Dft studies of oxygen vacancies on undoped and doped

La_2O_3 surfaces. *Journal of Physical Chemistry C - J PHYS CHEM C*, 114(7): 12234–12244, 2010. doi: 10.1021/jp103604b.

[341] N. Shibata, Y. Ikuhara, F. Oba, T. Yamamoto, and T. Sakuma. Atomic structure and solute segregation of a 3[110]/111 grain boundary in an yttria-stabilized cubic zirconia bicrystal. *Philosophical Magazine Letters*, 82(7):393–400, 2002. doi: 10.1080/09500830210137407.

[342] L. Minervini, M. O. Zacate, and R. W. Grimes. Defect cluster formation in M_2O_3-doped CeO_2. *Solid State Ionics*, 116(3):339 – 349, 1999. doi: 10.1016/S0167-2738(98)00359-2.

[343] G. Arora and D. S. Aidhy. Segregation and binding energetics at grain boundaries in fluorite oxides. *J. Mater. Chem. A*, 5(10):4026–4035, 2017. doi: 10.1039/C6TA09895A.

[344] M. Yoshiya and T. Oyama. Impurity and vacancy segregation at symmetric tilt grain boundaries in Y_2O_3-doped ZrO_2. *Journal of Materials Science*, 46 (12):4176–4190, 2011. doi: 10.1007/s10853-011-5352-8.

[345] Y. Lei, Y. Ito, N. D. Browning, and T. J. Mazanec. Segregation effects at grain boundaries in fluorite-structured ceramics. *Journal of the American Ceramic Society*, 85(9):2359–2363, 2002. doi: 10.1111/j.1151-2916.2002.tb00460.x.

[346] K. McKenna and A. Shluger. The interaction of oxygen vacancies with grain boundaries in monoclinic HfO_2. *Applied Physics Letters*, 95(22):222111, 2009. doi: 10.1063/1.3271184.

[347] W. Lee, H. J. Jung, M.H. Lee, Y. B. Kim, J. S. Park, R. Sinclair, and F. B. Prinz. Oxygen surface exchange at grain boundaries of oxide ion conductors. *Advanced Functional Materials*, 22(5):965–971, 2012. doi: 10.1002/adfm.201101996.

[348] Y.M. Chiang, E.B. Lavik, and D.A. Blom. Defect thermodynamics and electrical properties of nanocrystalline oxides: pure and doped CeO_2. *Nanostructured Materials*, 9(1):633 – 642, 1997. doi: 10.1016/S0965-9773(97)00142-6.

[349] H. Matzke. Atomic transport properties in UO_2 and mixed oxides $UPuO_2$. *J. Chem. Soc., Faraday Trans. 2*, 83(10):1121–1142, 1987. doi: 10.1039/F29878301121.

[350] F. Palheiros, R. Gonzaga, and A. Soares. Comparative study of the different industrial manufacturing routes for UO_2 pellet specifications through the wet process, 2009.

[351] H. Guo, C. Tian, X. Wang, N. Lv, M. Ma, and Y. Wei. Decay chain deduction of uranium fission products. *Health Physics*, 1(10):17–21, 2016. doi: doi.org/10.1097/HP.0000000000005211.

[352] B. C. H. Steele. Ceramic ion conducting membranes. *Current Opinion in Solid State and Materials Science*, 1(5):684 – 691, 1996. doi: 10.1016/S1359-0286(96)80052-0.

[353] H. Inaba and H. Tagawa. Ceria-based solid electrolytes. *Solid State Ionics*, 83 (1):1 – 16, 1996. doi: 10.1016/0167-2738(95)00229-4.

[354] S. Park, J. M. Vohs, and R. J. Gorte. Direct oxidation of hydrocarbons in a solid-oxide fuel cells. *Nature*, 404(7):265 – 267, 2000. doi: 10.1038/35005040.

[355] J. Sunarso, S. Baumann, J.M. Serra, W.A. Meulenberg, S. Liu, Y.S. Lin, and J.C. Diniz da Costa. Mixed ionic-electronic conducting (miec) ceramic-based membranes for oxygen separation. *Journal of Membrane Science*, 320(1):13 – 41, 2008. doi: 10.1016/j.memsci.2008.03.074.

[356] G. C. H. Steele. Materials for fuel-cell technologies. *Nature*, 414(7):345, 2001. doi: 10.1038/35104620.

[357] B. C. H. Steele. Appraisal of $Ce_{1-y}Gd_yO_2{-}y/2$ electrolytes for it-sofc operation at 500c. *Solid State Ionics*, 129(1):95 – 110, 2000. doi: 10.1016/S0167-2738(99)00319-7.

[358] R. A. De Souza, M. J. Pietrowski, U. Anselmi-Tamburini, S. Kim, Z. A. Munir, and M. Martin. Oxygen diffusion in nanocrystalline yttria-stabilized zirconia: the effect of grain boundaries. *Phys. Chem. Chem. Phys.*, 10(7):2067–2072, 2008. doi: 10.1039/B719363G.

[359] U. Anselmi-Tamburini, F. Maglia, G. Chiodelli, A. Tacca, G. Spinolo, P. Riello, S. Bucella, and Z. A. Munir. Nanoscale effects on the ionic conductivity of highly doped bulk nanometric cerium oxide. *Advanced Functional Materials*, 16(18):2363–2368, 2006. doi: 10.1002/adfm.200500415.

[360] Z. P. Li, T. Mori, G. J. Auchterlonie, J. Zou, and J. Drennan. Direct evidence of dopant segregation in gd-doped ceria. *Applied Physics Letters*, 98(9):093104, 2011. doi: 10.1063/1.3556650.

[361] S. Kim, J. Fleig, and J. Maier. Space charge conduction: Simple analytical solutions for ionic and mixed conductors and application to nanocrystalline ceria. *Phys. Chem. Chem. Phys.*, 5(7):2268–2273, 2003. doi: 10.1039/B300170A.

[362] J. Maier. Nanoionics: ion transport and electrochemical storage in confined systems. *Nature Materials*, 4(7):805, 2005. doi: 10.1038/nmat1513.

[363] D. S. Gunn, N. L. Allan, and J. A. Purton. Adaptive kinetic monte carlo simulation of solid oxide fuel cell components. *J. Mater. Chem. A*, 2(7):13407–13414, 2014. doi: 10.1039/C4TA01504E.

[364] S. S. Lee, W. Song, M. Cho, H. L. Puppala, P. Nguyen, H. Zhu, L. Segatori, and V. L. Colvin. Antioxidant properties of cerium oxide nanocrystals as a function of nanocrystal diameter and surface coating. *ACS Nano*, 7(11): 9693–9703, 2013. doi: 10.1021/nn4026806.

[365] C. A.J. Fisher and H. Matsubara. The influence of grain boundary misorientation on ionic conductivity in ysz. *Journal of the European Ceramic Society*, 19(6):703 – 707, 1999. doi: 10.1016/S0955-2219(98)00300-8.

[366] M. C. Gobel, G. Gregori, and J. Maier. Electronically blocking grain boundaries in donor doped cerium dioxide. *Solid State Ionics*, 215(7):45 – 51, 2012. doi: 10.1016/j.ssi.2012.03.036.

[367] J. Maier. Pushing nanoionics to the limits: Charge carrier chemistry in extremely small systems. *Chemistry of Materials*, 26(1):348–360, 2014. doi: 10.1021/cm4021657.

[368] E. Ruiz-Trejo, J. D. Sirman, Yu. M. Baikov, and J. A. Kilner. Oxygen ion diffusivity, surface exchange and ionic conductivity in single crystal gadolinia doped ceria. *Solid State Ionics*, 113-115(7):565 – 569, 1998. doi: 10.1016/S0167-2738(98)00323-3.

[369] F. Zhang, S. W. Chan, J. E. Spanier, E. Apak, Q. Jin, R. D. Robinson, and I. P. Herman. Cerium oxide nanoparticles: Size-selective formation and structure analysis. *Applied Physics Letters*, 80(1):127–129, 2002. doi: 10.1063/1.1430502.

[370] J. Maier. On the conductivity of polycrystalline materials. *Berichte der Bunsengesellschaft fur physikalische Chemie*, 90(1):26–33, 1986. doi: 10.1002/bbpc.19860900105.

[371] Y. M. Chiang, E. B. Lavik, I. Kosacki, H. L. Tuller, and J. Y. Ying. Defect and transport properties of nanocrystalline CeO_{2-x}. *Applied Physics Letters*, 69(2):185–187, 1996. doi: 10.1063/1.117366.

[372] M. C. Gobel, G. Gregori, X. Guo, and J. Maier. Boundary effects on the electrical conductivity of pure and doped cerium oxide thin films. *Phys. Chem. Chem. Phys.*, 12(7):14351–14361, 2010. doi: 10.1039/C0CP00385A.

[373] S. Kim and J. Maier. On the conductivity mechanism of nanocrystalline ceria. *Journal of The Electrochemical Society*, 149(10):J73–J83, 2002. doi: 10.1149/1.1507597.

[374] S. J. Hong, K. Mehta, and A. V. Virkar. Effect of microstructure and composition on ionic conductivity of rare earth oxide doped ceria. *Journal of The Electrochemical Society*, 145(2):638–647, 1998. doi: 10.1149/1.1838316.

[375] R. Gerhardt and A. S. Npwick. Grain-boundary effect in ceria doped with trivalent cations: I, electrical measurements. *Journal of the American Ceramic Society*, 69(9):641–646, 1986. doi: 10.1111/j.1151-2916.1986.tb07464.x.

[376] Y. Inaguma, J. Yu, T. Katsumata, and M. Itoh. Lithium ion conductivity in a perovskite lanthanum lithium titanate single crystal. *J. Ceram. Soc. Jpn.*, 105(1222):548–550, 1997. doi: 10.2109/jcersj.105.548.

[377] Y. Inaguma, L. Chen, M. Itoh, and T. Nakamura. Candidate compounds with perovskite structure for high lithium ionic conductivity. *Solid State Ion.*, 70-71 (7):196 – 202, 1994. doi: 10.1016/0167-2738(94)90309-3.

[378] Y. Inaguma, C. Liquan, M. Itoh, T. Nakamura, T. Uchida, H. Ikuta, and M. Wakihara. High ionic conductivity in lithium lanthanum titanate. *Solid State Commun.*, 86(10):689 – 693, 1993. doi: 10.1016/0038-1098(93)90841-A.

[379] A. Lindman, T. S. Bjorheim, and G. Wahnstrom. Defect segregation to grain boundaries in $BaZrO_3$ from first-principles free energy calculations. *J. Mater. Chem. A*, 5(7):13421–13429, 2017. doi: 10.1039/C7TA01080J.

[380] J. A. Purton and N. L. Allan. Multi-million atom monte carlo simulation of oxide materials and solid solutions. *Computational Materials Science*, 103(7): 244 – 249, 2015. doi: 10.1016/j.commatsci.2015.03.016.

[381] J. A. Purton, A. Archer, N. L. Allan, and D. S. D. Gunn. Growth of nano-domains in gd doped CeO_2 mixtures: hybrid monte carlo simulations. *J. Mater. Chem. A*, 4(7):4592–4602, 2016. doi: 10.1039/C5TA07506H.

[382] J. A. Purton, N. L. Allan, and D. S.D. Gunn. Simulations of doped CeO_2 at finite dopant concentrations. *Solid State Ionics*, 299(7):32 – 37, 2017. doi: 10.1016/j.ssi.2016.09.017.

[383] J. A. Purton. Diffusion in gadolinium doped ceria thin films: a combined monte carlo and molecular dynamics study. *Phys. Chem. Chem. Phys.*, 21(7): 9802–9809, 2019. doi: 10.1039/C8CP07136E.

[384] H. J. Avila-Paredes and S. Kim. The effect of segregated transition metal ions on the grain boundary resistivity of gadolinium doped ceria: Alteration of the space charge potential. *Solid State Ionics*, 177(35):3075 – 3080, 2006. doi: 10.1016/j.ssi.2006.08.017. Proceedings of the E-MRS Symposium P on Solid State Ionics: Mass and Charge Transport at Various Length Scales.

[385] S. Schmidt, W. Sigle, W. Gust, and M. Ruhle. Gallium segregation at grain boundaries in aluminium. *Zeitschrift für Metallkunde*, 93(5):428–431, 2002. doi: 10.3139/146.020428.

[386] V.A. Phillips. New evidence for segregation at grain boundaries, subgrain boundaries and dislocations in dilute iron-carbon-nitrogen alloys. *Acta Metallurgica*, 11(10):1139 – 1150, 1963. doi: 10.1016/0001-6160(63)90041-5.

[387] M. P. Seah, E. D> Hondros, and A. Kelly. Grain boundary segregation. *Proceedings of the Royal Society of London. A. Mathematical and Physical Sciences*, 335(1601):191–212, 1973. doi: 10.1098/rspa.1973.0121.

[388] M. P. Seah. Grain boundary segregation. *Journal of Physics F: Metal Physics*, 10(6):1043–1064, 1980. doi: 10.1088/0305-4608/10/6/006.

[389] M. P. Seah and C. Lea. Surface segregation and its relation to grain boundary segregation. *The Philosophical Magazine: A Journal of Theoretical Experimental and Applied Physics*, 31(3):627–645, 1975. doi: 10.1080/14786437508226543.

[390] J. Nowotny. Surface segregation of defects in oxide ceramic materials. *Solid State Ionics*, 28-30(7):1235 – 1243, 1988. doi: 10.1016/0167-2738(88)90363-3.

[391] J.A. Purton, J.C. Crabtree, and S.C. Parker. Dl_monte: a general purpose program for parallel monte carlo simulation. *Molecular Simulation*, 39(14-15): 1240–1252, 2013. doi: 10.1080/08927022.2013.839871.

[392] E. S. Ilton and P. S. Bagus. Xps determination of uranium oxidation states. *Surface and Interface Analysis*, 43(13):1549–1560, 2011. doi: 10.1002/sia.3836.

[393] R.J. McEachern and P. Taylor. A review of the oxidation of uranium dioxide at temperatures below 400°c. *Journal of Nuclear Materials*, 254(2):87 – 121, 1998. doi: 10.1016/S0022-3115(97)00343-7.

[394] N. A. Brincat, M. Molinari, G. C. Allen, M. T. Storr, and S. C. Parker. Density functional theory calculations of defective UO_2 at U_3O_7 stoichiometry. *Journal of Nuclear Materials*, 467(7):724 – 729, 2015. doi: 10.1016/j.jnucmat.2015.10.006.

[395] N. Liu, J. Kim, J. Lee, J. Youn, J. Kim, J. Kim, J. J. Noel, and D. W. Shoesmith. Influence of gd doping on the structure and electrochemi-

cal behavior of UO_2. *Electrochimica Acta*, 247(7):496 – 504, 2017. doi: 10.1016/j.electacta.2017.07.006.

[396] M. Razdan and D. W. Shoesmith. The electrochemical reactivity of 6.0 wt% gd-doped UO_2 in aqueous carbonate/bicarbonate solutions. 161(4):$H_2$25–$H_2$34, 2014. doi: 10.1149/2.050404jes.

[397] S. Oswald, G. Behr, D. Dobler, J. Werner, K. Wetzig, and W. Arabczyk. Specific properties of fine UO_2 powders connected with surface segregation. *Analytical and Bioanalytical Chemistry*, 378(2):411–415, 2004. doi: 10.1007/s00216-003-2277-3.

A Appendix A

A.1 Reduction Temperatures

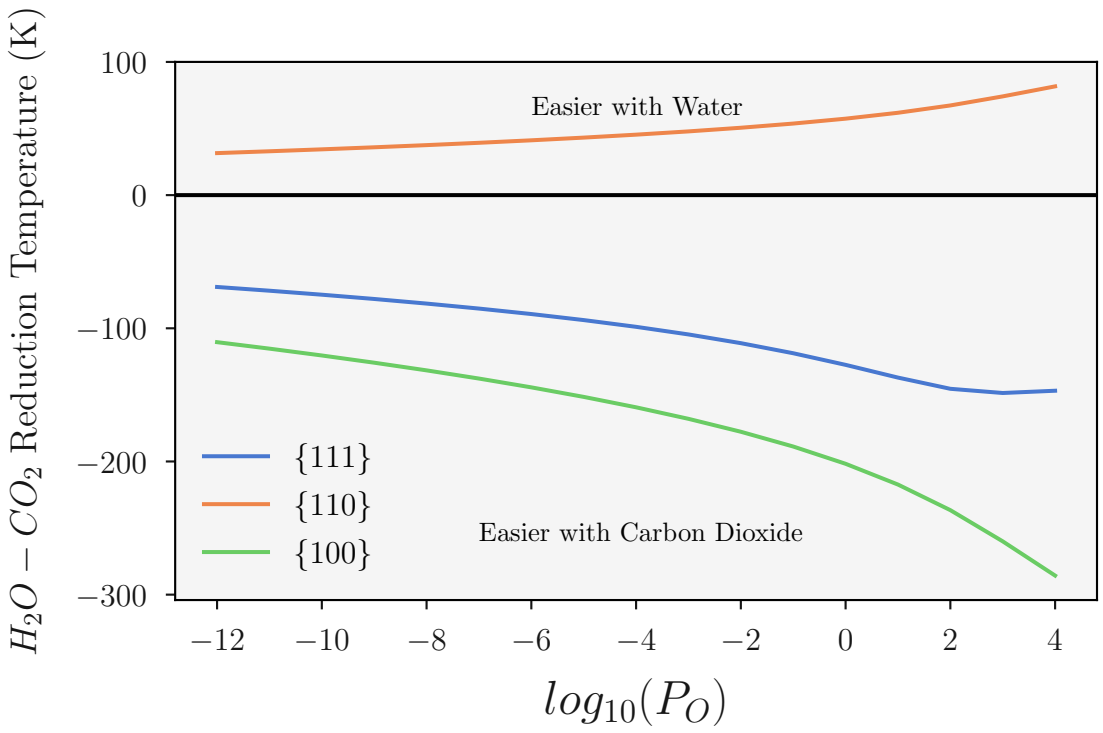

Figure A.1: Difference between the reduction temperature on surfaces with water and surfaces with carbon dioxide. If the difference is positive, the surface will reduce at a lower temperature when in the prescence of water and if it is negative the surface with reduce at a lower temperature in the prescence of carbon dioxide.

A.2 Scheme 1 - Hydroxylated Surfaces

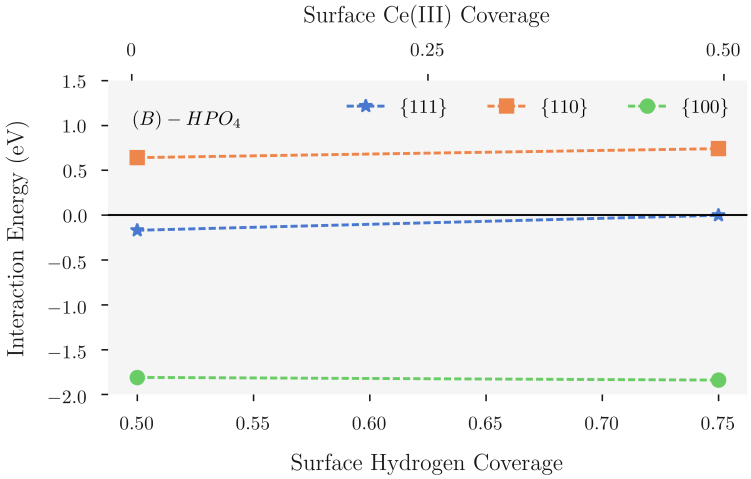

Figure A.2: The reaction energy for phosphate adsorption on the {111} (blue), {110} (orange) and {100} (green) surfaces at constant oxygen stoichiometry, varying hydrogen concentration and varying Ce^{3+} concentration.

A.3 Scheme 2 - CeO_{2-x} Surfaces

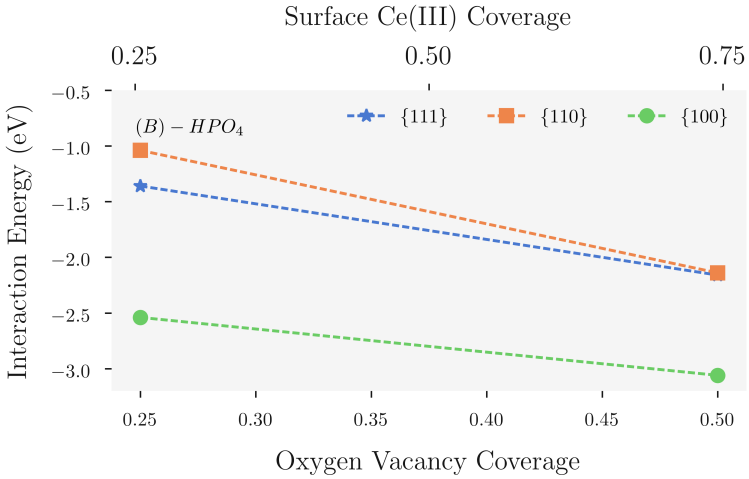

Figure A.3: The reaction energy for phosphate adsorption on the {111} (blue), {110} (orange) and {100} (green) surfaces at varying oxygen stoichiometry and varying Ce^{3+} concentration.

A.4 Scheme 3 - Hydroxylated CeO_{2-x} Surface

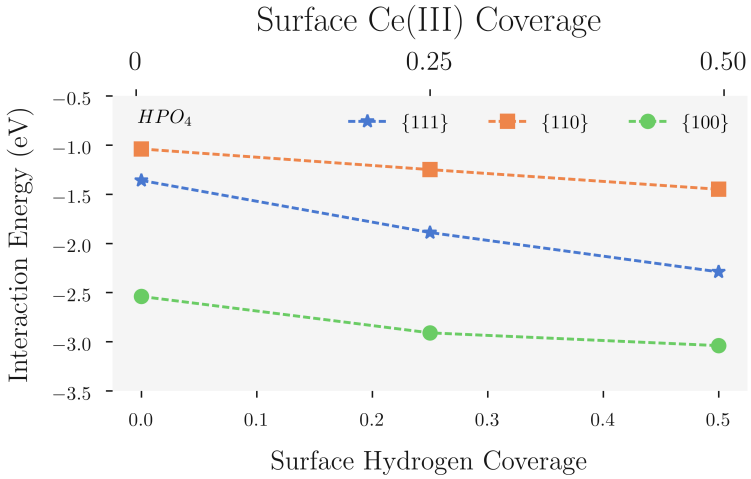

Figure A.4: The reaction energy for phosphate adsorption on the {111} (blue), {110} (orange) and {100} (green) surfaces at constant, but sub-stoichiometric oxygen stoichiometry, varying hydrogen concentration and varying Ce^{3+} concentration.